THE NORDIC CONCRETE FEDERATION 2/2011 PUBLICATION NO. 44

Nordic Concrete Research

Nordic Concrete Federation

PUBLICATION NO. 44 2/2011

NORDIC CONCRETE RESEARCH

EDITED BY
THE NORDIC CONCRETE FEDERATION

CONCRETE ASSOCIATIONS OF: DENMARK
FINLAND
ICELAND
NORWAY
SWEDEN

PUBLISHER: NORSK BETONGFORENING
POSTBOKS 2312, SOLLI
N - 0201 OSLO
NORWAY

VODSKOV, DECEMBER 2011

Preface

Nordic Concrete Research is since 1982 the leading scientific journal concerning concrete research in the five Nordic countries, e.g., Denmark, Finland, Iceland, Norway and Sweden. The content of Nordic Concrete Research reflects the major trends in the concrete research.

Nordic Concrete Research is published by the Nordic Concrete Federation that beside the publication activity also organizes the Nordic Concrete Research Symposia that have constituted a continuous series since 1953 in Stockholm. The Symposium circulates between the five countries and takes place every third year. The XXI Symposium on Nordic Concrete Research and Development was held in Hämeenlinna, Finland from 30 May to 1 June 2011. The next symposium, no. XXII, will be held Reykjavik, Iceland 17 – 19 June 2013 only two years ahead, just before an already planned conference, ECO-CRETE 19 – 21 June 2013.

During the latest years, growing interests in participating in the Nordic Concrete Research symposia, as well as for publishing in NCR have been observed.

Since 1982, 378 papers have been published in the journal. Since 1994 the abstracts and from 1998 both the abstracts and the full papers can be found on the Nordic Concrete Federation's homepage: www.nordicconcrete.org

Vodskov, December 2011

Dirch H. Bager
Editor, Nordic Concrete Research

PUBLICATION NO. 44 2/2011

CONTENTS

Fatigue life of high performance grout in dry and wet environment for wind turbine grouted connections

Eigil V. Sørensen
Ph.D., Associate Professor
Department of Civil Engineering, Aalborg University, Denmark
E-mail: evs@civil.aau.dk

ABSTRACT

The cementitious material in grouted connections of offshore monopile wind turbine structures is subjected to very high oscillating service stresses. The fatigue capacity of the grout therefore becomes essential to the performance and service life of the grouted connection.

In the present work the fatigue life of a high performance cement based grout was tested by dynamic compressive loading of cylindrical specimens at varying levels of cyclic frequency and load. The fatigue tests were performed in two series, one with the specimens tested in air and one with the specimens submerged in water during the test.

The fatigue life of the grout, in terms of the number of cycles to failure, was found to be significantly shorter when tested in water than when tested in air, particularly at low frequency.

Key words: High performance grout, dynamic loading, fatigue resistance, test environment, offshore wind turbine.

1. INTRODUCTION

The foundation of an offshore wind turbine often consists of a steel monopile driven into the sea bed (Fig. 1). At the upper end of the pile a transition piece, i.e. a steel tube with a larger diameter than the pile, is connected to the pile by casting a cementitious grout in the annulus between the pile and the transition piece. The thickness of the grout layer is normally in the range 50 – 125 mm. The transition piece has a flange at its top to which the first section of the tower is bolted.

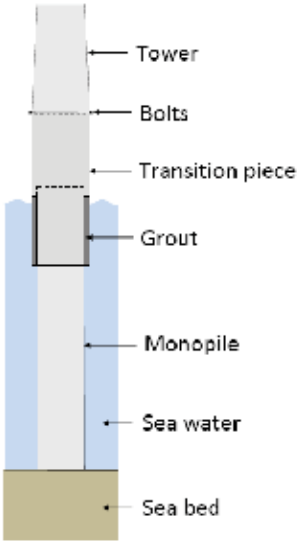

Figure 1 - Illustration of grouted connection

Recently it was found that cylindrically shaped grouted connections tend to have their load carrying capacity reduced with time when subjected to alternating dynamic bending moments [1].

The grouted connection is subjected to both axial (vertical) load from the dead weight of the structure above the connection, and moment due to the wind action on the blades and the tower, and due to wave action on the structure. Reaction pressure develops in the grout to resist the bending moment which induces high stresses in the grout locally at the grout section ends. This may lead to local fracture and crushing of the grout [1].

The stresses will typically appear periodically as oscillations caused by the wind and wave action. Hence, the resistance against fatigue failure of the grout material under dynamic compressive loading becomes essential to the performance and service life of the grouted connection. Furthermore, it has been found that the fatigue capacity of concrete subjected to stress ranges in compression is reduced when the concrete is surrounded by water rather than by air [1]. Due to the lack of fatigue test data for grout in water the DNV has recommended that further tests be performed [1].

The objective of the study presented in this paper was to investigate the fatigue capacity of a high performance grout material designed for grouted connections, in air as well as in water.

2. EXPERIMENTAL

2.1 Materials

The grouts used for grouted connections are usually high performance cementitious materials. The grout investigated in the present study was a commercially available product based on a high performance cementitious binder material, containing microsilica and other mineral additions, and being prepared at ultra-low water to cementitious material ratio facilitated by a high dosage of superplasticizing admixture. The aggregate consisted of natural sand with a maximum grain size of 4 mm.

Due to its composition the grout develops an extremely dense microstructure and attains a very high compressive strength and an excellent durability to resist the harsh marine service environment.

Mechanical properties of the grout were measured after 28 days curing in water at 20°C [2]. The details of the testing and the results are presented in Table 1.

Table 1. Mechanical properties of the grout after 28 days curing in water at 20°C

Property	Specimen type	Test standard	Result
Compressive strength	Cubes, 75x75x75 mm	EN 12390-3	141 MPa
Flexural strength	Mortar bars 40x40x160 mm	EN 196-1	18.4 MPa
Splitting tensile strength	Cylinders ø100x200 mm	EN 12390-6	8.6 MPa
Modulus of elasticity	Cylinders ø100x200 mm	EN 13412	50.9 GPa
Poisson's ratio	Cylinders ø100x200 mm	-	0.199

Traditional cement based grouts prepared at water to cement ratios by weight of about 0.40 and below exhibit significant shrinkage, even when sealed against loss of moisture to the surroundings. This so-called autogenous shrinkage increases with decreasing water to cement ratio [3]. The autogenous shrinkage of the present grout was measured over a period of 315 days and was found to be negligible due to shrinkage compensating measures included in the material formulation [2]. The lack of autogenous shrinkage enhances the friction between the grout and the steel surface of the grouted connection.

2.2 Fatigue test

The behaviour of the grout under cyclic loading was studied using cylindrical specimens, 60 mm in diameter and 120 mm high. The cylinders were stored in mould at 20°C for one day, then demoulded and stored in water at 20° until testing. The cylinder ends were ground plane immediately prior to using them for the test.

The tests were performed using a 500 kN servo-hydraulic test machine from MTS. At each stress range level the static compressive strength was first determined using 6 specimens at a loading rate of 0.88 MPa/s. Then another 6 specimens were tested in cyclic compressive loading, force controlled, with a minimum force of 20 kN, corresponding to a stress of 7.1 MPa, and the specified maximum force/stress, applied sinusoidally at a constant frequency. The minimum force of 20 kN was chosen to secure an efficient fixation of the specimen in the

testing machine at all times. The cyclic loading was continued until the specimen broke, or until it had been subjected to about 2 million loading cycles.

During the test the free (curved) surface of the specimen was surrounded by either the ambient air or by tap water held in a container placed around the specimen. Tests were run at constant frequency at three levels: 0.35 Hz (simulating real-time wave action), 5 Hz, and 10 Hz, and at three load levels: 45%, 60%, and 76% of the static compressive strength.

At the time of test all of the specimens could be characterized as mature. Their age varied from 4 to 26 months, during which period their compressive strength was virtually constant at a level of about 170 MPa, cf. Fig. 2.

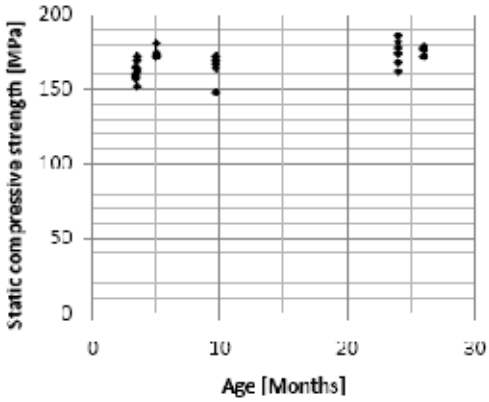

Figure 2. Static compressive strength vs. age of fatigue specimens

3 RESULTS AND DISCUSSION

The results of the fatigue tests are shown in Table 2 for each individual specimen tested. In general, each test series (at a given max. stress level, environment, and frequency) comprised 6 specimens. However, when testing at 0.35 Hz it takes more than two months to reach two million cycles, for which reason such test series were limited to a couple of specimens, and in one case the fatigue test had to be terminated after about 1.5 million cycles for practical reasons. The series at 60% stress level, in air, at 5 Hz contains only 3 results because 3 out of the 6 specimens were discarded due to incomplete compression surfaces. Two test series were performed in air at 76% stress because one of them was originally planned to be tested at a higher stress level but was limited by the capacity of the testing machine. The two series give an indication of the reproducibility of the test. At the 60% stress level all combinations of test environment and load frequency were investigated.

Table 2. Results of the fatigue tests

Max. stress level (% of the static compressive strength)	Environment	Max. No. of cycles at frequency: 0.35 Hz	5Hz	10 Hz
45%	**In water**	>1,537,229		
60%	**In air**	>2,000,000	>2,666,547	>2,000,007
		>2,000,000	>2,042,980	>2,000,007
			>2,039,759	1,223,862
			71,161	247,247
			41,554	164,451
			4,364	4,212
	In water	11,640	260,964	260,243
		9,158	135,153	151,062
		7,714	119,684	148,605
		6,744		123,141
		2,287		113,094
		3,248		33,324
76%	**In air**			23,535
				15,554
				7,486
				5,076
				4,180
				2,823
				18,496
				7,787
				3,337
				2,853
				1,300
				1,096
	In water	3,012		
		1,843		
		1,491		
		1,264		
		1,261		
		1,133		

It can be seen from Table 2 that there is a considerable scatter of the results within each test series. This is in line with the behaviour found for normal concrete which also shows large spread of fatigue capacity. Since it is impossible to measure the static compressive strength of each individual fatigue specimen by a non-destructive method, an uncertainty is introduced from the variation of the static compressive strength in the specimen population. The generally accepted procedure - as used in this work - is to base the alternating load on the predetermined mean compressive strength of a certain number of specimens tested prior to the commencement of the fatigue test. However, it has been shown that the variation of the true compressive strength, although it is usually relatively low, may have a significant impact on the apparent fatigue life [4]. This effect might be suspected to be even more pronounced for the more brittle high performance concrete.

The experimental data are shown in Fig. 3 as the ratio of the maximum stress to the static compressive strength versus the number of load cycles to failure (or until discontinuation of the test).

For comparison of the results of the high performance grout to ordinary concrete tested in air the relationship proposed by Aas-Jakobsen [5] is also shown in Fig. 3:

$$\frac{f_{max}}{f_c} = 1 - 0.064\left(1 - \frac{f_{min}}{f_{max}}\right) log_{10} N$$

where

f_{max} = the fatigue strength (the maximum stress of the load cycle)
f_c = the static compressive strength (= 170 MPa)
f_{min} = the minimum stress of the load cycle (= 7.1 MPa)
N = the number of load cycles to failure

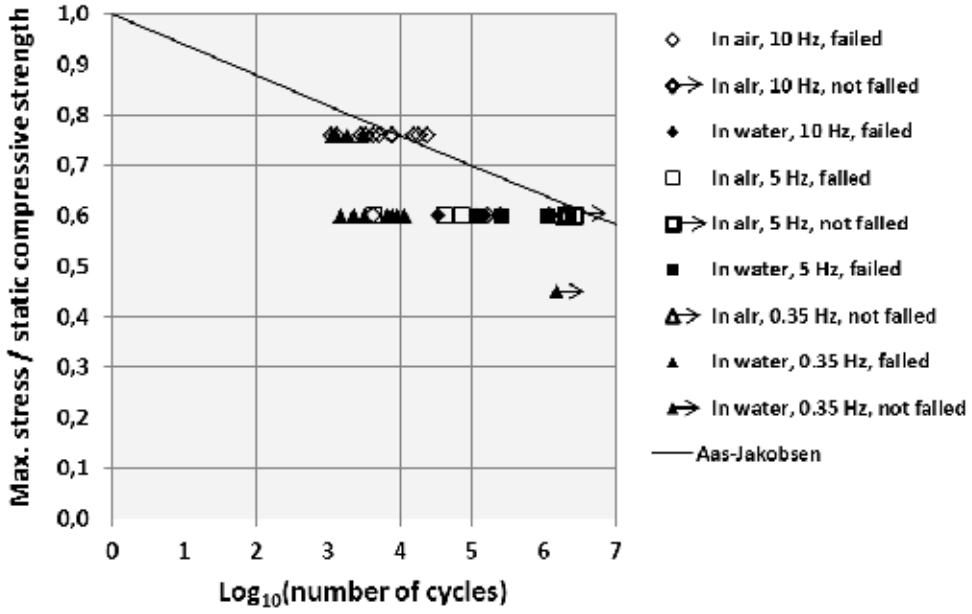

Figure 3 - Ratio of maximum stress to static compressive strength versus the number of load cycles to failure (or until discontinuation of the test).

Aas-Jakobsen's formula is considered to be a fair model for predicting the average fatigue life of plain concrete, tested in air, up to a loading level of 80% of the static compressive strength [7]. Hence, Fig. 3 shows that the results for those of the high performance grout specimens which were tested in air (open marks) agree with the behaviour of ordinary concrete tested in air, when the general scatter of fatigue results is taken into account.

However, the specimens tested in water (filled marks) exhibit markedly shorter fatigue life than those tested in air. This aspect is further illustrated in Fig. 4 showing the fatigue results at the 60% maximum stress level. Bearing in mind that several of the specimens tested in air survived

more than 2 million cycles it can be seen that testing in water led to shorter fatigue life at all of the frequencies investigated.

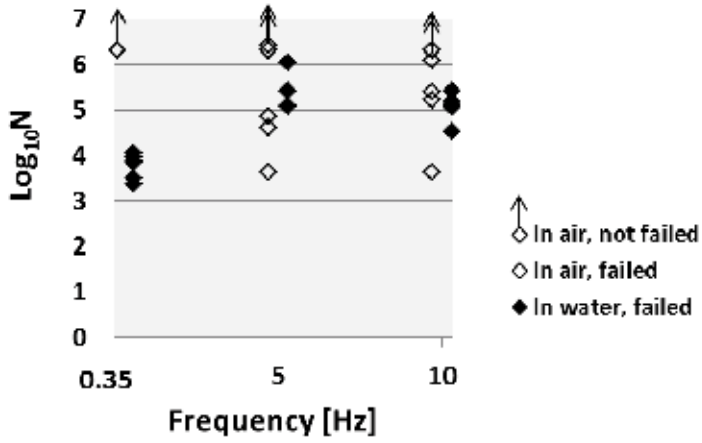

Figure 4 - Number of load cycles to failure (or stop) versus the frequency of the cyclic loading, at 60% maximum stress

The fatigue life in air seems to be almost independent of the loading frequency, having at least 2 specimens in each series surviving 2 million load cycles. This is in agreement with findings for ordinary concrete in the frequency range 0.1 to 200 Hz, when the maximum stress is lower than about 75% of the static compressive strength and any effect of creep therefore can be disregarded [4].

The specimens tested in water, however, showed significantly shorter fatigue life at 0.35 Hz than at either 5 Hz or 10 Hz.

The effect of testing concrete under water saturated or dry conditions is not fully understood, and some of the previously reported data are contradictory. Some tests have shown that the moisture condition of concrete prior to loading affects its fatigue capacity in flexure: oven-dried specimens show the highest strength and partially dried ones the lowest; wet specimens are in between. This behaviour was proposed to originate in differential strains induced by the moisture gradient [3]. Others have reported that dry specimens performed better than water saturated/submerged specimens and suggested that this reduced capacity was the result of a wedging action of water trapped in cracks [6]

In the present investigation the fatigue life in water was significantly reduced at both 5 Hz and 10 Hz as compared to testing in air. Actually, due to the way the specimens were cured prior to the testing, those tested in air were in fact partially dried, but nevertheless showed the highest fatigue capacity. Hence, possible differential strains induced by moisture gradients are not able to explain the fatigue life reduction observed in this study. This is even more pronounced at 0,35 Hz since the lower frequency by itself is not able to explain the drastically reduced fatigue life as mentioned above. Hence, it appears more probable that the effect of the surrounding water is to create internal stresses in the material.

It is well established that the general mechanism leading to failure of concrete under loading is the progressive formation of micro cracks as the stress level of the material is increased, and predominantly tensile stress which also occurs under compressive loading of an unconfined concrete cylinder. As more micro cracks are formed they will tend to merge and eventually provide access to the specimen surface and allow ingress of the surrounding water into the microstructure of the material. If water is trapped in cracks and pores in the microstructure during compression it may exert pressures high enough to contribute to crack opening and further crack formation. This might be expected to be particularly severe for high performance grout due to its brittle nature. Also, water pumping back and forth in the micro cracks could be suspected to cause degrading erosion – although no evidence to that effect could be observed, neither as debris in the water container nor by visual inspection of the specimen surface after the test.

The fact that the greatest reduction of fatigue life in water compared to air was observed at the (very) low frequency of 0.35 Hz might be explained by the lower frequency providing more time during each load cycle for sufficient water ingress and pressure build-up to cause damage.

It should be noted that at the lowest level of maximum stress investigated, i.e. 45% of the static compressive strength, the specimen tested in water survived more than 1.5 million load cycles and so might be expected to have satisfactory fatigue behaviour at that stress level.

Further tests are recommended to provide experimental evidence of the proposed microstructural changes due to dynamic loading in air and in water, including additional tests at lower stress levels relevant to the design loads.

4 CONCLUSIONS

Investigation of the fatigue behaviour in compression of a high performance cement based grout designed and used for grouted connections in offshore wind turbine structures showed that the fatigue life of the grout is comparable to that of ordinary concrete when tested in air.

When tested while the specimens were submerged in water, however, the grout exhibits drastically shorter fatigue life at maximum stress levels of 60% of the static compressive strength and above.

In air, the frequency of the loading (0.35 Hz, 5 Hz, and 10 Hz) has no influence on the fatigue life. In water, however, the fatigue capacity is substantially lower at 0.35 Hz than at either 5 Hz or 10 Hz.

It is suggested that the observed influence of water surrounding the specimens during fatigue testing is due to the water entering into the microstructure of the grout as micro cracks develop and merge, and subsequently may be trapped during the cyclic loading and exert pressures high enough to contribute to crack opening and further crack formation. This effect is more pronounced at low loading frequency with longer time available for water ingress and pressure build-up in each load cycle.

A single test at 45% maximum stress level and low frequency gave no indication of fatigue life reduction due to testing in water.

ACKNOWLEDGEMENT

The support of BASF A/S commissioning a large part of the tests described in the present paper and permitting publication of the results is gratefully acknowledged.

REFERENCES

1. "Joint Industry Project – Summary Report from the JIP on the Capacity of Grouted Connections in Offshore Wind Turbine Structures". Det Norske Veritas, Report No. 2010-1053, Revision No. 05 (2011)
2. Sørensen, E. V.: "Mechanical Properties of High Performance Cementitious Grout". DCE Contract Report No. 66, Aalborg University, Department of Civil Engineering, Aalborg, Denmark (2009)
3. Neville, A. M.: "Properties of Concrete". Pearson Education Limited. Fourth Edition (2008)
4. Tepfers, A. and Kutti, T.: "Fatigue Strength of Plain, Ordinary, and Lightweight Concrete". *ACI Journal* / May 1979, pp. 635 – 652
5. Aas-Jakobsen, K.: "Fatigue of concrete beams and columns". NTH Institutt for Betongkonstruktioner, Trondheim, Norway, Bulletin No. 70-1, p. 148, September 1970.
6. Mor, A.,, Gerwick, B. C., and Hester, W. T.: "Fatigue of high-strength reinforced concrete". *ACI Materials Journal*, **89**, No. 2, pp. 197-207 (1992)
7. Dyduch, K., Szerszen, M. and Destrebecq, J.-F.: "Experimental investigation of the fatigue strength of plain concrete under high compressive loading". *Materials and Structures,* **27,** pp. 505-509 (1994)

Photocatalytic cementitious materials containing highly active nanosized TiO_2: Mechanisms of air pollution remediation and the effect of the alkaline environment

Andrea Folli
M.Sc., Ph.D.
DTI - PostDoc Fellow
Gregersensvej 4
DK-2630 Taastrup (DK)
anfl@teknologisk.dk

ABSTRACT

The present work offers a general overview about application of titanium dioxide (or titania), TiO_2, photocatalysis to concrete technology in relation to depollution properties achieved by implementing TiO_2 into cement. Chemistry of oxidation of nitrogen oxides (NOx), gaseous atmospheric pollutants responsible for acid rains and photochemical smog, is investigated using a commercial available nanosized titania sample, n-TiO_2, in mortar specimens (average particle size 18.4 nm ± 5.0 nm). Experimental data on photocatalytic performances are discussed in relation to the physical chemical properties of the photocatalyst and the chemical environment of cement. Impacts on applications in construction concrete are also discussed.

Key words: TiO_2, photocatalytic concrete, visible light, NOx.

1. INTRODUCTION

The photochemistry of TiO_2 has become a subject of intense research since Fujishima and Honda [1] and Wrighton et al. [2] reported the photocatalytic splitting of water on TiO_2 and Sr-doped TiO_2 respectively in the 1970s. Applications of TiO_2 photocatalysts to construction materials began towards the end of the 1980s. Two important effects related to the nature of photoactive TiO_2 coatings had by this time been discovered: a) the self-cleaning effect due to redox reactions promoted by sunlight (or in general, weak U.V. light) on the photocatalyst surface [3], and b) the photo-induced hydrophilicity [4, 5] of the catalyst surface, which enhances the self-cleaning effect (inorganics causing dirt and stains on surfaces can be easily removed due to rainwater soaking between the adsorbed substance and the TiO_2 surface). Photocatalytic glasses provide an example of self-cleaning and anti-fogging (wetting) properties, e.g. Pilkington Active™ [6]. Recently, photocatalytic cementitious materials have been patented by Mitsubishi Corp.(NOxer™), and Italcementi SpA (TX-Aria™ and TX-Arca™) [7-10]. The application of TiO_2 photocatalysis to concrete aims to achieve two main goals, the self-cleaning effect discussed above [11, 12] and the *depolluting* effect due to the oxidation of nitrogen oxides (NO_x) in the atmosphere to NO_3^- [13-17], especially in street canyons where NO_x concentrations can be considerable due to combustion engine exhausts. The great advantage provided by such products is that the only requirements, beyond TiO_2 in the construction material used, are sunlight, oxygen and water.

Air pollution due to *nitrogen oxides* (NOx) is a dramatic issue that modern societies are facing. They are amongst the main responsible for *photochemical smog* [18] (mixture of hazardous chemicals formed in the atmosphere due to interaction of sunlight with already present pollutants); together with sulphur oxides (SOx) they generate acid rains [18-20]; direct exposures or acid vapours generated by reaction with atmospheric moisture can cause emphysemas and bronchitis due to their interaction with lung tissues [18] and, not least, they seriously affect plant regular metabolism [18]. In atmospheric chemistry NOx refers to the sum of nitric oxide, NO, and nitrogen dioxide, NO_2. NO is considered a *primary* pollutant [18] because mainly introduced in the atmosphere directly from a source (high temperature combustions in transport and industrial activities [18-21]). NO_2, on the other hand, is considered as a *secondary* pollutant because mainly formed in the atmosphere by interaction of a primary pollutant (NO) with O_2 (or O_3) and/or sunlight [18-21]. Further reactions in the atmosphere can transform NO and NO_2 in nitric acid, HNO_3, peroxyacyl nitrates (PANs), $RC(O)OONO_2$, peroxynitric acid, HNO_4, etc... The sum of all these species and NOx is known as NOy, *total reactive nitrogen*. NOx emission has been and still is subject of intense environmental regulations. Therefore their control and remediation have been the subject of intense research. Amongst the most used technologies for NOx remediation (combustions modifications, dry processes and wet processes [22, 23]) photocatalytic oxidation (PCO) of NOx has become, over the past ten years, a valid alternative as confirmed by the large number of literature produced [14, 16, 17, 24-34] and the continuous growing number of commercial products available in the market. These products are essentially paints or cements containing photoactive TiO_2 [7, 35, 36], photocatalytic pavement blocks [8], filters and membranes for indoor/outdoor air purifications, etc... Despite all the other technologies, PCO provides the great advantage to promote NOx oxidation on the surface of light activated TiO_2 using only atmospheric oxygen and water.

Depolluting performances of cementitious materials containing TiO_2 are usually assessed in gas flow reactors with a photocatalytic bed consisting in the concrete specimen to be analysed. Reactors are fed with air streams containing nitrogen oxides at a given partial pressure and NO and NO_2 concentrations are monitored in darkness and under illumination [13, 16, 24, 32, 37]. Alternatively, *real world exposure* tests offer a mean to address performances in actual outdoor conditions, by monitoring the concentration drop of NOx in the air where photocatalytic concrete is used as pavement blocks or in vertical walls [9, 17, 24].

2. EXPERIMENTAL

2.1 TiO_2 sample

Throughout this study a commercially available titania: *n-TiO_2* (nanosized, Millenium Chemicals PC-105), 100% anatase, has been tested. Before starting any degradation experiments, this sample has been characterised in order to evaluate main physical-chemical properties such as: light absorption characteristics, mineralogy, specific surface area, porosity and particle size. Light absorption measurements were undertaken to derive band-gap information and have been carried out on TiO_2 powders using U.V.-vis diffuse reflectance spectroscopy (StellarNet EPP2000 Spectrometer). Spectra were processed according to the Kubelka – Munk transform approach for indirect semiconductors as described in [38]. X-Ray Diffraction patterns have been obtained using a Bruker D8 Advance diffractometer equipped with a $Cu_{K\alpha 1}$ 1.54Å X-Ray source operating at room temperature, in order to confirm the mineralogy and crystallinity. BET (Brunauer – Emmett – Teller [39]) specific surface area

(S_{BET}) has been obtained by N_2 adsorption on powder samples using a Micromeritics ASAP 2020. These data enabled characterisation of sample porosity as determined by the BJH (Barrett – Joyner – Halenda) model [40], assuming cylindrical pores. Samples were degassed at 150 °C before adsorption measurements. Finally, particle size evaluation was carried out by three different techniques: TEM imaging (and further image analysis), XRD via the Scherrer Equation (Equation 1) and a simple geometrical model derived from the BET specific surface area assuming particles to be rigid spheres (Equation 2).

$$d = \frac{0.9 \cdot \lambda}{FWHM \cdot \cos\theta_P} \quad (1)$$

$$d = \frac{6}{\rho_A \cdot S_{BET}} \quad (2)$$

In Equation 1: λ is the X-ray wavelength, FWHM, the full width at half maximum height for the anatase 101 peak at 25.2 ° (2θ), θ_P, the Bragg's diffraction angle for the same peak. In Equation 2: ρ_A is the density of anatase taken as 3.895 g cm^{-3}, and S_{BET}, the BET specific surface area.

2.2 Depollution: NOx oxidation

Mortar samples for the NOx oxidation test have been prepared according to the procedure described in the European Standard ISO 679 [41]. Mortar specimens were cast in 9 cm diameter x 1 cm thickness plastic Petri dishes. Two sets of twelve mortar discs each were produced: one with n-TiO_2 and one without photocatalyst as a control. Photocatalytic mortar disks contained 3.5 % of TiO_2 in respect of the hydraulic binder, i.e. : 3.5 % TiO_2, 96.5 % cement. Samples were cured for seven days at room temperature in sealed plastic bags and further seven days at room temperature and 60 % of relative humidity.

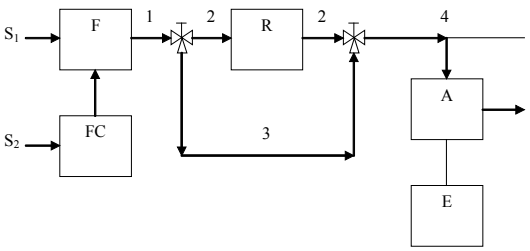

Figure 1 – NOx oxidation lab plant flow chart. S1 NOx cylinder, S2 air cylinder, F NOx flow meter, FC air flow meter, R photocatalytic reactor, A NOx analyser, E computer.

NOx oxidation experiments have been carried out in a continuous gas flow reactor according to the Italian Standard UNI 11247 [32]. The scheme of the lab plant used is illustrated in Figure 1. S1 is the NOx cylinder, S2 the air cylinder, F and FC the mass flow meters for NOx and air respectively, R the photocatalytic reactor, A the chemiluminescence analyzer and E the software/computer system for the analyzer. The photocatalytic reactor consists of a Pyrex glass chamber having a total volume of 3.58 l where the specimen under testing can be located on the bottom part supported by a proper sample holder. The gas inlet tube allows the air/NOx mixture to flow directly onto the specimen upper surface whilst the gas outlet tube is positioned

underneath the sample holder. The system is kept at room temperature. U.V. light is provided by an OSRAM ULTRAVITALUX lamp having a main emission in the U.V.-A field distributed around a maximum intensity wavelength of about 365 nm. The lamp – sample distance was set to achieve on the upper sample surface an average irradiance of 20 ± 1 W m^{-2}. A schematic diagram of the photocatalytic reactor equipped with the U.V. lamp is illustrated in Figure 2. Experiments were carried out at an inlet NO concentrations of 600 ppb in air with a ratio NO/NO_2 equal to 2 at three different flow rates: 3 l min^{-1}, 2 l min^{-1} and 1.5 l min^{-1}. All the oxidation experiments have been performed according to the following procedure. The disk sample was wrapped in a sealing film in order to let the upper surface free and protect the side surface. After introducing the disk sample in the photocatalytic reactor the gas stream (at given flow rate) was switched on and the system let to stabilise for half an hour in the dark in order to achieve constant NO and NO_2 concentrations. The U.V. light was then switched on and the NO, NO_2 concentrations monitored for a further 90 minutes.

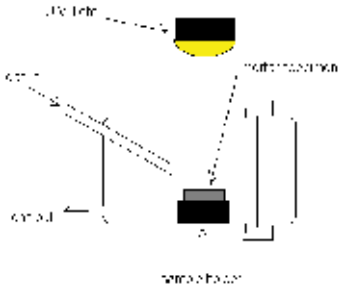

Figure 2 – Photocatalytic reactor for NOx oxidation.

3. RESULTS AND DISCUSSION

3.1 TiO_2 sample

Light absorption characteristics for the photocatalyst are shown in Figure 3 presenting the Kubelka – Munk transformed function derived from the UV-vis Diffuse Reflectance Spectra for the untreated TiO_2 powders, a common approach to derive band gap of indirect semiconductors [38]. The band gap is derived by extrapolating the linear portion of the spectrum on the x-axis. The computed band gap values are reported in Table 1. The values are typical of anatase samples [38].

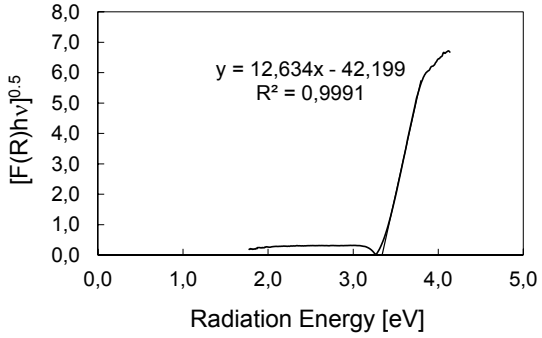

Figure 3 – Light absorption edge for n-TiO_2.

The results of X-ray diffraction analysis are shown in Figure 4. The peak positions confirm that *n*-TiO_2 is essentially anatase [42, 43] and no other crystalline polymorphs have been detected.

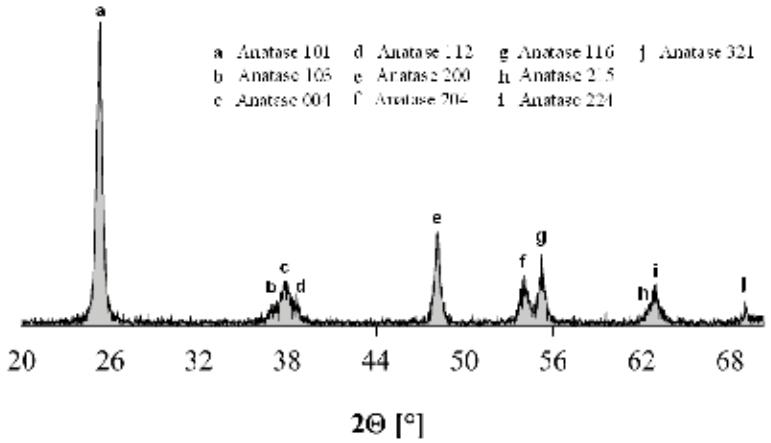

Figure 4 – XRD pattern for n-TiO_2.

Surface area data are presented in Figure 5(a). The shape of the isotherm (type II isotherm of the BET classification) is typical of a solid material compatible with the adsorbate (N_2) and presenting pores in the range of mesoporosity. The BJH analysis (Figure 5(b)) shows that the mesoporosity exhibited by *n*-TiO_2 is mainly centred around 79.6 Å.

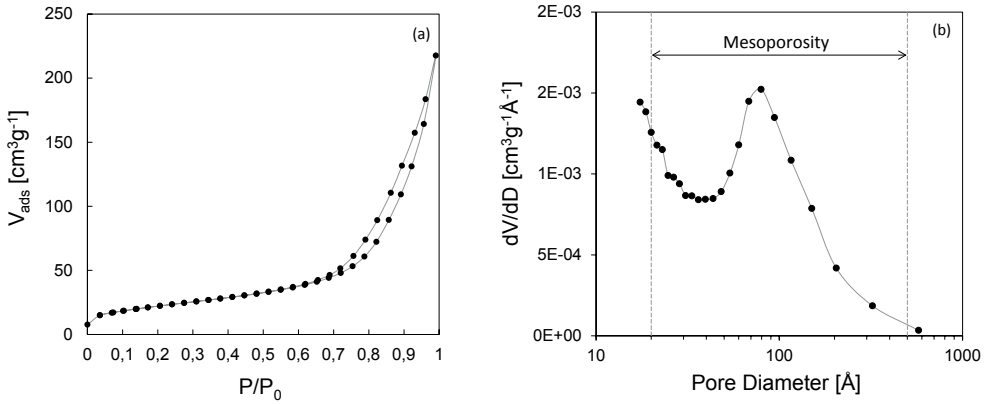

Figure 5 – (a) n-TiO_2 N_2 adsorption isotherm; (b) n-TiO_2 BJH plot for porosity evaluation.

Figure 6 shows transmission electron micrograph images. The crystallite size is quantitatively supported by the histograms shown as inset in the figure. Particle size data obtained through an image analysis of the TEM micrographs are compared in Table 1 with values obtained through the Scherrer equation applied to the XRD patterns and a simple geometrical model utilising BET data with the approximation of spherical particles. There is good agreement between the techniques and the results are consistent with manufacturer's data on particle size. TEM micrographs also suggest that considerable agglomeration has occurred in the nanosized sample

under the conditions of testing, i.e. the pores identified by the BJH analysis mainly arise from inter-particle volume.

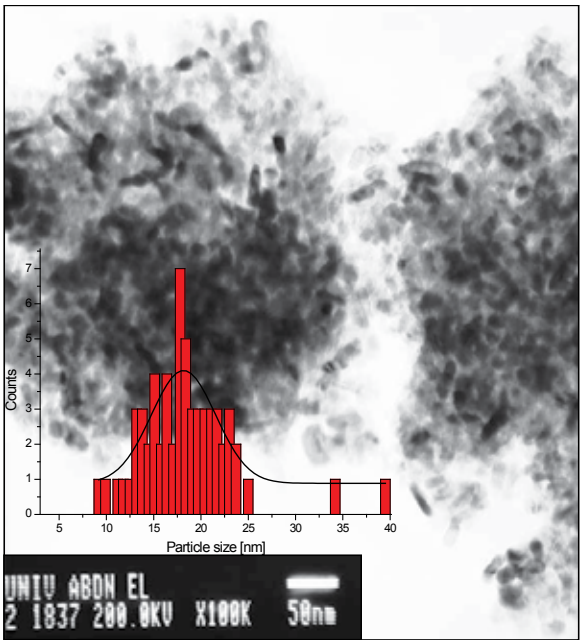

Figure 6 – T.E.M. micrographs and particle size distribution of: (a) m-TiO_2, (b) n-TiO_2.

3.2 Depollution: NOx oxidation

Figure 7 shows the nitric oxide, NO, nitrogen dioxide, NO_2 and total nitrogen oxides, NOx = NO + NO_2, concentration profiles obtained during the NOx oxidation test at three different flow rates and under illumination. In each graph trends obtained with photocatalytic cement mortars are compared to trends exhibited by TiO_2-free white cement mortars. The flat character of profiles where TiO_2 is not present indicates very low impact on NO and NO_2 oxidation by the cement environment itself and/or eventual not catalysed photooxidation. Trends also suggest that the lower the flow rate (i.e. the higher the average gas transit time) the lower the NO and NO_2 final concentrations (at 90 minutes) hence the higher the conversions. This is more evident in Figure 8 where the total NOx conversions at 90 minutes are plotted versus the gas flow rate. The decrease of the conversion with the increase of the flow rate indicates that 90 minutes of reaction time are not enough to reach the *actual* steady state (conversion constant at different flow rates). The calculated photonic efficiency, equal to 0.10 %, seems to be in the same range as the ones reported by Kalousek et al [44] on very similar systems.

Table 1 – n-TiO_2 physical chemical characterisation data.

Sample	**Crystalline Phase**	**Band Gap**	**S_{BET}**	**BJH Φ_{pore}**	**Particle size**		
					TEM	**XRD**	**BET**
		eV	***m^2g^{-1}***	***Å***	***nm***	***nm***	***nm***
PC-105	100% Anatase	3.34±0.02	78.9	79.6	18.4±5.0	16.6±2.0	19.5

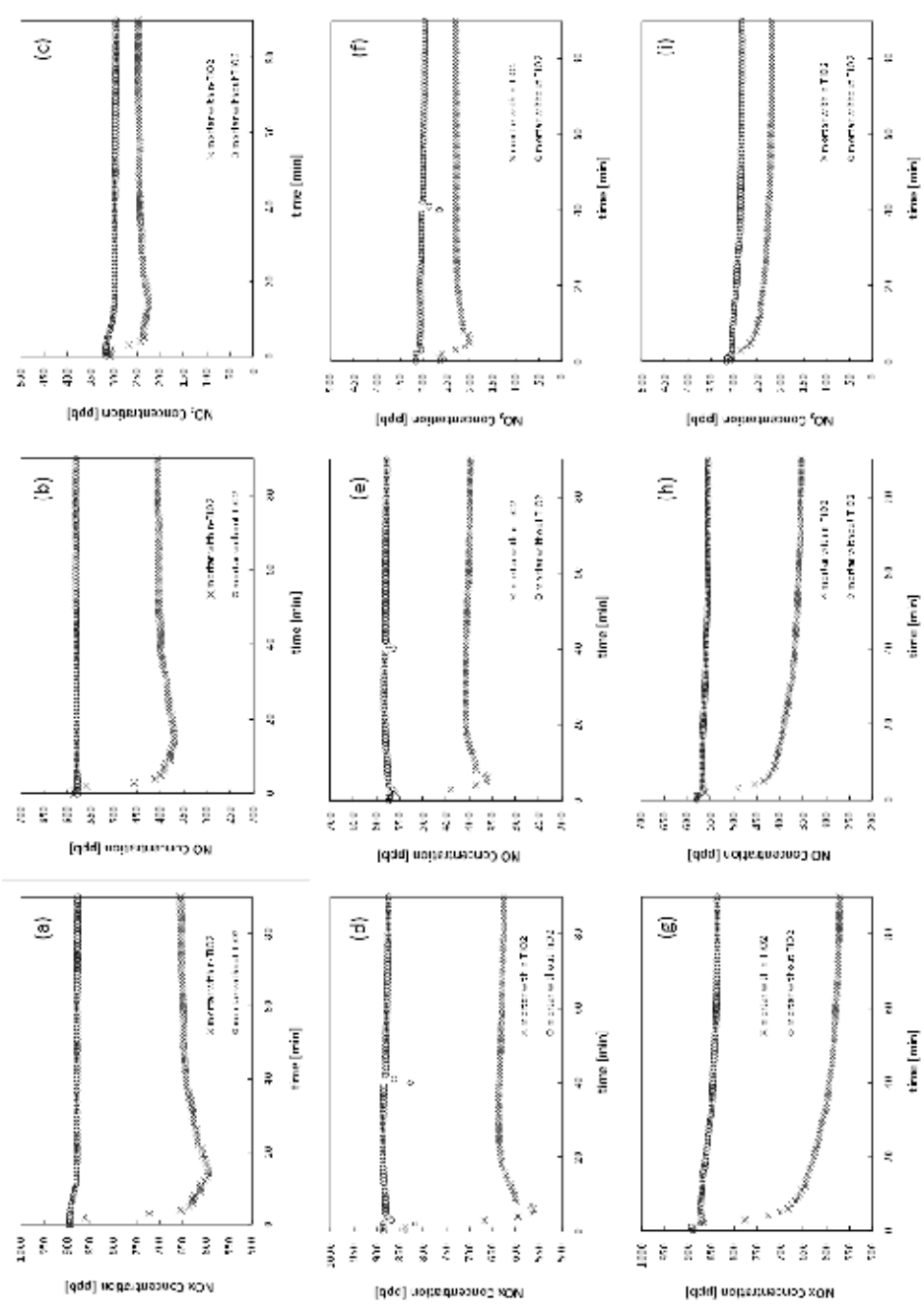

Figure 7 – NOx, NO and NO_2 concentration profiles at: (a), (b), (c) 3 l min^{-1}, (d), (e), (f) 2 l min^{-1}, (g), (h), (i) 1.5 l min^{-1}.

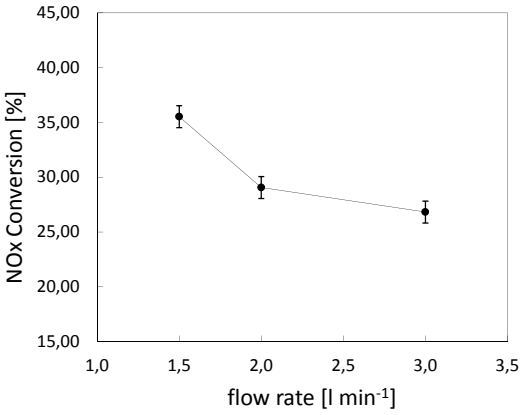

Figure 8 – NOx overall conversion versus flow rate for mortar specimens containing n-TiO_2.

The analysis of the concentration profiles (Figure 7) seems to indicate a very peculiar behaviour for the photocatalytic oxidation of NOx when TiO_2 is supported on cementitious materials (very high pH systems). The photocatalytic oxidation of NO on powder TiO_2 or TiO_2 supported on not high pH materials (e.g.: glass slides or beads, textile tiles, metal meshes, fabrics, etc…) is a complex series of chemical equilibria [13-15, 33]. Adsorbed H_2O and O_2 react with light generated valence band positive holes and conductance band electrons on the surface of TiO_2 to form adsorbed hydroxyl radicals, HO [13-15, 33]. These radicals directly react with NO and, passing through nitrous acid, HONO, and nitrogen dioxide, NO_2, as intermediates, they convert NO into nitric acid, HNO_3, [13-15, 33]. Since the reaction pathway occurs with a fast initial reactive photo-adsorption (NO→ HONO → NO $_2$) [13], the NO_2 concentration initially increases reaching a maximum and then decreases approaching a constant value (series of reaction kinetics). A very similar mechanism was supposed to be true for the case of cementitious materials containing TiO_2 where the very high pH would allow the formation of NO_2^- and NO_3^- rather than free HONO and HNO_3. However our experimental findings evidenced no presence of NO_2 initial concentration maxima. Although more experimental work needs to be done to fully understand this feature, some observations can be made considering the change of redox potentials of the nitrogen oxidation states in relation to change in pH.

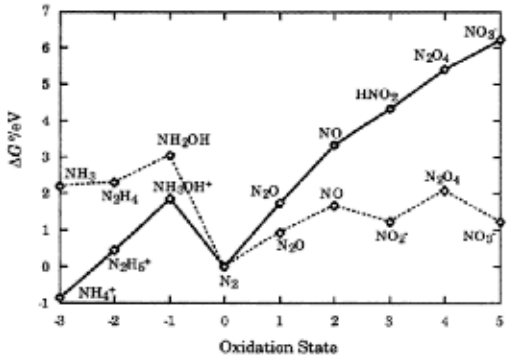

Figure 9 – Free energy – oxidation states diagram for the nitrogen oxidation states in acid (solid line) and basic (dashed line) solutions.

Figure 9 shows the Frost diagram for the nitrogen oxidation states in acid and basic environments (courtesy of Rieger, Philip H., Electrochemistry, 2nd edition [45]). In the Frost diagram species corresponding to minima are expected to be thermodynamically stable since redox events from immediate nearby species are energetically downhill [45]. In acidic conditions the series N~~O~~HONO→N $_2O_4$ (↔ $2NO_2$)→HNO_3 do not show any increased stability states. All the species are highly reactive and the very high ΔG° for HNO_3 accounts for its high oxidative power. In alkaline conditions however both NO_2^- and NO_3^- are positioned in two minima with very similar ΔG°. This could imply that NO is mainly converted to NO_2^- and NO_2 to NO_3^- where the series of reaction above no longer occurs since NO_2^- shows a much higher redox stability.

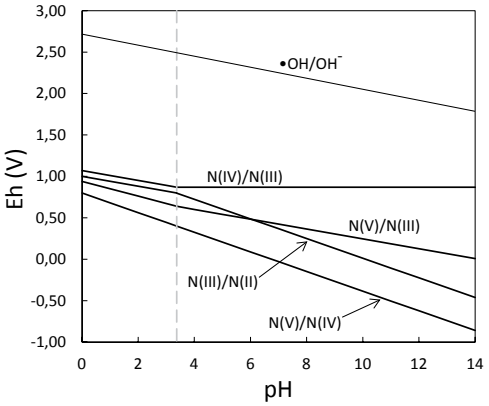

Figure 10 – Potential versus pH diagram showing the variation in half-cell potential with pH for the N(V)/N(IV), N(V)/N(III), N(IV)/N(III), N(III)/N(II) redox couples in comparison with the $^{\bullet}OH/OH^-$ redox couple. The vertical dashed line corresponds to the pKa of HONO.

It is also interesting observing the feature of Eh versus pH diagram (Figure 10, constructed using the Nernst equation) for N species when compared to the couple $OH^-/^{\bullet}OH$ (assuming $^{\bullet}OH$ as the main oxidant). Figure 10 clearly shows that ΔEh between the couples $OH^-/^{\bullet}OH$ and N(II)/N(III), $OH^-/^{\bullet}OH$ and N(IV)/N(V) and $OH^-/^{\bullet}OH$ and N(III)/N(V) remain quite constant all over the pH domain, however, the ΔEh between the couples $OH^-/^{\bullet}OH$ and N(III)/N(IV) significantly reduces in highly alkaline environments, making this oxidation step (NO_2^- to NO_2) not as favourable as the others. The effect of the high pH could therefore be the potential switch off or inhibition of the step from N(III) to N(IV) in the overall oxidation mechanism (Figure 11), hence accounting for the absence of initial maxima in NO_2 concentration profiles.

The influence of the high pH on the mechanism of NOx oxidation is however far from being completely understood. It can be questioned that cementitious surfaces are a very dynamic system from the point of view of the pH, due to the effect of carbonation. However it is important to stress that the specimens here used were already partially carbonated. NOx oxidation tests have been performed after a minimum of 14 days of curing, 7 of which in a 60 % relative humidity atmosphere (optimal conditions for carbonation). Yet it looks like that the general features of the photocatalytic oxidation of NOx are quite different when compared with unsupported TiO_2 (neutral environment). Further research work has been planned where NOx photocatalytic oxidation will be carried out on freshly prepared specimens as well as specimens at different curing ages. This will hopefully clarify the influence of carbonation on the

mechanism of nitrogen oxide degradation over TiO_2 – containing cementitious materials. These data will also help to assess potential catalytic deactivation phenomena occurring when concretes containing photoactive TiO_2 are exposed to outdoor conditions. As already shown by Lackhoff et al. [46], the photocatalytic activity of TiO_2 – containing cement can be reduced over several months due to carbonation of cement. Lackhoff attributed the drop in photocatalytic activity to changes of the cement surface microstructure followed by carbonation. However this negative effect of carbonation seems to be more moderate in specimens exposed to real outdoor conditions. Many structures built in Italy and France between 2001 and 2005 still maintain high level of NOx abatement [17, 35, 47]. Periodic washing with fresh water has been the only maintenance to retain the high photocatalytic efficiencies. In this respect over the next decade these structures will provide more data about the actual durability of the catalytic effect.

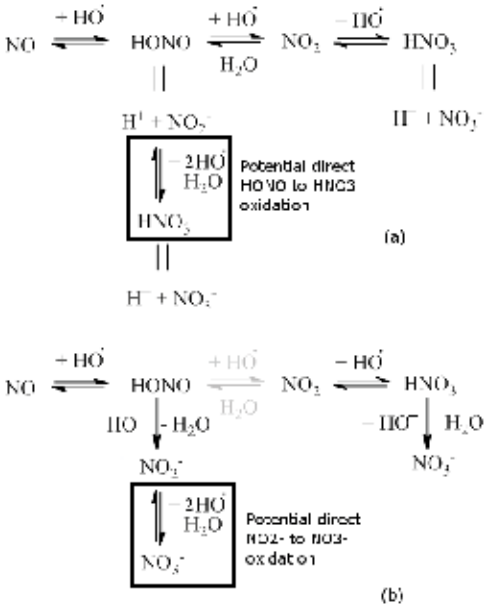

Figure 11 – Proposed mechanism of NOx oxidation on pure TiO_2 (a) [48] and on TiO_2 in mortar specimens (b). The equilibrium in grey indicates inhibition of the oxidative step.

4. CONCLUSIONS

Application of TiO_2 photocatalysis to cement and concrete provides an efficient strategy to simultaneously obtain: self-cleaning effect of building facades, retardation of natural surface ageing as well as depollution of air, simply with the support of sunlight, atmospheric oxygen and water present as humidity and/or rain water. In this paper, performances in degrading NOx, are presented for a nanosized TiO_2 samples (Table 1) tested in cement and mortars, together with an insight into the fundamental chemistry about TiO_2 photosensitised reactions responsible for the degradation processes involved.

The oxidation of NOx follows a photocatalytic pathway, where nitric oxide, NO, and nitrogen dioxide, NO_2, are oxidised to nitrites, NO_2^-, and nitrates, NO_3^-. The very high pH typical of the cement environment seems to drive a different mechanism than the one occurring using powder TiO_2. The absence of initial maxima in the NO_2 concentration profiles would suggest that the step NO_2^- to NO_2, in the series of reactions typical of the case with powder TiO_2, might be inhibited.
In all the reaction steps water and oxygen play a fundamental role since they are the precursors for the hydroxyl radicals, HO and other oxygen -based species (e.g. peroxides, superoxides) responsible for mineralisation and oxidation of organics and inorganics.

5. FUTURE WORK AND PERSPECTIVES

The work here presented has served as a solid experimental and theoretical support to design a new EU funded project (FP7 Eco Innovation Scheme) called **Visible Light Active PhotoCATalytic Concretes for Air Pollution Treatment (Light^{2}CAT)**. This new project, starting in early 2012, will be dealing with the development of a new generation of photocatalytic cementitious materials and concretes implementing visible light sensitive TiO_2s. The methods to obtain visible light sensitization will be scanned over a wide range of techniques such as: metal ion coupling, selective surface hydrogenation as well as crystal structure engineering to alter the ordinary band structure of the TiO_2 semiconductor lattice. The main scope of Light^{2}CAT is to significantly improve the performances of photocatalytic concretes in *Northern latitudes* where, due to atmospheric and sunlight conditions, the efficiencies of photocatalytic concretes based on ordinary TiO_2 cannot be as high as in Southern Europe (ordinary TiO_2 is activated by UV light only). Light^{2}CAT involves 12 partners amongst Universities and Research Institutions, SMEs and larger multinational companies as well as public bodies and Governmental Institutions, over a total of 5 European Countries, namely: Denmark, Sweden, UK, Spain and Italy. Light^{2}CAT project has a total budget of about 5 M € with an overall EU contribution equal to 3.6 M €.

6. ACKNOWLEDGEMENT

The author is grateful to the European Community under the Marie Curie Research Training Network MRTN-CT-2005-019283 “Fundamental understanding of cementitious materials for improved chemical physical and aesthetic performance” (http://www.nanocem.org/MC-RTN/) for the *full* support of this work.

REFERENCES

[1] Fujishima, A., Honda, K., *Nature*, Vol. 238, 1972, pp. 37-38.

[2] Wrighton, M.S., Ellis, A.B., Wolczanski, P.T., Morse, D.L., Abrahamson, H.B., Ginley, D.S., *J Am Chem Soc*, Vol. 98, 1976, pp. 2774.

[3] Fujishima, A., Hashimoto, K., Watanabe, T., "TiO_2 Photocatalysis: Fundamentals and Application", 1 ed., BKC, Tokyo, 1999.

[4] Irie, H., Tee, S.P., Shibata, T., Hashimoto, K., "Photo-induced Wettability Control on TiO2 Surface", *Electrochem Solid-State Lett*, Vol. 8, 2005, pp. 23-25.
[5] Wang, R., Hashimoto, K., Fujishima, A., Chikuni, M., Kojima, E., Kitamura, K., Shimohigoshi, M., Watanabe, T., "Light-induced amphiphilic surfaces", *Nature*, Vol. 338, 1997, pp. 431-432.

[6] Rimmer, D., Sanderson, K.D., Paul, T., "Coated glass", WO/2004/108619, 2010.

[7] Cucitore, R., Cangiano, S., Cassar, L., "High durability photocatalytic paving for reducing urban polluting agent", WO/2006/000565, 2006.

[8] Murata, Y., Tawara, H., Obata, H., Murata, K., "NOX-cleaning paving block", EP0786283, 2003.

[9] Cassar, L., Beeldens, A., Pimpinelli, N., Guerrini, G.L., "Photocatalysis of cementitious materials", in: L. Cassar, P. Baglioni (Eds.) International RILEM Symposium on Photocatalysis, Environment and Construction Materials, RILEM, Florence, 2007, pp. 131-145.

[10] Guerrini, G.L., Plassais, A., Pepe, C., Cassar, L., "Use of photocatalytic cementitious materials for self-cleaning applications", in: L. Cassar, P. Baglioni (Eds.) International RILEM Symposium on Photocatalysis, Environment and Construction Materials, RILEM, Florence, 2007, pp. 219-226.

[11] Folli, A., Jakobsen, U.H., Guerrini, G.L., Macphee, D.E., "Rhodamine B Discolouration on TiO2 in the Cement Environment: A Look at Fundamental Aspects of the Self-cleaning Effect in Concretes", *J Adv Oxid Technol*, Vol. 12, 2009, pp. 126-133.

[12] Folli, A., Pochard, I., Nonat, A., Jakobsen, U.H., Shepherd, A.M., Macphee, D.E., "Engineering photocatalytic cements: understanding TiO2 surface chemistry to control and modulate photocatalytic performances", *J Am Ceram Soc*, Vol. 93, 2010, pp. 3360-3369.

[13] Folli, A., Campbell, S.B., Anderson, J.A., Macphee, D.E., "Role of TiO2 surface hydration on NO oxidation photo-activity", *J Photochem Photobiol A*, Vol. 220, 2011, pp. 85-93.

[14] Devahasdin, S., Fan, C.J., Li, K., Chen, D.H., "TiO2 photocatalytic oxidation of nitric oxide: transient behavior and reaction kinetics", *J Photochem Photobiol A*, Vol. 156, 2003, pp. 161–170.

[15] Hashimoto, K., Wasada, K., Toukai, N., Kominami, H., Kera, Y., "Photocatalytic oxidation of nitrogen monoxide over titanium(IV) oxide nanocrystals large size areas", *J Photochem Photobiol A*, Vol. 136, 2000, pp. 103-109.

[16] Chen, D.H., Li, K., "Photocatalytic Coating on Road Pavements/Structures for NOx Abatement.", Lamar University Report (2007), pp. 1-17.

[17] Guerrini, G.L., Peccati, E., "Photocatalytic cementitious roads for depollution", in: L. Cassar, P. Baglioni (Eds.) International RILEM Symposium on Photocatalysis, Environment and Construction Materials, RILEM, Florence, 2007, pp. 179-186.

[18] Harrison, R.M., "Pollution: causes, effects and control", 2 ed., The Royal Society of Chemistry, Cambridge, 1992.

[19] Elsom, D., "Atmospheric Pollution", 1 ed., Basil Blackwell, New York, 1987

[20] Seinfeld, J.H., "Atmospheric chemistry and physics: from air pollution to climate change", 1 ed., Wiley, New York, 1998.

[21] Cotton, F.A., Wilkinson, G., "Advanced Inorganic Chemistry", 5 ed., Wiley-Interscience, USA, 1988.
[22] Latta, C.A., *Plant Eng*, Vol. 52, 1998, pp. 105-112.

[23] Gangwal, S.K., Howe, G.B., Spivey, J.J., Silveston, P.L., Hudgins, R.R., Metzinger, J.G., *Environ Prog*, Vol. 12, 1993, pp. 128.

[24] Beeldens, A., "Air purification by road materials: results of the test project in Antwerp", in: L. Cassar, P. Baglioni (Eds.) International RILEM Symposium on Photocatalysis, Environment and Construction Materials, RILEM, Florence, 2007, pp. 187-194.

[25] Chen, S., Cao, G., "Study on the photocatalytic oxidation of NO_2^- ions using TiO_2 beads as a photocatalyst.", *Desalination*, Vol. 194, 2006, pp. 127-134.

[26] Dalton, J.S., Janes, P.A., Jones, N.G., Nicholson, J.A., Hallam, K.R., Allen, G.C., "Photocatalytic oxidation of NOx gases using TiO_2: a surface spectroscopic approach.", *Environ Pollut*, Vol. 120, 2002, pp. 415-422.

[27] Ichiura, H., Kitaoka, T., Tanaka, H., "Photocatalytic oxidation of NOx using composite sheets containing TiO_2 and a metal compound.", *Chemosphere*, Vol. 51, 2003, pp. 855-860.

[28] Kawakami, M., Furumura, T., Tokushige, H., "NOx removal effects and physical properties of cement mortar incorporating titanium dioxide powder", in: L. Cassar, P. Baglioni (Eds.) International RILEM Symposium on Photocatalysis, Environment and Construction Materials, RILEM, Florence, 2007, pp. 163-170.

[29] Mills, A., Le Hunte, S., "An overview of semiconductor photocatalysis", *J Photochem Photobiol A*, Vol. 108, 1997, pp. 1 - 35.

[30] Ollis, D., Al-Ekabi, H., "Photocatalytic purification and treatment of water and air", Elsevier, New York, 1993.

[31] Poon, C.S., Cheung, E., "NO removal efficiency of photocatalytic paving blocks prepared with recycled materials", *Constr Build Mater* Vol. 21, 2006, pp. 1746-1753

[32] "Determination of the degradation of nitrogen oxides in the air by inorganic photocatalytic materials: continuous flow test method", UNI 11247 (2009), pp. 1-11.

[33] Wang, H., Wu, Z., Zhao, W., Guan, B., "Photocatalytic oxidation of nitrogen oxides using TiO2 loading on woven glass fabric", *Chemosphere*, Vol. 66, 2007, pp. 185–190.

[34] Zhao, J., Yang, X., "Photocatalytic oxidation for indoor air purification: a literature review.", *Build Environ*, Vol. 38, 2003, pp. 645-654.

[35] "TX Actice Applications - pavements (Italcementi Group)", http://www.italcementi.it/ITA/Prodotti+servizi+e+qualita/Prodotti+Fotocatalitici/Realizzazioni/Gallerie_Realizzazioni/Pavimentazioni.htm.

[36] "Highland Park, Illinois (Essroc, Italcementi Group)", http://txactive.us/images/ESSROC_Press_Release_Hyacinth.pdf.

[37] Hüsken, G., Hunger, M., Brouwers, H.J.H., "Comparative study on cementitious products containing titanium dioxide as photo-catalyst", in: L. Cassar, P. Baglioni (Eds.) International RILEM Symposium on Photocatalysis, Environment and Construction Materials, RILEM, Florence, 2007, pp. 147-154.

[38] Lin, H., Huang, C.P., Li, W., Ni, C., Ismatshah, S., Tseng, Y., "Size dependency of nanocrystalline TiO_2 on its optical property and photocatalytic reactivity exemplified by 2-chlorophenol.", *Appl Catal B-Environ*, Vol. 68, 2006, pp. 1-11.

[39] Brunauer, S., Emmett, P.H., Teller, E., *J Am Chem Soc*, Vol. 60, 1938, pp. 309-319.

[40] Barrett, E.P., Joyner, L.G., Halenda, P.P., *J Am Chem Soc*, Vol. 73, 1951, pp. 373-380.

[41] "Cement - Test methods - Determination of strength", ISO 679 (2009), pp. 1-30.

[42] Bruker AXS Inc., "DIFFRACplus EVA - Bruker X-ray diffraction pattern database software", Madison, WI.

[43] Dowty, E., "ATOMS Shape Software", Kingsport, TN.

[44] Kalousek, V., Tschirch, J., Bahnemann, D., Rathouský, J., "Mesoporous layers of TiO2 as highly efficient photocatalysts for the purification of air", *Superlattice Microst*, Vol. 44, 2008, pp. 506-513.

[45] Rieger, P.H., "Electrochemistry", 2nd ed., Chapman and Hall, New York, 1994.

[46] Lackhoff, M., Prieto, X., Nestle, N., Dehn, F., Niessner, R., "Photocatalytic activity of semiconductor-modified cement—influence of semiconductor type and cement ageing", *Appl Catal B-Environ*, Vol. 43, 2003, pp. 205-216.

[47] "PICADA Project", http://www.picada-project.com/domino/SitePicada/Picada.nsf?OpenDataBase.

Moisture Monitoring in Concrete Bridges 1990-2011

Torsten Lunabba
M.Sc., Lic. Tech.
Destia Ltd
Senior Expert
Heidehofintie 2
FI - 01301 Vantaa
torsten.lunabba@destia.fi

Hemming Paroll
M. Sc., (Physics)
Consult
Westendintie 93 C
FI - 02160 Espoo
hemming.paroll@kolumbus.fi

ABSTRACT

Several methods have been used for monitoring the moisture in concrete bridge structures, sampling, measuring the absolute humidity using gauges or optic fibres and measuring the relative humidity in concrete pores with resistive sensors. The capacitive sensors need stable conditions and are therefore not suitable for outdoor conditions. Optic fibres provide a reliable method to determine absolute humidity at a certain time for the entire bridge. Resistive sensors provide an efficient method for continuous monitoring. The relative humidity in concrete pores is strongly temperature dependent. Therefore, monitoring the relative humidity in concrete requires full understanding of the moisture – temperature equilibrium behaviour.

Key words: Moisture, monitoring, temperature, humidity, concrete bridge.

1. INTRODUCTION

1.1 General

Excessive water in bridge concrete is harmful. It is important to have an appropriate dryness of the substrate when the water proofing is laid on a new bridge or on an existing bridge during the repair work. Otherwise the bond between the water proofing and the concrete will not be good

and the risk of bubbling is evident. High water content may also cause frost damages and frost heave of the water proofing or other protective layer.

The amount of water in concrete varies normally between 60 and 90 kg/m^3/2/. Due to capillary rise, absorption and wetting, the amount of water can be up to 200-220 kg/m^3.

In Finland bridge concrete normally has a water cement ratio of 0.4-0.5. The amount of cement is around 350 kg/m^3. The amount may rise to 400 kg/m^3 for fine grade self compacting concrete. The hydration of cement consumes water corresponding to some 25 % of the weight of the cement /6/. Without access of water from outside, the water content would after hydration be between 2 and 4.5 mass % AH (AH = Absolute Humidity, mass % of the dry concrete) as presented in table 1. Some part of the water will vaporise during the hardening time. On other hand the concrete will absorb additional water from the air and from wetting. Therefore a water content of 4-5.5 mass % AH is typically measured after the concrete is cured.

Table 1 – An approximate calculation of the amount of water in bridge concrete.

Water-Cement ratio	Mixing water [kg], Cement 350 kg/m^3	Amount of water after hydration, mass-% AH	Mixing water [kg], Cement 400 kg/m^3	Amount of water after hydration, mass-% AH
0.5	175	3.6	200	4.2
0.4	140	2.2	160	2.5

The amount of mixing water in the concrete in table 1 having the amount of cement 350 kg/m^3 and a water cement ratio of 0.4 is for an evaluation only, the amount would probably not be that low if the concrete shall be pumped into the mould.

1.2 Absolute humidity and relative humidity of bridge concrete

In Finland the relative humidity of the outdoor air is 80 % RH in average and the air temperature +5 °C. In areas where the concrete is protected from rain and splash, the average relative humidity of the concrete pores is expected to be close to this average value. There will be fluctuation in the concrete top layer due to the variation of the relative humidity of the air. However, most of the fluctuation in relative humidity comes from the variation of the temperature.

The changes of the relative humidity in a concrete structure are reversely proportional to the relative humidity of the outdoor air. In other words, the relative humidity in the concrete pores of a bridge increases with increasing temperature. This occurs due the vaporisation of the water capillary bonded to the pores and the capillary passages between the pores. The equilibrium curve for two concrete classes, one having the water cement ratio 0.7 and the other 0.4 were presented in 1974 by Professor Sven Pihlajavaara /1/, figure 1. On the vertical axle of figure 1 the absolute mass-percent humidity rate has been replaced by the water content - cement paste ratio because moisture transfer will take place only in the cement paste.

When the temperature rises, the relative humidity is determined from figure 1 by reading from the corresponding temperature curve horizontally to the right along the same moisture content line. The horizontal direction follows from the condition that there is no change in the water content in a short time. From the curves of figure 1 it can be seen that the temperature has more impact on the relative humidity than on the change of the water content.

The relative humidity - temperature curves of the two concrete classes have been evaluated in figure 2 using the equilibrium curves of figure 1. The relative humidity of the two bridge concrete types is assumed to be in equilibrium with the average relative humidity of the air that is 80 % RH at +5 °C. When the temperature rises to +35 °C or +45 °C, the relative humidity will rise to 100 % RH. The relative humidity rise in a concrete having a water cement ratio 0.4 is steeper than in that having a water cement ratio 0.7. Comparing the measurements of the relative humidity in bridges with the curves facilitates the assessment of the drying stage of concrete as well as the quality of the concrete. However, the curves of figures 1 and 2 are valid only for the cement type used in the tests of Professor Sven Pihlajavaara in 1974. All common cement types have the similar trend to adsorb water from air humidity. Therefore similar moisture behaviour can be observed in all cement pore structures and the shape of the curves is similar as presented in the figures 1 and 2.

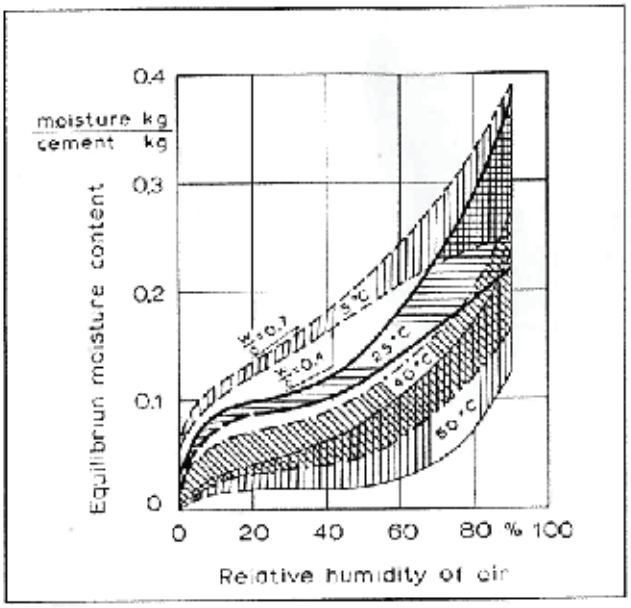

Figure 1 – Water content (absolute humidity) of cement paste – relative humidity equilibrium curve. Sven Pihlajavaara /1/.

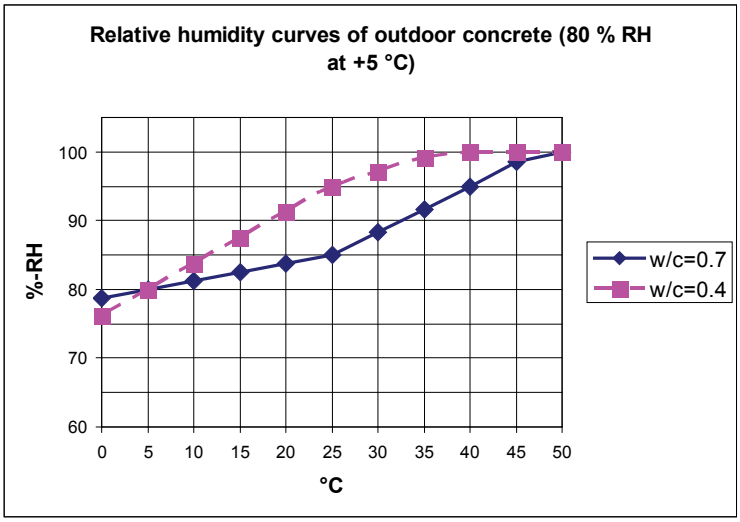

Figure 2 – Relative humidity – temperature curves evaluated from figure 1.

1.3 Hysteresis during drying of concrete

The curves of figure 1 and 2 require stable conditions, which can only be achieved during years after several watering and drying cycles. In the initial stage the water content - relative humidity curve highly depends on whether the concrete is in an adsorption (wetting) or a desorption (drying) stage. The curve number 1 in figure 3 represents the wetting phase. It starts from the left from a completely dry concrete. When the relative humidity goes up to 100 % RH, the concrete will absorb water and in the end have a water content of some 5-6.5 % AH depending on the concrete type. By wetting and capillary sucking, the water content may rise above this level up to the hydroscopic level that is the level where the relative humidity is always 100 % RH. When drying is taking place in the hygroscopic level, that is the level where the relative humidity is less than 100 % RH, the equilibrium curve will follow the curve number 2.

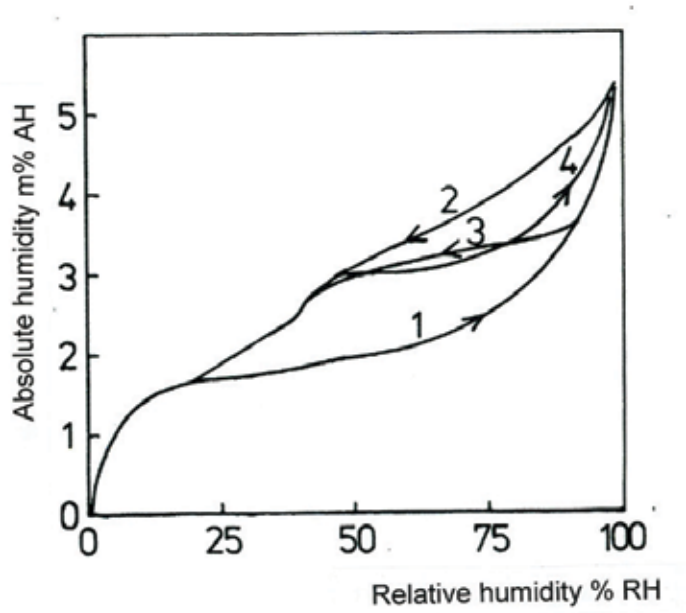

Figure 3 – Absolute humidity, mass-% AH - Relative humidity equilibrium curves according to the handbook /2/.

The effect of the hysteresis could be seen in a moisture flow study done at Tampere University of Technology /8/. The hysteresis curves of two types of concrete, one has water – cement ratio of 0.79 and another has water – cement ratio of 0.41, are presented in figures 4 and 5. The lower lines (blue with squares) of figures 4 and 5 are starting at the left from a dry concrete. The upper line (red with triangles) is starting at the right from a wet concrete. When the two concretes have reached the balance with the outdoor air, that is 80-90 % RH, there is a gap of some 2 mass % AH between the two lines. It will therefore be difficult to tell anything exact about the absolute rate of humidity even if we know the temperature and the relative humidity in the pores of the concrete.

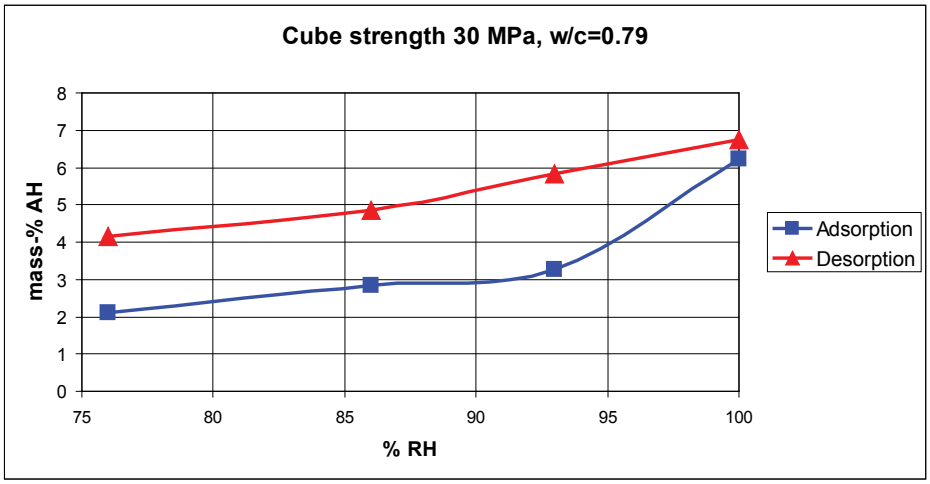

Figure 4 – Absolute humidity - Relative humidity equilibrium curves for a concrete having the water – cement ratio 0.79 /8/.

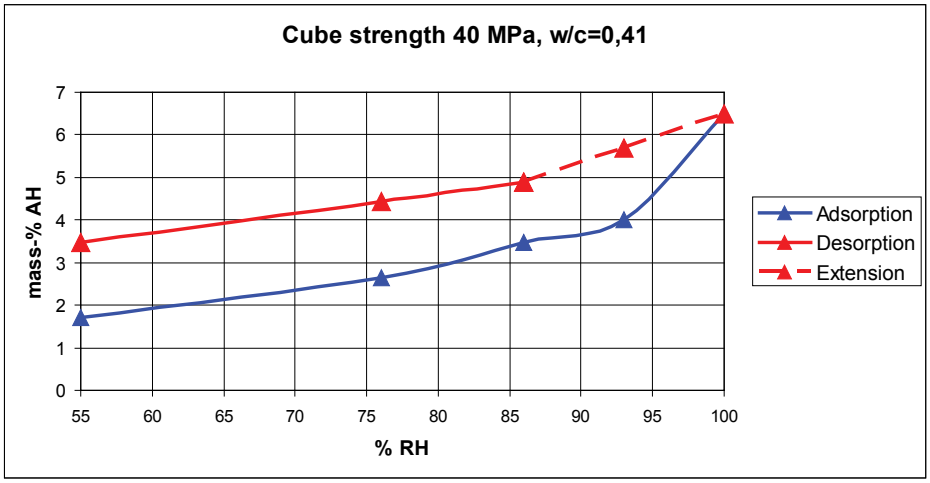

Figure 5 – Absolute humidity - Relative humidity equilibrium curves for a concrete having the water – cement ratio 0.41 /8/. The extension line is added by the authors.

1.4 Measuring and monitoring of moisture content

The moisture content of concrete in absolute humidity can be measured precisely from samples which are dried in an oven at a temperature +105 °C. It is quite difficult to drill out samples because drilling bits are heating up and cooling with water is not allowed. The accuracy of measurements may also be discussed since the amount of stone and gravel in the sample will have a major impact on the result.

The devices used for moisture content measurements are:

1. Capacitive devices (RH and temperature measurements)
   Vaisala HMP 31 UT and HMP 44
   Coating International AHEAD Hygrotemp II
   Rapid RH, Wagner Instruments.

2. Surface measurement devices (AH measurements)
   Tramex Moisture Encounter device

3. Optic fibres (AH measurements)
   Fortum Power and Heat Oy

4. Resistive devices (RH and temperature measurements)
   FuktCom AB

The capacitive sensors are small capsules (30-50 mm in diameter). The sensors are installed in bore holes and sealed into the concrete layer. The sensors may be equipped by data loggers for the recording of the results during a long period of time. Testing on the bridges /3/, /4/ and /5/ have revealed that capacitive sensors are not suitable for a bridge monitoring. It seems to be a problem to have the sensors sealed in the hole so that the relative humidity of the void will be the same as that of concrete pores. The problem is also that the relative humidity in concrete pores fluctuates rapidly with the fluctuation of the temperature and that the capacitive sensors do not have the capability to react quickly enough on that.

Figure 6 – Wagner instruments capacitive sensor.

The absolute humidity on site is often measured using surface moisture measurement devices like Tramex Moisture Encounters. Unfortunately the accuracy of these devices is quite poor particularly because the absolute humidity varies a lot with the distance from the surface in a newly cast or wetted concrete. These gauges are therefore only used for comparisons and for the detecting of leeks and quick quality checks.

The absolute humidity of the concrete has successfully been measured using optic fibres /9/. The advantages of this method are that the entire bridge can be covered. Unfortunately this method

needs a lot of effort for the installation of the fibres as well as for collecting and interpreting of the results. Therefore such measurements can be implemented only for a short periods of time.

The relative humidity in concrete pores is easily measured using resistive sensors /12/. These sensors have the capability of monitoring both relative humidity and temperature in real time. Since they are also provided with data loggers, the measurements may be taken every 20-60 minutes and the monitoring may go on for years. The sensor itself is a capsule having a diameter of 15 mm. The sensor shall be cast into the concrete. The accuracy of measurements is by the manufacturer guaranteed to ± 2 % RH.

Figure 7 – FuktCom AB resistive sensor.

2. MOISTURE CONTENT MEASUREMENTS OF BRIDG DECKS 1994-2010

2.1 Existing conventional bridges

Moisture content measurements were implemented on several bridges in 1994-2010 in Finland. The first studies were done in 1994-1995 by taking samples at different locations of the bridge /3/. The tests revealed that the thin top layer of the concrete had a much lower level of relative humidity compared to the concrete deeper inside the structure. It could also been seen that when the dew point was not reached, the level of absolute humidity did not change much during a period of several days. The relative humidity was measured from the samples in a laboratory. The impact of temperature fluctuation was not regarded.

The later studies confirmed that the capacitive sensors could not indicate correct results /4/. Only resistive sensors are reliable. By using resistive sensors it could be seen that the fluctuation of the relative humidity was parallel to the fluctuation of the temperature, figure 8.

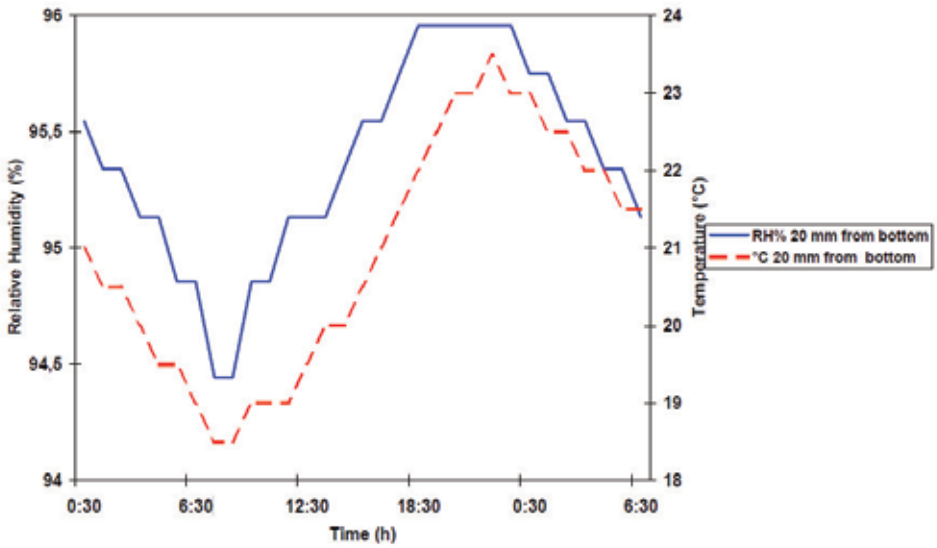

Figure 8 – Relative humidity – temperature measurements with resistive sensors on Iittala Bridge during one day 25.7.19963-4 months after casting /4/. In the figure the relative humidity (RH) follows temperature. This criterion for correct measurement is presented in /10/.

Studies on several newly cast massive concrete bridges revealed that the top layer of the bridge will dry to the required level of 5 mass-% AH or 90 % RH in 1-3 weeks in good weather conditions. At a depth 50 mm from the surface drying is not that fast, figure 9.

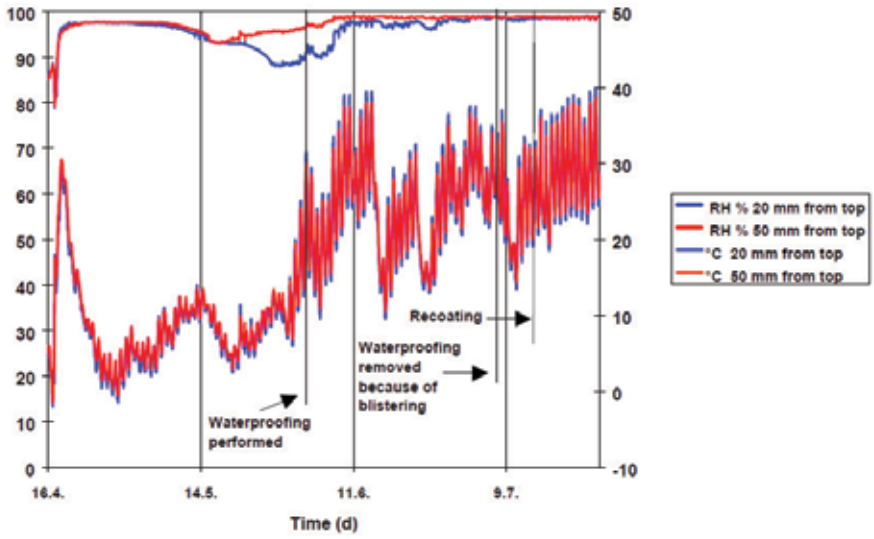

Figure 9 – Relative humidity – temperature measurements on Kasarminkatu Bridge in Oulu 16.4.1997-27.7 1997 cast 17.4.1997 /4/.

Figure 9 represents a typical bridge at the time of water proofing works. The water proofing installation starts when the surface is dry enough. After the water proofing is laid, the relative humidity will rise again close to 100 % RH particularly when the temperature is above +20 °C. This due to the water move from the deeper wet layer. At Kasarminkatu Bridge blistering of the sheet membrane started soon after the membrane was laid. The rise of temperature caused vapour pressure simultaneously as the bitumen glue of the membrane lost the bond. The temperature under the membrane is supposed to reach a level of +50 °C or more when the asphalt is laid or due to strong sun radiation. This will cause vapour pressure high enough to generate bubbles. Today the concrete top surface will always be sealed by epoxy before the membrane is laid. Epoxy shall according to the Finnish quality requirements have a bond strength of at least 1.5 N/mm^2, which is strong enough to prevent bubbling /11/. The pressure of a fully saturated vapour will exceed this level first at a temperature of +200 °C.

Monitoring by resistive sensors 1998-2006 /7/ on seven different bridges several years after the bridge concrete decks were cast revealed that the relative humidity under the water proofing and deep inside the concrete is at the level of 98 % RH at the temperature of +20 °C. Under the bridge deck the relative humidity of the concrete top layer fluctuates between 90-100 % RH and it may go down to 80 % RH when the temperature is below +0 °C.

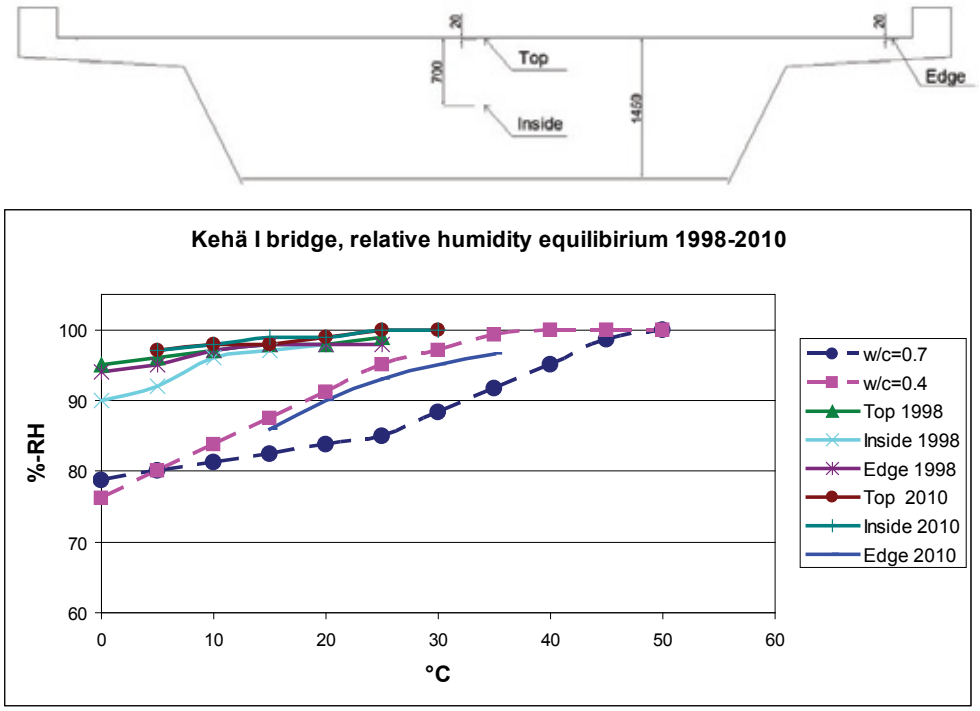

Figure 10 – Relative humidity – temperature measurements on Kehä I bridge in Helsinki 2008 and 2010 cast 26.6.1997 with concrete having a water cement ratio of 0.4.

The monitoring was resumed in 2010 on four bridges. This study revealed that most of the sensors were still working. Under the water proofing and inside the concrete no drying could be observed after 10-15 years, figure 10. Close to the edge beam where the construction thickness is just 200 mm, the dryness 20 mm below the water proofing was at a level that is in line the relative humidity of the outdoor air. In the slender part of the bridge deck the temperature could also go down with the night temperature to temperatures of +15 °C. In the central part of the bridge temperatures never went below +25 °C during the hot season. Unfortunately the sensor at the bridge edge stopped working later in the autumn.

2.2 Repair of bridge decks

A renewal of bridge surface structures often necessitates a repair of the concrete deck top layer. A typical repair comprises of a 30-50 mm layer of levelling concrete. By using low water – cement ratio concrete hydration should guarantee the moisture content as low as 2.5-3 mass-percent AH, table 1. However, the absolute humidity will never be that low. The concrete needs water for curing and there is always a suction of water from the deck structure below, which has been wetted by water jet chiselling and rinsing. Water proofing works will be started before the hydration of the cement is completed because of the needs to minimize the traffic disturbance. Hydration is normally not completed either when the bridge is opened for traffic.

To have a view of concrete drying the resistive sensors were cast into the levelling concrete in bridges repaired in the summer 2009 and 2010.

At sensor 1 of the Kuusjoki Bridge in Jokioinen in Southern Finland, figure 11, drying proceeded as expected during the first 6 months. Due to the low water cement ratio, the concrete was fairly dry already the first winter. The relative humidity of levelling concrete increased after a year probably due to water coming from wetted old concrete. At sensor 2, see figure 12, the situation was not as good. During the first 6 months the concrete was outside the hygroscopic range, that is the relative humidity was permanently 100 % RH. At sensor 3 the conditions were like the conditions at sensor 1 and at sensor 4 like the ones at sensor 2.

Measurements on sites have indicated that the absolute humidity of the top surface of the old concrete increase due to water jetting and rising by 1-2 mass % AH. The absolute humidity is typically between 6 and 7 mass % AH. Obviously this water will later be absorbed by the levelling concrete.

Pihlajanmäki Bridge in Helsinki was repaired in June 2010. The levelling concrete was the same as in Kuusjoki Bridge. At sensor 5, see figure 13, the concrete dried perfectly well but at one sensor of three the concrete was almost as wet as at sensor 2 in Kuusjoki Bridge.

The levelling concrete of Kuusjoki and Pihlajanmäki bridges were dry enough when the conditions were good. Parallel laboratory tests confirmed that the rate of the absolute humidity in the levelling concrete will be less than 5 mass % AH even when the test samples were lying in 10 mm layer of water. In dry conditions the absolute humidity varied between 3.5 and 4.5 mass % AH. These results correspond well with the measurements of the relative humidity and the equilibrium curves from figure 5. The absolute humidity seems to be more close to the adsorption curve than the wetting curve, which may be explained by the fact the drying comes from inside due to hydration.

The levelling concrete having a low water cement ratio and only granite type aggregates seems to dry enough also when the water proofing layer is laid only 2-3 days after the concrete was cast. To ensure optimal dryness, the substrate should be cleaned from excessive water as soon as possible. When water is needed for wetting the substrate and for curing of the finished surface a mist blower shall be used in stead of a water hose.

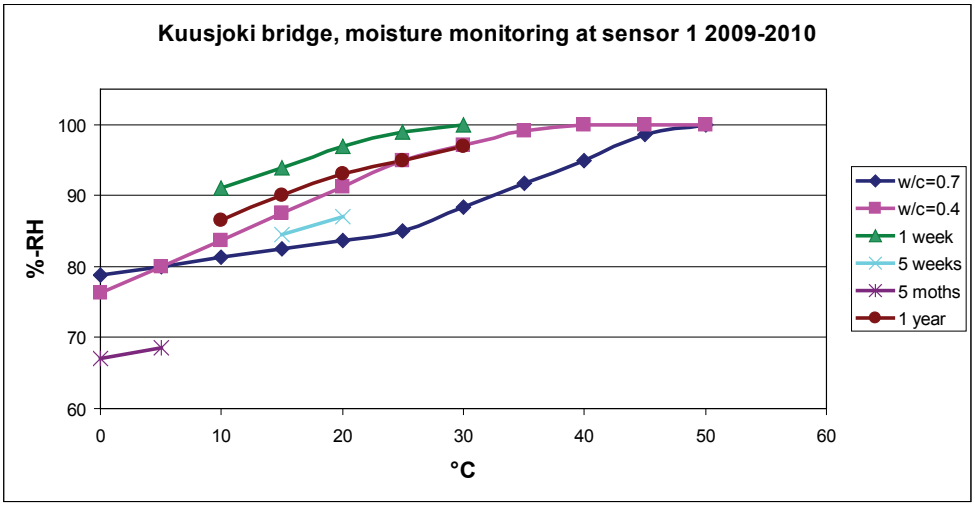

Figure 11 – Relative humidity – temperature measurements on Kuusjoki Bridge in Southern Finland 2009 and 2010 repaired in june2009 with 30-50 mm levelling concrete having a water cement ratio of 0.4 . Sensor 1.

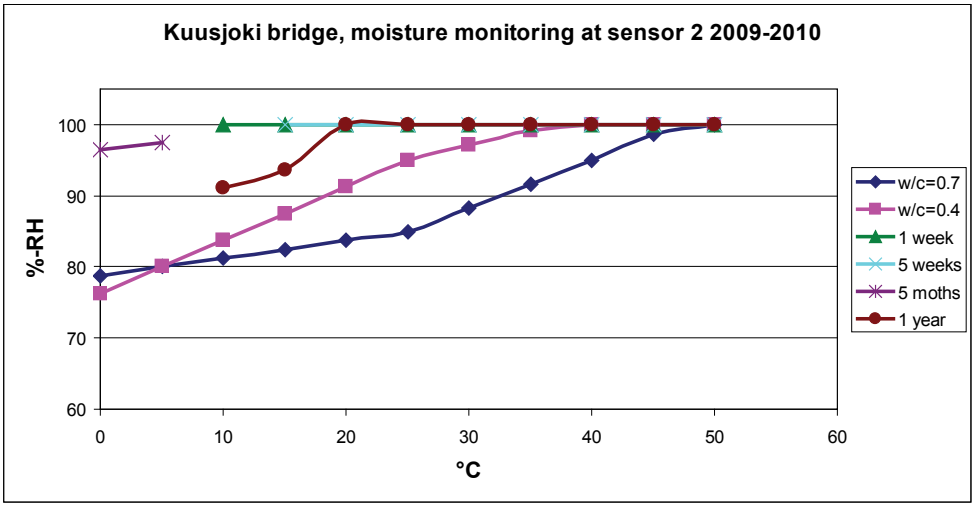

Figure 12 – Relative humidity – temperature measurements on Kuusjoki Bridge in Southern Finland 2009 and 2010 repaired in June2009 with 30-50 mm levelling concrete having a water cement ratio of 0.4 . Sensor 2.

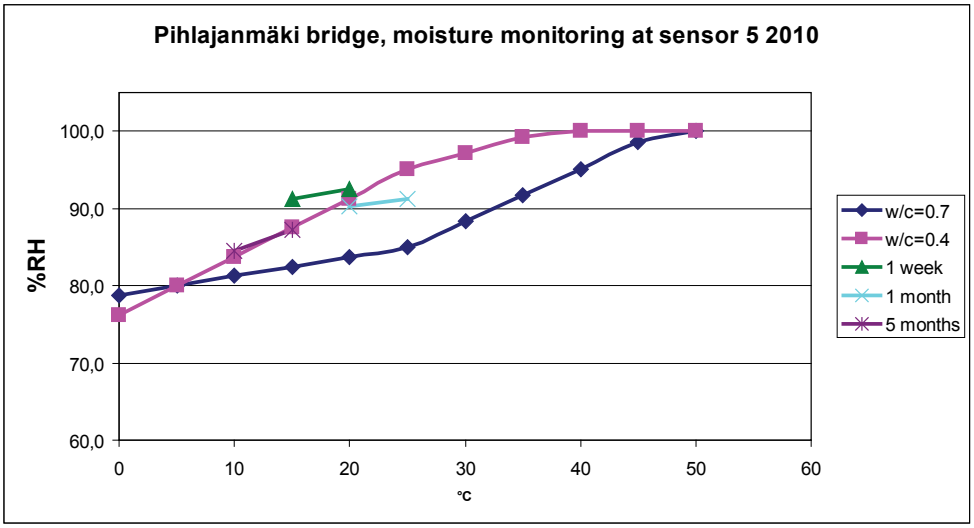

Figure 13 – Relative humidity – temperature measurements on Pihlajanmäki Bridge in Southern Finland 2009 and 2010 repaired in June2009 with 30-50 mm levelling concrete having a water cement ratio of 0.4 . Sensor 5.

The concrete used at Kuusjoki and Pihlajanmäki bridges had only granite type aggregate. The binder material was pure Portland cement strengthened by a small amount of silica fume. In another pilot project, where concrete with higher water cement ratio was used, the concrete was still outside the hygroscopic range after 6 months. This was also the case at the sensor number 2 of Kuusjoki Bridge, where there was obviously loose water on the bridge deck when the concrete was cast. Due to the wetness of the concrete there is a risk of frost damage during the first winter.

Professor's Road Bridge in Helsinki was repaired using a rapidly hardening concrete called RAPI-tec®. This concrete is provided with a significant amount of plastic fibres. The receipt of this concrete is company confidential. However, the amount of water used in the mix revealed that the water cement ratio is close to 0.7 in case the amount of cement is at a level of 400 kg/m^3. Microscopic analysis indicated that the binder comprises of Portland cement, silica and fly ash and the aggregate of granite and significant amounts of lime stone.

The relative humidity at Professor's Road Bridge was at least in the beginning at an acceptable level. At the sensor no 1, see figure 14, wetting started after a few months probably due to capillary suction from the substrate. At the sensor no 5, see figure 15, the conditions were obviously better, since the concrete here remained dry. The equilibrium (absolute humidity/ relative humidity) moisture curves from figure 4 and 5 cannot be applied for this concrete. Test samples from the site and from parallel test plates stored in outdoor conditions revealed that the absolute humidity will in the end be of a magnitude of 8-9 mass % AH. It has not so far been fully clarified whether this will endanger the bond of water proofing or the sustainability of the concrete in winter conditions. The thaw frost stresses implemented on test plates did not cause any remarkable frost damage or loss of bond of the liquid applied water proofing layer.

However, microscopic analysis revealed some cracking, which probably caused additional suction of water during winter storing.

The use of a special rapidly hardening concrete shortens the execution time. The use of lime stone aggregate and other compounds ensure sufficient dryness for water proofing works within a day. The concrete itself will remain wet. As mentioned above, it has so far not been clarified whether this will have impact on the sustainability of the concrete and the bond of the water proofing layer.

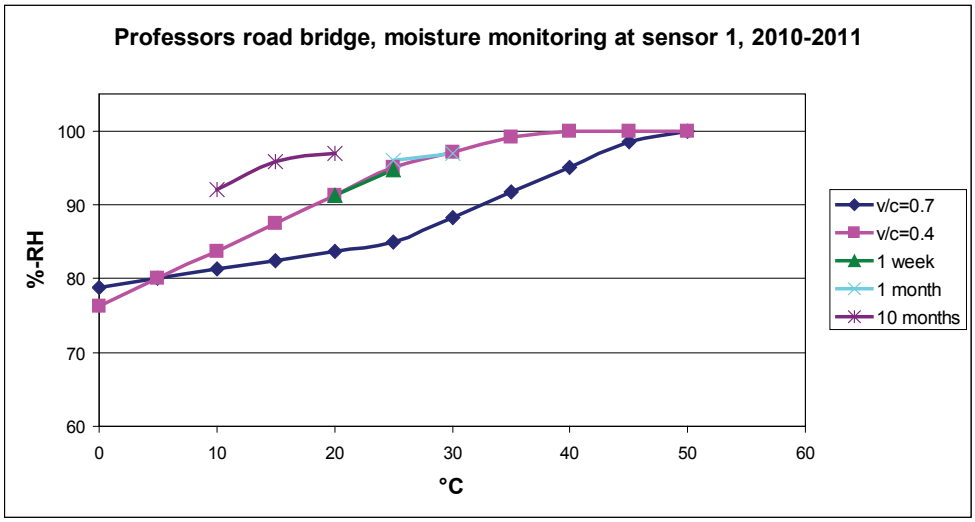

Figure 14 – Relative humidity – temperature measurements on Professor's Road Bridge in Helsinki 2010 and 2011 repaired in July 2010 with 30-50 mm levelling concrete having a unknown water cement ratio . Sensor number 1.

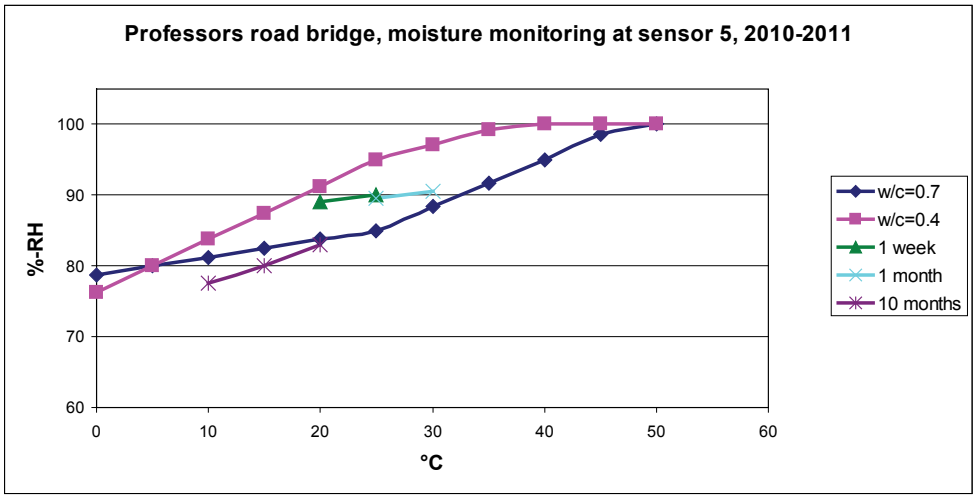

Figure 15 – Relative humidity – temperature measurements on Professor's Road Bridge in Helsinki 2010 and 2011 repaired in July 2010 with 30-50 mm levelling concrete having a unknown water cement ratio. Sensor number 5.

2.3 Moisture content measurements using optic fibres

Destia Ltd implemented in cooperation with Technical Research Centre of Finland VTT, Fortum Power and Heat Oy and FuktCom AB moisture content measurements of Boxby Bridge in Porvoo in Southern Finland /9/. The bridge was widened one metre on both sides and new edge beams were constructed.

The rate of the absolute humidity was in November 2007 (two months after casting) measured using optic fibres. These measurements were repeated in October 2008. The absolute humidity varied along the bridge between 4.0 and 7.5 mass % AH two months after casting, figure 17. After a year the rate of humidity was 1-2 mass % AH less, figure 18. The relative humidity was also continuously monitored using resistive sensors. The relative humidity varied between 90 and 100 % RH. The absolute humidity was close to 5 mass % AH in the adjacency of this sensors.

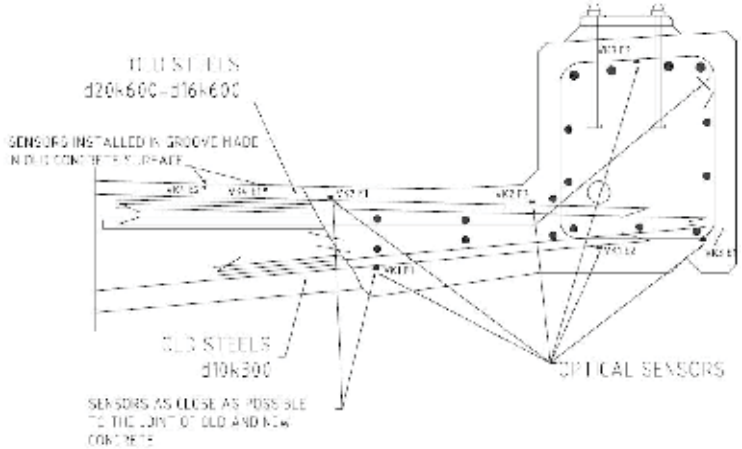

Figure 16 – Locations of the installed fibre optic temperature and moisture content sensors at Boxby /9/.

The optic fibre measurements revealed a substantial moisture fluctuation longitudinally along the bride (4.0-7.5 mass % AH). Obviously the concrete is not as homogenous as expected. The variation of the water cement ratio seems to be too high. The concrete close to the joint of the old structure is much dryer than the concrete in the edge beam. This is explained by the fact that wetting from rain is here much less.

Monitoring by resistive sensors confirmed that there is a unintended variation in the quality of the concrete, table 2. The concrete at the sensor number 4 was wet enough to keep the humidity permanently in the hydroscopic range. Depending on the weather conditions the relative humidity fluctuates and it might be at the level of 100 % RH also in winter time. This explains why there are thaw frost damages in edge beams.

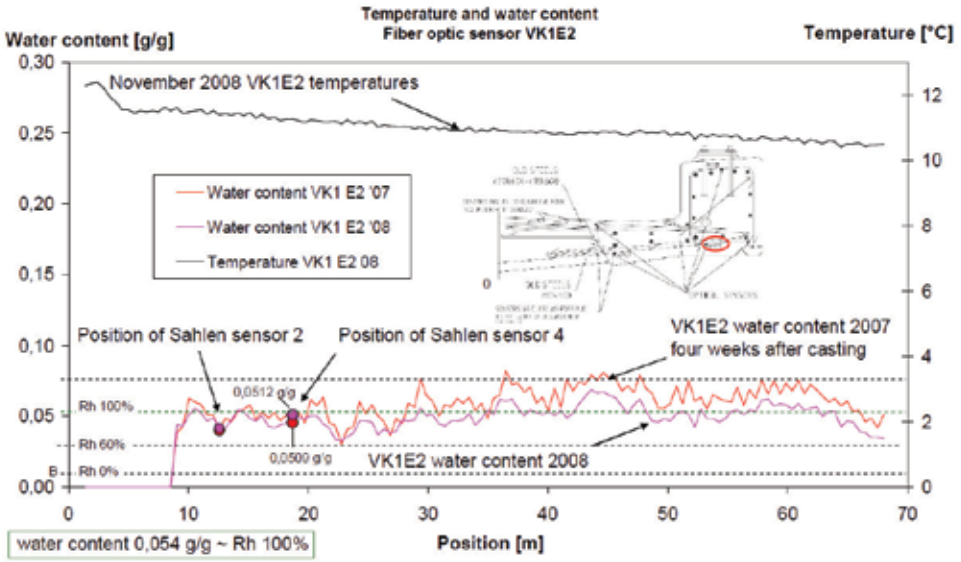

Figure 17 – The temperature and the water content measurement results vs. position close to the bottom of the edge beam (sensor VK1 E2) on 15th of November 2007and 13th of October2008. The positions of the Sahlen sensors 2 and 4 are marked to the graph with red spots. E.g. water content near Sahlen sensor 4 was0.0521g/g on the 15th of November 2007and 0.0509g/g on the 13th of October2008 /9/.

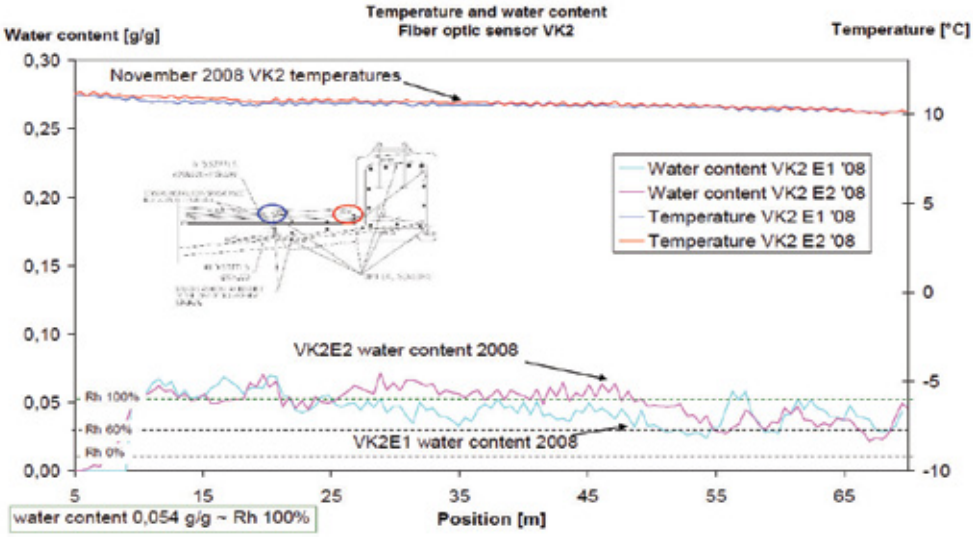

Figure 18 – The temperature and the water content measurement results vs. position close to the upper surface (sensor VK2 E1 and VK2E) on the 13th of October2008/9/.

Table 2 – The relative humidity of different sensors at the temperature 0 °C, sensors 1 and 3 are at the depth of 12-13 cm from the upper face of the edge beam and sensors 2 and 4 8-9 cm above the bottom face.

Time in months	Sensor 1	Sensor 2	Sensor 3	Sensor 4
3	100	100	100	100
4	98	97	100	
14	80	94	94	100
16	82	95	95	100
26	79	93	99	100
28	79	94	96	100

3. SUMMARY

The optic fibres are efficient tools for the measurements of the absolute humidity in outdoor conditions of entire concrete structures. The installation of the optic fibres and the recording and the interpretation of the results take several days of time by 2-3 specialists. The measurements may be repeated at any time, but due the efforts needed, the measurements will cover only short time periods.

Resistive sensors are efficient tools for the monitoring of the relative humidity at different locations for long time periods. The sensors are simple, cheap and easily installed. The reading of results is arranged wirelessly from a data logger installed on the bridge site. The logger is quite expensive, but it may be moved from one site to another. The relative humidity in concrete pores is an indication of small amounts vapour, just a few grams per cubic metres. Since the total amount of water in concrete is 60-90 kg/m^3 or even more, it is no surprise that the correlation between relative humidity and absolute humidity is quite poor. Unfortunately there is no simple and reliable devices available for the absolute humidity automatic measuring so far.

Moisture monitoring during several years after the bridge was cast have revealed that there is no remarkable drying inside the concrete and under the water proofing layer. After the hydration is completed drying takes place only on the bare concrete surface and in slender structures. Since there is wetting due to rain and dew, neither permanent drying will happen. To ensure sufficient dryness, the water cement ratio should be as low as possible. All unnecessary wetting during construction shall be avoided. It seems highly necessary to have better quality control of the concrete mix.

Moisture monitoring in the thin layer of levelling concrete used at repair has confirmed sufficient dryness may be achieved when low water cement ratio concrete is used. However, also here better workmanship is needed. The substrate chiselled by water jet must be dried from excessive water. The site must be protected from rain flow and unnecessary wetting completely avoided.

The implementation of new stricter requirements on the dryness of bridge concrete than the present one requires appropriate regulations. The clients must set the requirements on the upper limits of the moisture content regarding the type of concrete. A low water cement ratio in a concrete means low level of pores and it will be fully saturated with less water than a more porous concrete. Low porous concrete seems to resist better water penetration and it will probably be the most durable type of concrete.

REFERENCES

1. Sven Pihlajavaara: Lecture on practical estimation of moisture content of drying concrete structures. Concrete seminar. Technical Research Centre of Finland. VTT. Helsinki. 1974b. 174 p.
2. Fukthandbok. Lars Erik Nevander. Bengt Elmarsson. 3.upplagan. Svensk byggtjänst 1994.
3. Betonin lämpötila- ja kosteusmittaukset (Concrete temperature and moisture measurements) 1994. Tutkimusselostus nro RTE30255/95. VTT 29.12.1995.
4. Hemming Paroll, Measurement of relative humidity and temperature in new concrete bridges. Nordic Mini-seminar of the Nordic Concrete Federation, VTT Symposium 174, Espoo, Finland 22.8.1997. p. 51 - 65.
5. Hemming Paroll and Esa Nykänen, Measurement of relative humidity and temperature in new concrete bridges vs. laboratory samples. Nordic Concrete Research No. 21. 1998. p. 103-119.
6. Portlandsementin hydrataatio (Hydration of portland cement). Heli Virola. VTT Tiedotteita 2041. Espoo 2000.
7. Suhteellisen kosteuden ja lämpötilan mittaaminen uusilla betonisilloilla (Relative humidity and temperature measurements on new concrete bridges). Tutkimusselostus nro RTE4235/01. VTT 29.11.2001.
8. Ralf Lindberg. Jyrki Wahlman. Jommi Suonketo. Elina Paukku. Kosteusvirtatutkimus (Moisture flow research). Tampereen Teknillinen korkeakoulu. julkaisu 119. Talonrakennustekniikka. Rakennustekniikan osasto 2002
9. SIMO/VTTV689706. TEKES 1819/31/06. Monitoring of Bridges. The Technical Research Centre of Finland (VTT) publication 11th of December 2008.
10. Nilsson, L-O., (1980). Hygroscopic moisture in concrete – drying, measurements & related material properties. Lund Institute of Technology. Division of Building Materials. report TVBM-1003. 162 p.
11. Siltojen kermieristeiden kuplimisilmiöiden selvitystutkimus, väliraporrti 2 (The study of bubbling in sheet membrane water proofing, report 2). The Technical Research Centre of Finland (VTT) publication VTT 32/51/97-YKI 54, February 1998.
12. Pintarakenteiden nopeutetut korjausmenetelmät. Liikenneviraston tutkimuksia ja selvityksiä 39/2009. Kuopio 2011. Accelerated repair of bridge deck surface structures. The Finnish Transport Agency report 39/2009. Kuopio 2011.

Optical Moisture Measurement in Concrete Aggregates

Taisto Haavasoja
M.D., Ph.D. (Phys.)
Teconer Ltd
Runopolku 1b,
FI - 00420 Helsinki
taisto.haavasoja@teconer.fi

ABSTRACT

We have studied feasibility of using optical means to measure aggregate moisture content. We measured optical response of some commonly used aggregates at around 1.5 µm wavelengths. The results suggest that this wavelength range enables nominal accuracy of about 0.1% in moisture by weight. One of the major benefits in optical technology is a noncontact measurement allowing practically a onetime calibration procedure and a long lifetime of the sensor due to solid state design. On the challenge side there is a need to protect the sensor window from dust and condensing of moisture. These issues have been field tested in concrete plants and a long term accuracy of 0.3% is realistic in practise. We also measured the optical response to a maximum variation in aggregate grading.

Key words: Aggregate, moisture, water content, optical sensor, infra-red spectroscopy.

INTRODUCTION

Coarse aggregates can contain 0-2% surface moisture by weight and fine aggregates even up to 10%. These numbers exclude absorbed water, which ranges typically from 0.5 to 4% according to Ref. [1]. Ultimately, wet aggregates may contain moisture more than is desirable to preserve the water-cementitious material ratio (w/cm) in design limits without overdosing cement. In practise, moisture content of aggregates must be known to fractions of percent to minimise variability in concrete quality and to enable optimal usage of cement. Accurately measured moisture in aggregates allows optimising strength, durability and shrinkage of concrete products. Also knowing the right moisture content prior to mixing permits faster mixing times, when there is no need to add water during mixing.

There are a number of means to arrange measurement of aggregate moisture in concrete plants. The traditional measurement by weighing and drying a sample is satisfactory only in plants, where the aggregates are well mixed by the time of loading to silos so that variation of moisture is minimal between batches. Few plants have this strategy in practise and thus in many plants an automatic measurement is highly recommended.

Currently the most widely used automatic moisture measurement in concrete industry seems to be based on capacitive or microwave sensors and one of the most prominent producers are Franz Ludvig GmbH in Germany and Hydronix Ltd in UK. Capacitive and microwave sensors are installed typically in direct contact with the aggregate either in silos, silo feeders or even over a conveyor belt. The dipole nature of water molecule implies a high dielectric constant of water

enabling simple detection in aggregates by coupling to a sensing electromagnetic field. Since the dielectric constant of most aggregates is fairly small compared to water, capacitive sensing produces often a fairly stable result. Nevertheless, direct contact to sample causes mechanical wearing of the sensor requiring occasional recalibration and finally replacement of either the sensor plate or the whole sensor. Few concrete plants have personnel capable to calibrate or maintain the sensor.

Optical detection of material moisture would allow noncontact detection with clear advantages for concrete industry. Optical moisture sensors are based on absorption peaks by water molecules at near infra-red wavelengths. There have been optical moisture sensors available for process industry over tens of years, but they have not been widely used in concrete plants due to their high price compared to microwave sensors. However, development of optoelectronic components thanks to optical communication technology has enabled designing more optimal and economical sensors for measuring surface moisture in aggregates.

In the following chapters we present the basics of optical moisture measurement, a new optical sensor designed for detection of moisture and discuss the challenges of applying the sensor for optical detection of aggregate moisture.

1. OPTICAL MOISTURE MEASUREMENT

Optical moisture sensors employ an active light source transmitting preselected wavelengths bands on the sample. The back reflected light is collected on a detector element for analysis. There are typically at least two wavelength bands in use so that one is on an absorption peak of water molecule and the other is used for a reference signal. The reflected amount of light at absorption wavelength is compared to the reference signal and this information is used to determine moisture content by calibration.

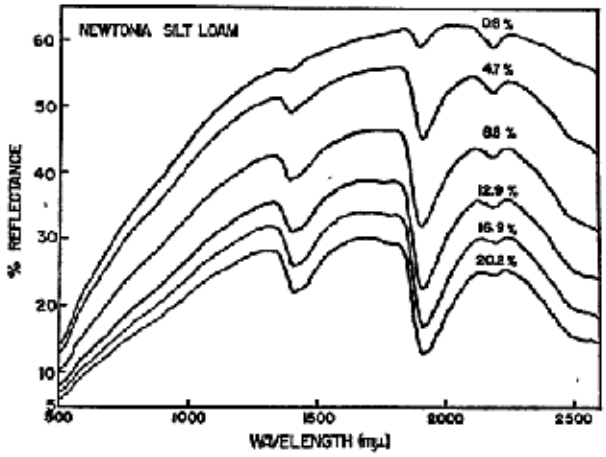

Figure 1 Reflectance of silt loam as a function of wavelength and moisture content in the range 0.8 – 20.2 % according to Bowers and Hanks [2]. There are two clearly observable absorption peaks at about 1.4 and 1.9 µm.

Figure 1 represents reflectance from visible to near infra-red wavelengths as measured by Bowers and Hanks [2] in silt loam. In concrete aggregates the behaviour is generally similar showing decreasing reflectance and increasing absorption peaks with increasing water content. Since water contents in aggregates range only to about 10 % depending on the fineness number, the absorption peak at 1.9 µm is most desirable for water content measurement in aggregates. In practise technological reasons may lead to preference of lower wavelengths.

Traditional optical moisture sensors use broadband emitting hot lamps and a set of filters arranged in a rotating wheel. This technology has the advantage that many wavelengths are available allowing higher detectability with various materials. Currently there are available fairly narrow band near infra-red light sources enabling construction of a simpler and reasonably accurate optical system with clearly less expensive end user price. To our knowledge these traditional optical moisture sensors cost three to four times more than widely used microwave sensors and have not been able to penetrate to this application. Thus we have taken microwave sensors as our reference in this study to compare a new optical technology to existing solutions from a practical point of view.

In literature there is not immensely research available on optical moisture measurement of aggregates with a potentially low cost technology. An example of such a research is by Clemmensen et.al. [3]. They took multispectral photographs of aggregate samples from visible to about 1 micron wavelength and compared various statistical dimension reduction methods for determining moisture of the samples. They notice increase of standard deviation when images are split into sub images indicating inhomogeneity of the samples. The authors recommend appropriate sampling techniques to compensate for the inhomogeneity when applied on process conveyors. To avoid this same problem we had to integrate continuously a moving sample laid freshly on a conveyor.

2. WATER CONTENT MONITOR WCM411

The optical sensor used in this study is called Water Content Monitor WCM411 produced by Teconer Ltd. A photograph of the sensor is shown in Figure 2 and an example of installation over a silo feeder in Figure 3. The sensor is installed typically within 0.5 – 0.8 meters from the sample surface with a dust protection tube as shown in Figure 3. The sensor is supplied with a cable for power (9-30 VDC) and communication (RS-232, 4-20 mA current loop). Repeatability and short time stability of the sensor is about 0.1% by weight. An absolute accuracy of about 0.3% is reachable with a careful calibration and homogeneous sample. This level of accuracy can be maintained for extended periods assuming dust protection of the sensor window is effective. The sensor does not have any moving parts and uses a long lifetime light source allowing an extensive maintenance free service life.

Figure 2 A photograph of Water Content Monitor WCM411. Diameter of the sensor is 75 mm and length 100 mm. The sensor cable is equipped with a 5 lead connector.

Figure 3 An example of a WCM411 installation over a silo feeder belt with a dust protection tube.

The response of an optical sensor to moisture comes from the sample surface. Some aggregates may be partially transparent and in that case the response may come from some depth beneath the upper surface. Typically this penetration depth is only a few millimetres. Therefore most of the response can be assumed to reflect surface moisture instead of volumetric moisture. In comparison to microwave moisture sensors the main difference is that optical sensors mainly respond to changes in free surface moisture and less to volumetric moisture in contrary to

microwave sensors. Thus optical sensors are less sensitive to local variation in particle size distribution.

3. PERFORMANCE

The detection area of WCM411 is fairly small, about 0.05 m by diameter at 1 m distance. Therefore the sample area is often not optically homogeneous, which prevents accurate measurements with static samples. Thus it is better to use a moving sample and calculate an average value to represent a larger amount of the sample. Most accurate calibration of the sensor with a given aggregate can be obtained by starting with about 1-2 % moisture and then adding water, e.g., in steps of 1 % up to about 5 %. A micro mixer is used to mix the sample continuously while adding water after obtaining a stable reading at the given water content. At low moisture content there is a risk of segregation of large aggregate particles on the surface whereas at high moisture content mixing may be ineffective due to the sample being like dough and getting lumpy.

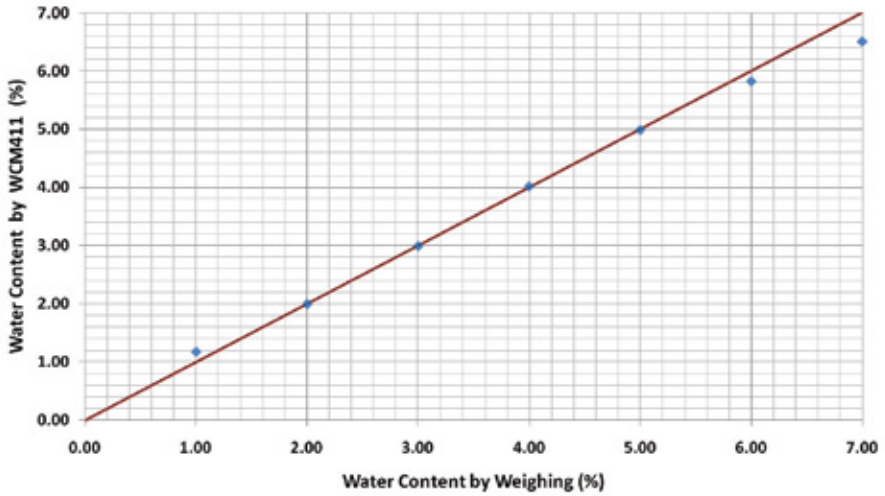

Figure 4 A typical calibration line for a 0-4 mm fine aggregate. The dots represent response to addition of water content in steps of 1%. The line is just a guide to the eye for an ideal response. The apparent deviations at 1%, 6% and 7% come from an incomplete mixing of the micro mixer, which can be revealed by employing another kind of a mixing technique.

Figure 4 shows an example of a calibration with the method described above in a 0-4 mm fine aggregate. As the figure implies an optical sensor can have an extremely high nominal accuracy, fractions of 0.1% at typical moisture contents. However, there are a number of reasons why this level of accuracy is not reachable in practise. Those reasons can be divided to sample dependent and external ones. The former include sample inhomogeneity, e.g. optical properties and local variation in grading. The external reasons are related to stability of the measurement environment and general sampling problems of reference values. A good measure of all these

factors together can be obtained by observing a long term scatter of occasional sensor readings and reference values obtained by weighing and drying.

We tested the sensitivity to variation in grading in a 0-8 mm fine aggregate. The grading was changed by adding fine particle fractions up 0.25 mm sieve as much as the norm [4] allows. This corresponded to an increase of about 15 units in fineness number and 8.7% in formal surface area. If the optical measurement interacts only with the top layer of the sample, we would expect the slope of the calibration curve to decrease by the increase of nominal surface area. The change was clearly smaller, from 1.000 to 0.952, corresponding on the average to a reduction of only 0.20 % units in moisture (Figure 5). The result supports the interpretation that the aggregate is to some extent transparent at near infrared wavelengths. Inherent differences in optical properties of finer gradation particles can also cause part of the observed change in calibration.

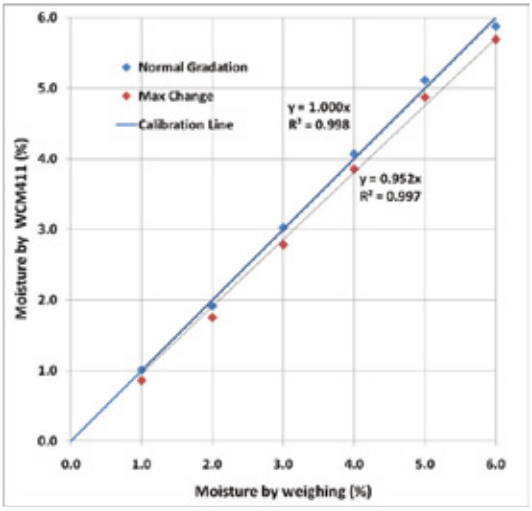

Figure 5 Response of a calibrated sensor (blue dots) to a maximum increase in fine gradation (red dots) corresponding to 15 units in fineness number.

Figure 6 shows the results of a long term test of in a plant environment. The data was collected within four months leaving the optical sensor untouched during the whole test period. The weighed reference values were collected by taking typically three manual samples from a given mixing batch and comparing water loss in drying to corresponding sensor readings.

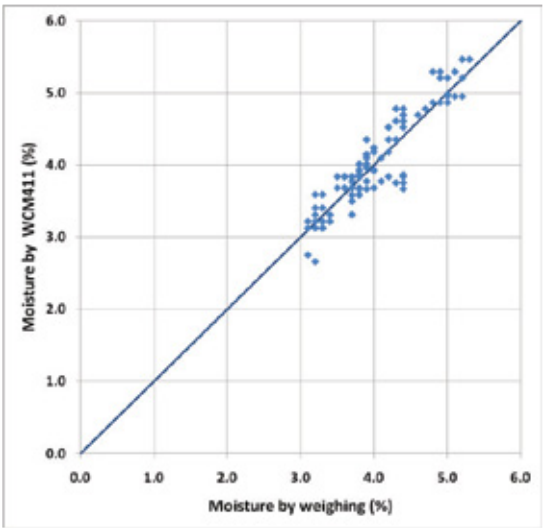

Figure 6 Comparison of sensor readings to a weighed reference value in a long term plant test. The standard deviation of the differences is 0.25% in moisture.

The apparent scatter in the data of Figure 6 has clearly increased as compared to calibration data. However, the standard deviation, 0.25% in moisture, is still fairly low. Surprisingly, the most significant reason for the scatter is not related to the performance of the optical sensor but instead to manual sampling problems of the weighed reference data. For practical reasons the reference samples are on the order of 1 kilogram by mass representing only a tiny fraction of the whole batch and thus being sensitive to local variation. Instead, the sensor readings represent average values of a much larger part of the batch thus representing more likely the average moisture of the batch. Often the three reference samples of a single batch varied almost one percent in moisture from each other whereas some other time the scatter was only a few tenths of percent.

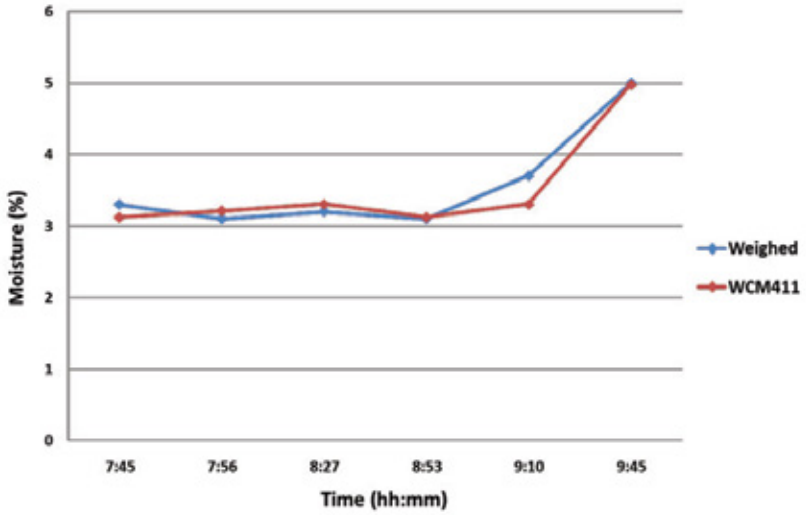

Figure 7 Comparison of sensor readings to a weighed reference value during one morning. The rapid increase in moisture starting at 9:10 levelled off later by the same day.

An example of sudden variation in a silo moisture is shown in Figure 7. Up to about 9:00 the reference values and the sensor readings showed a fairly stable moisture around 3.2%. Suddendly both of the readings started to increase ending to 5% and over. The large and fast increase in silo moisture was probably caused by a heavy raining period a few days earlier. This example shows why it is important to follow aggregate moisture continuously instead of taking only one daily reference sample.

4. CONCLUSION

Optical sensing of moisture in concrete aggregates has been available for some time but it has not been competitive with capacitive and microwave technologies so far. Recent advances in solid state light sources and detectors have enabled designing price competitive optical sensors which can be optimised for a given specific task. We have shown that the performance of an optical moisture sensor competes with microwave technologies. The challenge to keep the optical window clean can be solved with simple arrangements. Noncontact measurement, long lifetime due to solid state design, easy calibration, high accuracy and low need for maintenance will help to deploy optical sensing to measure moisture in concrete or many other industrial aggregates. Most promising applications include moisture in high reflectance materials of mining industry and power production by incineration of chopped wood or peat.

ACKNOWLEDGEMENT

We are indebted to an unnamed international concrete manufacturer for letting their facilities for this study. We want also to thank referees of their valuable comments and suggestions.

REFERENCES

1. Aggregates for Concrete, ACI Education Bulletin E1-07, developed by ACI Committee E-701, chaired by David M. Suchorski, American Concrete Institute 2007.
2. Bowers, S.A., and Hanks, A.J., Reflection of Radiant Energy from Soil. Soil Science, Vol. 100, p. 130-138, 1965.
3. Clemmensen, L.H., Hansen, M.E., and Ersbøll, B.K. "A comparison of dimension reduction methods with application to multi-spectral images of sand used in concrete", Machine Vision & Applications, Vol. **21** (6), p. 959-968, 2010, Springer UK.
4. BY43 Betonin kiviainekset 2008, Betoniyhdistys ry, Suomen Rakennusmedia Oy 2008.

Static and Fatigue Capacity of Partially Loaded Areas in Concrete Structures

Jan Arve Øverli
Associate Professor, Ph.D
Department of Structural Engineering
Norwegian University of Science and Technology
7004 Trondheim, Norway
E-mail: jan.overli@ntnu.no

Paola Mayorca
Principal Engineer, Ph.D
Concrete Structures
Det Norske Veritas AS
1363 Høvik, Norway
E-mail: paola.mayorca@dnv.com

Alexander Furnes
Master student
Department of Structural Engineering
Norwegian University of Science and Technology
7004 Trondheim, Norway
E-mail: afurnes@gmail.com

Ole-Martin Hauge
Master student
Department of Structural Engineering
Norwegian University of Science and Technology
7004 Trondheim, Norway
E-mail: olemartin.hauge@gmail.com

ABSTRACT

The compressive strength of concrete at bearing areas is increased due to confinement of surrounding concrete and reinforcement. Design codes propose criteria for resistance when the load can distribute in two directions for static loading but not specifically for fatigue loading. This study focuses on concentrated load distributing in one direction with confinement in the transverse direction. Six concrete specimens subjected to static loading and six specimens subjected to fatigue loading in compression were tested. In conclusion, the observed loads were in good agreement with the standards for static loading. For fatigue loading, definite conclusions could not be drawn due to the limited number of specimens tested.

Key words: Partially loaded areas, bearing strength, static and fatigue capacity.

1. INTRODUCTION

In design of concrete members a control of the bearing strength is necessary. Typical members are anchoring of post-tensioned beams, supports, and connections of columns or walls to foundations. Figure 1 shows the stress field under a centric loaded solid where the axial stresses spreads out over the area, to finally approach a constant distribution some distance from the load. Also the distribution of transverse stresses is given, compressive stresses close to the top and tensile stresses (bursting) in lower part.

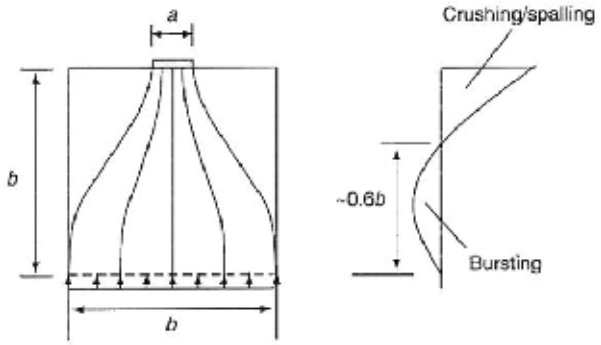

Figure 1 – Stress field under concentrated load according to linear analysis [1].

Close to the load, the expansion of the core is hindered by the surrounding concrete, introducing transverse compressive stresses in the core and a ring tension, see section I-I in Figure 2. This provides lateral confinement to the core. Hence, a triaxial stress state is established and the compressive strength is enhanced. The confinement could be further increased by employing transverse reinforcement in this area. In practice there is also often a restraint from shear stresses from the loading plate, which resist splitting at the loaded area.

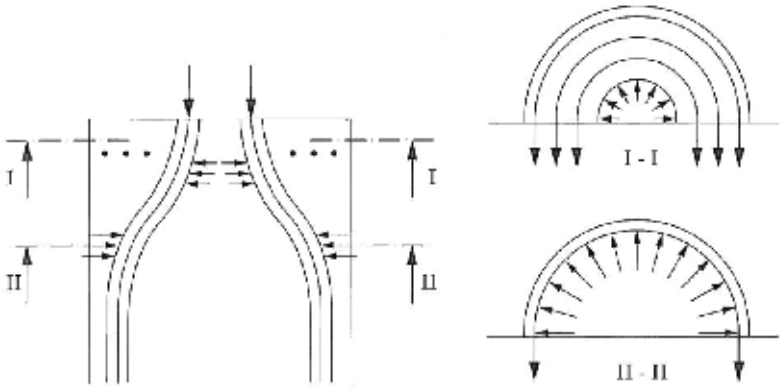

Figure 2 – Transverse stresses inducing splitting forces [2].

In the transition region, section II-II in Figure 2, the splitting forces must be balanced by an outer tensile ring to keep the vertical compressive force together. Thus, transverse reinforcement is necessary in this area.

The capacity of the partially loaded area is governed either by crushing/spalling near the loaded face or tension failure due to bursting forces in the lower region. The bearing capacity is affected by the loading condition, loaded area, cross-section of the loaded member, and transverse reinforcement, in addition to the compressive strength. In design codes the bearing strength are normally related to the area of loading and an area of distributed stresses [3], as seen in Figure 3.

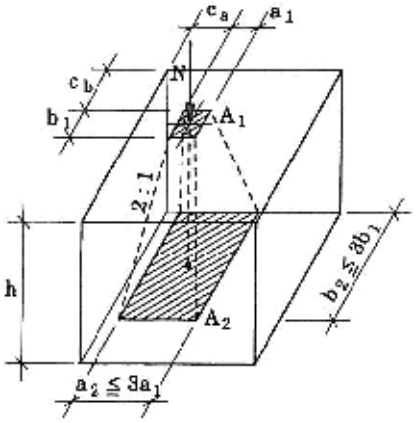

Figure 3 – Design distribution for partially loaded areas [2].

In design codes the bearing capacity f_c^* of a centric loaded member is often defined as [3], [4]:

$$f_c^* = f_c\sqrt{A_2/A_1} \tag{1}$$

where f_c is the uniaxial compressive strength, A_1 the loading area and A_2 the distribution area. Limitations of the distribution area are introduced to take into account loads close to an edge, eccentric loading or overlapping loads. In cases where the load is not uniformly distributed on the area A_1 or if there are high shear forces the bearing strength should be reduced.

Eq. (1) is derived on basis of the capacity of the tensile ring of section I-I in Figure 2 [5]. Hence, the equation represents a splitting failure close to the load and not a compression failure which often is assumed. To avoid crushing in the concrete close to the load, there is normally an upper limit of Eq. (1) on 3-4 times the uniaxial compressive strength. The strength of the locally compressed concrete against crushing can conservatively be estimated by means of soil mechanics models for footings, taken into account only the cohesive component of the concrete strength [5].

In order to avoid a splitting failure in the transition zone, section II-II in Figure 2, the transverse bursting force T, can be estimated in the two transverse directions for centric loading as [6]:

$$T = 0.25 \cdot N(1 - a_1/a_2) \quad (2)$$

where N is the concentrated load and a_1 and a_2 (or b_1 and b_2) are the lengths of the loaded and distributed area given in Figure 3. The bursting forces must be resisted by the tensile strength of the concrete, or more common, by providing local transverse reinforcement with adequate anchorage at both ends. In practise the transverse reinforcement is distributed over a length of the element. Design codes give detailing rules for the position of the centre of gravity of the distributed transverse reinforcement and the distribution width [3].

The compressive stress control in Eq. (1) is valid in cases where the load can spread in two directions. If the loaded area is much larger in one direction than the other, e.g. bearing strips for slabs, the tensile ring under the load cannot develop properly. Thus, the bearing capacity must be reduced. In design of precast concrete members, the following reduced capacity is often applied [2]:

$$f_c^* = f_c \sqrt[3]{A_2/A_1} \leq 2.5\, f_c \quad (3)$$

This study focus on the bearing capacity of concrete foundations subjected to a line load. Figure 4 illustrates a shaft on circular foundation. This could be the steel tower of a wind turbine. Dead load and wind loads enter the foundation as a line load in hoop direction, close to the outer edge. Hence, the partial loading can only spread in the radial direction. However, in hoop direction the foundation is restrained both geometrically and due to hoop reinforcement.

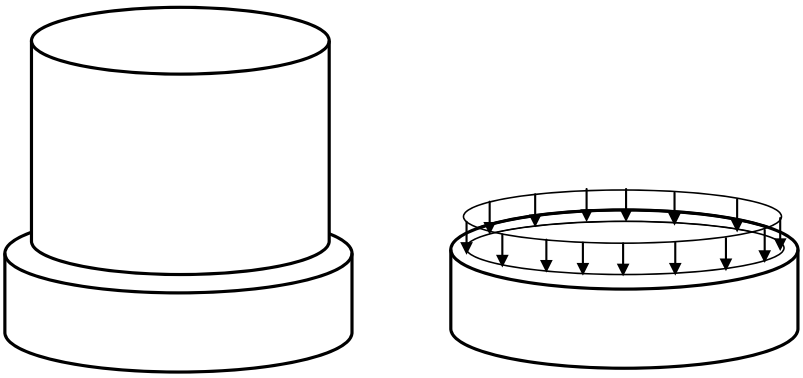

Figure 4 – Circular foundations with a line load.

The aim of this study is to investigate the bearing capacity of structural members of the type in Figure 4. An experimental program is set up to estimate both static and fatigue capacities. Static capacity is compared to Eq. (1). The effect of transverse reinforcement is also investigated. Fatigue loading is performed to verify if the increase of locally compressed concrete resistance compared to uniaxial strength is applicable also for fatigue loading. The work has been carried out as part of a Master thesis project at department of Structural Engineering at Norwegian University of Science and Technology (NTNU) in collaboration with Det Norske Veritas AS (DNV) [7].

2. EXPERIMENTAL INVESTIGATION

2.1 General

To investigate the structural behaviour of partially loaded concrete member, concrete blocks were exposed to a line load, and strains and failure loads measured. The partial loading could be considered a local loading since it is only partial in one direction. In direction of the line load the blocks were confined. The experimental program covers 12 blocks, where half of them were subjected to static loading and the rest subjected to fatigue loading to find the fatigue capacity. The fatigue strength was limited to cyclic compression, since this study focus on foundations with loading only in compression. To investigate the effect of splitting reinforcement, three of the static tests were performed without splitting reinforcement.

This experimental program is considered a first step on investigating the fatigue response of concrete subjected to local compression. Static bearing capacity is well documented in the literature. Also effects of confinement on fatigue properties of concrete, which is important in partially loaded members, are reported [8], [9]. However, information dealing with fatigue capacity of locally compressed concrete is limited.

2.2 Specimens

The specimens in the experimental investigation had a rectangular shape with dimensions 210×210×525 mm, as seen in Figure 5. The specimen could represent a part of the foundation illustrated in Figure 4. The dimensions are typical for connections between a steel shaft and a base foundation of wind turbines. The testing facilities in the laboratory also limited the size. The loading area is 70×210 mm, representing a surface load. By using the stress distribution definition from design codes [3], [4], the height of transition zone is 140 mm, see Figure 3. However, the distribution area does not comply with the codes where the load is distributed in two directions introducing a tensile ring, see Figure 2. In this study a modification is made, assuming the load to distribute in one direction only, as seen in Figure 5, since the loading cannot distribute in the opposite direction.

In addition, standard cube specimens, which were tested simultaneously with the specimens, were casted to evaluate reference uniaxial static strength. The humidity of cubes and specimens was kept similar.

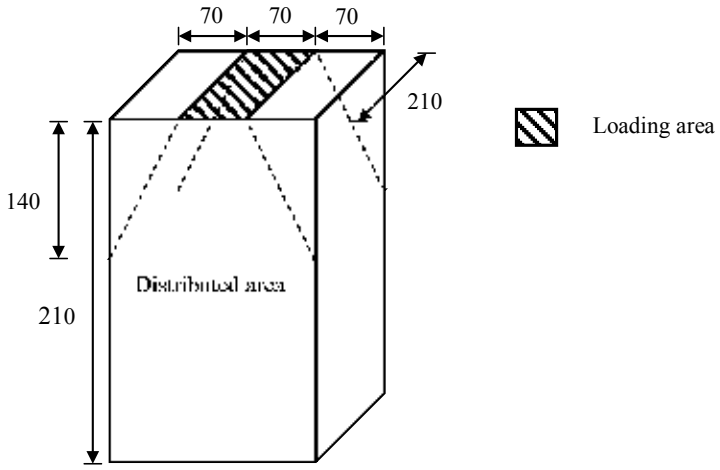

Figure 5 – Dimensions of specimens and loading area.

2.3 Concrete properties, casting and curing

In this study the concrete had the following properties, per cubic meter: Norcem standard FA cement 293 kg, fine aggregate 0-8mm 1081 kg, coarse aggregate 8-11 mm 721 kg, water 204 kg and 2 kg Scancem P plasticiser. In order to control the concrete strength, a test casting was performed. The mean 28-day cubic compressive strength, $f_{c,cube}$, obtained was 25.1 MPa. This strength was used in design of the specimens.

The specimens were cast in wood frames where each part held 6 specimens, as seen in Figure 6.

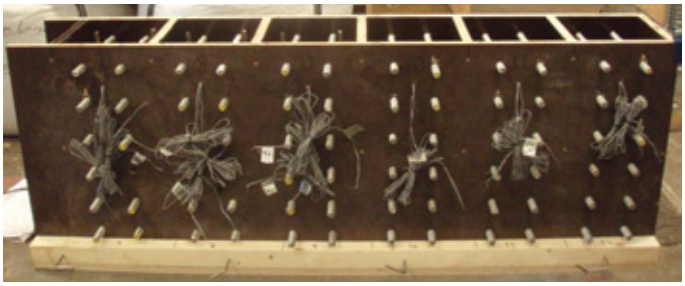

Figure 6 – Casting frame.

Water content in concrete affects the static strength [10]. Fatigue capacity is further influenced by whether concrete is submerged in water or in the air. Without drying the fatigue life is reduced. This reflects the fact that stronger concretes, due for example by drying, have longer fatigue life. To ensure the same testing conditions for all specimens, they were sealed in wet burlap sacks and wrapped with plastic. Prior to testing a synthetic resin based membrane, Sikafloor Proseal W, was applied to the specimens.

2.4 Reinforcement

The required splitting reinforcement was calculated according to Eurocode 2 [3]. The local compressive strength has the same form as Eq. (1) and the total concentrated resistance force, F_{Rdu}, is defined as:

$$F_{Rdu} = A_1 f_c \sqrt{A_2/A_1} \leq 3.0 \cdot f_c \cdot A_1 \quad (4)$$

The distribution area in Figure 5 is employed in the equation. Based on the mean cylinder compressive strength from the test casting of concrete, 20.1 MPa, determined as 80% of the cube strength, the capacity is 511 kN.

By employing Eq. (2), the transverse tensile bursting force is 85 kN for a concentrated load of 511 kN. For reinforcement grade B500NC this requires six Ø6 splitting reinforcement bars. In each corner of the specimens Ø10 vertical bars were used in order to support the stirrups. To avoid concrete cover spalling, Ø6 stirrups with centre vertical distance of 80mm were employed. The reinforcement layout is given in Figure 7. With a distribution height for the load of 140 mm, this means that the top two layers of stirrups are part of the splitting reinforcement. Hence, two additional splitting bars are required in the centre of the specimens. The concrete cover is 15 mm.

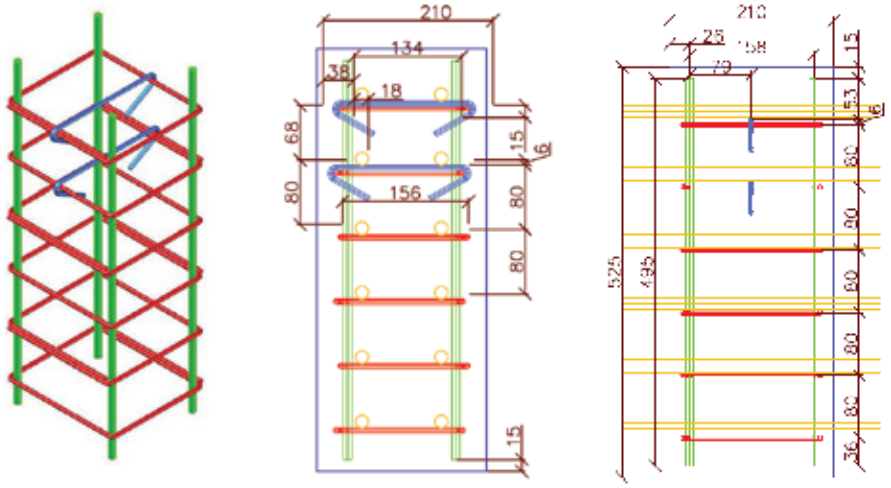

Figure 7 – Reinforcement layout (measures in mm).

Nine specimens were cast with the reinforcement layout in Figure 7. The last three specimens were cast without splitting reinforcement, and the stirrups were only placed at the lower part of the specimen, i.e. four layers with stirrups. The longitudinal reinforcement in the circular foundation in Figure 4, corresponds to the quadratic stirrups in the test specimens.

2.5 Threaded bars

In these experiments the specimens ought to be restrained from deforming in the direction parallel to the line load, forcing vertical cracks to form in one direction only. Therefore all of the specimens were provided with 12 threaded bars. The threaded bars are cast into the specimens and were restrained with plates and bolts, as seen in Figure 8. The threaded bars were of property class grade 8.8 with yield strength of 640 MPa and diameter 16mm.

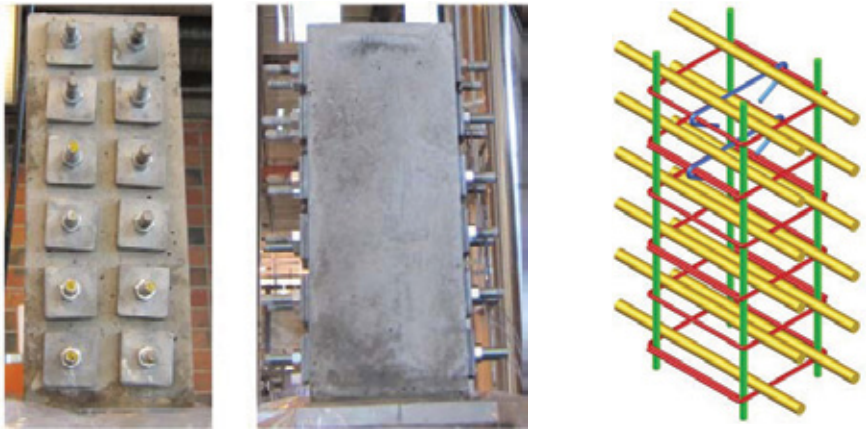

Figure 8 – Threaded bars with plates and bolts attached, and a 3D model of the threaded bars.

2.6 Instrumentation

Each specimen with splitting reinforcement was provided with four strain gauges, while the unreinforced specimens had two strain gauges. In the reinforced specimens the stirrup located in the second layer from the top had one, the two splitting reinforcement bars had one each, and the final gauge was placed at one of the threaded bars in the second layer. For the unreinforced specimens, the two strain gauges were placed on the two top layers of threaded bars. Figure 9 shows the location of the strain gauges for specimens with splitting reinforcement.

To capture the vertical deformation of the specimens, one LVDT was placed in one corner at each specimen. However, the deformation will not be uniform in the section, and with only one LVDT (due to limitations in the logging equipment) the deformation cannot be used directly in this study. The measuring was merely to follow the global response of the concrete members and not for evaluating results in this study.

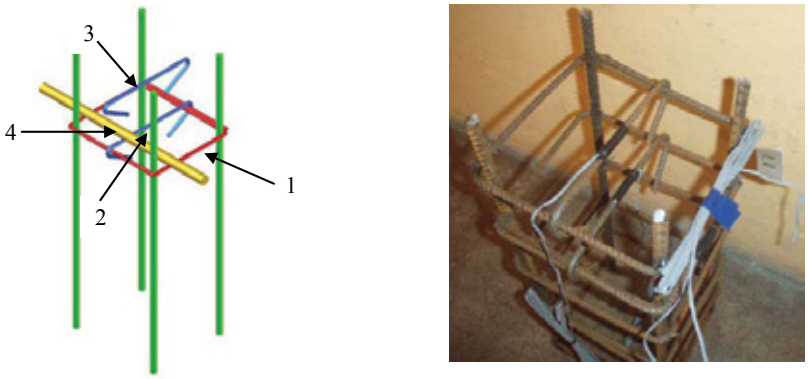

Figure 9 – Placement of strain gauges1-4.

2.7 Test facilities

To apply the static and fatigue loading a hydraulic Material Testing System, MTS Instron 8500, with a capacity of 1000 kN was used together with a control computer. To transfer the load from the hydraulic jack, a solid steel plate with thickness 29 mm was used, see Figure 10. Between the specimen and the steel plate an aluminum plate with thickness 1 mm was placed to achieve a better load distribution on the concrete.

The logging was done with a sampling rate of 5 Hz for static test, and 25 Hz for the fatigue loading.

Figure 10 – Test arrangement and loading plate.

2.8 Experimental program

In the first part of the investigation six specimens were loaded statically in compression until failure. Failure was defined when the deformation continued to increase as the loading decreased. Test 1-3 were specimens with splitting reinforcement and Test 4-6 were without reinforcement. Test 1 had a load rate of 0.18 mm/min, while Test 2-6 had load rates of 0.4 mm/min.

Six specimens were tested for fatigue capacity, Test 7-12. All specimens had splitting reinforcement. The specimens were subjected to constant amplitude cycling between two load levels. The frequency of loading was 1 Hz with a sinusoidal waveform.

In fatigue the maximum load level is the primary variable. Before starting the fatigue loading, there were uncertainties of the effect of the splitting reinforcement on fatigue capacity. Hence, it was decided to employ 83% of ultimate capacity of the static loaded specimens without splitting reinforcement. Test 7 was a runout (no failure occurred after one week). Therefore it was decided for the last five specimens to use the ultimate capacity determined from the static tests with splitting reinforcement as the reference load level. The maximum load level employed was 72% and 80% of the static capacity. For all fatigue tests the minimum load level was 10% of the ultimate compressive capacity. The maximum and minimum load levels are given in Table 1.

Table 1 – Test procedure for fatigue testing

Test	Maximum load (S_{max}) [kN]	Minimum load (S_{min}) [kN]
7	330	40
8	520	65
9	520	65
10	520	65
11	468	65
12	468	65

For each specimen, the uniaxial compressive strength was measured with standard cubes at the time of testing.

3. TEST RESULTS

3.1 Static loading

Figure 11 shows typical crack patterns in the specimens subjected to static loading. Vertical cracks appeared in the middle face of the specimen, between the first and second level of threaded bars and plates, at around 70-75% of the failure load of the specimens without splitting reinforcement. However, due to the plates at the end of the threaded bolts, there is a possibility cracks could have formed earlier behind the plates before the first observations of cracks. With increasing loading cracks formed at corners of the load plate and propagated down with an inclined angle below the first two rows of threaded bars. At peak load large almost vertical cracks formed close to the outer edges, as seen in Figure 11. In these experiments the threaded

bars works as crack markers. Especially for specimens without splitting reinforcement, the cracks steer through the threaded bars.

a) Test 1.

b) Test2.

c) Test 3.

d) Test 3.

e) Test5.

f) Test 4.

Figure 11 – Specimens after the static tests.

The failure loads, P_{fail}, together with corresponding mean uni-axial compressive cylinder strength, f_{cm}, tested at the same time as the specimens, are given in Table 2. The mean failure loads for specimens with and without splitting reinforcement are 618 kN and 398 kN, respectively. In the table also the increased local capacity due to confinement is compared to the uni-axial capacity. To verify and validate the increased capacity comparison is made with design codes [3], [4]. However, the design codes implies that the load can be distributed in two directions, as illustrated in Figure 3. In these tests the load distributes only in one direction, but is instead restrained in the other direction by threaded bars. Hence, the comparisons are not directly applicable, but indicate the effect of the confinement.

In the design codes the increased capacity is proportional to the square root of A_2/A_1, see Eq. (4), which yields a factor of 1.73 for the dimensions in these experiments. Compared to the, mean value of approximately 1.9 obtained for specimens with splitting reinforcement, the agreement is quite good.

Table 2 – Test results for static loading

Test	f_{cm} [MPa]	P_{fail} [kN]	$P_{uniaxial}=A_1 \cdot f_{cm}$ [kN]	$P_{fail}/P_{uniaxial}$
With splitting reinforcement				
1	20.4	566	300	1.89
2	22.2	626	326	1.92
3	22.2	662	326	2.03
Without splitting reinforcement				
4	22.2	386	326	1.18
5	22.2	430	326	1.32
6	22.2	379	326	1.16

The tests without splitting reinforcement resulted in an increased capacity of approximately 1.2 compared to the uni-axial strength. According to CEB-FIB Model code 1990 [5] the bursting force resisted by the tensile strength of the concrete can be estimate as:

$$T \leq f_{ct} \cdot 0.6 \cdot b \cdot h \tag{5}$$

where f_{ct} is the tensile strength and h and b are the height and width of the distribution area for the load. By employing Eq. (2) for the bursting force, assuming a tensile strength of 10% of the compressive strength and $b \times h$ = 210×140, the capacity is calculated to 313 kN. Thus, the experiments indicate larger capacities. The concrete under the loading area is in a complex state of triaxial stress due to friction of the loading plate. A simplified approach is to estimate the local compressive capacity close to the load by assuming the concrete to be in a biaxial compression state of stress. With a Poisson ratio of 0.2 and the specimens assumed to be fully restrained in lateral direction, the increased capacity is approximately 1.2 [11], which is close to the experimental results.

The graphical plots of strains in the reinforcement for specimens with splitting reinforcement are shown in Figure 12. Figure 13 presents the development of steel strains in specimen 3. Location of the strain gauges can be found in Figure 9. The general observations of the results were as follows:

a) Steels strains are small up to a load of ~300kN, in accordance with the first crack observation.
b) The stirrups are activated later than the splitting reinforcement in the middle part of the specimens, indicating that the steel plate is not able to distribute the load uniformly. In addition, the state of stresses at both locations is different due to the specimen boundary.
c) The splitting reinforcement at the top layer was activated before the reinforcement at the second layer.
d) Strains in the threaded bars are lower than the yield strain. Hence, the bars are in the elastic state, giving a confining effect.

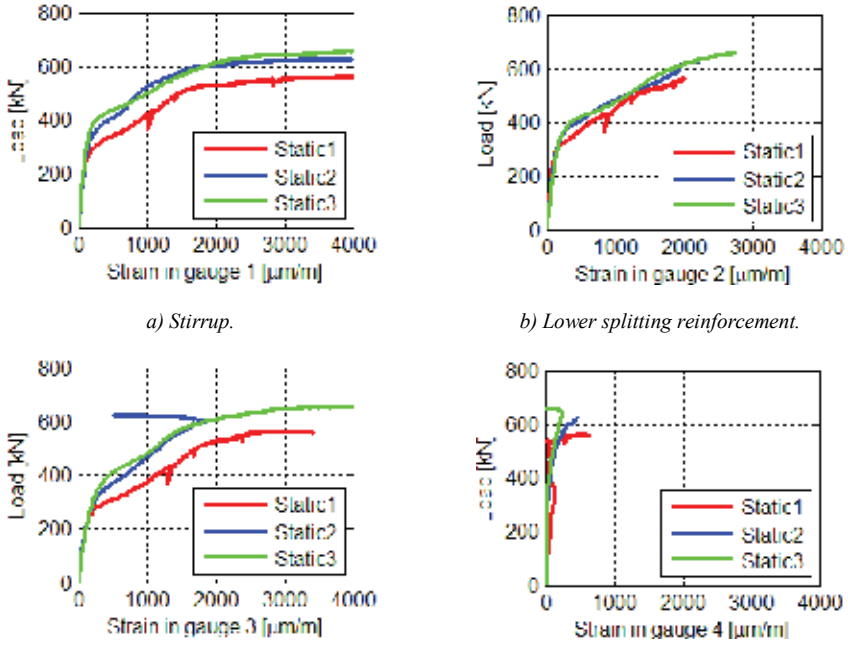

a) Stirrup.

b) Lower splitting reinforcement.

c) Upper splitting reinforcement 3.

d) Threaded bar.

Figure 12 – Results for specimens 1-3, load versus steel strains (gauges).

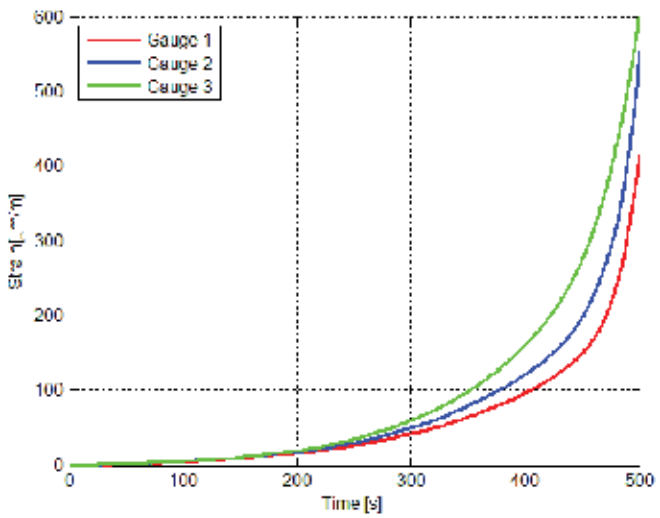

Figure 13 – Results for specimens 3, steel strains (gauges) versus time.

3.2 Fatigue loading

Figure 14 shows specimens 7-12 after fatigue loading. The formation of cracks during the fatigue testing was quite similar to the cracks observed during the static tests. Initially vertical cracks appeared in the middle face, and with increased loading inclined cracks formed. Compared to the static tests, there were more severe damages in the fatigue tests. At failure load the concrete directly under the load area was crushed and extensive spalling of the side faces were observed.

a) Test 7.

b) Test8.

c) Test 9.

d) Test 10.

e) Test 11.

f) Test 12.

Figure 14 – Specimens after the fatigue tests.

Table 3 sums up the results from the fatigue testing. Test 7 and 12 were runouts. Scatter in the results are expected for fatigue loading. Drying of the concrete influences the result. Even with a membrane applied to the specimens, it was not possible to avoid drying of the specimens through the cracks that opened and closed during the fatigue testing, especially the ones with

longer duration. Test 7 was stopped after one week because a too low load level was employed. Test 12 stopped due to a power outage in the laboratory. The runouts specimens were instead tested statically in compression. As seen in the table, the static strength increased compared to test 1-3 subjected only to static loading. Compared to Test 3, which had the highest static strength of 662 kN, the increase was 13%. The strengthening effects of fatigue loading have been attributed to a combination of a beneficial release of local stress concentrations, increase in inter particle attraction forces, forced hydration due to the compaction of the material structure and drying of the specimens, which increases the reference strength [10], [12], [13].

Table 3– Test results for fatigue loading

Test	f_{cm} [MPa]	S_{max}-S_{min} [kN]	Cycles until failure N_f	Notes	Static strength [kN]
7	22.2	330-40	-	Runout after 581859 cycles.	750
8	22.6	520-65	9028		
9	23.2	520-65	2004		
10	23.2	520-65	6763		
11	22.8	468-65	57499		
12	22.3	468-25	-	Runout after 841252 cycles.	695

The deformation in concrete members subjected to cyclic compressive forces is often described by three phases. Initially there is phase with a non-linear response, followed by an almost linear response. Finally there is non-linear phase at the end of the fatigue life. In Figure 15 the measured vertical deformations are plotted versus the relative fatigue life. The three phases can clearly be observed. The initial and final non-linear behaviour covers approximately 10% of the fatigue life each. The increase in deformation in the middle phase is much slower for test 11, which has a lower maximum load level, than test 10. In the final stage of the loading, test 11 has a more distinct non-linear response.

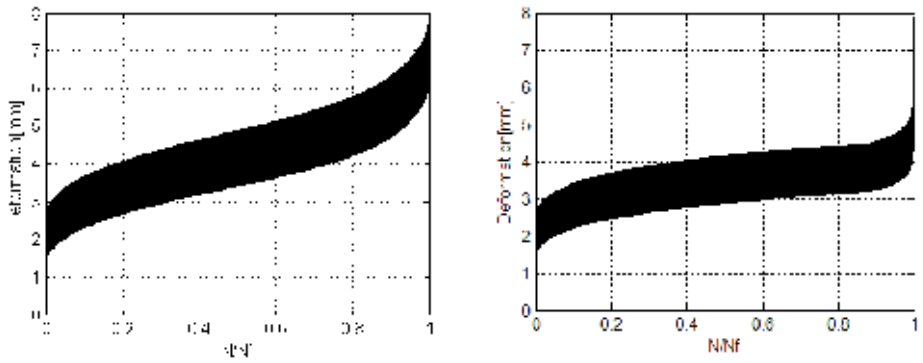

a) Test 10. *b) Test 11.*

Figure 15 –Vertical deformation of the specimens.

Figure 16 shows the strain development in the transverse reinforcement for specimen 10. This was a typical distribution for all tests. Only the stirrup had a constant increasing strain during loading, and finally yielded. For the splitting bars in the centre of the specimens the strains were almost constant. Close to failure the strains in the upper bar were reduced, indicating a redistribution of stresses to the lower part of the member. At the very last stage, strains at the lower splitting reinforcement also reduced.

a)

b)

c)

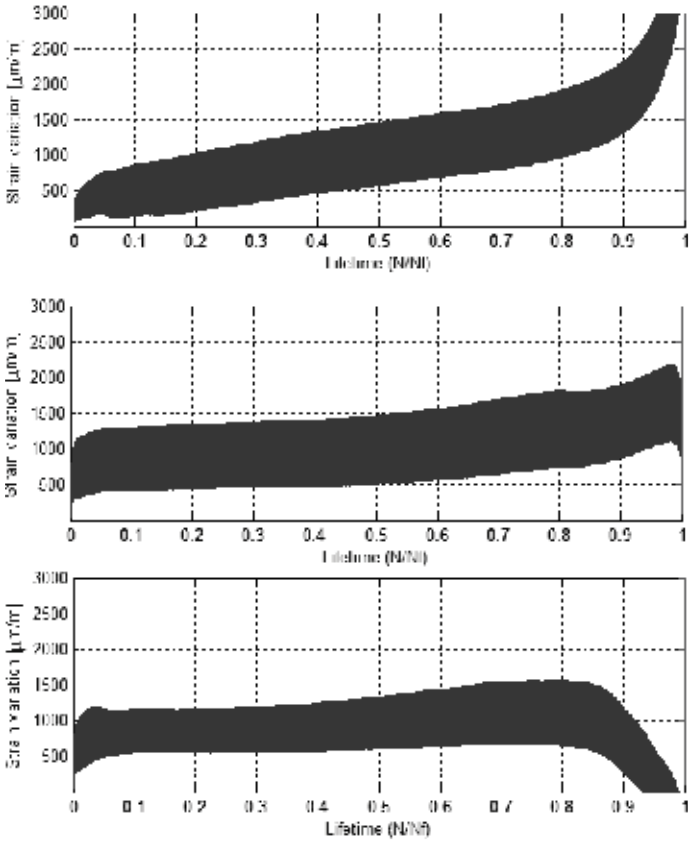

Figure 16 – Steel strains for test 10, a) Stirrup; b) Lower splitting reinforcement; c) Upper splitting reinforcement.

Verification of fatigue capacity is normally performed using *S-N* diagrams. The number of load applications, N_f, which causes failure is then a function of the applied maximum, σ_{max}, and minimum stress σ_{min}. In design codes the fatigue capacity in pure compression is often considered linear in the logarithmic scale [4]:

$$log\, N_f = C_1 \cdot (1 - \frac{\sigma_{max}}{f_{ck,fat}})/(1 - \frac{\sigma_{max}}{f_{ck,fat}}) \qquad (6)$$

where $f_{ck,fat}$ is a reference compressive strength, introduced to take into account the increase in fatigue strength with increasing concrete compressive strength. C_1 is a factor influenced by the

moisture condition in concrete. For sealed concrete and members in water, which is the most unfavourable condition in fatigue, a factor of 10 is typically used [4], [5] for members subjected only to compression. Eq. (6) can be adjusted to take into account the effect of confinement on the fatigue life [8], [9]. However, the results depend if the reference strength is related to the confined or unconfined strength, and if the confinement is active or passive.

In this study only four specimens were available for evaluation of the results. Thus, making *S-N* diagrams were not appropriate. Instead Eq. (6) is employed directly in the validation of the results. Design codes relate the fatigue capacity on stress level. In this work capacity of a partial loaded area is considered a structural property. Therefore the maximum and minimum stresses in Eq. (6) are replaced by the total load and the reference strength is taken as the static resistance, P_{fail}, from test 1-3. With this approach the results are only valid for the current experimental set up.

$$log\, N_f = C_1 \cdot (1 - \frac{S_{max}}{P_{fail}})/(1 - \frac{S_{min}}{P_{fail}}) \tag{7}$$

In Table 4 the value of coefficient C_1 is given for the different tests, assuming Eq. (7) is valid. Results using the mean static capacity of 618 kN from test 1-3, the maximum capacity of 662 kN from test 3 and the maximum capacity of 750 kN from test 7 are presented. Depending on the static capacity, C_1 varies between 10 and 22. This highlights the large dependency of the estimated fatigue life on the reference strength. Due to the limited number of tests and the simplified approach to verify them, a definite conclusion cannot be drawn.

Table 4– Variation of coefficient in design equation

Test	N_f	C_1		
		P_{fail} = 618 kN	P_{fail} = 662 kN	P_{fail} = 750 kN
8	9028	22.3	16.6	11.8
9	2004	18.6	13.9	9.8
10	6763	21.6	16.1	11.4
8-10 mean	4973	20.9	15.5	11.0
11	57499	17.5	14.6	11.6

4. CONCLUSIONS

In this study 12 partially loaded concrete specimens subjected to static and fatigue load in compression has been tested. The partial load was a line load able to spread in one direction. In the line load direction the specimens were restrained with threaded bolts. This was an attempt to model the connection between a shaft for wind turbines and a circular foundation. To control the bursting forces stirrups and splitting reinforcement were used.

An important factor in the capacity of locally compressed concrete members is the placement of the splitting reinforcement. According to the design codes the centre of gravity of the reinforcement should be in the transition zone. In practice there is often splitting reinforcement

close to the load which increases the local compressive strength in this area. In the present investigation it was decided to use splitting reinforcement both in the transition zone and close to the load.

The response of the concrete elements was as expected. The first cracks formed in the centre some distance below the loading area, which is in agreement with linear elastic theory. For all tests the failure mode was governed by crushing/spalling just below the loading area, combined with extensive spalling of the outer surfaces, almost like a delamination.

The static capacity for elements with splitting reinforcement is in agreement with requirements in design codes. The obtained increased capacity of the bearing strength compared to the uniaxial strength was approximately a factor of 1.9. For specimens without splitting reinforcement, the increase was approximately 20%, induced by a biaxial stress state due to the confinement from the plates anchored by the threaded bolts.

Due to the limited number of elements failed in fatigue, it is difficult to draw definite conclusions. To verify the obtained fatigue capacities, a simplified approach was taken. Based on expression from a design code on stress level [4], the fatigue capacity was evaluated on basis of the total forces. Different levels of specimen static strength were used as reference strength leading to a wide range of values for the coefficient C_1. This highlighted the large influence of the reference strength in the calculation of fatigue life. In further studies more elements must be tested, to be able to make *S-N* diagrams applicable for design of the fatigue life of partially loaded members.

ACKNOWLEDGEMENTS

The authors would like to gratefully acknowledge valuable discussions and suggestions of DNV staff, especially Knut Waagaard and Odd Sund.

REFERENCES

1. Hendy, S.R & Smith, D.A, “Designers’ guide to EN 1992-2*”* Thomas Telford, 2007.
2. Betongelementforeningen (BEF), “Betongelementboken – Bind B: Avstivning og kraftoverføring”, Oslo, Norway, 2005 (in Norwegian).
3. Standard Norge, “NS-EN 1992-1-1:2004+NA:2008, Eurocode 2: Design of concrete structures. Part 1-1: General rules and rules for buildings”*,* 2008.
4. Norges Standardiseringsråd, “NS3473 Concrete structures – Design and detailing rules”, Norwegian Standard Institution, 2003.
5. CEB. "CEB-FIP Model Code 1990". Bulletin d'Information 213/214, Lausanne, Switzerland, 1994.
6. Leonhardt, F.,”Vorlesung über Massivbau – Zweiter Teil, Sonderfälle der Bemessung in Stahlbetonbau”, Springer Verlag, 1975 (in German).
7. Furnes, A. & Hauge, O.M., “Fatigue capacity of partially loaded concrete structures”. Master thesis at Department of Structural Engineering, NTNU, Trondheim, Norway, June 2011.
8. Hooi, T. T., “Effects of passive confinement on fatigue properties of concrete”, *Magazine of Concrete Research*, 52, No. 1, 2000.

9. Wang, H. L. & Song Y. P., ”Fatigue capacity of plain concrete under fatigue loading with constant confined stress”, *Materials and Structures,* 44, 2011.
10. Neville, A. M., “Properties of Concrete”, 4th Edition, Prentice Hall, 1995.
11. Kupfer, H. & Gerstle, K. H., “Behavior of concrete under biaxial stresses”, *Journal of Engineering Mechanics Division*, ASCE, vol. 99, EM4, 1969.
12. Shah, S. P. & Chandra, S.,” Fracture of concrete subjected to cyclic and sustained loading, *ACI Journal*, 67(10), 1970.
13. Holmen, J. O.,”Fatigue of Concrete by Constant and Variable Amplitude Loading”, Dr.ing. dissertation, The Norwegian Institute of Technology, Trondheim, 1979.

The Swedish User´s View of Self-Compacting Concrete

Richard Mc Carthy
MSc (Civil Eng), Researcher,
Head of Dissemination of Knowledge Section
The Swedish Cement and Concrete Research Institute (CBI)
SE-100 44 Stockholm
E-mail: richard.mccarthy@cbi.se

Johan Silfwerbrand
Professor, Managing Director
The Swedish Cement and Concrete Research Institute (CBI)
SE-100 44 Stockholm
E-mail: johan.silfwerbrand@cbi.se

ABSTRACT

Self-compacting concrete (SCC) offers a variety of benefits and most of them are well known in the concrete sector today. The most important advantages are increased degree of productivity, easiness of placing, improved quality of the finished structure (the inside as well as the outside), improved working environment, lower construction costs, shortened construction time and possibilities to save labour. Despite all the benefits, the market share of cast-in-place SCC in Sweden today is still under 10 %. In order to increase the market share, there are some challenges and limitations which have to be dealt with. Some examples are greater need for knowledge and experience, some uncertainty around formwork pressure, a current lack of updated standards and codes regarding formwork design, unsatisfactory robustness, varying material properties at site and wrong focus during cost assessments. Swedish contractors have taken part in an investigation consisting of a series of interviews. The questions have been asked during site visits or, more commonly, by telephone. The questions asked were about formwork, casting technique, quality of the finished structure and benefits of the SCC technique. A majority of the contractors who were interviewed are in favour of the SCC technique, but SCC must be considered as a method instead of a material in order to encourage them to consider the wider effects and benefits of SCC. Finally, clients and owners need to be involved as early as possible in the process and material selection considering the advantages of SCC. This will improve the possibilities to increase the use of SCC.

Key words: SCC, productivity, production technique, formwork pressure, formwork design.

1. INTRODUCTION

Self-compacting concrete (SCC) offers a variety of benefits and most of them are well known in the concrete sector today [1,2]. Some examples are increased degree of productivity, easiness of placing and improved quality of the finished structure (the inside as well as the outside). One advantage seldom considered, but significant, is the improved working environment. Using SCC, the health and safety are increasing considerably compared to traditional vibrated concrete, due to less noise level, no/few awkward working positions and less heavy lifting of material and equipment. Ergonomic analysis through a certain method, ErgoSAM, has been carried out at Swedish construction sites [3]. As an example, a comparison was made between casting of a 3 m high wall with SCC and a similar wall with traditional concrete. SCC indicates a threefold improvement of physical loading on workers as far as work-related musculoskeletal health is concerned. Also, literature clearly states that SCC can have a positive effect on costs [4,5]. A Norwegian programme of interviews with ready-mix concrete producers and contractors has shown that SCC enables significant cost savings [6]. An improved economy is possible through lower construction costs, shortened construction time and possibilities to save labour. Two identical bridge decks, each with a span of 18 m and width of 9 m, were cast next to each other in Sweden [7]. Initially, traditional castings were planned to be performed during a total work time of 270 man hours. However, SCC was used instead of traditional vibrated concrete. Just by changing from traditional vibrated concrete to SCC, the actual outcome turned out to be 180 man hours, i.e. a saving of 33 %. If the full potential of SCC is utilized, using two work shifts, savings could be as high as 65 % according to the contractor.

Despite all the benefits, the SCC technique still remains underused in Sweden. The market share of cast-in-place SCC in Sweden today is still under 10 % (the share in the precast industry is substantially higher). There are some challenges and limitations [2,8] which have to be dealt with in order to increase the market share. Some examples are greater need for knowledge and experience, uncertainty around formwork pressure, a current lack of updated codes regarding formwork design, robustness [9,10] and varying material properties. When assessing the costs, the entire process has to be taken into account, i.e. not only the initial material cost. SCC must be considered as a method instead of a material [11,12], in order to encourage the contractor to consider the wider effects and benefits of SCC.

Finally, the structure and organisation of the construction industry influence the use of SCC. It is important that owners and clients are involved as early as possible in the process and material selection considering the holistic benefits of SCC. This will improve the possibilities to increase the market share.

2. AIM

The aim of the paper is to investigate the existing production technique with SCC (preparation, formwork, formwork design, handling, casting technique, productivity, quality, etc.) through site visits and interviews in order to identify the potential and the shortcomings of SCC. The ultimate goal is to increase the use of SCC in order to take its technical, economical and environmental benefits into account.

3. METHODS

3.1 Target group for interviews

23 persons were interviewed and they were all employed by a Swedish contractor. They might have slightly different positions and titles but they all were responsible for the projects referred to in some of the interview questions, see Table 1. They all had great experience in the civil engineering area. The projects were implemented over a number of years. During some periods, the variation of material properties was larger than normal, which may have influenced some of the responses. 1st author was responsible for the selection process, basically by contacting a large number of persons in the concrete sector and look for interesting contemporary SCC projects.

3.2 Short description of the projects

Some things were common to the projects in Table 1. They were structures in the outdoor environment and focus of the questions was about vertical parts. The concrete used was designed for civil engineering structures with durability requirements. The cement type used in all projects was CEM I 42.5 N MH/SR/LA, according to SS-EN 197-1.

Table 1 - Projects referred to in some of the interview questions.

No.	Construction type	Height (m)	Thickn. (cm)	Constr. length (m)	Constr. year
1	Wall, cast against rock surface, sealed formwork	6	40	20	2001
2	Retaining wall	3-4	25-30	10	2003
3	Wall, cast against rock surface, sealed formwork	5	35	7	2005
4	Circular columns	7	200		2007
5	Wall, cast against rock surface, sealed formwork	3,5-8	30	7	2006
6	Frame leg in a 100 m long tunnel, cast against existing surface	4,5	40-80	10	2003
7	Frame leg (4 m) in a slab frame bridge with two wing walls	9	80	4 (plus two wing walls)	1999
8	Support wall (under a slab bridge with integrated back walls)	2,20	50	12,80	2006
9	Integrated back wall (14 m) with two (2 m) wing walls on a slab bridge	2	65	2 + 14 + 2	2007
10	Support wall (under a slab bridge with integrated back walls)	6,5	80	20	1999
11	Frame leg in a tunnel, cast against existing surface	6	80	13	2002
12	Wall, cast against rock surface	5	50	10	1998
13	Wall, cast against rock surface	4	85	13	1999
14	Support wall (under a slab bridge with integrated back walls)	3	40	13	2000
15	Circular columns	2,80	100		2007
16	Frame leg (16 m) in a slab frame bridge with two wing walls (3 m)	4	40	4 + 3 (the one wing wall)	2003
17	Retaining wall, a free-standing part of a larger wall	4,2	40	12	2002
18	Tunnel walls, between tunnel ceiling and slab, sealed formwork, cast against existing surface	7	1,10	12	2002-2006
19	Wall, cast against rock surface, sealed formwork	8	25	8	2005
20	Frame leg in a slab frame bridge (pedestrian tunnel)	3	40-60	10	2001
21	Columns (rectangular with rounded corners, 3,5 x 1,20 m	6			2007
22	Frame leg (3 m, with a 2x2 m opening) and wing walls (3 m) at tunnel entrance	3	30	3 + 3 + 3	2006
23	Abutment, railway bridge. Front wall (7 m) and side walls (5 m)	4	60+40	5 + 7 + 5	2007

3.3 Interview questions

A number of questions were prepared before the interviews started. The responses are presented in different ways in this paper with different level of detail. Most of the questions asked were related to the projects in Table 1 and about formwork, casting technique and quality of the finished structures. The respondents were asked exactly the same questions in the same order with the aid of a formal interview schedule, which means structured interviews [13]. Other questions were more general, for instance benefits of the SCC technique. Since these questions could be followed by additional questions and discussions, this type of interview can somewhat be considered as semi-structured.

Questions about formwork used in the projects were:

- What type of formwork was used?
- Has the formwork been designed using formulas or according to experience?
- Who was responsible for the design of the formwork?
- Was the formwork designed to withstand hydrostatic pressure?
- Did the formwork fail during or after casting?

The questions about casting technique were:

- What was the casting rate?
- Was there any use of additional compacting?
- What was the distance between each filling spot?
- Is a greater casting rate preferable?

Questions about quality of the finished structures were:

- What was the quality of the finished surface?
- Was there a need for any surface repair?

The general questions about the benefits of SCC were:

- What are the advantages of the SCC technique?
- What are the disadvantages of the SCC technique?
- Labor cost savings?

3.4 Execution of the interviews

The questions were asked orally, either over the phone or during visits at building sites. The questions asked were the ones listed in section 3.3. No questionnaire was sent out in advance to the persons who were interviewed.

4. RESULTS

4.1 Advantages and disadvantages of the SCC technique

14 of the 23 persons in Table 1 have stated the advantages and disadvantages of the SCC technique in Table 2. The respondents did not choose between any arguments prepared and submitted in advance, only their own words have been reproduced. In addition, there were no restrictions on the number of arguments stated. Different respondents could also state the same

arguments as the others. It was actually quite a few similar arguments stated. The numbers (Person No.) are related to the numbers (No.) in Table 1.

Table 2 - Advantages and disadvantages of the SCC technique (detailed answers from the 14 respondents).

Pers. No.	Advantages	Disadvantages
6	Easy to work with, good working environment, good surfaces now (more problems when the SCC technique was new), possible to cast in sealed formwork.	Varying material properties at site, need of sufficiently tight formwork to prevent leakage of concrete.
7	Good working environment, excellent technique with the right mix design, ensures good quality, no need of systematic compaction, ensuring the filling, great time savings in walls (not as much time saving in bridge decks)	Varying material properties at site.
8	Good working environment, in particular from the ergonomic point of view (3 times as good). Lower labor costs, faster casting time, possible to reorganize the staff at building sites.	Varying material properties at site.
2	Prices are decreasing, which is good. Good surface quality on most bridges.	Delayed deliveries result in casting folds. Risk of dry surfaces when casting bridge decks, especially in dry weather conditions.
14	The handling process, the entire chain, time-saving, this technology is big plus. Requires fewer working men, even when casting bridge decks.	Varying material properties at site. More difficult to cast bridge decks, due to inclinations etc.
15	Difficult to assess economy due to many reasons, no obvious labor savings when workers still are at building site. Very good working environment! Quieter, simpler, less physically demanding. Should be possible to get good economy because of less workers. Most vertical castings can be carried out with one person except the pump driver.	Varying material properties at site.
19	No raising and lowering of pokers, especially in high walls. Possible to reduce the number of workers, good ergonomics, avoiding slipping of poker tubes, faster castings. Very good surface quality when pumping from below. "Can not be bad." However, still prefers pumping from above with 1-1.5 m overthrow, for production-related reasons. Easier to control.	Varying material properties at site.
18	SCC is not quite fully developed. It all depends on if you get the right concrete. Within 10 years, it will work. The great benefit is the decreased risk of honeycombing due to poor compaction.	One should rather buy the concrete “in the formwork” and assign the responsibility to the concrete producer. The reason is that one can not control the concrete.

20	The benefits are obvious, when the concrete has the right properties it is a better product, good working environment, ergonomics, less noise, avoidance of careless compaction, less number of workers. A bit faster castings, especially in vertical structures. Basically only one worker is needed at wall castings except the pump driver when there is no need for compaction. Possible to reduce one worker when casting bridge decks.	Varying material properties at site.
21	Very good working environment, possible to reduce number of workers.	Requires additional testing at site, risk of early dry surfaces and casting folds, risk of stripes between lifts.
22	Good working environment, good surface quality, less cleaning of wooden formwork. Actually, only benefits with SCC. Saves number of workers, only one is needed when casting vertical structures. Less concrete is leaking through gaps in the formwork, faster casting. The myths that existed before, that the formwork will "explode" is not true. Also the myth that concrete will leak through the gaps is untrue.	Some uncertainty exists today in formwork design. More difficult to cast bridge decks, due to inclinations. Requires additional testing at site.
1	The SCC technique saves time, good working environment, possible to cast in sealed formwork.	Increased formwork pressure, varying material properties at site, requires more planning and additional testing .
5	Saves number of workers, good surface quality.	Greater risk for formwork failure, varying material properties at site.
10	Good working environment, increased strength, avoidance of careless compaction, possible to cast in sealed formwork.	The clients are reluctant to the SCC technique, only a few factories have pre-tested the frost resistance, requires additional testing at site.

The arguments in Table 2 are summarized and condensed in Table 3. They have also been categorized and the distributions are shown in the pie charts. There were totally 40 arguments for SCC and 34 arguments against SCC.

Table 3 - Distribution of responses in the different categories.

Category	Arguments for SCC (condensed)	Arguments against SCC (condensed)
Economy	Lower labor costs, faster casting	None
Production technique	Easy to work with, casting technique, process, sealed formwork possible	Varying material properties at site, additional testing, difficult with inclinations on bridge decks, formwork pressure uncertainty, lack of control, more planning needed, only a few factories have pre-tested the frost resistance
Quality	Surface quality, good filling ability, no honeycombing	Segregation, leakage, casting folds, dry surfaces, stripes between lifts, varying material properties at site
Working environment	Noise, ergonomics	None

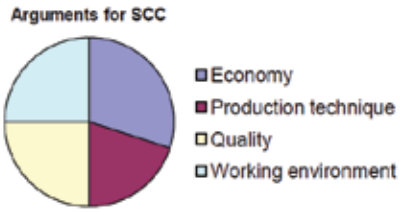

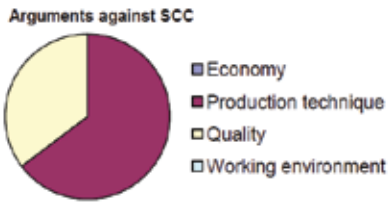

Some observations can be made:

- The arguments for SCC are distributed almost equally on economy, production technique, quality and working environment
- 65 % of the arguments against SCC are about problems regarding production technique

In Figure 1, the responses to the question “Generally, are you positive about SCC?" is shown. The respondents are the same as in Table 2.

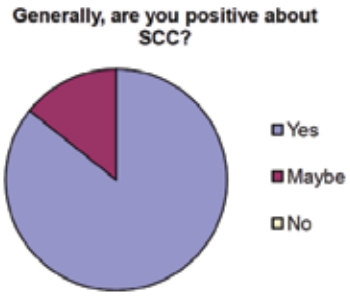

Figure 1 - General opinion on SCC.

4.2 Formwork design

This section is about the formwork used in the 23 projects in Table 1, formwork design and formwork pressure. There is a link between casting rate and formwork design. Figure 2 shows the distribution of the responses regarding these issues.

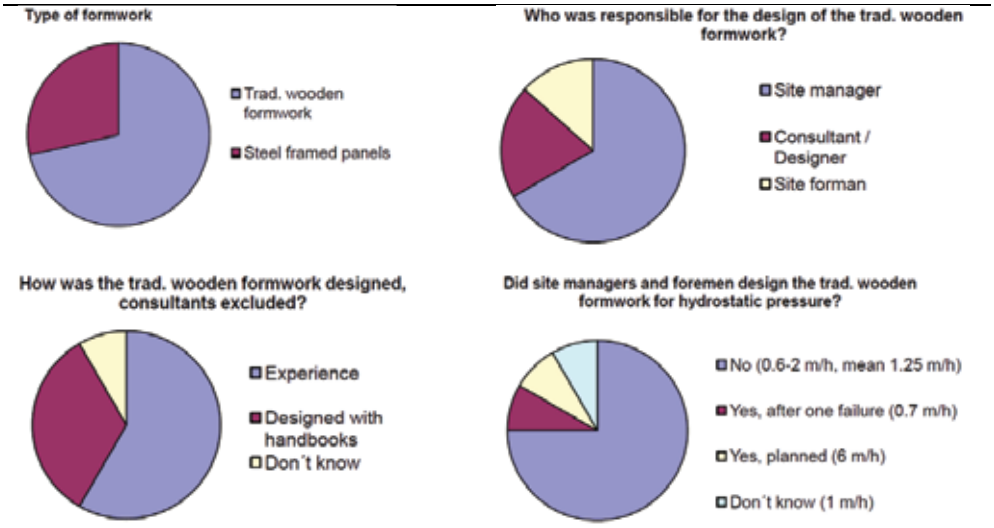

Figure 2 - Distribution of responses regarding formwork used in the 23 projects.

As seen in Figure 2, traditional wooden formwork was the dominating type of formwork. Three quarters of the traditional wooden formwork were designed by the site managers and site foremen. More than half of them were designed without any handbooks. In only a few cases, the formwork was designed to withstand hydrostatic pressure.

Another question asked was if one would like to cast with a higher rate if possible. 80 % responded "yes" and 20 % were not certain. The latter group of respondents stated that the uncertainty of the formwork pressure was too great and that there were other more important issues to focus on. Some of those responding "yes" gave additional comments:

- Yes, but difficult to estimate the pressure
- Yes, but a higher risk of surface pores
- Yes, but only in certain types of structures

Each respondent stated that he or she always had a designated person who was watching for signs for too high pressure in traditional wooden formwork. There were some simple tips on how that can be done:

- Listen for snaps
- Check if the tie bar washers are pressed into the wood
- Check if the tie bar ends (20-30 cm of length) are bending downwards (if wedge-shaped tie bar clasps)

4.3 Casting results

Table 4 shows some results from the castings regarding additional compaction, formwork failure and surface quality. The respondents did not choose between any surface quality numbers prepared and submitted in advance. 1st author selected the numbers after the interviews and they were based on the responses. Surface quality number 5 means excellent or more than good, number 4 means good, number 3 means generally good, number 2 means not so good and number 1 means poor surface quality. 61 % of the surfaces were considered good or better than good. The surfaces of four projects were repaired, half of them to a small extent for aesthetic reasons. The remaining surfaces were more damaged because of late deliveries and hot weather conditions.

Table 4 - Casting results.

Project No.	Casting rate (m/h)	Additional compaction	Formwork failure	Surface repair	Surface quality No. (1-5)
6	0,6	•	•	Yes	2
23	0,6	•			5
5	0,7			Yes	2
13	0,7				2
8	0,8				2
2	1,0				5
15	1,0				4
18	1,0				5
10	1,0	•			3
7	1,0				4
21	1,0				3
22	1,0				5
3	1,2				5
9	1,3				4
1	1,4		•		4
11	1,5	•			4
14	1,5				3
16	1,5				4
20	1,5	•		To a small extent	3
17	2,0				4
4	2,0				5
12	2,5			To a small extent	3
19	6,0				5

Figure 3 shows the relation between surface quality and the casting rate, but no linear relation can be found. In order to explain the relation, more information is needed on material properties such as slump flow, weather conditions, temperature, delivery status of the concrete batches etc.

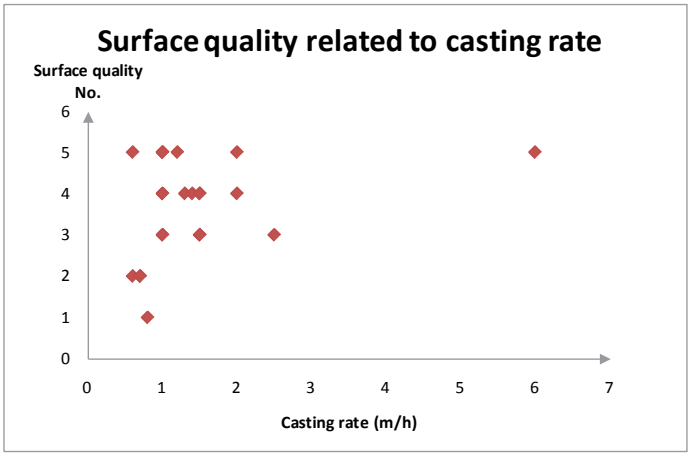

Figure 3 - Surface quality related to the casting rate.

4.4 Labour cost savings

14 of the 23 persons in Table 1 have also estimated the possible number of workers which can be saved generally (not necessarily related to the projects in Table 1) when using SCC instead of traditional vibrated concrete. The respondents did not choose between any percentages prepared and submitted in advance, only their own estimations have been reproduced in Table 5. The numbers (Person No.) are related to the numbers (No.) in Table 1.

Table 5 - Saving of workers when using SCC (%).

Person No.	Wall, cast from above	Foundation slab	Bridge deck (levelling of surfaces included)
1	50	50	50
2	67	60	50
5	50	55	50
6	50	50	60
7	50	50	50
8	67	60	60
10	50	50	50
14	50	50	40
15	50	65	55
18	67	67	50
19	50	50	60
20	67	67	50
21	50	50	50
22	50	70	40
Mean value	55	57	51

5. INTERPRETATION OF RESULTS AND OBSERVATIONS

A majority of the persons who were interviewed are in favour of the SCC technique, but there are some limitations and challenges which have to be focused on. Some examples are greater need for knowledge and experience, uncertainty around formwork pressure, a current lack of updated standards and codes regarding formwork design, unsatisfactory robustness, varying material properties at site and a lack of communication between the stakeholders.

The most important advantages are increased degree of productivity, improved working environment, improved quality of the finished structure (the inside as well as the outside), easiness of placing, lower construction costs, shortened construction time and possibilities to save labour. However, successful labour savings require greater planning of the castings and courage to think "outside the box". SCC must be considered as a method instead of a material, in order to encourage the contractor to consider the wider effects and benefits of SCC. As seen in Table 5, at least 50 % less workers are needed when casting walls and foundation slabs with SCC. When casting bridge decks, at least 40 % less workers are needed. The reason for the lower percentage for bridge decks is the need for levelling of surfaces, regardless of the concrete used.

Among the projects in Table 1, six out of ten projects had a surface quality which was considered good or better than good.

There is an uncertainty about the formwork pressure and that is why the casting rate generally is low. Yet, 80 % of the respondents would like to cast with a higher rate if possible. The potential of SCC is seldom fully utilized. It is far more common to cast with a lower rate instead of making the formwork stronger. In only a few cases, the formwork was designed to withstand hydrostatic pressure.

One observation made by 1st author was that some of the interview questions were about attitudes rather than technical facts. The respondents do approach this (new) technique in different ways, depending on their experience in the area. There are often strong opinions about the technique. Most important, everybody agreed that it is an excellent technique if everything works as it should.

6. CONCLUSIONS

Although some uncertainty exists around the use of SCC, the majority of the respondents are in favour of the SCC technique. However, greater planning and understanding are required in order to fully utilize the benefits of SCC. During construction decisions, the processes are focused on selecting the "best" method, with material selection usually only as secondary consideration. That is natural and correct, but considering SCC as a material does not encourage the contractor to consider the wider effects and benefits of SCC. If SCC is considered as a method, the stakeholders will understand that SCC needs and requires greater planning and understanding. Important questions are how, when and where to incorporate SCC into a project. The use (or not) of SCC are dependent on the structure and organisation of the construction industry. Clients and owners need to be involved as early as possible in the construction process and material selection considering the holistic advantages of SCC. This will improve the possibilities to increase the use of SCC.

7. ACKNOWLEDGEMENTS

Financial support from the Swedish Road Administration is greatfully acknowledged. Special thanks to those who contributed to this paper through their interview responses.

REFERENCES

1. De Schutter, G. et al., "Self-Compacting concrete," Whittles Publ., Dunbeath, 2008, 296 pp., ISBN 978 1 904445 30 2.
2. Bartos, P.J.M., "Self-Compacting Concrete in Bridge Construction – Guide for Design and Construction," Concrete Bridge Development Group, Technical Guide No.7, Camberley, England, 2005, 55 pp., ISBN 1 904482 20 1.
3. Simonsson, P. & Emborg, M., "Increasing Productivity through Utilization of New Construction Techniques and Lean Construction Philosophies in Civil Engineering Projects," Nordic Concrete Research, 2009, Vol 39, pp. 53-74, Norsk Betongforening, Oslo.
4. Gaimster, R. & Foord, C., "Self-compacting concrete," Concrete, "2000, Vol. 34, No. 4, pp. 23-25.
5. Goodier, C.I., "Development of Self-compacting Concrete," Proceedings of the Institution of Civil Engineers. Structures and Buildings, 2003, Vol. 156, No. 4, pp. 405-414.
6. Haugan, L. & Hammer, T.A., "Markedsføring av selvkomprimerende betong (SKB) – oppsummering av referanseprosjekter", SINTEF-Rapport SBF BK F08040, 2009, Trondheim.
7. Simonsson, P. & Emborg, M., "Industrialized Construction: Benefits using SCC in Cast in-situ Construction", Nordic Concrete Research, 2009, Vol. 39, pp. 33-51, Norsk betongforening, Oslo.
8. Desmyter, J.R., "Barriers to the Application of Cast-in-place Self-Compacting Concrete", Proceedings of the 5th International RILEM Symposium on Self-Compacting Concrete, 2007, Vol. 1, pp. 373-380, De Schutter, G., Boel, V. (Eds.), RILEM Publications SARL, Bagneux, ISBN 978 2 35158 050 9.
9. Billberg, P. & Westerholm, M., "Robustness of Fresh VMA-modified SCC to Varying Aggregate Moisture," Nordic Concrete Research, 2008, Vol. 38, pp. 103-119, Norsk Betongforening, Oslo.
10. Wallevik, O.H., Kubens, S. & Müller, F., "Influence of Cement-admixture Interaction on the Stability of Production Properties of SCC," Proceedings of the 5th International RILEM Symposium on Self-Compacting Concrete, 2007, Vol. 1, pp. 211–216, De Schutter, G., Boel, V. (Eds.), RILEM Publications SARL, Bagneux, ISBN 978 2 35158 050 9.
11. Rich, D., Williams, D., Glass, J., Gibb, A & Goodier, C., "To SCC or Not To SCC? UK Contractors' Views", Design, Production and Placement of Self-consolidating concrete-SCC2010, Montreal, 6th International RILEM Symposium on Self-Compacting Concrete, 4th North American Conference on the Design and Use of SCC, Proceedings, 2010, Vol. II. pp. 647-654, Khayat, H.K & Feys, D. (Eds.).
12. Rich, D, "Self-compacting Concrete is a Construction Method not a Material", Concrete, 2010, Vol. 44, No. 9, pp. 46-47.
13. Bryman, A., "Social Research Methods", 2nd Edition, Oxford University Press Inc., 2004, 747 pp., ISBN 978 0 19 920295 9.

Non-linear Finite Element Analysis of Deep Penetration in Unreinforced and Reinforced Concrete

Håkan Hansson
M.Sc., Ph.D. student
KTH Royal Institute of Technology
Division of Concrete Structures
SE-100 44 Stockholm, Sweden
E-mail: hakan.hansson@byv.kth.se

Defence & Security, Systems and Technology
FOI Swedish Defence Research Agency
SE-127 45 Tumba, Sweden

Richard Malm
Ph.D., Researcher
KTH Royal Institute of Technology
Division of Concrete Structures
SE-100 44 Stockholm, Sweden
E-mail: richard.malm@byv.kth.se

ABSTRACT

Penetration and perforation of concrete targets are studied by the use of numerical simulations to enhance the understanding of the penetration phenomenon. Comparisons were made with test results obtained for both reinforced and unreinforced 48.0 MPa normal strength concrete. The studied projectiles were made as generic models of penetrators for buried hardened target defeat. Varying impact velocities and angles for the penetrators were investigated. The simulations gave reasonable results for the different simulation cases, with the best results were obtained for reinforced concrete targets.

Key words: Computational mechanics, concrete structures, protective structures, reinforced concrete.

1. INTRODUCTION

Reinforced concrete structures are used for permanent and field military fortifications, and also for civil buildings and infrastructure projects. The protective performances of concrete structures have been of great interest since the introduction of modern concrete and later reinforced concrete, which roughly coincided with the introduction of rifled artillery and detonation shells with improved high explosives at the end of the nineteenth century. The introduction of warplanes and aerial bombing during the First World War, and the major development of aeroplanes and warheads in the nineteen thirties and during the Second World War (WWII), raised the interest of penetration performance in concrete in the beginning of the

twentieth century. A milestone regarding the prediction of weapon effects was the work performed in the US during WWII by the National Defence Research Committee (NDRC) [1]. However, the presented empirical penetration model included a calibration factor that needed to be determined for each target type. The NDRC formula was later modified by Kennedy [2,3] to consider the effect of concrete strength for the targets, and this modified empirical model is still one of many empirical equations used to estimate the penetration performance of warheads in concrete structures. Empirical penetration models were evaluated by several authors [3-9]. Furthermore, the penetration performance in concrete structures of penetrating warheads has increased the last 10 to 20 years by introducing hardened buried target penetrators with an increased length to diameter ratio and sharp nose sections. This development of enhanced warheads requires new designs for future protective structures, and also for strengthening existing structures. However, the majority of the empirical penetration models were developed before the above mentioned existed, and as a results these empirical models are unlikely to predict the behaviour of this penetrator type in concrete targets. The preferred analysis tool for general studies of weapon effects on protective structures is instead finite element (FE) analysis. However, this requires a thorough understanding of the materials behaviour and a validated numerical methodology to obtain reliable results.

The objective of the study was to investigate the protective performance of concrete structures by using non-linear FE analysis. The simulation results were compared with model scaled penetration tests performed in reinforced and unreinforced 48.0 MPa normal strength concrete (NSC) [10]. Investigations of highly dynamic events like projectile penetration, or loading by blast waves, are often supported by numerical simulations. These calculations are usually performed by explicit FE analyses. In addition, material models that describe the mechanical response of the used materials with an acceptable accuracy need to be included within the computer code. Constitutive equations for concrete exposed to weapons effects have been a major area of interest for a long time and several material models for describing the concrete behaviour have been developed. The HJC [11] and the RHT [12] material models are two constitutive models often used for penetration studies, with both models including pressure dependent strength, strain rate dependency, damage evolution and porous compaction. The later and more recent RHT model was used for this study, with the basic behaviour of this model discussed later in section 3.3. Furthermore, an evaluation of material models for concrete used for explicit FE-analysis of high dynamic events was published by Tu and Lu [13]. It is not until recent years that non-linear FE analysis has become a practical tool to study the behaviour of concrete targets during projectile penetration with acceptable results. The aim for this study was to evaluate the possibilities of using numerical simulations to determine the performance of hardened buried target penetrators in concrete structures, and also identify the limitations of the used methodology. Other FE analysis studies on penetration in concrete were for example performed by Holmquist et al. [11], Tham [14,15], Cullis et al. [16], Polanco-Loria et al. [17] and Liu et al. [18]. The development of the RHT material model and its historical usage were described in by Riedel [19]. This concrete material model was also used earlier for studies of structural response by Magnusson et al. [20].

2. PENETRATION EXPERIMENTS

The penetration experiments were performed at the Swedish Research Agency with model scale hardened target penetrators, with the test reported by Hansson [10]. The mass of the penetrators used for the test was 4.50 ±0.02 kg. The diameter and length of the penetrators were 50 mm and 450 mm, respectively. Unreinforced normal strength concrete targets were used for both tests

with normal and oblique impact of the penetrator with target diameters equal to 1.20 and 1.50 m, respectively. This give the ratios between target and penetrator diameters equal to 24 and 30 for the two target diameters. The target diameters were chosen to avoid large influence on the experimental result from the boundary. Furthermore, this was confirmed by concrete penetration experiments performed with target to penetrator diameter ratios of 12, 18 and 24 published by Frew et al [21]. The concrete was cast in 8.0 mm thick thin walled steel cylinders acting as confinement for the concrete. The set-up of an unreinforced oblique target is shown in Figure 1, with the insert showing an unused penetrator. Heavily reinforced concrete targets were also used for both normal and oblique impacts of the penetrators, with approximately 5 vol% reinforcement in these targets. The compressive concrete strength after 91 days of curing was approximately 48 MPa, and the measured concrete density was approximately 2.31×10^3 kg/m^3. The mix proportions for the concrete and results from standard strength tests of the concrete are presented in the test report by Hansson [10]. Furthermore, the age of the concrete targets were between 134 and 249 days at the time of the experiments [10]. The penetration results are given in Table 1, with post-test photos of the targets later shown in Figures 10, 13 and 16 for comparison with the damage plots from the simulations.

Figure 1. Experimental set-up for oblique target tests [10], with background and mirror for high-speed filming of the horizontal and vertical projections of penetrator shown. The insert show the external design of the penetrator.

Table 1. Experimental results [10] and corresponding FEA case identification.

Test no.	Target type	Target thickness, l (m)	Impact angle (°)	Impact velocity (m/s)	Penetration depth (m)	Exit velocity (m/s)	Corresponding FAE case setup
2004-6	Unreinforced	0.60	90.0 ± 0.5	425	---	139	FEA1
2004-25	Unreinforced	0.54	59.5 ± 0.5	424	---	16	FEA2
2004-26	Unreinforced	0.54	59.5 ± 0.5	422	0.50	---	FEA2
2004-3	Unreinforced	0.90	90.0 ± 0.5	409	0.62	---	FEA3
2004-4	Unreinforced	1.20	90.0 ± 0.5	463	0.69	---	FEA4
2004-20	Reinforced	0.60	90.0 ± 0.5	424	0.53	---	FEA5
2004-24	Reinforced	0.54	59.5 ± 0.5	421	0.39	---	FEA6

3. MATERIAL MODELS

3.1. Steel material

The Johnson and Cook (J&C) constitutive model for metals describes the relation between the yield stress of a metal and the plastic strain (ε_{pl}), plastic strain rate $\dot{\varepsilon}_{pl}$ and temperature (T) [22] as:

$$\sigma_{yield} = \left(A + B\,\varepsilon_{pl}^{n}\right)\left(1+\frac{\dot{\varepsilon}_{pl}}{\dot{\varepsilon}_{pl,0}}\right)^{C}\left(1-\left(\frac{T-T_{Ref}}{T_m-T_{Ref}}\right)^{m}\right) \tag{1}$$

where $\dot{\varepsilon}_{pl,0}$ is the reference strain rate, i.e. 1 s^{-1}, and C is the strain rate exponent. Parameter A is the yield strength, and parameters B and n determines the strain hardening of the material. The influence of temperature softening is given by the melting temperature (T_m) and the thermal softening exponent (m), with T_{Ref} taken as the reference temperature for the material. Normal room temperature of approximately 300 K is normally used as reference temperature. This material model was used both for the penetrator casing and the steel confinement for the unreinforced targets.

A Mie-Grüneisen shock equation of state (EOS) was used for the steels, see for example Meyers [23]. The concept of an EOS for a material requires that only certain sets of the variables pressure, internal energy and density can exist. The shock wave velocity (v_s) defines the propagation speed of a wave through a material subjected to a high pressure loading, and it can be given as a function of pressure or particle velocity (v_p) at the shock front, e.g as:

$$v_s = c_0 + s\,v_p \tag{2}$$

The bulk sound velocity (c_0) was equal to 4569 m/s and experimentally determined slope (s) for steel was equal to 1.49 [24]. Furthermore, the Grünesien gamma defines the temperature dependency of the EOS [23] and was equal to 2.17 [24]. These parameters can be related to other necessary state parameters. However, for the studied impact velocities, the used Mie-Grünesien EOS corresponds to a constant bulk modulus (K) equal to 163 GPa given by the expression:

$$K = \rho c_0^{\,2} \tag{3}$$

The material parameters for J&C material model for the penetrator casings and steel confinements for the unreinforced concrete targets were assumed to correspond to AISI S-7 and AISI 1006 steels [22], respectively. However, in the nose section of the penetrator an increased value of 2500 MPa was used for the yield strength parameter A. The parameters for the J&C material model are given in Table 2. Furthermore, a shear modulus equal to 81.8 GPa was used for the steels. However, the penetrators are only subjected to small deformations during for the case of concrete penetration, with negligible influences of strain rate and temperature on the yield strength of the steel.

Table 2. Material model parameters for the penetrator and steel confinements for unreinforced concrete targets.

Material location	Reference density (kg/m³)	A (MPa)	B (MPa)	n	C	m	T_m (K)	Specific heat capacity, C_p (J/kg K)
Penetrator casing	7830	1539	477	0.18	0.012	1.00	1763	477
Penetrator nose	7830	2500	477	0.18	0.012	1.00	1763	477
Confinement of concrete	7890	350	275	0.36	0.022	1.00	1811	452

A linear EOS was used for the B500BT type 1 steel reinforcement with bulk modulus (K) equal to 159 GPa, and with the same shear modulus as the other steels. A piece-wise linear stress-strain relationship was determined at the reference temperature for this reinforcement steel at quasi-static loading. A local plastic failure strain of 50% and strain softening were also assumed for the reinforcement bar elements, see Figure 2. Furthermore, the material model for the reinforcement uses the same thermal softening model as the J&C model, with the following parameters assumed: $m = 1.03$, $T_m = 1793$ K and $C_p = 477$ J/kg K. These temperature softening parameters and also the reference density of 7.830×10^3 kg/m³ were originally obtained for AISI 4340 steel [22]. However, strain rate dependency and thermal softening are likely to have a negligible effect on the simulations since only reinforcement bars located in the path of the penetrator are subjected to high deformation rates.

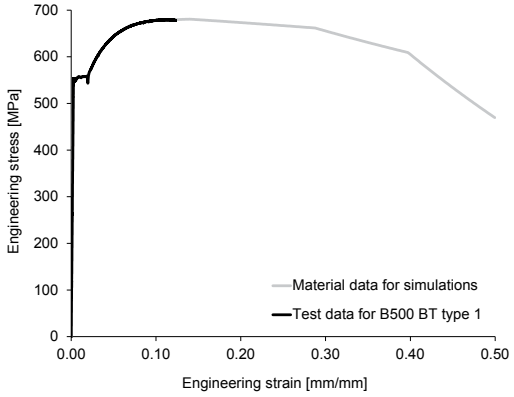

Figure 2. Stress-strain relationship at the reference temperature for reinforcement bars.

3.2. Inert filling material

No experimentally determined material properties existed for the inert filling material inside the penetrators, except for the density of the material with a value of 1.8×10^3 kg/m³. However, the density of the filling material was adjusted to 2.40×10^3 kg/m^3 to obtain approximate the same mass for the simplified penetrator in the simulations as for the penetrator in the experiments. An elastic-plastic constitutive model with the yield strength 100 MPa was assumed for this material. Furthermore, the following parameters were also assumed for the material: $K = 20.0$ GPa, $G = 12.0$ GPa and $C_p = 640$ J/kg K. It was assumed that the performance of the penetrators is not likely to be significantly influenced by the strength properties of the low strength inert filling material.

3.3. Concrete material

Concrete is a complex composite material with aggregates, varying in size, embedded in a matrix of porous cement. The RHT material model [12] is here used for FE analyses of penetration in concrete targets. Concrete has non-linear compression behaviour due to the inhomogeneity and the porosity of the material, and concrete is subjected to a considerably volumetric compaction for pressure exceeding the initial compaction pressure (p_{crush}) at which the concrete pores start to collapse. A general porous EOS was proposed by Herrman [25] to account for this behaviour for non-solid materials, with use of a non-porous EOS for description of the solid matrix material according to Figure 3.

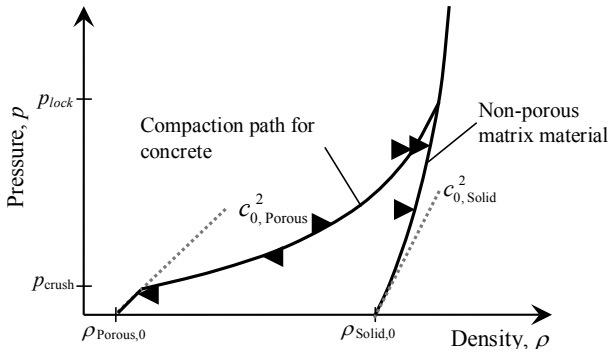

Figure 3. Schematic behaviour of the porous EOS, modified from Riedel [12].

This EOS was incorporated as part of the RHT concrete constitutive model developed at the Ernst-Mach Institut (EMI). Furthermore, one of the available material parameter sets was developed for a normal strength concrete with a compressive strength of 35 MPa, with the ability to change individual parameters to obtain an improved description of the used concrete [12]. This constitutive model incorporates pressure dependent strength, strain rate dependency and damage evolution. Three pressure dependent yield surfaces, i.e. the elastic limit yield surface, the failure surface and the residual strength surface, are used to determine the stress state of the concrete. The material model reduces the concrete strength for stress states not located on the compressive meridian according to William and Warnke [26]. This results in non-circular cross section for the failure surface. The elastic parts of the uniaxial tensile and compressive strengths are used to define the elastic limit yield surface as a contraction of the failure surface. Furthermore, a cap option for the elastic limit yield surface is normally activated to close the elastic yield surface at high pressure [12]. The fully damaged status of the concrete corresponds to a damage value of unity and represents material without tensile strength. This residual strength yield surface is only a function of pressure, and without any influence of strain rate or stress state. Reference points on the failure surface determined by testing of concrete for different stress states and the three dimensional representations of the yield surfaces are shown in Figure 4, with the corresponding behaviour for a uniaxial stress given in Figure 5a.

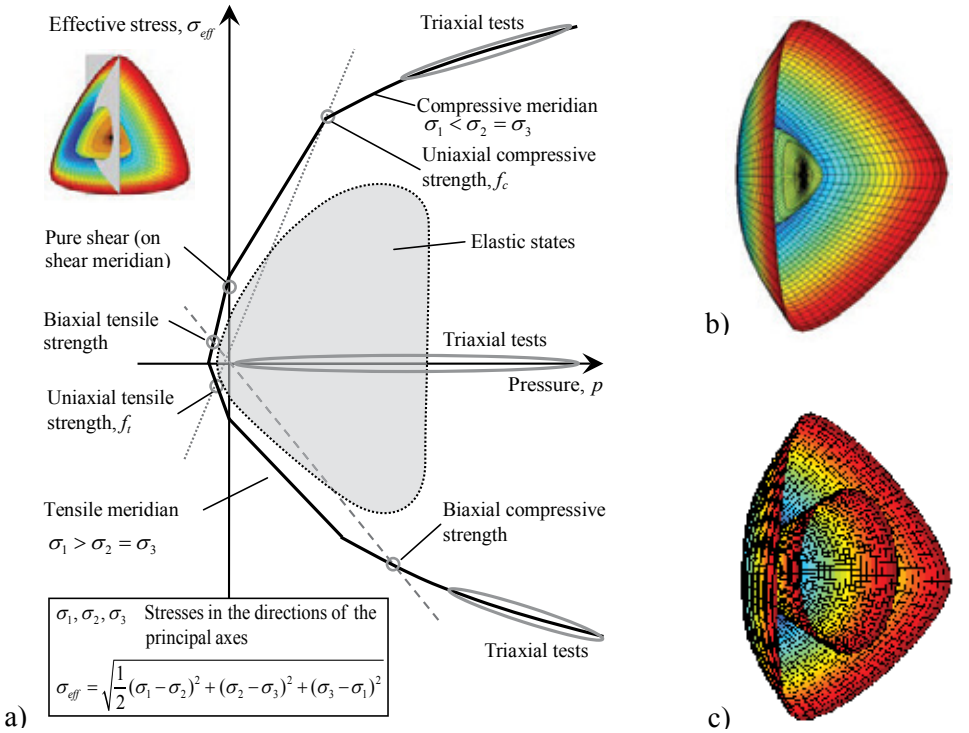

Figure 4. Schematic figure of reference points on the failure surface (a), modified from Riedel [12]. The insert shows the cut plane through the failure and elastic limit surfaces. Three-dimensional representation of the yield surfaces, with elastic yield surface and failure surface (b) and the residual strength surface within the failure surface (c).

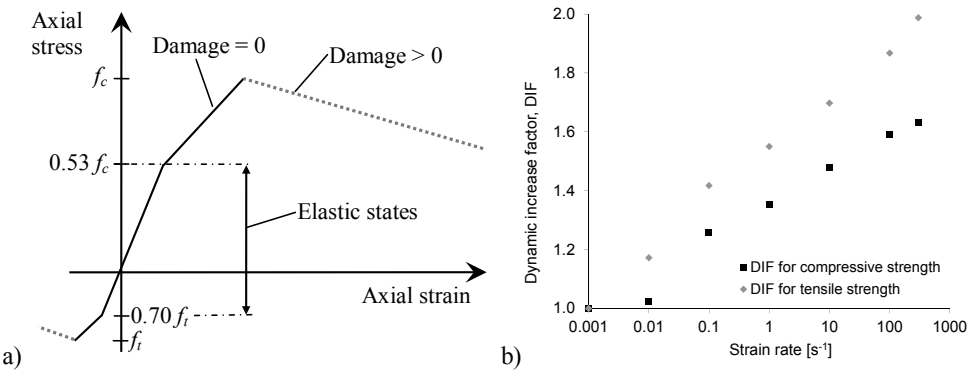

Figure 5. The behaviour of the model for uniaxial stress (a), and simulated strain rate dependency for uniaxial stress states (b).

The material model scales the strength and failure parameters based on the compressive strength (f_c) of the concrete and only a few additional parameters needs to be modified to obtain a consistent set of material parameters for similar concretes. However, it is not possible to use the same base data parameter set for concretes with fundamental different properties. The default material properties for normal strength concrete according to Riedel [12] were used with the exceptions below. A uniaxial compressive strength equal to 48.0 MPa and an initial compaction pressure (p_{crush}) equal to 35.0 MPa were used for the concrete. Furthermore, a tensile strength (f_t) of 4.0 MPa was assumed for the concrete. This results in static fracture energy (G_f) equal to 111 Nm/m² for the default parameters for the model and a 5.0 mm element length, with the fracture energy being proportional to the element length. The fracture energy equals 126 Nm/m² for the simulations with increased tensile strength of 4.8 MPa and the same element size. Furthermore, the fracture energy for the concrete increases with increased deformation rate, and is approximately proportional to the ratio between dynamic and static tensile strength at a given strain rate. The strain rate dependency for compressive and tensile uniaxial stress conditions are shown in Figure 5b. Furthermore, the default value of 2.314×10^3 kg/m³ for the initial porous density ($\rho_{\text{Porous,0}}$) of the concrete was used [12]. These data were the base set parameters, and were used unless other values are specified, for example for f_t and $\rho_{\text{Porous,0}}$. Furthermore, heavily distorted elements were removed from the simulations at the recommended effective strain value of 2.0. This methodology is necessary to avoid inverted elements with a negative volume since the occurrences of these heavily deformed elements aborts the simulation.

4. NUMERICAL SIMULATIONS

The FE analyses were performed with Autodyn 3D single precision version 5.0 [27]. Simulations were performed with a normal impact angle for the penetrators and with inclined targets, and with both unreinforced and reinforced concrete targets. The six simulation cases were based on the performed tests. The nominal impact velocities of 420 and 460 m/s were used for the simulations. Additional parameters were also studied within the six base cases.

4.1. Model set up

A Lagrangian formulation using 8-noded brick elements with a single integration point was used for both the penetrators and targets for all simulations. The geometry models for penetrators, unreinforced and reinforced concrete targets were then combined to obtain the six simulation cases in Table 3. A simplified geometric model of the penetrator design, with 50.0 mm diameter, 10.0 mm casing thickness and an ogive nose shape with a radius of 400 mm, was used for the simulations as shown in Figure 6. This ogive radius gives a CRH (Calibre Radius Head) value of 8.0, and this design was considered to be representative for a modern hardened target penetrator. The penetrators for the simulations and tests used the mass 4.53 kg and 4.50 ±0.02 kg [10], respectively. In addition, the yaw and pitch for the penetrator were neglected for all simulations, i.e. yaw and pitch angles were 0.0°. The ½ symmetry geometry for the penetrator consisted of approximately 900 brick elements, as shown in Figure 6b. This element size was not considered adequate to calculate the local deformations of the penetrator, especially close to the nose of the penetrator. This was due to the geometry of the penetrator's nose part, resulting in an initial contact between target and penetrator at a very small area. Furthermore, large local deformations of the first elements in the penetrator's nose may cause a progressive failure of the penetrator. To avoid this, an increased yield strength of 2500 MPa was used for the first two element rows in the penetrator's nose. Accurate modelling of the local behaviour in the penetrator's nose

would require a substantial decrease for the element size in the penetrator and the central part of the target. Furthermore, it is likely that extensive material testing and establishment of good quality material model parameters are needed to obtain reliable numerical results for the local behaviour of the penetrator. This was considered to be outside the scope of this study. The nominal impact velocities were applied as initial conditions for the materials for the penetrators.

Table 3. Properties for the targets and impact conditions for the penetrators in the simulations. Note that the target thickness given for case no. FAE2 refer to the base case setup, with increased target thickness used within the parameter study according to Table 4.

FEA case	Type of tested target	Model symmetry	Impact angle (°)	Impact velocity (m/s)	Target dimensions Thickness, *l* (m)	Diameter (m)	Width and height (m)	No of elements Brick elements	Beam elements
FEA1	Unreinforced	½	90.0	420	0.600	1.200	---	1 094 400	---
FEA2	Unreinforced	½	60.0	420	0.540	1.500	---	1 648 510	---
FEA3	Unreinforced	¼	90.0	420	1.200	1.200	---	820 800	---
FEA4	Unreinforced	¼	90.0	460	1.200	1.200	---	820 800	---
FEA5	Reinforced	None	90.0	420	0.600	---	1.200	1 792 000	17 968
FEA6	Reinforced	None	60.0	420	0.540	---	1.200	1 612 800	17 772

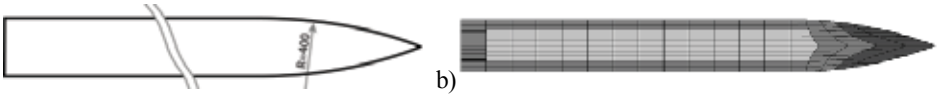

Figure 6. Definition of ogive radius (R) equal to 400 mm for the nose section (a) and the penetrator model shown with material locations for the different materials (b).

The unreinforced targets were cylindrical with diameters 1.200 or 1.500 m, and with a thickness between 0.540 and 1.200 m. The targets thickness is measured perpendicular to the front face of the targets, and the dimensions of the targets are given in Table 3. The unreinforced targets with the larger 1.500 m diameter were used the oblique impact tests and simulations. The FE models used a 5.0 mm thick steel confinement for the unreinforced targets to reduce radial expansion Furthermore, there is no surface to surface interaction defined between the concrete and steel confinement, instead the elements joined at the node locations. This method is likely to overestimate the stiffness between steel confinement and concrete. However, this is to some extent compensated since the tests used a thicker steel confinement with 8.0 mm thickness. The element size was 5.0 mm for the central part of the targets, with a graded mesh used outside the main area of interest. Simulations were also run with the use of 10.0 mm element sizes for the targets, i.e. simulations FEA1-04 and FEA1-05. Furthermore, the simulations FEA2-02, FEA2-03 and FEA2-04 of oblique impacts used increased target thickness as a part of the parameter study. The FE model of the reinforced concrete targets had the frontal area 1.200×1.200 m², with target thickness of 0.540 m and 0.600 m for the oblique and normal impact simulations, respectively. These models used beam elements for representing the reinforcement and solid elements for the concrete. The element size was 7.5×7.5×3.75 mm³ for the concrete, with the shortest dimension used through the thickness of the target. The reinforcement layers consist of 19 bars in each direction with a centre to centre distance of 60 mm, modelled with 15.0 mm element length. The reinforcement beam elements were joined to crossing beam elements and to the coinciding solid elements for the translation degrees of freedom, i.e. without the ability to

transfer moment. The individual reinforcement layers were then joined to longitudinal reinforcement with a centre to centre distance of 180 mm, and modelled with 7.5 mm element length. The second and fourth reinforcement layers were shifted 42.4 mm diagonally in the geometric model of the targets, see Figure 7a. This geometry was a simplification of the target geometries used for the tests shown in Figure 7c, for which the reinforcements were moved approximately 40 mm instead [10]. The geometries for the reinforced concrete targets are also given in Table 3. Furthermore, simulations were also performed with a reduced amount of reinforcement, see Figure 7b. The models used an assumed friction coefficient (μ) of 0.05 for the interaction between target and penetrator, except for simulation identity FEA3-03 that was run without friction. Free boundaries were used for all targets and all simulation cases, i.e. the only restraint for the movement of the targets was the inertia of the targets. The ratio of the mass for the target to the mass of the penetrator was between approximately 340 and 690, resulting in low velocities and very small movements of the targets during the simulated penetration events. An automatic time step was used for all simulations, with the time step defined as

$$dt = \frac{2l_e}{3}\sqrt{\frac{\rho}{K}} \tag{4}$$

where l_e is the length of the element [28], and ρ and K are the current values for the density and bulk modulus for each element.

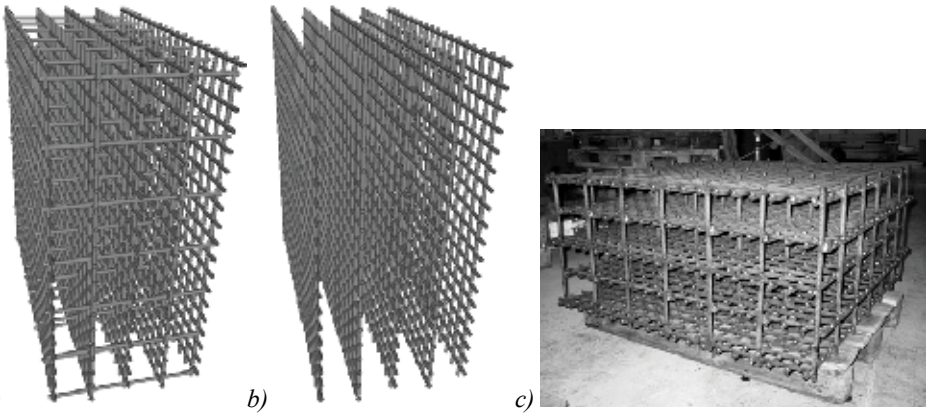

a) *b)* *c)*

Figure 7. Simplified reinforcement layouts, with (a) and without (b) connecting rebars between the reinforcement layers. The photo shows the reinforcement used for the experiments (c) [10].

4.2. Unreinforced targets, normal impact angle

Simulations were performed of simulation case FEA1 with short 0.600 m concrete targets to study perforation, and simulation cases FEA3 and FEA4 with 1.200 m concrete targets to study penetration into a practically semi-infinite target. The simulations are compiled in Table 4. The influences of tensile concrete strength, initial density and element size were briefly investigated with the use of the simulation case with perforation of the unreinforced concrete target, see Figure 8a. A plot of the damage and deformation of the model FEA1-01 is shown in Figure 9a,

with post-test photos of the corresponding target shown to the left in Figure 10. Influences on the penetrator deceleration for different impact velocities in simulations FEA3-01 and FEA4-01 with the base set parameters are shown in Figure 8b. Furthermore, the simulation FEA3-03 was performed without the use of friction between the penetrator and the target to estimate the increased penetration depth obtained with neglected friction for a simulation.

Table 4. Simulations of penetration in unreinforced concrete targets, with the impact conditions for the penetrators given in Table 3 for the different FEA cases.

Simulation identity	Target thickness, l (m)	Tensile strength, f_t (MPa)	Initial density, $\rho_{Porous,0}$ (kg/m³)	Element size (mm)	Friction coefficient, μ	Penetration depth (m)	Exit velocity (m/s)	Remarks, see Table 3.
FEA1-01	0.600	4.0	2314	5.0	0.05	---	143	
FEA1-02	0.600	4.0	2330	5.0	0.05	---	155	
FEA1-03	0.600	4.8	2330	5.0	0.05	---	98	
FEA1-04	0.600	4.0	2314	10.0	0.05	---	64	
FEA1-05	0.600	4.8	2314	10.0	0.05	---	60	
FEA2-01	0.540	4.0	2314	5.0	0.05	---	117	60.0° impact
FEA2-02	0.567	4.0	2314	5.0	0.05	---	57	60.0° impact
FEA2-03	0.589	4.0	2314	5.0	0.05	---	< 8	60.0° impact
FEA2-04	0.600	4.0	2314	5.0	0.05	0.445	---	60.0° impact
FEA3-01	1.200	4.0	2314	5.0	0.05	0.527	---	
FEA3-02	1.200	4.8	2314	5.0	0.05	0.505	---	
FEA3-03	1.200	4.0	2314	5.0	0.00	0.609	---	
FEA4-01	1.200	4.0	2314	5.0	0.05	0.587	---	460 m/s impact velocity

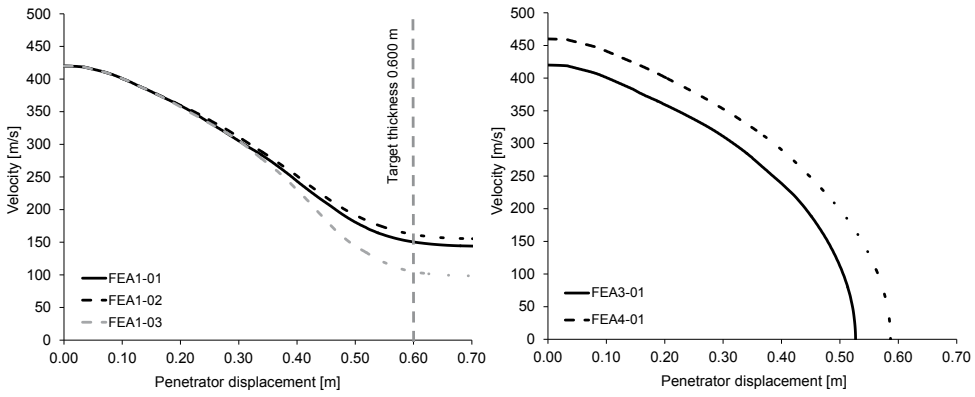

Figure 8. Velocity vs. penetrator displacements for 90.0° impacts of unreinforced targets, with perforation of targets shown in Figure (a) and simulations of stopped penetrators shown in Figure (b).

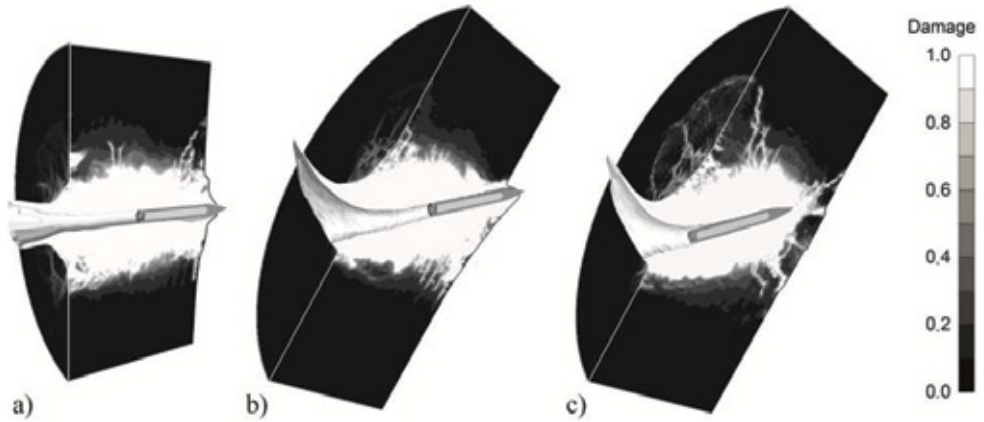

Figure 9. Damage and deformation plots for simulations FEA1-01 with a normal impact of a 0.600 m target (a), and oblique impacts simulations FEA2-01 with 0.540 m target thickness (b) and FEA2-04 with 0.600 m target thickness (c).

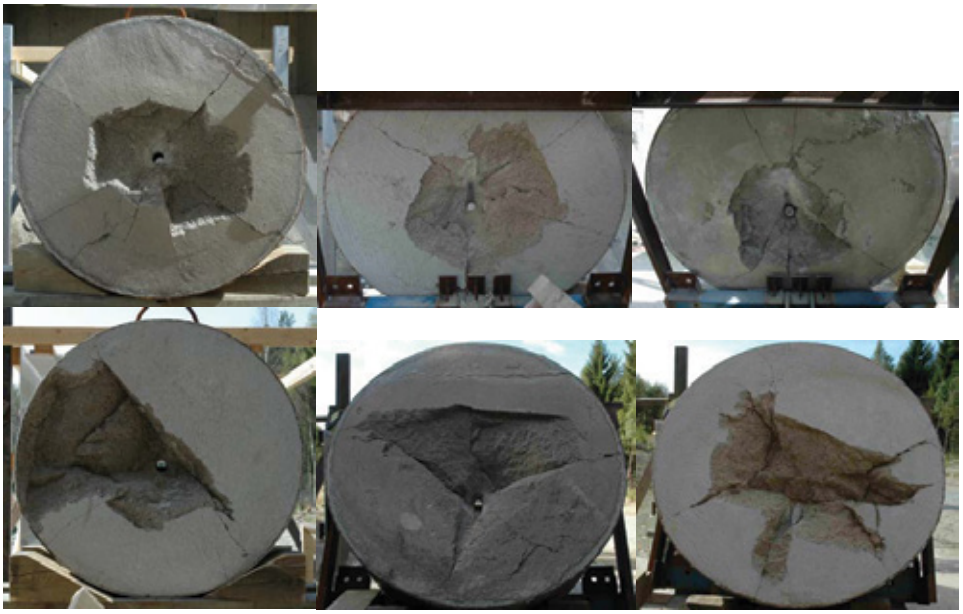

Figure 10. Post-test photos of front and back faces of targets from tests no. 2004-6 (FEA1-01), 2004-25 (FEA2-01) and 2004-26 (FEA2-01) [10], shown from left to right. The upper row of figures shows the front faces of the targets. The identity of the corresponding FEA base case simulations are given within parenthesises.

4.3. Unreinforced targets, oblique impact

Simulations FEA2-01, FEA2-02, FEA2-03 and FEA2-04 were performed with inclined unreinforced targets, with a 60.0° angle between the front face of the target and the penetrator. The FE simulations of oblique impact of unreinforced concrete targets are compiled in Table 4, with the penetration depth measured perpendicular from the front face of the target to the nose of the penetrator. The target thickness was increased in steps from the nominal value of 0.540 m for simulation FEA2-01 to 0.600 m for simulation FEA2-04 to estimate the required thickness for the target to stop the penetrator. The damage and deformations for the models with 0.540 m and 0.600 m thickness are shown in Figures 9b and 9c, respectively. Post-test photos of the targets from the corresponding tests no. 2004-25 and 2004-26 for the base case simulation FEA2-01 are shown in Figure 10 (middle and right). The velocities versus the penetrator displacements for varying target thickness for oblique impact conditions are shown in Figure 11.

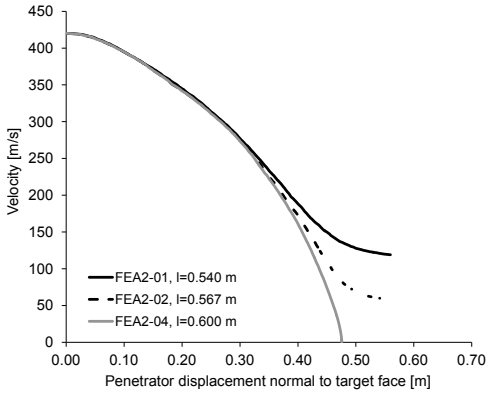

Figure 11. Velocity vs. penetrator displacement normal to target faces for simulations FEA2-01, FEA2-2 and FEA2-04 with oblique impacts of unreinforced targets and varied target thickness.

4.4. Reinforced targets, normal impact angle

Simulations FEA5-01 and FEA5-02 were performed using normal impacts of reinforced concrete targets, with the results for the simulations given in Table 5. The simulations were performed with two different amounts of reinforcement, with simulation FEA5-01 using the original reinforcement design and simulation FEA5-02 using a reinforcement design with the interconnecting rebars between the individual layers removed. See Figure 7b. To study the influence of the confinement effect due to the reinforcement on the penetrator penetration, simulation FEA5-03 was run without reinforcement. Furthermore, the values for the friction coefficient, initial density and tensile strength for these simulations were the base set data, which corresponds to the values given for simulation identity FAE1-01 in Table 4. Figure 12 shows the damage and deformations for the model using the original reinforcement design used for the test, with post-test photos of the corresponding target shown in Figure 13. The reinforcement in the targets contributed considerable to the velocity decrease of the penetrators for these simulations. The velocity versus displacement for simulations with different amounts of reinforcement is shown in Figure 14.

Table 5. Simulations of penetration in reinforced concrete targets.

Simulation identity	Target thickness, *l* (m)	Reinforcement design	Impact angle (°)	Impact velocity (m/s)	Penetration depth (m)	Exit velocity (m/s)
FEA5-01	0.600	Original reinforcement design	90.0	420	0.510	---
FEA5-02	0.600	Reinforcement layers 1 to 5	90.0	420	0.535	---
FEA5-03	0.600	No reinforcement	90.0	420	---	174
FEA6-01	0.540	Original reinforcement design	60.0	420	0.391	---
FEA6-02	0.540	No reinforcement	60.0	420	---	128

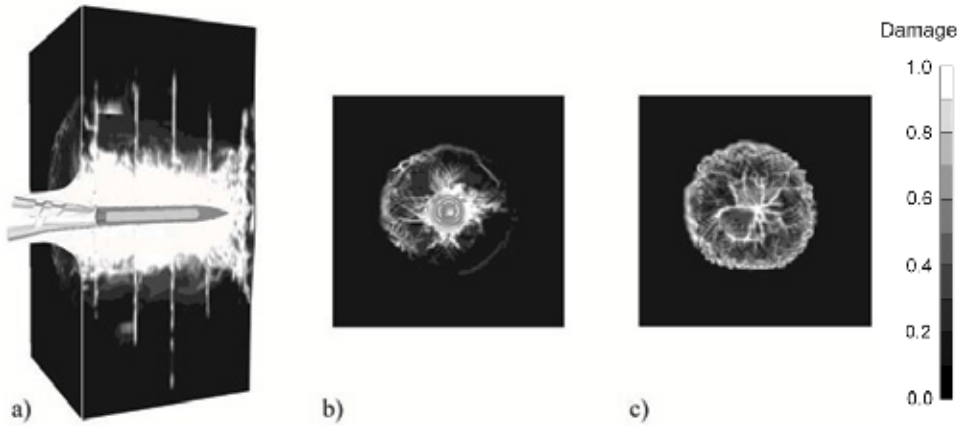

Figure 12. Damage and deformations plots for model FEA5-01 with a normal impact of a reinforced concrete target. The plots show a cut through the model (a), the front face (b) and back face (c) of the model.

Figure 13. Post-test photos of front and back faces of target from test no. 2004-20 [10], which corresponds to the simulation identity FAE5-01.

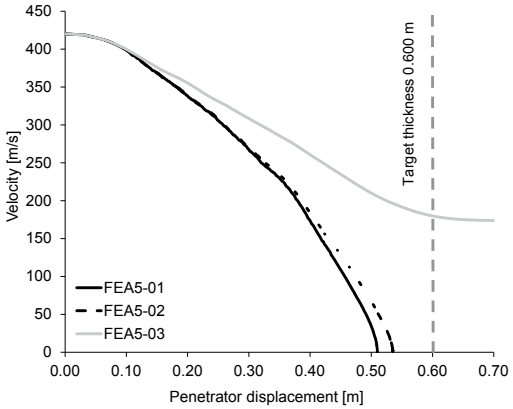

Figure 14. Velocity vs. penetrator displacement for simulations of reinforced targets impacted at a normal angle.

4.5. Reinforced targets, oblique impact

Simulation FEA6-01 of penetrator penetration in an inclined reinforced concrete target was also performed. Further, the same target geometry was also used for simulation FEA6-02 but without reinforcement. These simulations used the same target configurations and material properties as the simulations of the normal penetrator impact, with the difference that the targets were rotated to obtain a 60.0° impact angle for the penetrator. The simulation results are given in Table 5, with Figure 15 showing the damage and deformation for the reinforced target simulation and post-test photos of the corresponding target show in Figure 16. The penetration depths for the reinforced inclined targets were also measured perpendicular from the targets front face to the nose of the penetrator.

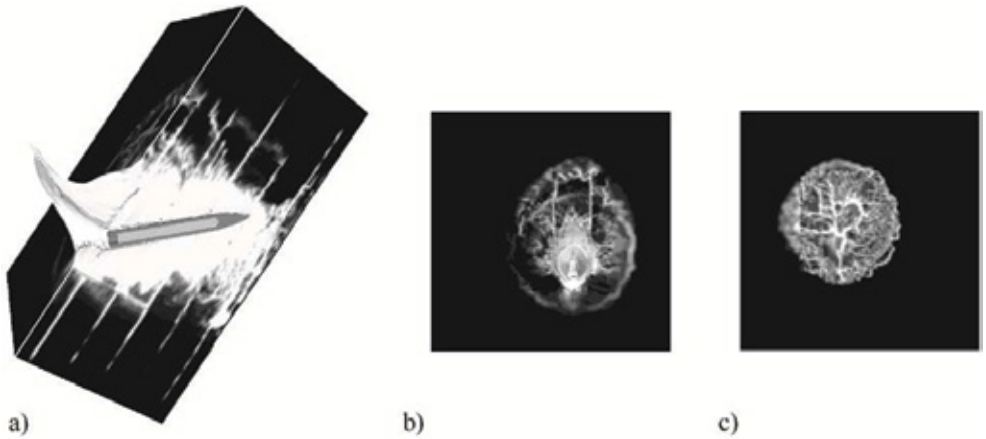

Figure 15. Damage and deformations plots for model FEA6-01 with oblique impact of a reinforced concrete target. The plots show a cut through the model (a), the front face (b) and back face (c) of the model. The scale for the damage is shown in Figure 12.

Figure 16. Post-test photos of front and back faces of target from test no. 2004-24 [10], which corresponds to the simulation identity FEA6-01.

5. EVALUATION OF PENETRATION SIMULATIONS

All simulations used the nominal impact velocities of 420 and 460 m/s, and impact conditions without yaw or pitch of the penetrator. However, the impact velocity, yaw and pitch for the penetrators showed small variations for the tests [10]. The maximal stress in the steel confinement for the unreinforced targets was approximately 150 MPa, without any plastic deformations of the thin walled steel cylinders that may influence the results from the FE analyses. The simulation results for unreinforced and reinforced concrete targets are given in Tables 4 and 5, respectively, with the experimental data given in Table 1 for comparison.

The simulation FEA1-01 of the unreinforced 0.60 m concrete target using the base data set resulted in an exit velocity of 143 m/s, which corresponds well with the experimental result. However, only one experiment was performed and the experimental error is unknown. There was a correlation between changes of model parameters and the exit velocities for the simulations with 5.0 mm element size, e.g. exit velocity was reduced by approximately 50 m/s to approximately 100 m/s for simulation FEA1-03 with the increased concrete tensile strength of 4.8 MPa. This decrease of the exit velocity was probably caused by increased energy consumption for the crater formation, with the main influence due to the formation of the exit crater. The change of the initial density of the concrete from 2.314×10^3 kg/m^3 to 2.330×10^3 kg/m^3 resulted in a non-significant change of the exit velocity. The simulations FEA1-04 and FEA1-05 with 10.0 mm elements showed that this element size was unsuitable and probably caused locking effects due to heavily distorted elements, e.g. the use of different tensile strengths of the concrete showed no significant change for the exit velocity of the penetrator. The simulation FEA3-01 with the base data set for the simulation parameters, and normal impact of the unreinforced concrete target, resulted in an underestimation of the penetration depth by 15%. The increased concrete tensile strength of 4.8 MPa for simulation FEA3-02, compared to 4.0 MPa for simulation FEA3-01, only showed a minor decrease of the penetration depth from 0.527 m to 0.505 m. The dominating failure mode of the concrete for these cases was assumed to be crushing since free surfaces only exist near the front face of the target, causing only a minor influence on the penetration depth due to a change of the tensile strength for the concrete. The use of a frictionless interaction between the penetrator and target resulted in an increased penetration depth by approximately 16%, resulting in an underestimation of the penetration depth compared to the experiment by approximately 2%.

However, it is not likely that the friction coefficient between the crushed concrete and a penetrator can be neglected for hardened target penetrators impacting concrete targets. The increased impact velocity of 460 m/s for model FEA4-01 resulted in an increased penetration depth by 11% to 0.587 m, and an underestimation of the penetration depth by 15% compared to the experimental results. The two simulations FEA3-01 and FEA4-01 used the same target mesh with a thickness for the target equal to 1.20 m, and this was assumed to have no significant influence on the calculated penetration depth for the simulation FEA3-01.

The simulation FEA2-01 of penetration with an oblique impact of the unreinforced target resulted in an exit velocity of 117 m/s, and an increased target thickness by 11% to 0.60 m needed to prevent perforation of the target. The tests on the other hand showed that the thickness of 0.54 m for the concrete target was close to the thickness required to prohibit perforation of target.

The simulations of the reinforced targets, i.e. simulations FEA5-01 and FEA6-01, showed good agreement with the test results. The penetration depths were estimated within 4% of the test results for these cases. Furthermore, for both normal and non-normal impacts of the penetrators, it was shown that the reinforcement prevented perforation of the targets. The simulation with a reduced reinforcement amount, i.e. FEA5-02, resulted in a minor increase of penetration depth compared to the base set model FEA5-01 that used the same reinforcement amount as the test targets. The simulations FEA5-03 and FEA6-02 of unreinforced concrete blocks showed similar results as for simulations of the unreinforced targets with steel confinement, i.e. simulations FEA1-01 and FEA2-01.

6. DISCUSSION

The results for penetration simulations FEA3-01 and FEA4-01 with unreinforced targets were considered to have a fair agreement with the test results, with underestimations of the calculated penetration depths by 18% and 11%, respectively. The numerical results for the perforation case with a normal impact, i.e. simulation FEA1-01, showed an exit velocity of 143 m/s, which was in good agreement with the test data. For the inclined unreinforced target, i.e. simulation FEA2-01, the simulation underestimated the required thickness to prevent perforation with approximately 11%. This may indicate a problem related to the removal of heavily distorted elements, and the decreased rotation of the penetrator within the target.

The simulations with the RHT constitutive model and the used parameters were considered to give good results for simulations of reinforced targets, where the influence from surface effects caused by cratering of the front and back faces are negligible, and where the radial cracking prohibited by the reinforcement. Furthermore, it is important that correct material properties are determined for the used material to be able to predict penetration depths in concrete. However, the formation of craters and the extension of damage within the concrete targets are not described to an acceptable degree with this simulation methodology. Furthermore, the simulations with unreinforced concrete targets showed that including reinforcement in the models contributed to an increased penetration resistance.

The use of symmetry planes for a model would reduce the number of required elements, with reduced memory and CPU time as a result. However, constraints are applied to the nodes along these planes. This may influence the local results along these planes, e.g. the damage evolution.

However, the influence on the global response for the models seems to be small for simulation of a penetration in normal strength concrete.

7. CONCLUSIONS

The used RHT constitutive model proved useful for simulations of both unreinforced and heavily reinforced concrete. The results showed reasonable agreement regarding penetration into concrete targets, and also perforation of concrete targets, when compared to the test data for the cases that were studied. However, only a few tests were conducted with only one experiment performed for each FE analyses case. The exception of this was the oblique impact of the unreinforced target, with two experiments performed for this setup giving almost identical results. See Table 1. The experimental variations for the test are therefore unknown, and complementary experimental results are of great interest for future studies to validate the used methodology. Furthermore, the parameters for the simulations need to be chosen with care to obtain useful results from the simulations. Further work is therefore needed to obtain reliable predictions of warhead performance against hardened structures. The use of FE analysis as a tool to estimate the penetration performance for warheads requires a thorough understanding of the behaviour of the material subjected to high pressures, high strain rates and large deformations.

The use of numerical erosion for the simulations removes heavily distorted elements and is likely to reduce the pressure build up around the penetrator. For non-normal impact conditions this may reduce the rotational forces acting on the penetrators, with a reduced rotation for the penetrator during the penetration of the target. This is likely to result in an underestimation of the penetration resistance of an inclined concrete target.

One conclusion regarding the simulations was that the solid elements representing concrete within the target and beam elements for reinforcement should have the same length, in order to reduce hourglass deformations of solid elements. Hourglass deformations, or other zero energy modes, will induce damage propagation in reduced integration solid elements, and may thereby reduce the strength of the target. An improved methodology to account for reinforcement bars within a target would be to use solid elements also for the steel bars. However, this would require a decreased element size for the models to have an acceptable description of the target geometry.

8. FURTHER RESEARCH

This simulation methodology can be used to study penetration of deformable penetrators in concrete and other protective materials, e.g. penetrators penetrating inclined reinforced concrete targets are subjected to large bending forces that might break warheads. It is therefore of interest to also include a failure description in the modelling of the penetrator casing for future simulation studies. A methodology to include case fracturing for hardened target penetrators in finite element codes was published by Johnson et al. [28] and Popelar et al. [29]. However, the use of this type of methodology would require a decreased element size in both the penetrator and target to determine failure conditions for the material based on local deformations and stresses during penetration.

Simulations were only performed with penetrators with a CRH value equal to 8.0, since this design was considered to be comparable to modern types of hardened target penetrators. Future studies with different penetrator designs are needed to enhance the understanding of the interaction between target and penetrator. These studies may also need to include additional research regarding the interaction interface between penetrator and concrete target. This topic is strongly coupled to the use of a suitable erosion algorithm for the concrete target, and the influence on the simulation results that the erosion algorithm is likely to have. However, it may be difficult to distinguish between errors caused by numerical problems, e.g. distorted elements and erosion, and errors caused by the constitutive model. One numerical methodology that might improve the results replaces eroded elements with particles during a simulation. With this approach it is possible to retain mass, volume and strength properties of the eroded material. This methodology should be evaluated in future simulation studies, due to the limitations for the used Lagrange element formulation for FE analysis of large deformations.

Improved concrete models with different properties are developed at several research institutes, e.g. an improved version of the RHT material model with enhanced failure conditions was developed at EMI [30]. The strain rate dependencies for both tensile failure strength and fracture energy were improved for this modified version of the material model. Furthermore, the damage evolution of concrete subjected to deformation in a confined state was also changed for the model. Another improved damage evolution model for the use together with the RHT concrete model was also studied by Tu and Lu [31]. It is of special interest to study the damage evolution of confined concrete subjected to large deformations to enhance future predictions of the performance of hardened target penetrators, and to determine the vulnerability of protective structures. Furthermore, crater formation and damage extension within the target are likely to be better estimated with the use of advanced failure models for the concrete.

ACKNOWLEDGEMENTS

The Swedish Armed Forces funded the presented investigation and the penetration test with model scaled hardened buried target penetrators performed by the Swedish Research Defence Agency.

REFERENCES

1. National Defence Research Committee, “Effects of impacts and explosions”, Summary technical report of division 2, Volume 1, Washington D. C., 1946, 512 pp.
2. Kennedy, R.P., “Effects of an aircraft crash into a concrete reactor containment building”, Holmes and Naver Inc., Anaheim, June 1966.
3. Kennedy, R.P., “A review of procedures for the analysis and design of concrete structures to resist missile impact effects,” *Nuclear Engineering and Design,* Vol. 37, No. 2, May 1976, pp. 183-203.
4. Sliter, G.E., “Assessment of empirical concrete impact formulas,” *Journal of Structural Division,* Vol. 106, No. 5, May 1980, pp. 1023-1045.
5. Adeli, H., Amin, A.M., “Local effects of impactors on concrete structures,” *Nuclear Engineering and Design,* Vol. 88, No. 3, October 1985, pp. 301-317.
6. Forrestal, M.J., Altman, B.S., Cargile, J.D., Hanchak, J., “An empirical equation for penetration depth of ogive-nose projectiles into concrete targets,” *International Journal of Impact Engineering,* Vol. 15, No. 4, August 1994, pp. 395-405.

7. Corbett, G.G., Reid, S.R., Johnson, W., "Impact loading of plates and shells by free-flying projectiles: A review," *International Journal of Impact Engineering,* Vol. 18, No. 2, March 1996, pp. 141-230.
8. Frew, D.J., Hanchak, S.J., Green, M.L., Forrestal M.J., "Penetration of concrete targets with ogive-nose steel rods," *International Journal of Impact Engineering,* Vol. 21, No. 6, June 1998, pp. 489-497.
9. Li, Q.M., Chen, X.W., "Dimensionless formulae for penetration depth of concrete target impacted by a non-deformable projectile," *International Journal of Impact Engineering,* Vol. 28, No. 1, January 2003, pp. 93-116.
10. Hansson, H., "Penetration in concrete for projectiles with L/D≈9," FOI-R--1659--SE, Swedish Defence Research Agency, Tumba, June 2005, 124 pp.
11. Holmquist, T.J., Johnson, G.R., Cook, W.H., "A computational constitutive model for concrete subjected to large strains, high strain rates and high pressures," Proceedings, 14th International Symposium on Ballistics, Vol. 2. Quebec City, September, 1993, pp. 591-600.
12. Riedel, W., Beton unter dynamishen lasten, Meso- und makromechanische modelle und ihre parameter, EMI-Bericht 6/00, Fraunhofer EMI, Freiburg, July 2000, 210 pp.
13. Tu, Z., Lu, Y., "Evaluation of typical concrete material models used in hydrocodes for high dynamic response simulations," *International Journal of Impact Engineering,* Vol. 36, No. 1, January 2009, pp. 132-146.
14. Tham, C.Y., "Reinforced concrete perforation and penetration simulation using AUTODYN-3D," *Finite Elements in Analysis and Design,* Vol. 41, No. 14, August 2005, pp. 1401-1410.
15. Tham, C. Y., "Numerical and empirical approach in predicting the penetration of a concrete target by an ogive-nosed projectile," *Finite Elements in Analysis and Design,* Vol. 42, No. 14-15, October 2006, pp. 1258-1268.
16. Cullis, I., Hinton, M., Gilbert, S., Church, P., Porter, D., Andrews, T. Proud, W., Pullen, A. "Towards predictive modelling for concrete," *International Journal of Impact Engineering*, Vol. 35, No. 12, December 2008, pp. 1478-1483.
17. Polanco-Loria, M., Hopperstad, O.S., Børvik, T., Berstad, T., "Numerical predictions of ballistic limits for concrete slabs using a modified version of the HJC concrete model," *International Journal of Impact Engineering,* Vol. 35, No. 5, May 2008, pp. 290-303.
18. Liu, Y., Ma, A., Huang, F., "Numerical simulations of oblique-angle penetration by deformable projectiles into concrete targets," *International Journal of Impact Engineering,* Vol. 36, No. 3, March 2009, pp. 438–446.
19. Riedel, W., "10 Years of RHT: A review of concrete modelling and hydrocode applications," In Predictive modelling of dynamic processes (Hiermaier, S. (ed.)). Springer, London, April 2009, pp. 143-165.
20. Magnusson, J., Ansell, A., Hansson, H., "Air-blast-loaded, high-strength concrete beams Part II: Numerical non-linear analysis," *Magazine of Concrete Research,* Vol. 62, No. 4, April 2010, pp. 235–242.
21. Frew, D.J., Forrestal, M.J. and Cargile, J.D., "The effect of concrete target diameter on the projectile deceleration and penetration depth," *International Journal of Impact Engineering,* Vol. 32, No. 10, October 2006, pp. 1584-1594.
22. Johnson, G. R., Cook, W.H., "A constitutive model and data for metals subjected to large strains, high strain rates, and high temperatures," Proceedings, 7th International Symposium on Ballistics, The Hague, April 1983, pp. 541-547.
23. Meyers, M. A., "Dynamic behavior of materials," Wiley, New York, 1994, 668 pp.
24. Los Alamos Scientific Laboratories, "*Selected Hugoniots by Group GMX-6*," LA-4167-MS, LASL, Los Alamos, May 1969.

25. Herrmann, W., "Constitutive equation for the dynamic compaction of ductile porous materials," *Journal of Applied Physics*, Vol. 40, No 6, 1969, pp. 2490-2499.
26. William, K.J. and Warnke, E.P., "Constitutive model for the triaxial behaviour of concrete," Seminar on concrete structure subjected to triaxial stresses, Bergamo, 17th - 18th May 1974, Int. Association of Bridge and Structural Engineers Proceedings, Vol. 19, Session no. III, paper no. 1, Zurich, 1975, 30 pp.
27. Century Dynamics, "Autodyn theory manual - Revision 4.3," Horsham, 2003, 235 pp.
28. Johnson, G.R., Beissel, S.R., Anderson Jr., C. E., Popelar, C.H., Walker, J.D., "Penetrator case fracture predictive technology: Volume II - Numerical algorithms and computations," AFRL-MN-EG-TR-1999-7054, Air Force Research Laboratory, Eglin AFB, June 1999, Vol. 2, 53 pp.
29. Popelar, C.H., Walker, J.D., Anderson Jr., C. E., Johnson, G.R., Beissel, S.R., "Penetrator case fracture predictive technology: Volume I - Dynamic fracture mechanics methodology," AFRL-MN-EG-TR-1999-7054, Air Force Research Laboratory, Eglin AFB, Vol. 1, June 1999, 151 pp.
30. Schuler, H., "Experimentelle und numerische untersuchungen zur schädigung von stossbeanspruchten beton," Schriftenreihe Forschungsergebnisse aus der Kurzzeitdynamik," Band 6., Fraunhofer EMI, Freiburg, January 2004, 184 pp.
31. Tu, Z., Lu, Y., "Modifications of RHT material model for improved numerical simulation of dynamic response of concrete," *International Journal of Impact Engineering,* Vol. 37, No. 10, October 2010, pp. 1072-1082.

Concrete shear keys in prefabricated bridges with dry deck joints

Robert Hällmark
M.Sc./Bridge Designer
LTU/Ramböll
Kyrkogatan 2, Box 850
SE – 971 26 Luleå
robert.hallmark@ramboll.se

Martin Nilsson
Ph.D.
Luleå University of Technology
SE – 971 87 Luleå
martin.c.nilsson@ltu.se

Peter Collin
Professor/Bridge Manager
LTU/Ramböll
Kyrkogatan 2, Box 850
SE – 971 26 Luleå
peter.collin@ramboll.se

ABSTRACT

A prefabricated concrete deck with dry joints between deck elements has been developed to make prefabricated bridges even more competitive. This type of bridge deck has been used on single span bridges in Sweden, and is now under development for multi span bridges. This paper describes how the deck system works. Results from laboratory tests of shear keys between deck elements are also presented together with an analysis comparing the predicted capacity with the measured failure load.

Key words: Bridge, prefabrication, element, dry joints, shear keys, laboratory tests.

1. INTRODUCTION

There is always a need to widen, build or rebuild bridges. To reduce the construction time and to minimize the impact on the traffic situation, prefabricated bridges can be used. Prefabricated steel girders are rather common but prefabricated concrete deck elements are still a rare exception. In order to make prefabricated bridges even more competitive, a deck of prefabricated concrete elements with dry joints between the elements has previously been developed. This system has been used on a few single span bridges in Sweden and is now under development for multi span bridges. The aim of the R&D project is to enable the use of dry joints between elements in multi span bridges without pre-tensioning. Particular attention has been paid to the ease of manufacturing, [1][2][3].

To transfer both lateral and vertical forces through the transverse joints, and to prevent vertical displacements between the deck elements at the joints, overlapping concrete keys are used. These keys are designed as a series of overlapping male-female connections along the joints, see Figure 1 and 2. In order to ensure a good accuracy of fit in the dry joint, the elements are match cast.

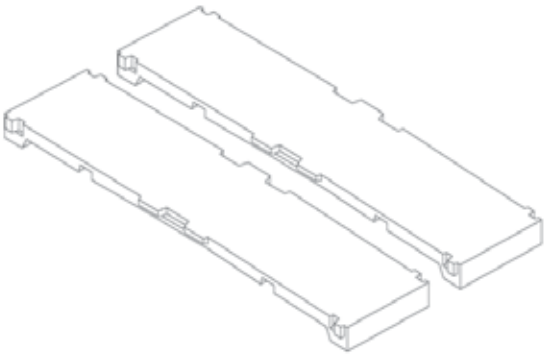

Figure 1 – 3D-sketch of two elements, illustrating the joint.

Figure 2 – Element during assembly

The theoretical distance between the transversal reinforcement bars in the concrete deck elements and the shear studs on the steel girders is limited, and the tolerances can be demanding since the overlapping concrete keys require a longitudinal displacement of the elements at the assembling. The displacement has to be at least the horizontal depth of the overlapping concrete keys plus the tolerances in the longitudinal direction of the bridge, see Figure 3. [2]

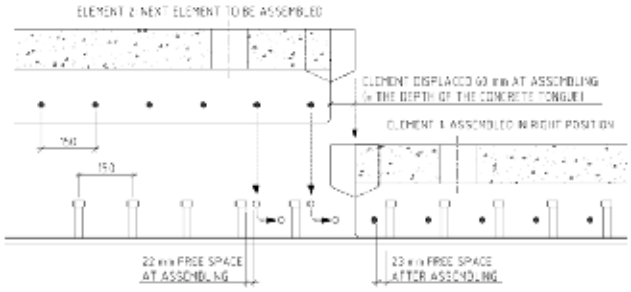

Figure 3 – Illustration of the limited tolerances. [2]

If possible, it would be preferable to use shear keys with smaller depth. However, the shear keys must be able to transfer the forces given in the design codes [4]. By using a FE-model of the bridge it can be shown that a maximum of about 40% of the traffic load acting on a single element is transferred through one of the joints. The rest of the load is transferred directly to the steel girders, or through the dry joint at the opposite side of the element. Therefore, the shear keys must be able to resist a load that is at least 40% of the design load given in the codes.

In order to find out how the shear keys transfer forces, and to be able to predict their strength and verifying the FE-model, laboratory tests have been performed.

2. LABORATORY TESTS

Twelve static tests with three different layouts of the shear keys have been tested. The test set-up and the specimens are briefly described in the following sections.

2.1 Test set-up

The tests were focusing on pure shear capacity of the concrete keys. This means that no positive or negative effects were simulated, such as prestressing from the steel girders, or any misfit between the elements. A schematic and simplified sketch of the test set up is shown in Figure 4.

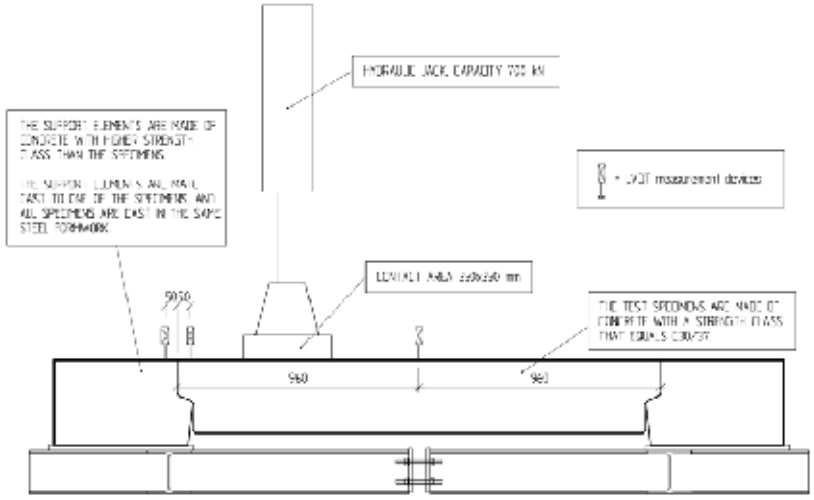

Figure 4 – Schematic and simplified sketch of the test set up.

The test specimens were placed in a test rig that consists of two concrete supports on top of a steel frame. The concrete support elements was match cast to one of the test specimens. All test specimens were made in the same steel formwork, and fitted well to the match cast supports. The supports were made in concrete with higher strength class (C40/50) than the specimens (C30/37). They were also heavily reinforced to avoid any failure in the support elements, and to make it possible to reuse them. The steel frame was used to keep the supports in the right positions and to make the demounting easier. The frame was constructed of HEA180 profiles. Figures 5 and 6 below show more detailed drawings of the support elements and the steel frame.

Before each the test was started, the bolt connections in the steel frame was tightened so that the frame could take care of the horizontal tensional forces that occurs due to the inclined contact surface in the shear keys. The bolts were tightened gently, aiming to get a remaining horizontal gap of ~0.5 mm at each shear key. The bolt connections were not used to clamp the specimen and the support elements together, giving a horizontal compressive force in the concrete.

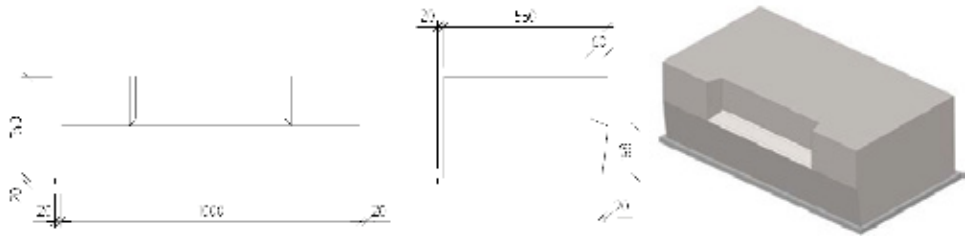

Figure 5 – Geometry drawings of support elements.

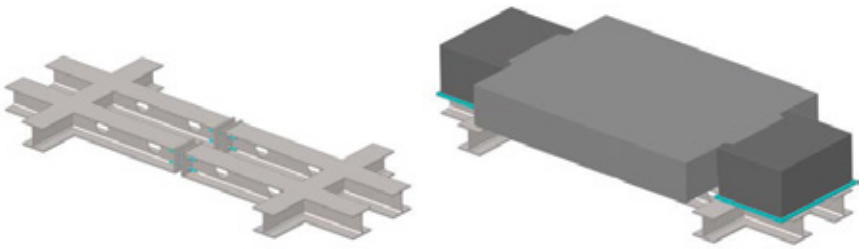

Figure 6 – Illustration of test rig.

Each specimen had two shear keys that were tested under static load. The first shear key was tested until failure. After that, the hydraulic jack was moved to the opposite side of the specimen, and the second key was tested. When the second shear key was tested an extra vertical support was used, to make sure that the specimen was levelled horizontally and that the support area was uncracked, see Figure 7.

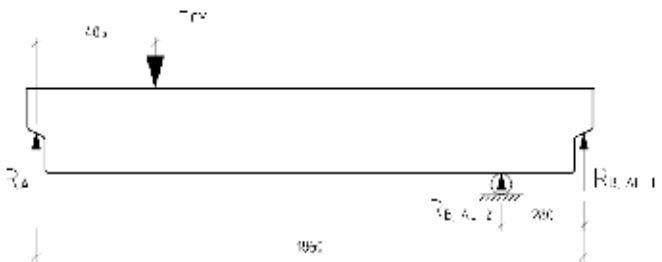

Figure 7 – Load situation with the extra support.

During the tests, data were recorded on 12 channels. Two channels were used to record the time elapsed and the load from the cylinder. The remaining ten channels were used to record deformations. Six measurement points were placed on top of the specimen. Three were placed on top of the support element and the last one was placed towards the floor measuring the reference deformation. The test set-up and the measurement devices are shown in Figure 8.

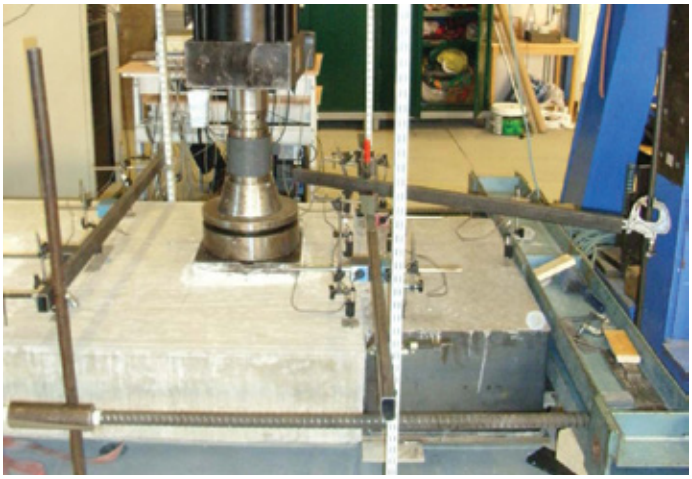

Figure 8 – Picture of test set-up.

2.2 Test specimens

The general geometry of the test specimens were 1.8 × 1.3 m, with a concrete shear key depth of 60 mm and a length of 540 mm, see Figure 9. The concrete strength in the specimens was aimed to be equal to strength class C30/37. For each specimen, six concrete cube tests were performed: 3 compressive and 3 tensile. The material test results are presented in Chapter 3.

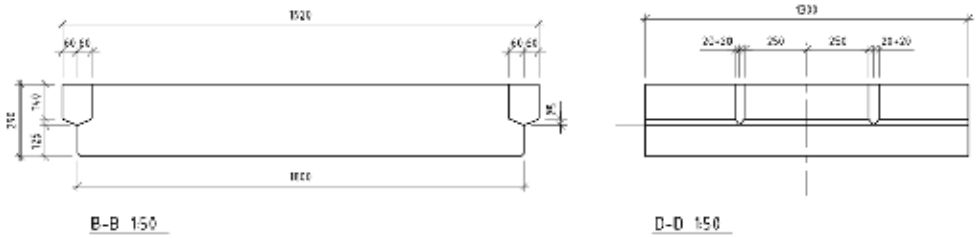

Figure 9 – General geometry of test specimens.

The first specimens (2 elements) were reinforced with exactly the same amount of reinforcement as used in deck elements in previously constructed single span bridges. In these specimens the shear keys were the same in both ends, shear key type 1. The second type of specimens (4 elements) had reduced shear key reinforcement in one of the shear keys, shear key type 2, compared to the first specimens. The other shear key, shear key type 3, was completely without reinforcement. With this design, four test results are gained for each type of shear key. Figures 10 and 11 show the reinforcement drawings of the specimens.

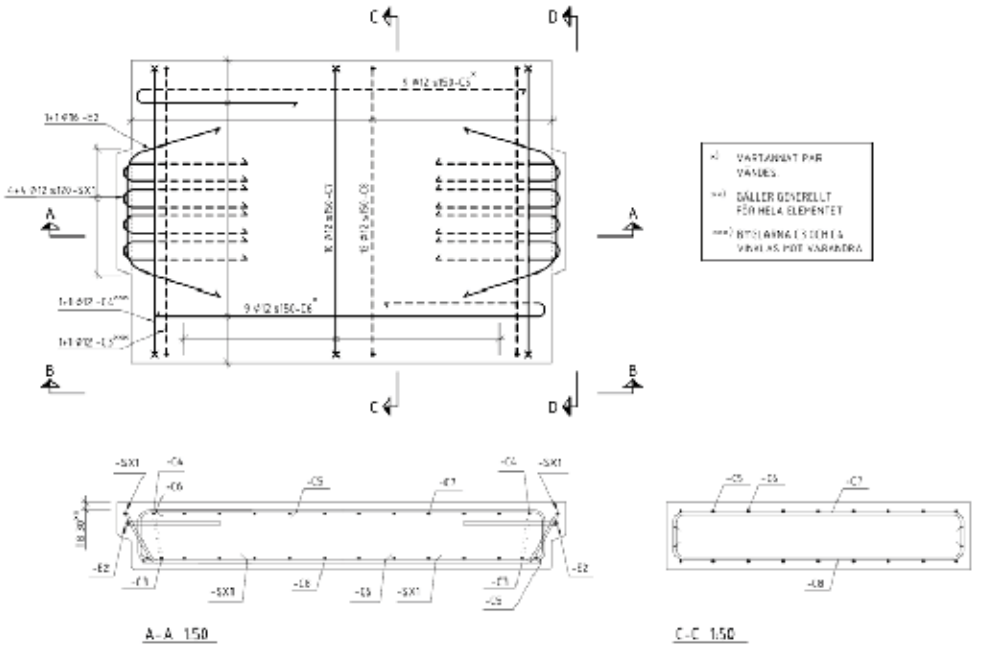

Figure 10 – Reinforcement drawing for specimens of type 1.

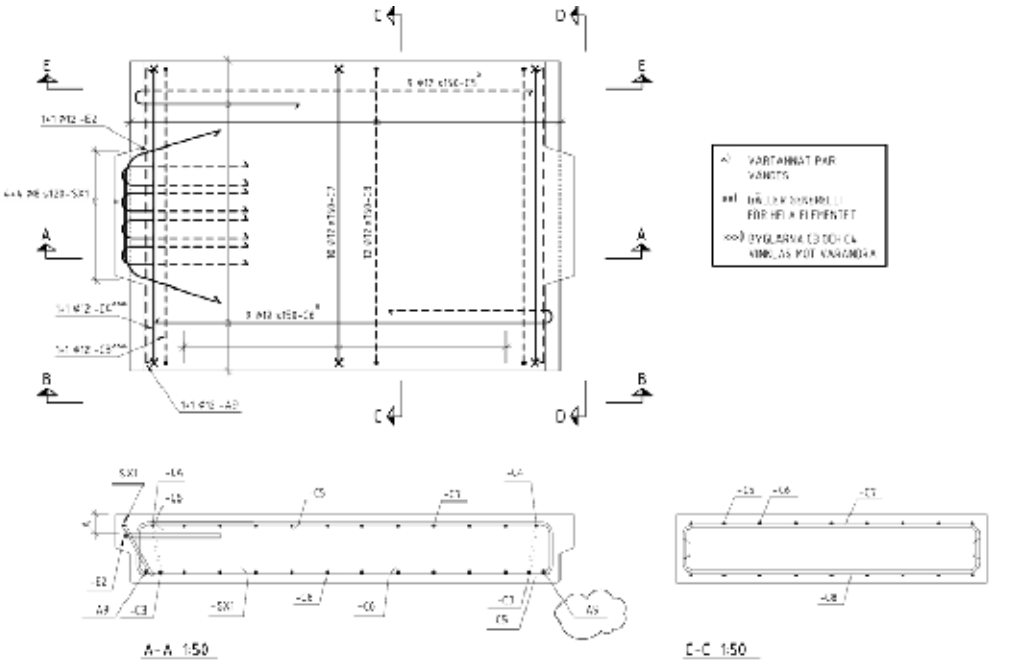

Figure 11 – Reinforcement drawing for specimens of type 2.

3. RESULTS

3.1 Material tests

For each specimen, six cubes were cast out of the same concrete mix. Three of the cubes were used to determine the compressive strength and the other three were used to determine the tensile strength. The test cubes had the dimensions of 150×150×150 mm. The mean values for each specimen are presented in Table 1 below.

Table 1 – Concrete parameters.

Cast date	Test date	Age [days]	δ [kg/m³]	P_c [kN]	f_c [MPa]	P_{ct} [kN]	f_{ct} [MPa]	Specimen type
2010-03-15	2010-06-16	93	2334	1045	46.1	118	2.6	1
2010-03-16	2010-06-11	87	2345	1132	49.7	123	2.8	1
2010-03-18	2010-06-02	76	2372	1082	47.6	103	2.3	2
2010-04-07	2010-06-08	62	2330	967	42.6	94	2.1	2
2010-04-08	2010-06-11	64	2358	1009	44.5	115	2.6	2
2010-04-12	2010-05-31	49	2371	970	42.9	99	2.3	2

P_c = failure load, compressive test f_c = compressive strength
P_{ct} = failure load, splitting test f_{ct} = splitting tensile strength

3.2 Shear key tests

All tests were deformation controlled, with a stroke of 0.02 mm/s. Two different kinds of failures were observed when the reinforced shear keys were tested. Firstly, five of eight reinforced shear keys failed by cracks that activated the reinforcement, giving a ductile behaviour – failure type 1. The shear keys remained as one piece, but with some concrete crushing in the lower parts. Three specimen failed by cracks that were developed outside the reinforcement, resulting in a failure that separated the shear key from the rest of the specimen – failure type 2. This type of failure occurred under lower loads than the previously described failure.

Shear key type 1 – Ø12 reinforced (4 tests)
Two of four shear keys of type 1 resulted in failure type 1. The load-deformation curves from these two tests are shown in Figure 12 with solid lines, together with some photos of the failed shear keys, Figure 13.

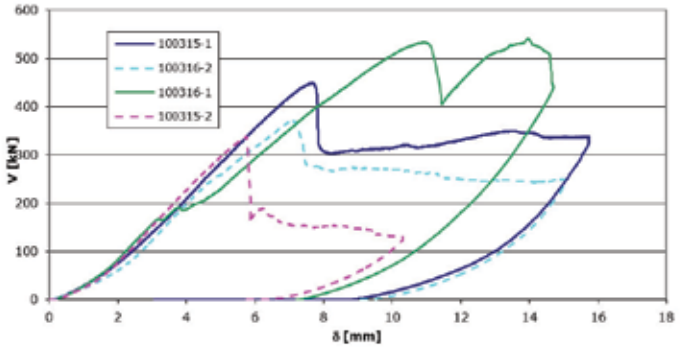

Figure 12 – Load-deformation curve for shear key type 1, failure type 1 (solid) and 2 (dashed).

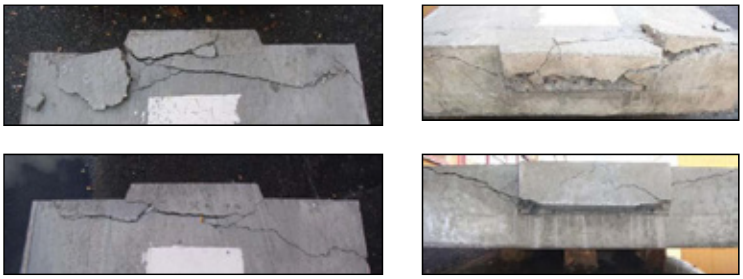

Figure 13 – Photos of shear key type 1 with a failure activating the reinforcement.

The last two specimens failed by cracks that developed outside the reinforcement, resulting in a failure that separated the shear key from the rest of the specimen. The load-time curves from these two tests are shown with dashed lines in Figure 12, together with some photos of the failed shear keys, see Figure 14.

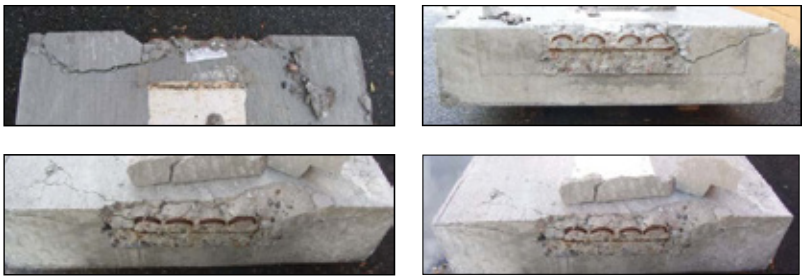

Figure 14 – Photos of shear key type 1 after failure in the concrete covering layer.

Shear key type 2 – Ø8 reinforced (4 tests)
The load-time curves from the tests are shown below together with some photos of the failed shear keys, see Figures 15 and 16.

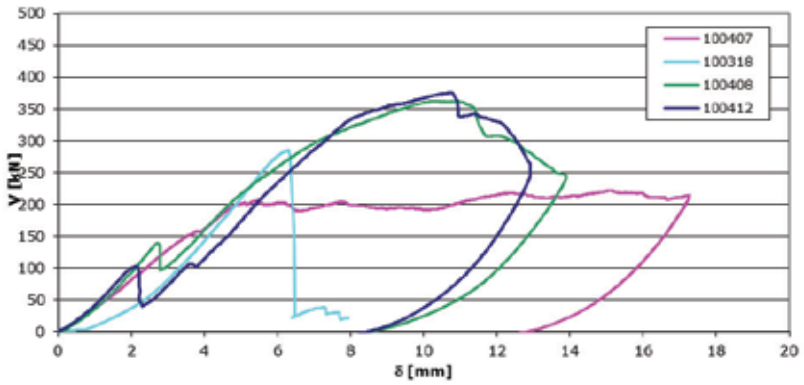

Figure 15 – Load-time curve for shear key type 2.

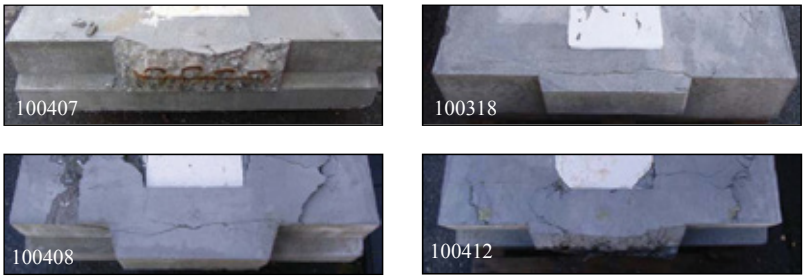

Figure 16 – Photos of shear key type 2 after failure.

In one aspect, the results from these tests reminds of the tests of shear key type 1 – Ø12 reinforced, since three shear keys remains rather unaffected after cracking, and one shear key fail outside the reinforcement. The latter shows a very plastic behaviour before it finally fails in the concrete cover layer.

Shear key type 3 – unreinforced (4 tests)
The load-time curves from the tests are shown below together with some photos of the failed shear keys, see Figures 17 and 18.

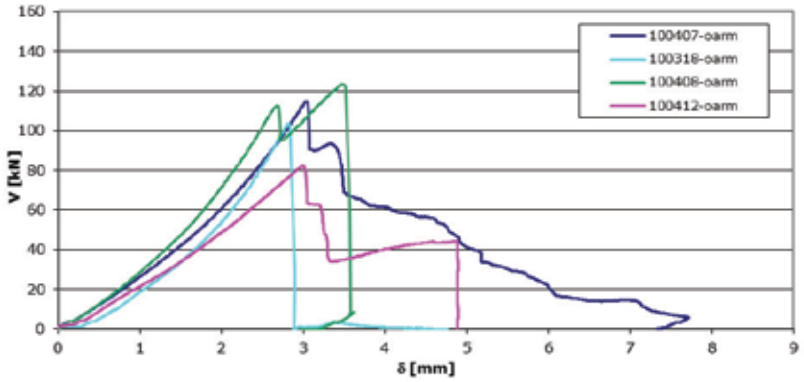

Figure 17 – Load-time curve for shear keys of type 3

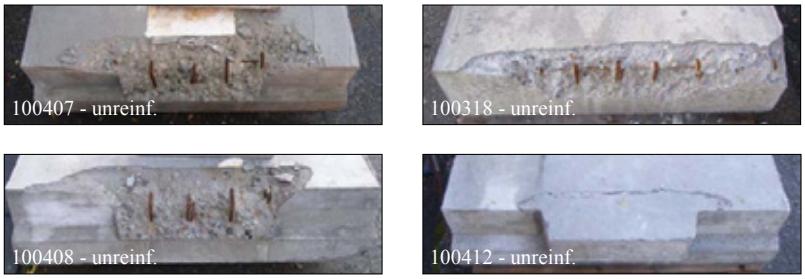

Figure 18 – Photos of shear-keys after failure.

4. ANALYSIS

The strength of the shear keys has been estimated by using four different design models:

1. classical beam linear elastic analysis – shear key type 3 with failure type 2
2. Eurocode 2 – shear key type 1 and 2 with failure type 2 [6]
3. Eurocode 2 – shear key 1 and 2 with failure type 1 [6]
4. force equilibrium model

The material parameters from the test of concrete cubes are used to calculate the shear capacity for each shear key. The results from the design models are presented in Table 2.

Shear resistance for shear key type 3 with failure type 2

The shear resistance for failure type 2 in shear key type 3 without reinforcement can be estimated as, according to classic beam analysis and assuming that the shear strength is half the tensile strength [7],

$$V_{Rd,c} = \frac{2}{3} b_w h f_{shear} \approx \frac{1}{3} b_w h f_{ct} \tag{1}$$

where

b_w = 540 mm; the smallest width of the cross-section within the effective height

h = 165 mm; height of shear key

f_{ct} = is the splitting tensile strength of the concrete, see Table 1

Shear resistance for shear key type 1 and 2 with failure type 2 [5]

The shear resistance for failure type 2 can also be estimated by using formulas from [5],

$$V_c = b_w d f_v \tag{2}$$

$$f_v = 0.3 \cdot \xi \cdot (1 + 50\rho) f_{ct} \tag{3}$$

$$\rho = A_{s0} / (b_w \cdot d) \leq 0{,}02 \tag{4}$$

$\xi = 1.4$ when $d \leq 0.2$ m

d = 140 mm

b_w = 540 mm

b_w the smallest width of the cross-section within the effective height

d effective height

f_v shear strength of the concrete

f_{ct} tensile strength of the concrete

A_{s0} the smallest amount of bending reinforcement in the tensile part of the studied cross-section. This is set to 0, since there is no bending reinforcement in the shear key, only shear reinforcement.

Shear resistance for shear key 1 and 2 with failure type 1 [6],
This approach has been used on at least two bridges in Sweden, a bridge over Rokån and a bridge in Norrfors.

According to Eurocode 2 [6] the shear resistance for a section with inclined shear reinforcement is

$$V_{Rd,s} = \frac{A_{sw}}{s} z f_{ywd} (\cot\theta + \cot\alpha)\sin\alpha \tag{5}$$

When shear reinforcement is used locally, with inclined rebars in one line (the –SX rebars), then the equation above can be simplified to

$$V_{Rd,s} = A_{sw} f_{ywd} \sin\alpha \tag{6}$$

where

A_{sw} = is the area of the shear reinforcement

f_{yw} = 500 MPa, is the yield strength of the shear reinforcement

θ = is the angle of the shear crack (~45° observed in the test)

α = 60° is the inclination of the shear reinforcement

Force equilibrium model.
This model has been suggested, by Dr. Bo Westerberg (KTH, Stockholm), in order to describe the load carrying capacity in more detail. It is a force equilibrium model that involves both the reinforcement and compressive struts in the concrete, see Figure 19.

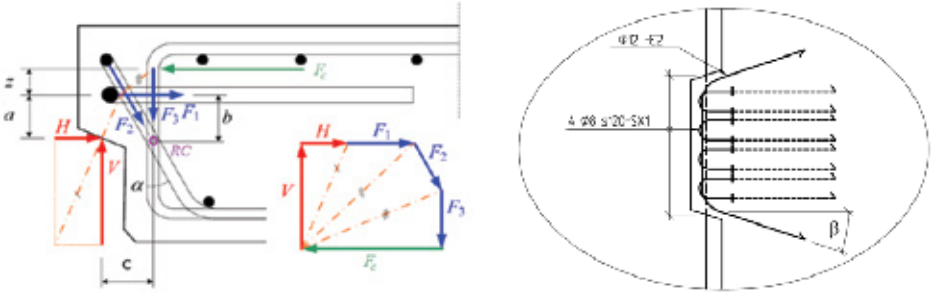

Figure 19 – Illustration of force equilibrium model and the notations.

The horizontal force *H* is believed to have great influence on the load carrying capacity. Without a compressive horizontal force, there is a risk for shear failure of the concrete cover at the edge of the shear key. The load carrying capacity is hard to predict in such a scenario, but it cannot be more than the shear strength of the concrete.

In the laboratory tests, the size of the force *H* is dependent on the shape of the supports, the rigidity of the test-rig etc. In a real bridge, this force will vary along the bridge and will depend on the global load situation as well as the local load situation.

Equilibrium equations:

$$\Sigma F \uparrow: \quad V - F_2 \cos\alpha - F_3 = 0 \tag{7}$$

$$\Sigma F \rightarrow: \quad H - F_c + F_2 \sin\alpha + F_1 = 0 \tag{8}$$

$$\Sigma M_{RC}: \quad V \cdot c + F_1 b + H(b-a) - F_c(b+z) = 0 \tag{9}$$

The load carrying capacity of the shear key can be estimated by using the maximum capacity of each rebar.

$$F_1 \le f_y A_{s1} \cos\beta \tag{10}$$

$$F_2 \le f_y A_{s2} \tag{11}$$

$$F_3 \le f_y A_{s3} \tag{12}$$

giving

$Ø_1$ = 12 mm	$Ø_2$ = 8 mm
$F_{1,\max} = 500 \cdot 2 \frac{\pi \cdot 16^2}{4} \cdot \cos 18.5° = 191$ kN	$F_{1,\max} = 500 \cdot 2 \frac{\pi \cdot 12^2}{4} \cdot \cos 18{,}5° = 107$ kN
$F_{2,\max} = 500 \cdot 8 \frac{\pi \cdot 12^2}{4} = 452$ kN	$F_{2,\max} = 500 \cdot 8 \frac{\pi \cdot 8^2}{4} = 201$ kN
$F_{3,\max} = 500 \cdot 3 \frac{\pi \cdot 12^2}{4} = 170$ kN	$F_{3,\max} = 500 \cdot 3 \frac{\pi \cdot 12^2}{4} = 170$ kN

As a first assumption the horizontal force, *H*, is set equal to zero. Then we assume that we are utilizing the shear reinforcement up to 100%. This gives the following result by Equation (7).

$Ø_1$ = 12 mm	$Ø_2$ = 8 mm
$V_{\max} = 452 \cos 30° + 170 = 561$ kN	$V_{\max} = 201 \cos 30° + 170 = 344$ kN

The moment equilibrium Equation (9) gives:

$Ø_1$ = 12 mm	$Ø_2$ = 8 mm
$F_c = \frac{561 \cdot 66 + 191 \cdot 65}{65 + 20} = 582$ kN	$F_c = \frac{344 \cdot 66 + 107 \cdot 65}{65 + 20} = 349$ kN

Assuming that the compressive strut in the concrete is developed over a height of 30 mm and the width of 540 mm, the compressive stress in the concrete can be calculated as:

$Ø_1$ = 12 mm	$Ø_2$ = 8 mm
$\sigma_{Fc} = F_c/(w \cdot h)$	$\sigma_{Fc} = F_c/(w \cdot h)$
$\sigma_{Fc} = 582/(540 \cdot 30) = 35.9$ MPa	$\sigma_{Fc} = 353/(540 \cdot 30) = 21.8$ MPa

These compressive stresses are below the compressive strengths that have been measured, and failures caused by concrete crushing could not be observed in the tests. The assumed distribution

of forces in the rebars would be a possible solution according to this load model, resulting in yielding in the shear reinforcement. Anyhow, this is only one possible solution for this model, based on theoretical positions of the rebars. This load model should be calibrated to the test results, as should the influence of the horizontal force *H*. For example, frictional forces between the concrete surfaces will influence the result.

5. TEST RESULTS VS. CALCULATION MODELS

Table 2 – Test results compared to results from calculation models.

Cast date	Test results V_{max} [kN]			Model 1 V_{max} [kN]				Model 2 V_{max} [kN]				Model 3 V_{max} [kN]				Model 4 V_{max} [kN]			
2010-	Ø12	Ø8	-	Ø12	Ø8	-	η*	Ø12	Ø8	-	η*	Ø12	Ø8	-	η*	Ø12	Ø8	-	η*
03-15	449	-	-	80	-	-	*5.61*	*84*	-	-	*5.36*	392	-	-	*1.15*	561	-	-	*0.80*
03-15	337	-	-	80	-	-	*4.21*	*84*	-	-	*4.03*	392	-	-	*0.86*	561	-	-	*0.60*
03-16	532	-	-	83	-	-	*6.41*	*88*	-	-	*6.07*	392	-	-	*1.36*	561	-	-	*0.95*
03-16	370	-	-	86	-	-	*4.30*	*88*	-	-	*4.22*	392	-	-	*0.94*	561	-	-	*0.66*
03-18	-	285	-	-	68	-	*4.19*	-	*73*	-	*3.88*	-	174	-	*1.64*	-	344	-	*0.83*
03-18	-	-	104	-	-	68	*1.53*	-	-	73	*1.42*	-	-	0	-	-	-	0	-
04-07	-	222	-	-	63	-	*3.52*	-	67	-	*3.30*	-	174	-	*1.28*	-	344	-	*0.65*
04-07	-	-	114	-	-	63	*1.81*	-	-	67	*1.70*	-	-	0	-	-	-	0	-
04-08	-	363	-	-	77	-	*4.71*	-	82	-	*4.42*	-	174	-	*2.09*	-	344	-	*1.06*
04-08	-	-	123	-	-	77	*1.60*	-	-	82	*1.50*	-	-	0	-	-	-	0	-
04-12	-	376	-	-	68	-	*5.53*	-	71	-	*5.30*	-	174	-	*2.16*	-	344	-	*1.09*
04-12	-	-	82	-	-	68	*1.21*	-	-	71	*1.16*	-	-	0	-	-	-	0	-

* η = test result divided by the predicted value for the given calculation model.

According to the result presented in Table 2, calculation model 1 and 2 can be useful to estimate the strength for a shear key without reinforcement. The design values are on the safe side with a safety factor from 1.16 – 1.81. Model 3 gives results that are on safe side except for the failures in the concrete cover for test specimen type 1. With the assumptions made, design model 4 is the same as model 3, except the fact that model 4 makes the vertical reinforcement bars in the slab active. The result is often on the unsafe side, which could indicate that the vertical rebars does not influence the load carrying capacity as much as assumed in the calculations. This model needs to be studied more detailed, calibrated to the test results and maybe modified.

One thing that can be noted is that the shear keys that fail in the concrete covering layer still transfer forces that are far higher than the capacity of the concrete itself. Therefore, the reinforcement must have been activated, and should be included in the design formula in one way or another.

6. CONCLUSIONS

The results from the tests have a considerable scatter. Still some interesting points can be noted. Firstly, the tests show that unreinforced concrete can not transfer the design shear forces, caused by the vehicle models in Eurocode, from one element to another. This was an expected result, in line with the result from the calculations. However, in the reality we believe that the shear keys can transfer a higher load since the surrounding elements will deflect together with the loaded element, which probably gives longitudinal compressive forces which would counteract the tensile stresses that occurs due to the shear forces.

Secondly, the load carrying capacity of the previously used shear keys seems to be larger than necessary, especially if we can avoid a failure that is developed by a crack growing through the concrete covering. The shear keys with less amount of reinforcement (Ø8mm) are still strong enough to carry the load. However, we suggest some changes in the shear key reinforcement since we see some potential improvement. Two new reinforcement layouts are presented in Figure 18. In both cases the concrete cover layer has been reduced. In the left case, additional reinforcement have been added (-E8), and in the right case the SX-rebars have been replaced by EX-rebars. The geometry of the EX- and SX- rebars can be seen in Figure 10 and 20. By using stainless steel in some of the rebars in the shear keys, it would be possible to decrease the thickness of the concrete covering layer, and hopefully avoid a failure in the covering layer.

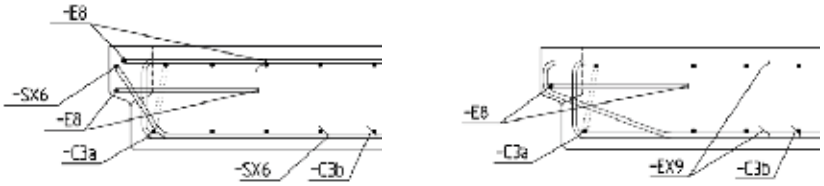

Figure 20 – Illustration of two suggested reinforcement layouts.

REFERENCES

1. Hällmark, R., Collin, P & Nilsson M., "Prefabricated composite bridges," Proceedings, IABSE Symposium, Bangkok, Thailand, Sept. 2009, Vol. 96, pp. 282-283.
2. Hällmark, R., Collin, P & Stoltz A., "Innovative Prefabricated Composite Bridges," Structural Engineering International, 2009, Vol. 19, no:1, pp. 69-78.
3. Collin et al., "International workshop on prefabricated composite bridges", March 4th 2009, Stockholm, ISBN: 1402-1536.
4. EN 1991-2, Eurocode 1 – Actions on structures - Part 2: Traffic Loads on Bridges. CEN, European Committee for Standardization: Brussels, 2005.
5. BBK04, Swedish Concrete Regulations, Boverket, Karlskrona, 2004.
6. EN 1992-1-1, Eurocode 2 – Design of concrete structures, Part 1: General rules and rules for buildings. CEN, European Committee for Standardization: Brussels, 2004.
7. Betonghandboken – Konstruktion, Ch. 3.7:2, AB Svensk Byggtjänst, Stockholm.

New Årsta Railway Bridge – A case study on the long-term Structural Health Monitoring with Fibre Optic Sensors

Merit Enckell
M.Sc., Tec. Licentiate
Royal Institute of Technology (KTH), Stockholm, Sweden
& COWI A/S,
Parallelvej 2
DK 2800 Kongens Lyngby
E-mail: meen@cowi.dk & merit.enckell@byv.kth.se

ABSTRACT

The New Årsta Railway Bridge was built in 2000-2005. The structure is a unique pre-stressed concrete girder bridge with slender and optimised design. Structural Health Monitoring System was installed on the bridge during construction. One characteristic span is mainly instrumented with several sensors and monitoring is still ongoing.

This paper presents the Fibre Optic Sensor system including thermocouples; and their function. Observations, malfunctions and inconvenience during construction, testing and operation are collected, carefully documented and analysed. Strain and temperature data are collected from first casting up to date.

Results are highlighted and conclusions are drawn. Recommendations are given, based on the experience gained so far. Furthermore, general, accumulated knowledge about monitoring is given.

Key words: Concrete bridges, pre-stressing, Structural Health Monitoring, Fibre Optic Sensors, long-term monitoring, creep and shrinkage.

1. INTRODUCTION

Two recent decades were full of Structural Health Monitoring (SHM) activities. New technology with a variety of equipments was emerged and SHM of bridges, dams, tunnels, heritage structures, high rise buildings, and various other civil structures took place. Several international organisations and networks were founded, conferences held and primary guidelines published. Research on new sensory technology, especially in fibre optics, lasers and Microelectromechanical Systems (MEMS) developed around the world. Organised SHM made its entrance into Swedish field in the last decade. Monitoring activities had taken place in the past [1] but were small in scale and most likely temporary.

SHM helps civil engineers with control, verification and information of the real condition or change in the condition of a structure. Reliable information for management, maintenance, research and decision making is obtained. Structural Health Monitoring System (SHMS) for a

structure consists of sensors, data acquisition systems, data transfer and storage systems, data management and data interpretation. Design of SHMS is complicated and many times unique procedure influenced by several factors. The main goals of data interpretation in connection to the monitored structure are; structural identification during construction and operation, FE model updating, condition assessment, alarm configuration if required and service life prediction helping maintenance process. SHMS can consist of a few sensors up to hundreds or even thousands of them depending on the demands of the monitoring object.

The New Årsta Railway Bridge was built in 2000-2005. The unique, slender structure with high amount of non-tension reinforcement and pre-stressed cables sets high demands for the concrete. The Swedish National Railway Administration (Former Banverket, present Trafikverket) initiated a monitoring campaign in order to study and understand the dynamic and the static behaviour of the bridge. The SHMS consists of traditional strain transducers, thermocouples, long-gauge fibre optic sensors and accelerometers. One chosen, characteristic span, starting from Pier 8 (P8) to Pier 9 (P9) is mainly instrumented and the monitoring started in 2003 from first pour of concrete and is ongoing.

Two different research projects were associated to the project in order to learn about static and dynamic behaviour of the bridge as well as about the novel technology used in the project. The aims of the study are to check both static and dynamic behaviour of the structure during 10 years including construction period, load testing and long-term behaviour. Data, observations, malfunctions and challenges during construction, testing and operation were collected, carefully documented and analysed. Detailed information about the previous research can be found in technical reports [2, 3], in two licentiate theses [4, 5] and in one Doctoral thesis [6].

This paper gives a short presentation about the project. A few interesting topics of accomplished results so far are presented. Aim of this paper is to present advantages and disadvantages of the Fibre Optic Sensor (FOS) system including thermocouples; and their function. Furthermore, the aims are also to learn about novel fibre optic sensors and compare them with the traditional transducers, to accumulate knowledge about monitoring procedures, SHM, FOSs and practical points of views e.g. installation, when working in the field. Suitability and usage of FOS is discussed for concrete applications. Finally, recommendations are given based on the experience gained so far.

2. PREVIOUS RESEARCH

The development in sensor technology was tremendous in 1990's and several new technologies from other branches were emerged into civil engineering field, such as fibre optics [7, 8, 9, 10, 11, 12]. ISIS Canada Research Network was established in 1995. Aktan et al [13] published the report *"Development of a Model Health Monitoring Guide for Major Bridges"*. ISIS published a report *"Guidelines for Structural Health Monitoring"* in 2001 [14]. A European network, SAMCO was founded in 2001 followed by the European Association for SAMCO founded in 2006. SAMCO deals with Structural Assessment, Monitoring and Control. International Society for Structural Health Monitoring of Intelligent Infrastructure (ISHMII) was founded in 2003. ISHMII publishes a periodic journal called *"The Journal of Civil Structural Health Monitoring (JCSHM)"*. The EU project, Sustainable Bridges also started to work with functional requirements for railway bridges in 2003 and reports can be seen in [15]. *"Monitoring and Safety Evaluation of Existing Concrete Structures"* [16], a report from CEB-Fib is very broad and comprehensive.

It was also necessary to understand the behaviour of the sensors in the fresh concrete and the behaviour of the concrete itself. The issues around matured concrete and research around concrete and concrete at early age, very early age and long-term effects in concrete constructions were studied [11, 17]. Glisic [11] worked with fibre optic sensors and developed a validated new numerical model that describes the evolution of the thermal expansion coefficient with respect to degree of hydration.

Pre-stressed, segmental built concrete bridges do suffer from excessive deflections and pre-stress losses that can be explained with long term creep and shrinkage effects. Studies on long-term creep and shrinkage are ongoing and the subject is eagerly discussed [18, 19, 20, 21]. Different codes like CEB-*fib*, ACI-209, GL, JSCE and RILEM-B3 [22-29] are compared and checked and data measured for 56 pre-stressed segmental built box girder bridges was investigated and results are highlighted in [30].

Glisic et al. [31, 32] describe long-term monitoring of high-rise buildings over four years. The long-gage fibre optic sensors were embedded in the ground-level columns during the construction and the monitoring started with the birth of the structure.

Robertson [33] presents results of a long-span pre-stressed bridge monitoring program after nine years of data collection. Short-term and long-term responses of the structure were monitored and analysed. Creep and shrinkage testing with associated strength testing was performed beforehand and these test results were used for long-term creep and shrinkage predictions.

3. DESCRIPTION OF THE BRIDGE AND MONITORING SYSTEM

3.1 Background

The political idea of building a new bridge beside the Old Årsta Bridge from 1929 started already in 1988. Stockholm needed an increased track capacity in order to meet the needs for increasing rail traffic. The New Årsta Railway Bridge was built as part of an upgrading from two tracks to four between Stockholm South and Årstaberg. Thereby, Stockholm got an increased track capacity that helped the positive development of rail traffic in the region.

3.2 Bridge Description

The New Årsta Railway Bridge is 833 m long, 19.5 m wide and has a vertical clearance of 26 meters. The bridge accommodates 2 railway tracks, pedestrian and cycle road on the west side as well as a service road on the west. Length of the nine main spans is 78 m. The construction work started in summer 2000 and the bridge was opened for regular railway traffic in May 2005, see Fig 1. These two bridges enable approximately 500 trains to cross over Årstaviken per day, and transporting about 50 million passengers per year.

Figure 1- New Årsta Bridge during construction with the Old Årsta Railway Bridge seen in the background

The slender design of the bridge required a high amount of reinforcement in order to satisfy the needs for bearing capacity. The superstructure contains an average of 220 kg/m^3 non-tensioned reinforcement that is approximately the double compared to a normal bridge. Also 50 pre-tensioning cables are spread over the cross-section of the bridge. These pre-stressed cables are fixed inside durable plastic pipes in order to separate them from the superstructure and make replacement of damaged cables possible in the future.

3.3 Construction

Traditional scaffolding and in situ reinforcing were used on the north construction side where the bridge has a slight curvature while a launching formwork, tower wagon and prefabricated reinforcement cages were used on the south construction side where the bridge is straight.

The prefabricated reinforcement cages were made in special moulds, usually known as jigs, and from there lifted into their exactly right position inside the casting mould with the help of a gantry crane using a quantity of 60 suspension points for each reinforcement cage. The joints between the cages were reinforced in situ.

Each span had 11-12 casting sections. The sections were cast in optimised order regarding this type of construction and production solution. Each casting section, numbered 1 to 5 can be seen in the Fig. 2. The section part number in figure indicates the casting sequence. The trough was cast first and the track slab after in the same section before going on casting the next section.

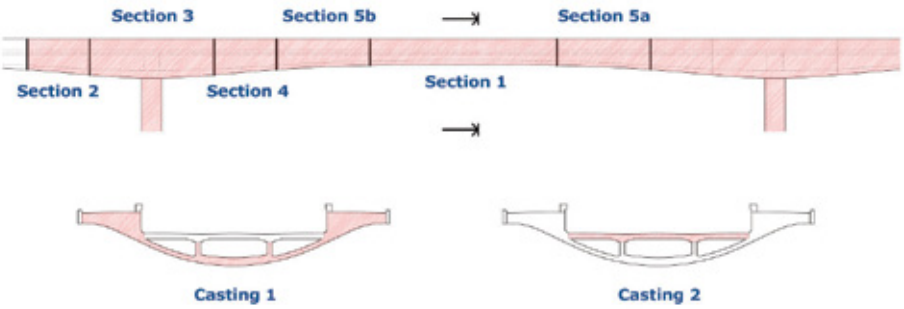

Figure 2 - Illustration of casting the sections in the spans. The sections are cast in sequence 1 to 5 and Castings 1 and 2 indicate the trough and track slab, respectively.

Red Concrete

Architectural designers, Sir Norman Foster and his team wanted the bridge to symbolise Sweden and to interact with the surrounding environment. Therefore, a fully impregnated 'Falun red' coloured concrete was used except on foundations slabs under water and on the carriageway as these parts are not visible. This red coloured concrete has lower demands for maintenance, better mechanical strength and longer predictable lifetime compared to a painted one. The red colour is accomplished by mixing iron oxide pigments to the cement paste. Efflorescence of concrete gives a red-white colour instead of the supposed red one but this is solved by washing the concrete surface with high pressure water from time to time.

Concrete grading K40 (cubic concrete compressive strength= 40 MPa) according to the Swedish standard BBK94 [34] was used for abutments and retaining walls and K60 (cubic concrete compressive strength= 60 MPa) for the rest of the bridge. Portland cement with set retarding, air entrainment, superplastiziser and expanding agents was used. Superplastiziser gave increased flow ability which was necessary due to congested reinforcement. Retarders prevented from undesirable partial setting before the complicated and time taking pour was completed. Expander helped to cope with shrinkage issues. Air entrainments add tiny air void in the concrete and reduce damage during freeze-thaw cycles and therefore improve the durability. The properties of ready concrete mixture were carefully tested; both at the concrete plant and when arriving to the bridge, see Fig.3, left. In order to avoid colour variations, the formwork was covered with red pigmented cement slurry, see Fig.3, Right.

Figure 3 - Left: Concrete workability was tested on site for every concrete batch arriving on the lorries. Right: Also the formwork is red coloured.

The bridge was heavily reinforced and concrete had to have excellent flowing ability and workability in order to be distributed uniformly throughout the whole casting section. Following technical requirements were also essential: capability of withstanding long transport distances, consistency from section to section as the strength variation might have caused cracking in the structure. The largest continuous casting sections took about 24 hours and were as large as 350 m³. Totally 23.000 m³ of red coloured K60 concrete and 6.000 m³ normal K60 were used in the project.

3.4 Fibre Optic Sensor System and Thermocouples

Concrete can be affected by local defects like cracks, air pockets and inclusions. Short Gauge (SG) sensors may measure local material effects and their indications may present an error when looking the global behaviour of a structure. In order to avoid these discontinuities, Long Gauge (LG) deformation sensors can be effectively used to monitor global deformation.

Fibre Optic Sensors (FOS)
The monitoring system selected for this project is called *SOFO* (French acronym for Surveillance d'Ouvrages par Fibres Optiques – Structural Monitoring using Optical Fibres) and is based on low-coherence interferometry in optical fibre sensors. The principle of the Michelson fibre optic interferometer shown in Fig.4 (left) is to measure relative displacement between two pre-defined locations in the structure. An installed SOFO sensor can be seen in Fig. 4 (right). The LG sensors consist of two arms that are both single mode optical fibres and have chemical mirrors in end parts. One fibre is the sensing fibre and it is fixed in definite points and the other fibre is a reference fibre being loose in such way that it will always stay unstrained. The loose fibre compensates for the temperature so that additional measurement for the temperature variation is not needed. These fibres are contained in the same protection tube made of PVC so they are protected from the environmental effects. Detailed information over FOS technologies can be seen in [3, 5]

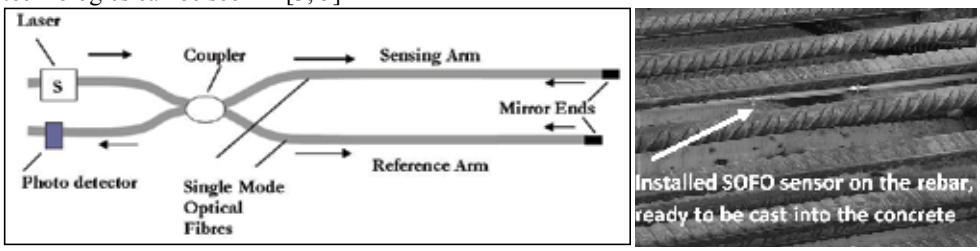

Figure 4 - Principals of Michelson fibre optic interferometer [5] to the left. An installed SOFO sensor ready to be cast into the concrete to the right.

The average strain measured by a sensor is given by the following equation:

$$\varepsilon = m_s / l_s \quad (1)$$

where ε denotes the average strain over the sensor length, m_s, deformation measured by the sensor, and l_s, length of the sensor.

Thermocouples
SOFO compatible thermocouples are temperature sensors based on principle that electrical resistance in bimetallic joint is temperature dependent. These thermocouples consist of bimetallic joint (thermocouple) and electrical connecting cable. The sensor is quickly and easily installed and its resolution is 0.2 °C (-10°C / +100°C).

Data Acquisition System (DAS)
The SOFO system consists of 40 permanent fibre optic sensors, nine thermocouples, a portable interrogator with 12 channels and data acquisition and analysis software. Static measurements are performed with the system. The system on the New Årsta Railway Bridge also accommodates a central cabinet with patch panel with 28 channels. Central cabinet is located in pier P9 and includes a portable interrogator, an external switch, devices for thermocouples and for the permanent broad band connection. Two so called ADAM units and one ADAM Bridge for the thermocouples are installed in the central cabinet and connected to the interrogator. ADAM modules are used in order to allow the configuration and automatic reading of these electrical sensors with SOFO interrogator. Results are stored in the same database structure and can be viewed and manipulated in the similar way as the SOFO deformation measurements. Two heaters are installed in the central cabinet in order to remain the temperature around +5°C inside the cabin.

One portable interrogator was used to measure different sections during construction but as soon as the span was finished, it was set up inside central cabinet with a switch and all sections were connected to the central cabinet located in section A. Sections B, C, D and E have their own small connection boxes where all the sensors are collected and led further with one 8 channel multi fibre cable to the central cabinet. Downloading and remote configuration of the database via broadband connection from the office started in January 2004.

3.5 Installation and function of FOS and Thermocouples

The selected characteristic span P8 to P9 was divided into five sections; A, B, C, D and E; where section A is nearest to pier 9, section B the quarter span nearest pier 9, section C the mid-span, section D the quarter span nearest to pier 8 and section F nearest to pier 8, see Fig.5.

Figure 5 – Sections for monitoring of deformations in span P8 to P9.

When SOFO sensors are to be cast in concrete, the installation procedure starts with fastening the SOFO sensor to the rebar with plastic clips, see Fig.6 (left). Afterwards the sensor is measured and eventually tensed or loosened to the reference value given by manufacturer. Passive cable is also fixed to the rebar and protected if necessary and sensors are connected to the portable interrogator. Temporary arrangement and protection for cables and portable interrogator is fixed so they will not be damaged while casting. Sensor is again controlled by measuring just before the casting in order to be sure that the reference value is maintained. If

any deviation is noted, the sensor is corrected before the casting starts. Automatic measurements are set on. After the formwork is removed, the sensors are tested again (see Fig.6 right) and new arrangements and necessary protections are prepared for temporary arrangements that do take place during the construction period.

Figure 6 - Installation of a SOFO LG sensor on the rebar to the left and testing of sensors after casting to the right

Details for FOSs installation schedule and date of connection to the central cabinet are shown in. Table 1.

Table 1 – The history of installation and connection for various sections

Installation of FOS and connection of sections and Data Aquisition System (DAS)			
Point	Installation Date	Casting Date, if any	Connection to DAS
SECTION A: trough	January 2003	3-4 February 2003	3 July 2003
SECTION A: track slab	February 2003	31 March 2003	3 July 2003
SECTION F: temp. section, surface installation	May 2003	Existing section	3 July 2003
SECTION C: trough	June 2003	16-17 June 2003	16 December 2003
SECTION C: track slab	June 2003	7 July 2003	16 December 2003
Data Aquisition System located in Section A	June 2003	Data Aquisition system	DAS was installed 30 June 2003. Broad band was connected 13 January 2004
SECTION E: trough	July/August 2003	7-8 August 2003	9 January 2004
SECTION E: track slab	Sebtember 2003	7-8 September 2003	9 January 2004
SECTION D: trough	October 2003	1 October 2003	9 January 2004
SECTION D: track slab	October 2003	16 October 2003	9 January 2004
SECTION B: trough	Sebtember 2003	6 October 2003	20 November 2003
SECTION B: track slab	October 2003	16 October 2003	20 November 2003

Amount of sensors, their nomenclature, direction, location, sensor length as well as permanent function is summarised in Table 2.

Table 2 - Summary of the important sensor information in span P8-P9.

PERMANENT LONG GAUGE (LG) FIBRE OPTIC SENSORS IN SPAN P8-P9				
SECTION: SENSOR NAME	Number of sensors	Direction and location	Gage Length (m)	Function in long term (2003-2011)
Section A; AS1, AS2, AS3 & AS4	4	Longitudinell, upper cantilevers	4	AS1 in function; AS2, AS3 and AS4 either damaged or unable to measure
Section A: AS5	1	Longitudinell, trough bottom	4	AS5 in function
Section A: AS6, AS8	2	Transversal, track slab	0.4	AS6 in function; AS8 damaged.
Section A: AS7	2	Transversal, track slab	2	AS7 in function
Section A; AS9X	1	Longitudinell, upper cantilevers	1	AS9X in function
Section A: AS10X	1	Longitudinell, transversal wall	1	AS10X in function
SECTION B:B S1, BS2, BS3 & BS4	4	Longitudinell, upper cantilevers	6	BS1, BS2, BS3 and BS4 in function.
Section B: BS5	1	Longitudinell, trough bottom	6	BS5 in function.
Section B: BS6, BS7	2	Transversal, track slab	6	BS6 and BS7 in function.
Section C; CS1, CS2, CS3 & CS4	4	Longitudinell, upper cantilevers	6	CS1, CS2 AND CS3 in function; and CS4 damaged.
Section C: CS5	1	Longitudinell, trough bottom	6	CS5 in function.
Section C: CS6, CS8	2	Transversal, track slab	0.4	CS6 and CS8 in function.
Section C: CS7	2	Transversal, track slab	2	CS7 in function.
SECTION D: DS1, DS2, DS3 & DS4	4	Longitudinell, upper cantilevers	6	DS1, DS2,DS3 and DS4 in function.
Section D: DS5	1	Longitudinell, trough bottom	6	DS5 in function.
Section D: DS6, DS7	2	Transversal, track slab	6	DS6 and DS7 in function.
Section E; ES1, ES2, ES3 & ES4	4	Longitudinell, upper cantilevers	4	ES1, ES2, ES3 and ES4 in function.
Section E: ES5	1	Longitudinell, trough bottom	4	ES5 in function.
Section E: ES6, ES8	2	Transversal, track slab	0.4	ES6 and ES8 damaged
Section E: ES7	2	Transversal, track slab	2	ES7 in function.

SOFO sensors show good results and 33 out of 40 are working properly still after 8 years. Sensors AS2, AS8, CS4, ES6 an ES8 were damaged during construction period and sensors AS3 and AS4 were either gliding during casting or were not pre-tensioned enough and therefore unable to measure. All nine thermocouples are working and no malfunctions were noted so far, for name, number and location of SOFO thermocouples see Table 3.

Table 3 - Name, number and location of SOFO thermocouples in span P8-P9.

Permanent Thermocouples in span P8-P9		
Section: Name of Thermocouples	Number of sensors	Location
Section A; AST1& AST2	3	Upper cantilevers
Section A; AST3	1	Trough bottom
Section C; CST1& CST2	2	Upper cantilevers
Section C; CST3	2	Trough bottom
Section E; EST1& EST2	1	Upper cantilevers
Section E; EST3	1	Trough bottom

4. RESULTS AND ANALYSIS OF THE SHMS

4.1 General

Massive amounts of measured data have been collected and also various skills and practices are gained. As the subject is large, only a few typical results are highlighted here.

The New Årsta Railway Bridge is a massive pre-stressed concrete structure. It is necessary to comprehend the behaviour of the concrete in all stages, from pouring to long-term effects. There are seven main sources of strains appearing in the concrete during its service life [11, 17]: Plastic shrinkage, ε_p; autogenous shrinkage ε_a; drying shrinkage and swelling, ε_h; carbonisation shrinkage ε_{car}; thermal strain ε_T; strain due to load, ε_s and creep, ε_φ.

Therefore the total strain at time t after the pouring of concrete can be expressed as:

$$\varepsilon(t) = \varepsilon_s(t) + \varepsilon_\varphi(t) + \varepsilon_T(t) + \varepsilon_p(t) + \varepsilon_a(t) + \varepsilon_h(t) + \varepsilon_{car}(t) \quad (2)$$

SOFO sensors measure the total sum of strain and SOFO thermocouples measure temperature. The strain is expressed in figures and discussed as microstrain, meaning strain of $1 \cdot 10^{-6}$. Tension is positive and compression negative. The temperature is in ° Celsius. Measurements were performed every 10 minutes when casting and testing. In long-term static measurement a measure was taken every hour. In order to evaluate each part of the strain it is necessary to know the concrete properties, environmental parameters like temperature and humidity as well as the loading conditions. SOFO sensors are set to zero just after pouring of the concrete where the sensor started to measure the behaviour of the swelling concrete.

4.2 Early-age Results

Fresh concrete is a fluid multiphase mixture of different components that gradually matures into solid material. Initial intense period with chemical reactions produces a high amount of heat and swelling only occurs during the early age. After this the temperature cools down and the

hydration process begins.

Around 50 to 80 percent of the cement is hydrated under the first seven days and the complete hydration may take decades or it is never completed. Autogenous shrinkage is caused by the chemical and physical processes in the concrete and reduces the volume of concrete. Plastic shrinkage is caused by unabsorbed water when the concrete is still in plastic state. Swelling is caused by absorption of water by a cement gel and drying shrinkage by vaporisation of water to the surrounding unsaturated air [11, 17]. Values of drying shrinkage are found to range from 450 to 850*10 $^{-6}$m/m.

Following Fig.7 shows results for sensors in section A. This casting part consisted of over 300 m^{3}concrete and took around 24 hours.

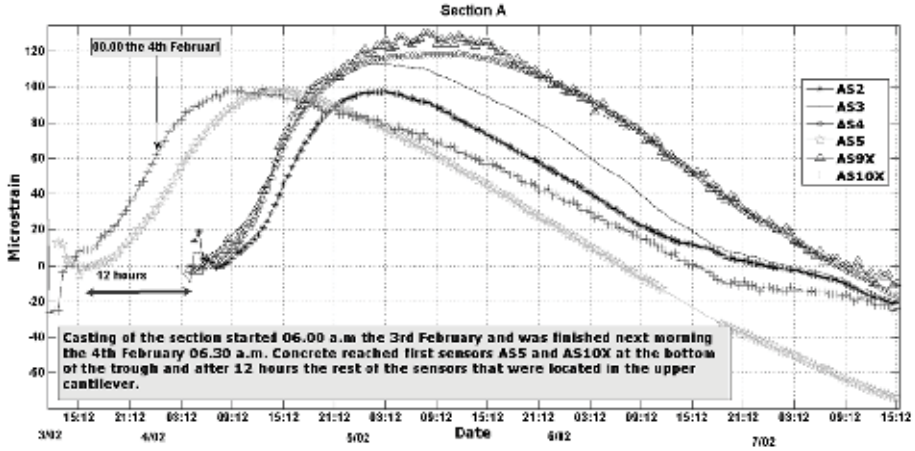

Figure 7 - Monitoring results in section A show initial early-age swelling of concrete. Straight line occurs where a measure is not taken.

Results for section E are shown in Fig. 8. Measurements are set to zero when the concrete reached the sensors and the sensor started to follow the behaviour of the concrete.

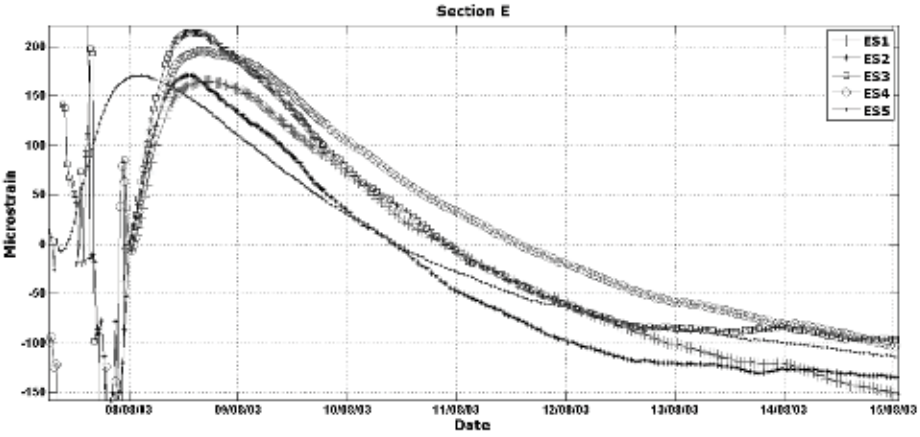

Figure 8 - Monitoring results in section E show initial early-age swelling of concrete

Fig.9 show strain curves for sensors AS9X and AS10X for the first 28 days after casting.

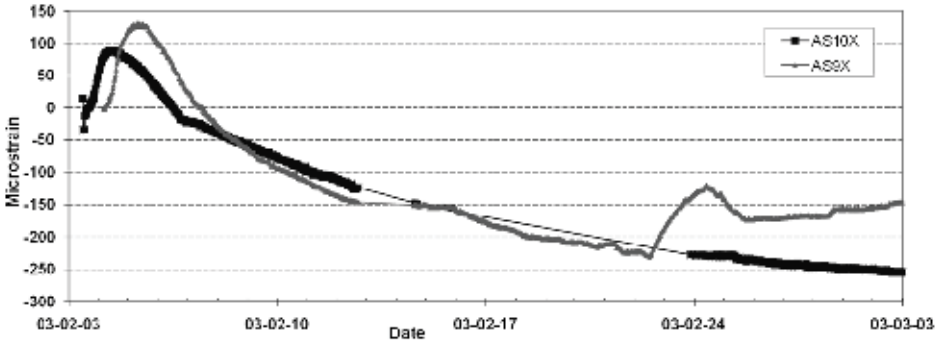

Figure 9 - 28 day strain curves for two sensors in section A. Straight line occurs where a measure is not taken. Sensor AS10X is located in the middle of a two meter thick transversal wall in P9 and show very stable behaviour. Sensor AS9X is located in the cantilever and is affected by next casting that started eighteen days after casting

Monitoring sections A and E in Fig.7 and Fig.8 are similar: A is located nearest P9 and E is located close to P8. Casting of A took place in winter and it is affected by low temperatures below 0 °C. E was cast in October with relatively warmer temperatures and higher initial swelling is noticed. Initial swelling in the concrete causes a temperature release around 30-50°C, unfortunately only manual temperature measurements were performed during the construction period and only a few data are provided.

Fig.9 shows sensors AS9X and AS10X. Both sensors are one meter long and measure average strain over their length. AS9X is located in the west cantilever while AS10X is located inside the 2 meter thick transversal wall in P9. AS10X shows very stable behaviour and reaches around -250 microstrain in compression. That would correspond to initial stress level of 9 MPa.

AS9X is located at the edge of the western cantilever and is affected by next casting and the curve turn and reaches -150 microstrain at the 28th day after casting. That corresponds to 5.4 MPa in compression. Shrinkage is very stable inside the massive transversal beam.

4.3 Results during construction

Pre-stressing of the New Årsta Railway Bridge was a very complicated process and a detailed description can be seen in [2]. Fig.10 illustrates the pre-stressing steps from the 22th to the 25th of October 2003. The strain levels that were measured were around -150 to -200 microstrain in the cantilevers (Sensors: DS1, DS2, DS3 and DS4) but as high as -500 microstrain in the trough bottom (Sensor DS5) that at this stage still was lying on the formwork. The pre-stressing took place 21 days after casting. Removing of the formworks causes a positive reaction in the trough bottom that can be seen at the end of the curve in sensor DS5.

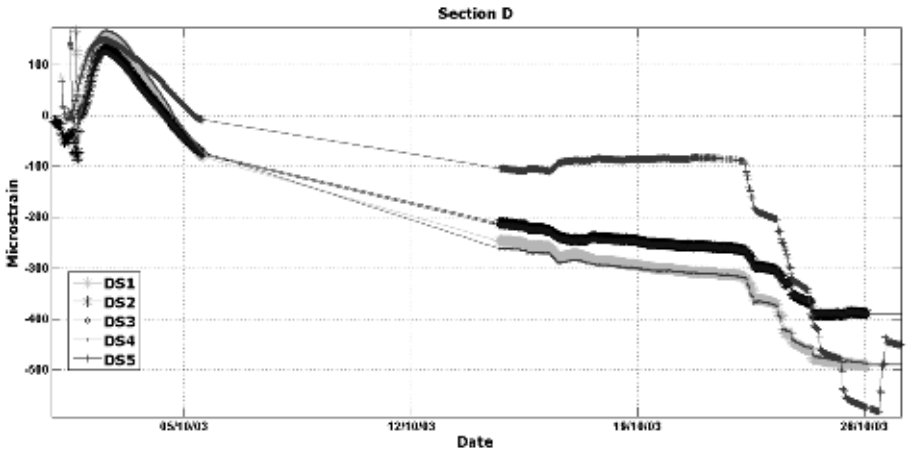

Figure 10 - Pre-stressing the concrete 21 days after casting causes high compressive strain around 500 µs in trough bottom, see sensor DS5. Straight line occurs where measurements has not been taken. Sensor DS5 in the trough bottom is also is influenced by the removal of the formworks and this can be seen at the end of the curve.

Pre-stressing causes high strain values in measured sensors. Initial strain levels correspond to initial stress of 3.6 MPa in the trough bottom and 10.8 MPa in the cantilevers. The trough reaches compressive stress level of 21.4 MPa and the cantilevers approximately 18 MPa after first pre-stressing.

SOFO sensors do provide a good tool that can be used to control complicated construction stages. A portable interrogator can be used and measurements can take place on site while the activity is ongoing. If any deviation occurs, it is noted immediately and possible damage can be prevented.

4.4 Long-term results

Long-term deformations due to shrinkage and creep are normally several times larger than elastic deformations in the concrete. Pre-stressing in tendons is reduced with time due to long-term shrinkage and creep effects. Strain-induced deflections in the spans result from the pre-stressing losses due creep and shrinkage and relaxation in the tendons. There is a need to evaluate adequate methods to predict creep and shrinkage, especially for slender pre-stressed concrete structures. It would be also favourable to measure relaxation in tendons.

The shrinkage of concrete, normally considered to be the sum of the drying and chemical shrinkage components, continues infinitely but with a decreasing rate. Shrinkage is believed to approach a final value as time come close to infinity. Shrinkage is dependent on all the factors which affect the drying of concrete; the relative humidity and temperature, the mix characteristics, the type and quantity of the binder, the water content and water to-cement ratio, the ratio of fine to coarse aggregate, and the type of aggregate, and the size and shape of the member [35]. Deformation that occurs under constant load and increases with time is called creep. Creep is dependant on at which age of the concrete the loading takes place. The earlier the loading takes place the larger is the value of the ultimate creep strain.

Detailed effects of long-term shrinkage and creep are complex to evaluate and seem to be difficult to calculate and many design models are inaccurate [36]. Gilbert [35] illustrates that shrinkage strain models may have huge error margins up to 30-40 % of the measured ones. Gilbert has proposed a simplified theory for evaluating common concrete shrinkage. Design shrinkage, ε_{cs} is a sum of both drying and chemical shrinkage at any time after the commencement of drying and may be calculated with following equation

$$\varepsilon_{cs} = \varepsilon_{csd} + \varepsilon_{cse} \quad (3)$$

where ε_{cse} is chemical shrinkage strain, ε_{csd} is drying shrinkage strain and f'_c, is the compressive strength of the concrete expressed in MPa. Table 4 shows calculated shrinkage strains for three various thicknesses proposed by Gilbert [35].

Table 4 - Simplified shrinkage strain calculations according Gilbert [35].

		Strain								
Thickness	f'_c	28 days (x 10^{-6})			1675 days (*10^{-6})			10 000 days (x 10^{-6})		
(mm)	MPa	ε_{cse}	ε_{csd}	ε_{cs}	ε_{cse}	ε_{csd}	ε_{cs}	ε_{cse}	ε_{csd}	ε_{cs}
400	42	71	96	167	76	415	491	76	461	537
1000	42	71	37	108	76	292	368	76	368	444
2000	42	71	19	91	76	227	303	76	337	413

Fig. 11 shows long-term strain curves for longitudinal SOFO sensors and Fig.12 shows long-term strain curves for transversal SOFO sensors in section A. These curves do measure total strain and both seasonal and daily variations are clearly illustrated in these figures.

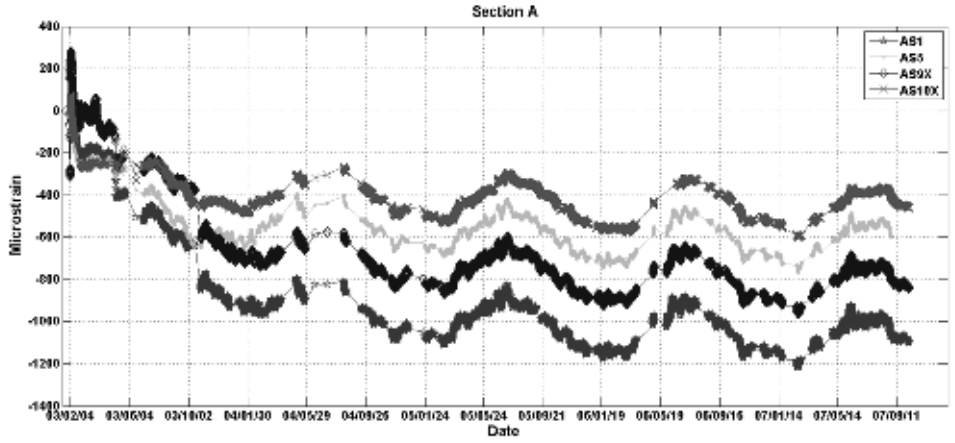

Figure 11 - Results for longitudinal sensors in section A from 2003 to the end of 2007.

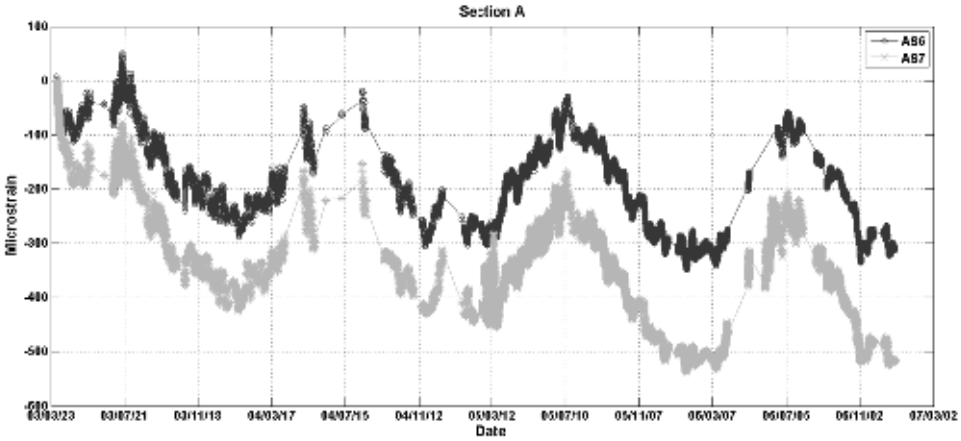

Figure 12 - Results for transversal sensors in section A from 2003 to the end of 2007.

Long-term effects like shrinkage and creep are reasons for deflection of bridges and also for relaxation in pre-stressing cables. Sensors measure total strain in the real life structure under thermal and service load. Simplified methods have shown to give pretty good results compared to FE models. Calculated shrinkage strains in Table 4 are compared to the ones in Fig.11 and Fig.12. The measured values for shrinkage comply well with the calculated ones provided that the thermal effects are extracted and excluded. The four meters long sensor AS1 reaches around -500 microstrain in compression. Results are also comparable to the ones measured by Robertson [33]. Creep values show quit low values but need to be compared to laboratory results in order to be separated from measured total strain.

In order to be able to distinguish these different components, a closer study is needed. Existing theories on shrinkage and creep models still have a large margin of error and the results from this study can be used in long-term maintenance planning of the New Årsta Railway Bridge. General conclusions can be drawn when this study is compared to several similar studies, so that a larger population of data can be compared and conclusions can be drawn. It is also recommended to instrument more general structures so that many uncertainties and special conditions can be avoided. It would also be preferable to instrument pre-stressed cabled in order to measure the real relaxation in them.

5. DISCUSSION

5.1 General

A monitoring project is a delicate matter with many different aspects that all need to be taken into account in order to be able to perform qualitative measurements. A lot of resources and time can be saved with cautious planning at the beginning of the monitoring project. Installation procedure in the field is highly important for trustworthy results and for the long-tern quality of the monitoring system, especially with fibre optic installation. Even though there is a lot of literature about the subject, the engineering society seems not able to apply this information and only the experience brings up with deeper understanding for the complexity of the subject. The purpose of this section is to highlight some important issues and help the reader to build better

SHMS as well as to avoid the mistakes. Following course of action is recommended in order to pull together the most significant issues in a SHMS project:

- Organisational issues and responsibilities are clearly stated.
- Documentation methods are decided and the whole process is carefully documented
- Firstly, desired parameters to be monitored are identified; secondly, other indirect parameters like environmental parameters that might be needed in the analysis process are also identified.
- Monitoring design with technical requirements is prepared: Responsible stakeholders need to have a sound knowledge for measuring techniques and methods in order to be able to optimise the monitoring systems as well as reduce the costs. If this expertise is lacking in the own organisation it is necessary to rely on external assistant.
- If there are any insecurities or emerging technologies involved, a Factory Acceptance Test (FAT) is prepared in order to verify that the specified technical requirements can be fulfilled with the chosen system.
- As soon as the final decision for sensor technologies, data acquisitions and data analysis tools and methods are chosen, a detailed installation and monitoring plan is prepared.
- Database requirements are stated and procedures for data handling are described in detail.
- Installation is carried out, any malfunction or deviation is reported immediately to stakeholders and solution is found. Installation diary is written and completed with photos.
- Site Acceptance Test (SAT) is performed after complete installation at the presence of stakeholders; sensors, database tools and analysis methods are tested and verified. Long-term function of the SHMS is also tested and verified.
- The first period of monitoring is also a learning period: structural behaviour of the monitored structure is studied and adjustments and refinements are completed in order to optimise the system. Alarms and warnings are set up if necessary.

5.2 Monitoring during early age and construction

Concrete is a complex material that takes time to form. In order to obtain proper measurements and data that can be analysed, following is recommended:

- Measurement should start when pouring to concrete and go on at least 28 days
- Perform strain measurements frequently meaning minimum every hour but preferably more frequently and do measure temperature of the concrete at the same frequency
- Measure environmental parameters like temperature and air humidity
- Measure every construction step like pre-stressing and removal of the formwork. If having several separated sections and only one portable interrogator, it is recommended to rent another unit or several units in order to measure all activities as this will help a lot when analysing the data. If that is not possible, it is important to evaluate the most important event to be monitored

5.3 Long-term monitoring

Monitoring produces a lot of data that need to be analysed. Concept "less is more" can be very useful as it is better has a few data that can be properly analysed that a lot of data without analysis. Large projects do need tailor made database handling but even a medium size project

like New Årsta Railway Bride produces large amount of data as the monitoring is continuous and over several years.

Irregular daily strain variation revealed cracking in the structure. Crack mapping was done on the New Årsta Bridge and confirmed that. More info can be seen in [5].

Some sensors that were temporary installed on the concrete surface and covered with steel beams were affected by sun radiation and provided unsecure results.
Measurements with traditional strain transducers are beyond the scope of this paper but can be seen in [2, 3, 5]. Many malfunction, drift and unsecure measures were noted with strain transducers, and the long-term function was also poor compared to FOSs.

Following recommendations are given based on the experience so far:

- Employment of database where statistical studies of parameters can easily be performed is preferable. The statistical methods are a good tool in revealing malfunctions in long-term monitoring.
- Statistical methods were used successfully to locate cracks and can be used to control their propagation.
- If sensors are installed on the concrete surface, they should not be exposed to solar radiation or shaded with objects that will raise the local temperature and give biased readings
- Data should be stored in compatible format for end users; this can decrease the cost of analysis fundamentally.

6. CONCLUDING REMARKS

The New Årsta Railway Bridge is not only a challenging structure but also a large research project and huge amount of data and experience are gathered over the years. Applied research with novel technology and without previous experience is really challenging and many mistakes have been made. On the other hand, a lot can be learned and it is essential to capture lessons learned in order to develop best practices and successful criteria for future projects. Advantages and improvements, concern, malfunctions and challenges experienced during the lifecycle of the project need to be to be carefully documented, analysed and evaluated.

The following conclusions are based on the results and experiences gained during the monitoring project of the New Årsta Railway Bridge:

1) This paper highlights the plentiful possibilities FOS monitoring do provide. Fibre Optic LG sensors were shown optimal to cast in concrete and do measure early age concrete behaviour, construction stage behaviour, testing of the bridge and long-term behaviour efficiently.
2) Successful SHMS includes the following; clearly stated responsibilities and careful planning in the presence of a SHM expert. In addition, fewer sensors but adequate data analysis and appropriate database management. A comprehensive study of the monitored structure is required at the beginning of the project in order to optimise and refine the procedures used in monitoring.
3) The survival rate of the SOFO sensors cast in concrete was 84 %.
4) A number of data loss was caused by the limited memory capacity of the SOFO

interrogator.

5) Monitoring revealed cracking in the concrete, confirmed also by crack mapping.
6) SOFO sensors do show stable long-term behaviour compared to traditional strain transducers that do drift, malfunction or stopped working.
7) Long-term effects like shrinkage and creep were studied. A simplified calculation can give a better estimate than a large FE model. The existing codes and models are inaccurate and need to be revised. More investigation is needed.
8) Long-term function of SOFO sensors is excellent.
9) The New Årsta Railway Bridge is a very unique structure and its influence is seen in the results of this study. Hence it is not possible to draw general conclusions. On the other hand, a huge amount of general knowledge is gained and the results can be compared to other similar structures. Results are also fundamental in the future maintenance of the New Årsta Railway Bridge.
10) Some recommendations are given and can guide the reader to build better SHMSs.

ACKNOWLEDGEMENT

People from several companies and disciplines participated in the project discussed. The author would like to thank every single person for their hard work, professionalism, and most of all; genuine interest and enthusiasm in new technologies. The project would not have been possible without your highly valuable collaboration. Special thanks go to Mr. Bo Eriksson-Vanke from Trafikverket (former Banverket) for his commitment in the project and to Professor Johan Silfwerbrand from Royal Institute of Technology (KTH) and Swedish Cement and Concrete Research Institute (CBI) for his valuable comments.

REFERENCES

1 Anger, D., "Tranebergbron. Offprint from Cement och Betong 1932-1934", Aktiebolaget Thule, Stockholm, 1935. (In Swedish)
2 Enckell, M. and Wiberg, J., "Monitoring of the New Årsta Railway Bridge. Instrumentation and preliminary results from the construction phase", Tec. Rep., 2005, Royal Institute of Technology, KTH
3 Wiberg, J. and Enckell, M., "Monitoring of the New Årsta Railway Bridge. Presentation of measured data and report on the monitoring system over the period 2003-2007", Tec. Rep., 2008, Royal Institute of Technology, KTH.
4 Wiberg, J., "Bridge Monitoring to Allow for Reliable Dynamic FE Modelling: A Case Study of the New Årsta Railway Bridge", Licentiate thesis, 2006, Royal Institute of Technology, KTH.
5 Enckell, M., "Structural Health Monitoring using Modern Sensor Technology – Long-term Monitoring of the New Årsta Railway Bridge", Licentiate thesis, 2006, Royal Institute of Technology, KTH.
6 Wiberg, J., 2009, "Railway bridge response to passing trains. Measurements and FE model updating", Dissertation, Royal Institute of Technology (KTH)
7 Udd, E., "Fiber Optic Sensors", 1991, Wiley, New York.
8 Udd, E., "Fiber optic smart structures", 1995, Wiley, New York.
9 Inaudi , D., "Fiber Optic Sensor Network for the Monitoring of Civil Structures", 1997, Dissertation, Ecole Polytechnique Federale de Lausanne (EPFL).

10 Vurpillot, S., "Analyse automatisée des systèmes de mesure de déformation pour auscultation des structures", 1999, Dissertation, Ecole Polytechnique Federale de Lausanne (EPFL).
11 Glisic, B., "Fibre optic sensors and behaviour in concrete at early age", 2000, Dissertation, Ecole Polytechnique Federale de Lausanne (EPFL).
12 Clark, P., Boriniski, J., Gunther, M., Poland, S., Wigent, D. and Watkins, S., "Modern fibre optic sensors", 2001, Smart Mater. Bull. V 2001, pp.8-11.
13 Aktan, A. E., Catbas, F. N., Grimmelsman, K. A. and Pervizpour, M., "Development of a Model Health Monitoring Guide for Major Bridges", 2001,Report, Drexel Intelligent Infrastructure and Transportation Safety Institute, USA.
14 Mufti, A., "Guidelines for structural health monitoring. ISIS Design Manual No. 2", 2001, ISIS Canada.www.isiscanada.com.
15 www.sustainablebridges.net, Website visited 4th October 2009.
16 Bergmeister, K., Aktan, A.E., Bucher, Chr., Dorfmann, L., Fehling, E., Frey, R.P., Geier, R., Huth, O., Inaudi, D., Maier, J.E., Santa, U., Schwesinger, P., Slowik, V. and Wenzel, H.," Monitoring and safety evaluation of existing concrete structures", 2003, Ceb-Fib State-of-art report, ISBN 978-2-88394-062-8.
17 Neville, A. M., "Properties of concrete" 1981, Pitman Pub. London and Marshfield, Mass., ISBN 0273016415.
18 Robertson, I. N. and Li, X., "Shrinkage and Creep Predictions Evaluated using 10-year Monitoring of the North Halawa Valley Viaduct", ACI SP-227 Shrinkage and Creep of Concrete, Editors: N.J. Gardner and Jason Weiss, American Concrete Institute, April 2005,pp. 143-162
19 Bažant, Z.P., and Li, Guang-Hua., "Comprehensive database on concrete creep and shrinkage." ACI Materials Journal. 106, 2008, pp.635-638.
20 Wu, X. and Yao, K.; "The effect analysis about creep and shrinkage for long-term deflection of long-span continuous rigid frame bridge". Electric Technology and Civil Engineering (ICETCE), 2011 International Conference. pp 2730 - 2733. Doi.10.1109/ICETCE.2011.5774695
21 Bažant, Z.P., Yu, Q., Li, G.-H., Klein, G.J., and Křístek, V. (2010), "Excessive deflections of record-span prestressed box girder: Lessons learned from the collapse of the Koror-Babeldaob Bridge in Palau." ACI Concrete International 32 (6), June, 44-52.
22 ACI Committee 209 (1972, 2008) "Prediction of creep, shrinkage and temperature effects in concrete structures" ACI-SP27, Designing for Effects of Creep, Shrinkage and Temperature, Detroit, pp. 51—93 (reapproved 2008).
23 ACI Committee 209 (2008). "Guide for Modelling and Calculating Shrinkage and Creep in Hardened Concrete." ACI Report 209.2R-08, Farmington Hills.
24 CEB-FIP Model Code 1990. "Model Code for Concrete Structures". Thomas Telford Services Ltd., London, Great Britain; also published by Committee euro-international du béton (CEB), Bulletins d'Information No. 213 and 214, Lausanne, Switzerland.
25 Draft of fib Model Code 2010. "Fédération internationale de béton (fib)." Lausanne.
26 Gardner, N.J., and Lockman, M.J. (2001) "Design provisions for drying and creep of normal-strength concrete." ACI Materials Journal, 98 (2): 159-167.
27 Standard Specifications for Design and Construction of Concrete Structures. Part I, Design. Japan Soc. of Civil Engrs. (JSCE), 1996 (in Japanese).
28 Specifications for Highway Bridges with Commentary. Part III. Concrete. Japan Road Association (JRA), 2002 (in Japanese).
29 RILEM TC 107-GCS, "Creep and shrinkage prediction model for analysis and design of concrete structures - model B3",1995, V.28 , N.180 pp.357 - 365
30 Bazant, Z. P., Yu, Q., Hubler, M. H., Kristek, V. and Bittnar, Z., "Wake-up call for

creep, myth about size effect and black holes in safety: what to improve in fib model code draft", fib Symposium Prague 2011, pp. 731-746.
31 Glisic, B., Inaudi, D., Hoong, K. C. and Lau, J. M., "Monitoring of building columns during construction", 2003, 5th Asia Pacific Structural Engineering & Construction Conference, pp. 593-606.
32 Glisic, B., Inaudi, D., Lau, J. M, Mok Y C and Ng C T., "Long-term monitoring of high-rise buildings using long-gage fiber optic sensors", 7th International conference on multi-purpose high-rise towers and tall buildings, Dubai, 2005.
33 Robertson I. N., "Prediction of vertical deflections for a long-span prestressed concrete bridge structure", 2005, Engineering structures N.27,pp.1820-1827
34 Boverket, (The National Board of Housing, Building and Planning), "Boverkets handbok om betongkonstruktioner (BBK 94), Band 1, Konstruktion", 1995, Boverket, Stockholm, Sweden. (In Swedish)
35 Gilbert, R.I., "Shrinkage, Cracking and Deflection - the Serviceability of Concrete Structures", Electronic Journal of Structural Engineering, 1, pp.15-37, 2001.
36 Fanourakis, G. C. and Ballim Y., "An assessment of the accuracy of nine design models for predicting creep in concrete". Journal of The South African Institution of Civil engineering, 2006, V. 45 4, pp.2-8.

Robust self compacting concrete for bridge construction

Peter Simonsson
Ph.D. Associated. Professor
Luleå University of Technology (LTU), Luleå
971 87 Luleå, Sweden
E-mail: Peter.Simonsson@ltu.se

Mats Emborg
Professor LTU / Head R&D Betongindustri AB
LTU, 971 87 Luleå, Sweden
Betongindustri AB 100 74 Stockholm, Sweden
E-mail: Mats.Emborg@Betongindustri.se
Mats.Emborg@ltu.se

ABSTRACT

Although Self Compacting Concrete (SCC) has many advantages over traditional vibrated concrete (TVC) its rate of adoption in cast in-situ construction is still low. To increase the use of SCC technical problems need to be solved and it is important to convince the market of all the direct and indirect benefits that can be realized by using SCC. This research aims to establish recommendations for robust mixes. Particular focus is on invariance to changes in aggregate composition and it is demonstrated that it is possible to develop robust SCC mixes that are tailored to the requirements of flowability.

Key words: SCC, flowability, robustness, aggregate moisture, viscosity modifying agent

1. INTRODUCTION

1.1 Industrial construction and SCC

Within the construction industry there is a need for improved productivity, increased profits and reduced waste creation. To increase the productivity on building sites and create more industrialized construction, it is important to study all the processes that make up a project, from start to finish. The aim is to design structures, such as bridges, that are less complicated to build and therefore easier to produce; that is, they have a high level of buildability ("the extent to which the design of a building facilitates ease of construction" [1; 2; 3]). Various definitions have fluctuated over the years; this is however the most accepted.

When managed properly, SCC is an important part of the development of an industrialized process for on-site concrete construction. If SCC is utilized properly, and if castings are planned correctly, then the use of SCC can reduce the number of workers needed during castings. The unused workers can then take on other work tasks. Thus, the total production rate will increase on construction sites whilst waste and costs are reduced [1].

However, the volume of SCC being used has not reached the level predicted around ten years ago when SCC was introduced to the market. At that time it was assumed that around 50 % of all ready-mixed concrete would be SCC within a few years. However, currently, the market share of SCC in EU nations overall is as low as about 1 % [4] but there are large variations between countries: 1 % in Finland, the Netherlands and the UK; 2% in France and Norway; 10 % in Sweden and as high as 28 % in Denmark [5; 6; 7; 8].

There are many reasons cited for not using SCC. One such reason is that SCC is more costly to manufacture than TVC and, hence, more expensive to purchase and use. Another reason might be that there, to some extent, can be variations in the consistency of the concrete when it is delivered from the manufacturers i.e. the robustness of the product is by some users considered as low. This has resulted in contractors becoming skeptical of the product and thus not using it very often.

1.2 Problem formulation and research objective

Ready mixed concrete companies find manufacturing SCC rather more complex than producing Traditional Vibrated Concrete (TVC). The product is more sensitive to variations of its constituents, and conditions when transporting the product and handling it on the site. Thus, the challenge is to control and produce a strong, reliable product when casting in any situation.

Moreover, for civil engineering applications in Sweden, there is often only one type of SCC offered. There is a question mark over whether this is really what the customer is asking for. To increase the use of SCC and realize its potential benefits, the contractor needs to become more engaged in the whole process. The contractor should specify their own criteria for the product, taking into consideration pouring methods, section geometry, weather conditions etc. The above can be formulated into the following research questions:

- How should SCC be adapted to deal with different structural parts and casting conditions?
- Is it possible to develop robust solutions by using adapted SCC?

The overall objective of this research is to increase the use of SCC. This goal is achieved when the concrete used is that best suited the project of interest. It is aimed at establishing a formula for robust mixes, based on specifications from contractors. We focus particularly on invariance to changes in aggregate composition such as moisture, grading etc.

2 SCC

2.1 General

According to international findings, SCC is on the cutting edge of scientific and technological developments [5]; [9] and it is essential to introduce the technique in a broader manner to cast in-situ concrete construction. The elimination of compaction work was one of the major factors triggering the development of SCC in Japan in the 1980s, where they had difficulties in finding

workers to perform compaction work to a suitably high standard [10; 11; 7]. This was also verified, by De Schutter et al. [12] that stated that the development of SCC has led to considerable improvements in the working environment, and also in the global environment, since there is lower energy consumption during casting. In addition, the level of noise and disturbance to surrounding areas is less since the sound of the vibrating equipment is eliminated.

The lack of quality assurance of concrete performance is considered to be one obstacle when marketing and using SCC. The performance of the product, according to the EU project 'Testing SCC' [13], can be characterized using three main parameters: filling ability, passing ability and segregation proneness. For these parameters, it could be possible to establish acceptance criteria that are dependent on the geometry of the structure to be cast, form type, reinforcement, and the method and/or local tradition applied to the pouring of the concrete. For instance, Walraven [14] suggested nine consistency classes described by factors such as workability tests (see Figure 1).

In the Nordic Countries, similar procedures have been suggested. In Denmark, three classes of plastic viscosity and yield stress have been established, based on certain rheology tests [15]. A workability diagram (slump flow vs. T50 time) is another base for the definition of flowability with regard to the type of structure, geometry and reinforcement, see Figure 2, [16; 8]. The effects of either excessively high slump flow or excessively low T50 are clearly shown and an area corresponding to usable SCC can be established.

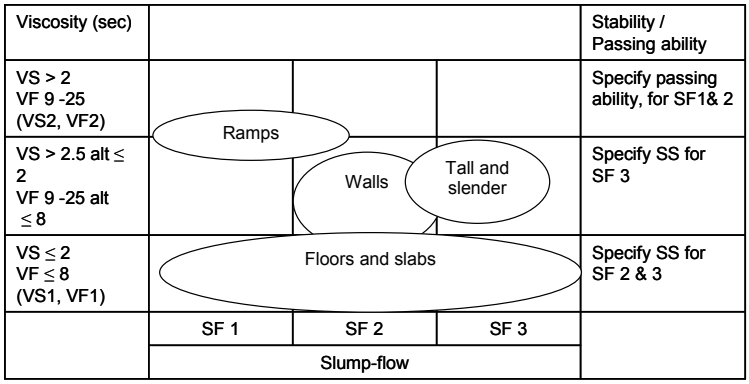

Fig. 1. Properties of SCC for various types of applications [14; 4]. VS is T50 flow time, VF is V-funnel flow time and SS is segregation index, see Testing SCC [13].

Two sets of slump flow and T50 data are shown in Figure 2: SCC-a is adapted for vertical parts of a bridge e.g. front wall and column, where a more flow able concrete that exhibits low risk of blocking, improved quality surfaces (besides other influencing factors i.e. formwork, form oil) and low input of resources is required. SCC-b is designed for horizontal elements e.g. bridge deck and foundations, where a stiffer concrete is a better choice, creating opportunities for a controlled casting front etc. Together with the target values of slump flow and T50 flow time, maximum variances are established; +/-40 mm and 0.5 s respectively, thus forming a acceptance criteria for quality control at construction site.

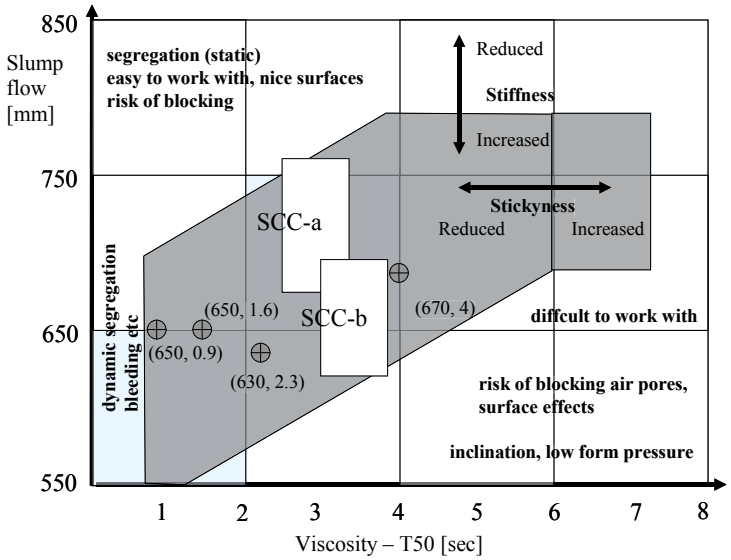

Fig. 2. Workability diagram (slump flow vs. T50). Concrete targeted for use in civil engineering structures. Suggestion for two types of adapted concrete, SCC-a and SCC-b (target values) 720 mm +/- 40 mm, 3s +/- 0.5s and 650 mm +/- 40 mm, 3.5 +/-0.5 s respectively. Effects of excessively high/low values are also shown as well as an example of performance of some Swedish commercial SCC (modified from Emborg, [16]).

2.2 Mix design

Several philosophies regarding mix design of SCC can be found in the literature. Some methods, such as the LCPC Compressive Packing Method [17] and the CBI method [18]; [19], use the air voids of the aggregate to achieve optimum packing using aggregates with different grading curves and volumes of cement paste. Other methods are based on rheological testing as an integral part of the mix development process [20]. According to Utsi [21], there are a number of factors that have complex interactions with each other, all of which need to be addressed by the mix-design.

De Schutter et al. [12] argued that SCC can be designed to produce a wide range of properties and that it is possible to establish an initial estimate of mix proportions by considering typical previously successful mixes – in fact, this does not use the methods mentioned above.

The use of Viscosity Modifying Agents (VMAs) in SCC is not a new phenomenon and it is becoming more common. The VMA is used to stabilize the properties of the fresh concrete by modifying the rheological properties of the cement paste [22]; [4]; [23]; [24]; [25]. The intention of introducing VMA is to reduce the powder content and to make the concrete less sensitive to changes in the component materials.

2.3 Test methods

Although several test methods exist for SCC e.g. slump-flow, T50, V-funnel, L-box and J-ring to name but a few (see Table 1), there is no universally accepted standard developed for them. Hence, it is sometimes difficult to obtain reliable and comparable data; this is clearly an obstacle to the further development of this particular type of concrete [12].

Traditionally, SCC is characterized using the slump-flow and T50 tests to classify the concrete on the building site. In the laboratory, when establishing mix design, rheological parameters (yield stress and plastic viscosity) can also be utilized to give a more detailed description of the SCC by e. g. using the ConTec viscometer [26] The workability and rheology tests methods can to some extent be related to each other as shown in various studies, see e.g. [13]; [26].

Table 1. Test methods for SCC according to [13] and [4].

Characteristic	Test method	Measured value
Flowability / filling ability	Slump-flow	Total spread
	Kajima box	Visual filling
Viscosity / flowability	T50	Flow time
	V-funnel	Flow time
	O-funnel	Flow time
	Orimet	Flow time
Passing ability	L-box	Passing ratio
	U-box	Height difference
	J-ring	Step height, total flow
	Kajima box	Visual passing ability
Segregation resistance	Penetration	Depth
	Sieve segregation	Percent laitance
	Settlement column	Segregation ratio

2.4 Robustness of SCC

According to Taguchi [27], robustness is generally defined as insensitivity to disturbance. For SCC, this disturbance can manifest itself in the form of variations in the properties of the constituents of the concrete, variations that happen because of the mixing procedure and the conditions of transport. Thus, one important feature of SCC is the ability to maintain its fresh properties during the casting of a single batch or multiple batches [13]. In the European guidelines for SCC [4] it is mentioned that a well designed and robust SCC can typically tolerate a variation of 5-10 liters/m^3 in mix water content, which in practice is about 3-6 % of the total water content per m^3. To develop a robust concrete mix is as important for obtaining a successful result as it is complex to accomplish. Both theoretical analysis (by means of packing theories etc.) and laboratory tests on cement paste, mortar and/or concrete are required in order to design reliable robust mixes, [28].

3. RESEARCH

3.1 Mix composition and test procedure

The experimental program was divided into three test series each examining different concrete mixes for use on some full scale bridge construction in Sweden. The mixing procedure remained the same for all the series (see Table 2) and the properties of the fresh concrete were documented by means of visual inspection, workability and rheology tests (slump flow and ConTec viscometer [26]). The visual inspection focused on how the concrete "felt" while working with it e.g. if there were any tendencies for segregation or if it felt homogenous.

Table 2. Mixing procedure at laboratory tests.

Step	Activity	Duration [s]
1	Dry mixing of aggregate, cement and filler	60
2	Adding of water	20
3	Adding of chemical additives (SP, air, VMA)	20
4	Mixing of all ingredients	200

Generally all concretes are pre-tested with regard to frost resistant i. e. designed for environmentally class XF4 with air content of 5 – 10 %. Concrete SCC 1 was used in a demonstration project in the north of Sweden where industrial construction was studied. After finalizing the project, the concrete was analyzed for its sensitivity to certain quantity of water addition. The point with this is to simulate the change in sand moisture during concrete production, at the ready mix plant. Reference mix composition was thus adjusted by combinations of filler content and grading curve. As a continuation, another concrete, SCC 2, was designed to fulfill the criteria, but used another aggregate type and a slightly different recipe. Target values (slump flow and T50) for the concretes were 720 mm and 3 s respectively (see Figure 2).

Test Series 2 examined the robustness of three characteristic concrete mixture compositions used in central Sweden (Norrköping, Linköping and Stockholm area), these being SCC 3 – SCC 5 (see Table 3). Laboratory tests were performed both in the University laboratory and also in the local RMC plant laboratories.

Series 3 tested concretes SCC 6 and SCC 7, which were designed for bridge deck construction and had a target slump flow and a T50 of 650 mm +/- 40 mm and 3.5 s +/- 0.5 s respectively. Series 3 also tested SCC 8 which was designed for front wall and other vertical sections i.e. a slump flow of 720 mm +/- 40 mm and a T50 of 3.0 s +/- 0.5 s, according to the criteria suggested in Figure 3. Reference mix compositions were adjusted by combinations of filler content and VMA (see Table 3). Insensitivity to sand moisture content changes, without the compensation that would happen in an RMC plant, was studied by varying the water content in the mix, as in earlier tests. SCC 6 was used throughout areas of Stockholm while mix SCC 7 was manufactured at a RMC plant 200 km north of Stockholm. Thus, it used material from another aggregate pit.

Table 3. Mix composition in laboratory tests.

	Series 1 SCC 1	Series 1 SCC 2	Series 2 SCC 3	Series 2 SCC 4	Series 2 SCC 5	Series 3 SCC 6	Series 3 SCC 7	Series 3 SCC 8
Std Portland cement [1] [kg]	450	430	430	420	430	430	400	430
Water [kg]	175	178	185	168	178	178	160	172
w/c [-]	0.38	0.40	0.43	0.40	0.40	0.40	0,40	0.40
Sand[2] 0 - 8mm [kg]	1016 varied	990	846[3]	902	990	1020	937	1020
Gravel[2] 8 - 16mm [kg]	542	595	813	680	595	589	664	589
limestone fill [4] ref. content [kg]	122 varied	130 varied	170 varied	170 varied	160 varied	100 varied	153 varied	140 varied
SP [% of C]	0.65% EVO26	1.8% Sikament 56	1.5% CemFlux Bro	1.7% CemFlux Bro	1.8% Sikament 56	0.7% Sikament 56	0.88 Glenium51	0.8% N a
WMA Sika Stab 4 R	0	0	0	0	0	varied	varied	varied
Target;.SF T50 [mm]	720 3	720 3	720 3	720 3	720 3	650 3.5	650 3.5	720 3
Air entr agent Microair [%]	0.023% of C	0.19%	0.06%	0.06%	0.19%	0.05%	0.04%	0.05%

1) Standard Portland Type I, 42,5 N MH/SR/LA, Degerhamn, Cementa 2) Local aggregate are used, different in all mixes 3) 0 – 4 mm, 4) Limestone filler, Limus 40, Nordkalk, Sweden,

3.2 Results

Figures 3 to 12 present the results from the test series visualizing slump flow, T50 flow time, yield stress, plastic viscosity and, in some cases, V-funnel flow time in relation to the corresponding sand moisture change. The relationship between different test methods is also shown in Figure 4.

For Test Series 1, it can be seen that the reference concrete mix SCC 1 is too stiff when compared to the criteria (slump flow = 720 mm, T50 = 3 s) if the moisture is varied (Figure 3). The flow (i.e. the stiffness) is rather sensitive to moisture variations especially when the water content is reduced. On the other hand, the stickiness, i.e. the viscosity registered by T50, is too low. This performance may lead to segregation of the concrete. A reduction of the filler content leads to a more insensitive mix with regard to slump flow, however, at the cost of an even lower viscosity and therefore probably too large a risk of segregation on the building site. On the other hand, it can be noted that no segregation was observed by the visual inspection in the laboratory. Increase of filler content to 160 kg/m^3 indicates a controlled viscosity but at the same time the stiffness is too high i.e. the slump flow was some 100 mm lower than intended. From the tests can also be seen that the grading curve has a crucial impact on the properties. A coarser grading curve compared to the reference mix leads, as expected, to a very flow able concrete with T50

times less than 1 second, which is very unusual for Swedish civil engineering concretes; a finer grading curve indicates a very stiff concrete.

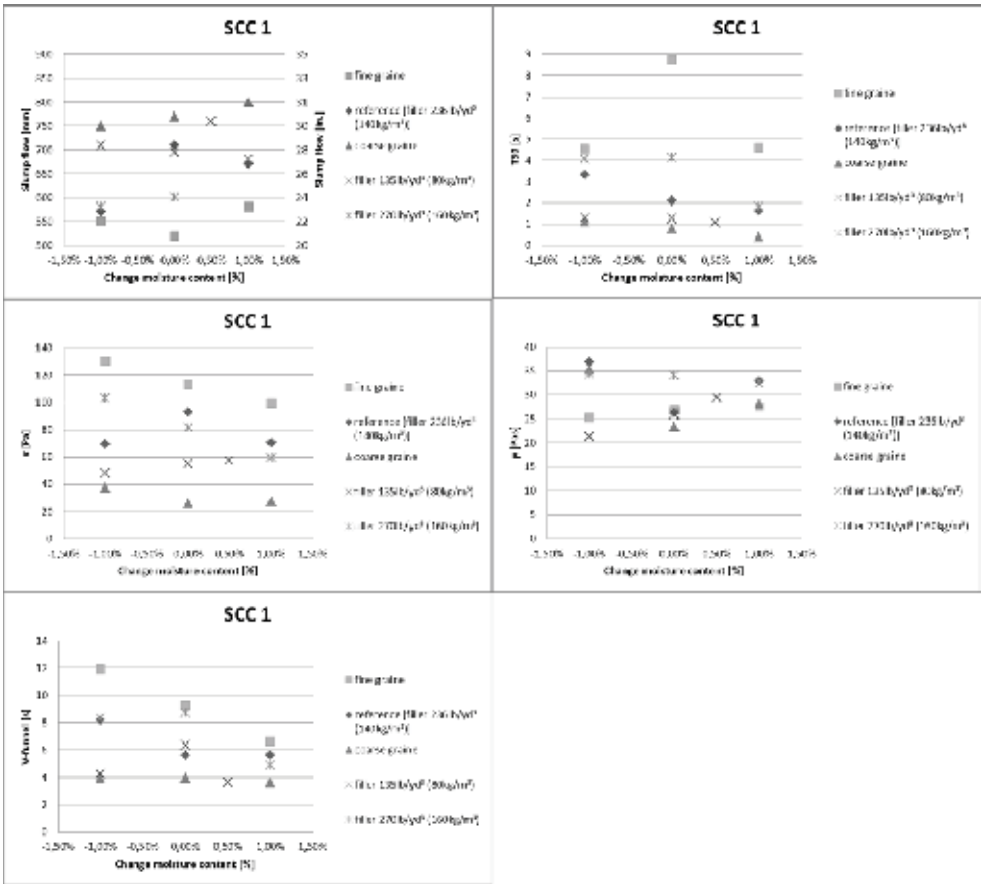

Fig. 3. Influences in Test Series 1 on the workability (slump flow, T50, V-funnel flow time) and rheology (yield stress, τ in ConTec 3 viscometer tests) of sand moisture variations, variations of filler content and grading curve. Concrete SCC 1, w/c=0.40, reference limestone filler content: 120 kg/m^3 (see Table 3). Note that the divergence of T50, fine grain, and reference moisture is probably due to an unsuccessful test.

Regarding the rheological parameters documented, it can be stated that the yield stress exhibits, to some extent, the same tendencies as the slump flow, maybe with a larger exactness (see Figure 3). In addition, the plastic viscosity exhibits similar responses to moisture changes as the slump flow. Figure 4 show the relationship between workability and rheology and supports observations such as the fact that yield stress in general, although with a rather large scatter, appears to be related to the slump flow. Furthermore, as can be seen in the figure, the V-funnel and T50 test methods complement each other to some degree.

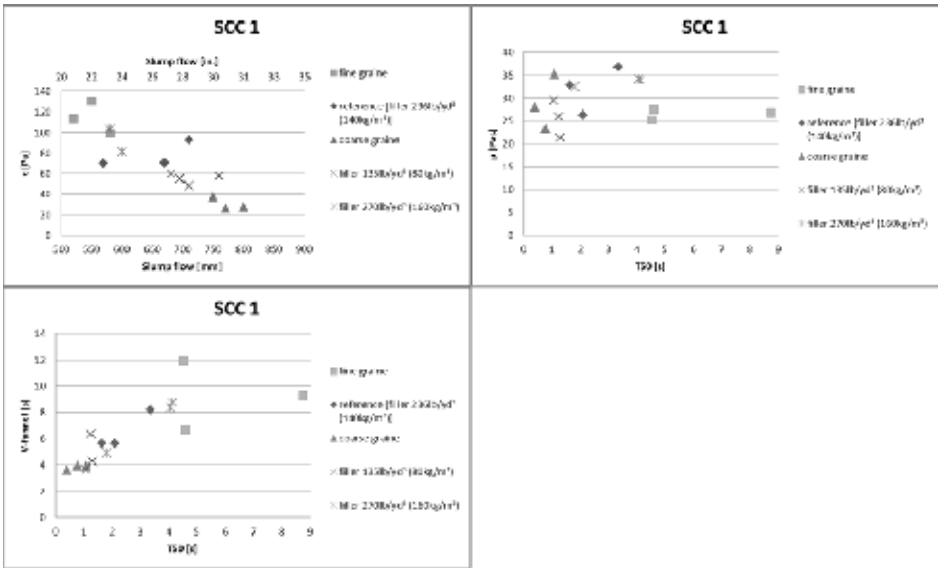

Fig. 4. Correlation in Test Series 1 between yield stress with plastic viscosity and slump flow and T50 time respectively, as well as between V-funnel and T50 times, for concrete SCC 1, see Figure 3.

For SCC 2 in Test Series 1, the influence on T50 and plastic viscosity is smaller for moisture variation when compared to SCC 1 (see Figure 5), i.e. a more robust mix is achieved. However, the concrete is too stiff, thus not meeting the criteria shown in Figure 2, and the viscosity is too low i.e. the risk of segregation is obvious. Surprisingly, both an increase and decrease of filler content leads to a more flowable material without affecting the T50 time. Furthermore, it should be noted that the influence of moisture change is more pronounced when studying the plastic viscosity than with respect to T50 time.

In Test Series 2 with mix SCC 3, reducing the limestone filler content is not a successful method of achieving an acceptable flowability that meets the specified criteria (see Figure 6). The filler content 140 kg/m^3 appears to be below the optimum level, with low flowability both in respect of slump flow and T50. The 170 kg/m^3 filler concrete behaved rather well in the tests. The concrete with low filler content (110 kg/m^3) may be combined with VMA in future tests; the test with low filler content and wet sand should be checked as this combination gave unreliable test results.

These findings are also supported by the rheological testing, in which sufficiently low values were obtained for yield stress and plastic viscosity of the reference and low filler concretes i.e. values below 100 Pa and 60 – 70 Pas respectively, with the exception of the test with low filler concrete for high moisture content.

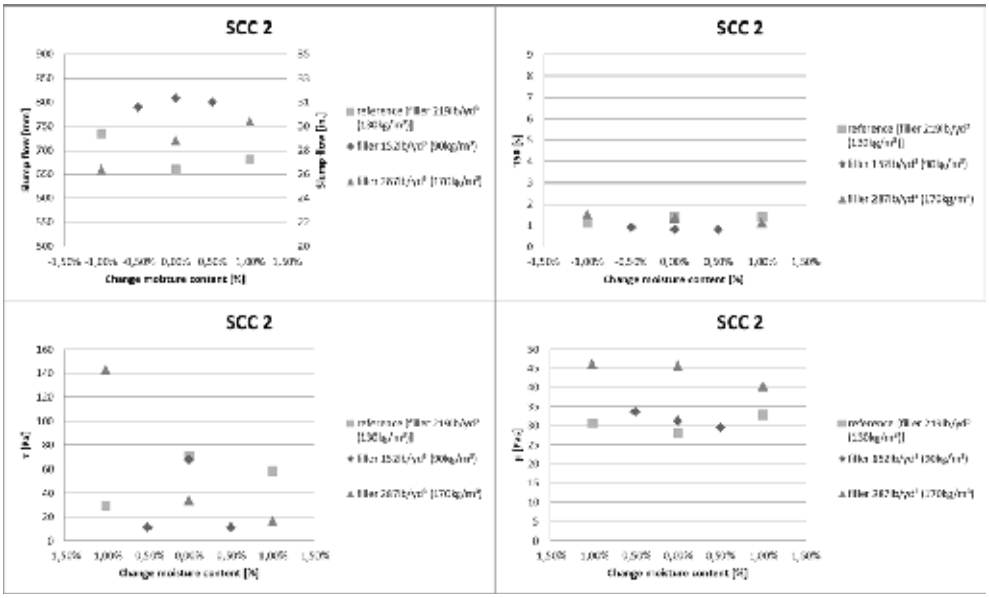

Fig. 5. Influences in Test Series 1 on the workability (slump flow, T50, V-funnel flow time) and rheology (yield stress, τ in ConTec 3 viscometer tests) of sand moisture variations and variations of filler content. Concrete SCC 2, w/c=0.40, reference limestone filler content: 130 kg/m³ (see Table 3).

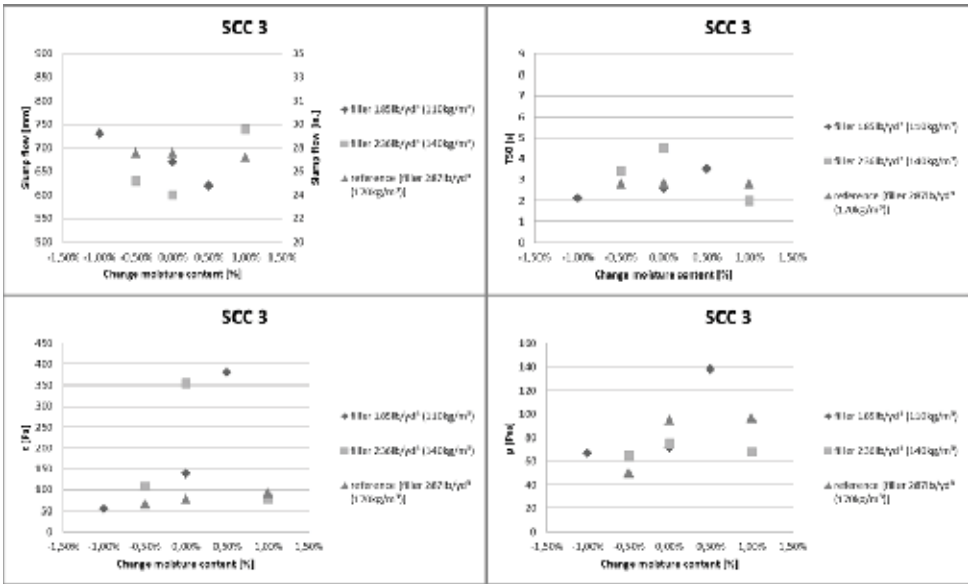

Fig. 6. Influences in Test Series 2 on the workability (slump flow, T50 flow time) and rheology (yield stress, τ in ConTec 3 viscometer tests) of sand moisture variations and variation of filler content. Concrete SCC 3, w/c=0.43, reference limestone filler content: 170 kg/m³ (see Table 3).

Clearly, concrete SCC 4 used in Test Series 2 is more robust with respect to moisture changes compared to SCC 3, and easily fulfills the criteria mentioned earlier (see Figure 7). Here, a reduction of limestone filler content to 110 kg/m^3 is appropriate to produce a mix that works well, with enough large slump flow still remaining stable, indicated by the sufficiently high viscosity as measured by T50 and by a rheometer test. It can be noted that tests at the actual RMC plant to some extent supported the results (see Figure 8). However, the sensitivity of slump flow with the low filler mixture against moisture variation was somewhat larger. More limited tests were performed for concrete SCC 5 with a reduction of filler content from the reference 170 kg/m^3, showing that a filler content of 130 kg/m^3 seems to be an optimum solution with regard to flowability and robustness (see Figure 9). Concrete that is far too stiff and sticky is obtained when there is too great a reduction in filler content; this is especially true for a dry mix. Test Series 2 suggests that local production conditions, thus with local aggregates used, have an important effect on the performance that cannot be underestimated.

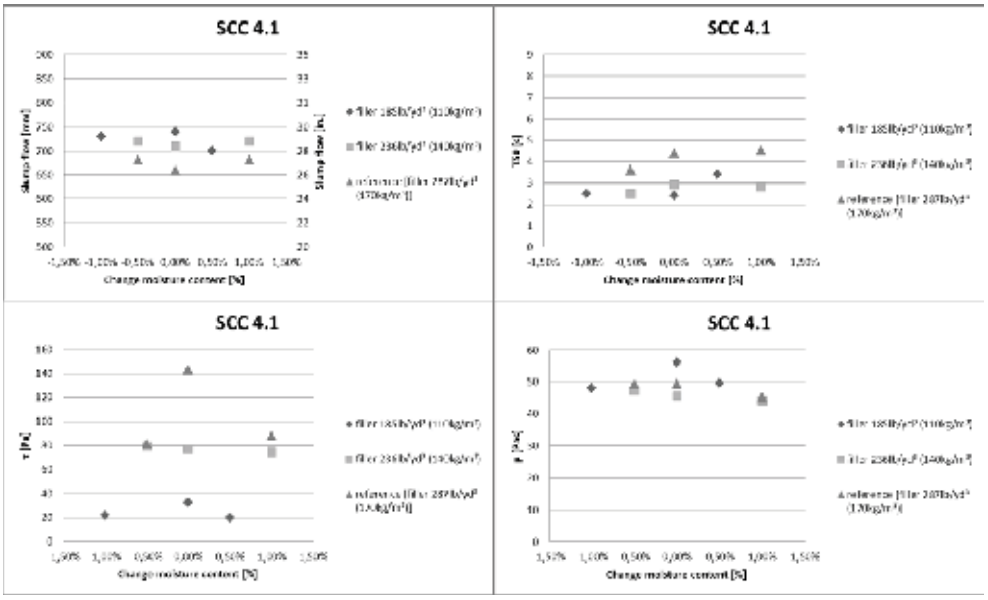

Fig. 7. Influences in Test Series 2 on workability (slump flow, T50 flow time) and rheology (yield stress, τ in ConTec 3 viscometer tests) of sand moisture variations and variations of filler content. Concrete SCC 4, w/c=0.40, reference limestone filler content: 170 kg/m^3 (see Table 3).

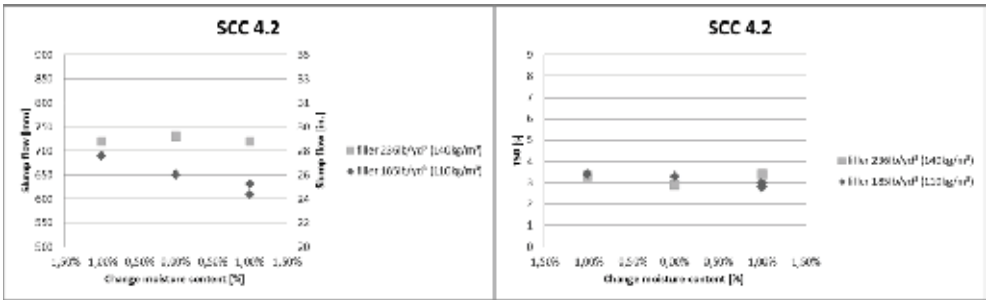

Fig. 8. Influences in Test Series 2 on workability (slump flow, T50 flow time) of moisture variations of fine aggregate and variation of filler content using concrete SCC 4 (see Table 3). Tests at RMC plant laboratory with low filler combinations as shown in Figure 7.

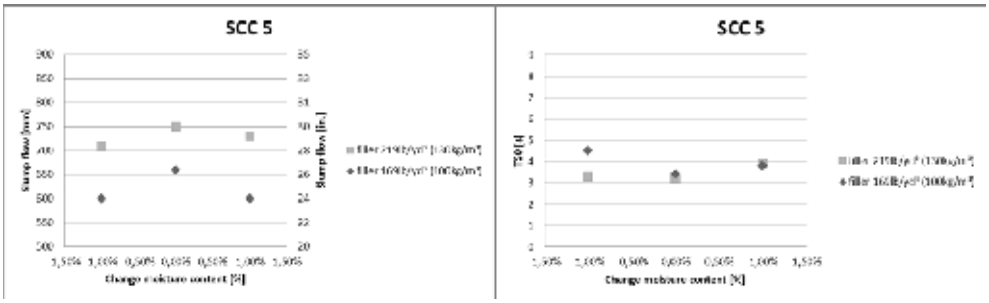

Fig. 9. Influences in Test Series 2 on workability (slump flow, T50 flow time) of sand moisture variations and reduction of filler content. Concrete SCC 5, w/c=0.40, reduction reference limestone filler content: 170 kg/m^3 (see Table 3). Tests carried out in an RMC plant laboratory.

When testing mix SCC 6 of Test Series 3, which is a concrete with a target slump flow of 650 mm +/- 40mm and T50 of 3.5 s +/- 0.5 s, some difficulties arose in achieving insensitivity to water content variations, especially for high filler content and dry concrete (see Figure 10). Filler reduction had a detrimental effect on the concrete flow with excessive sensitivity to sand moisture variations. Adding a viscosity modifying agent to the mix evidently increased the robustness; yielding values more or less within the limits (see the figure). In fact, it seems possible to exclude the filler by adding an appropriate volume of VMA.

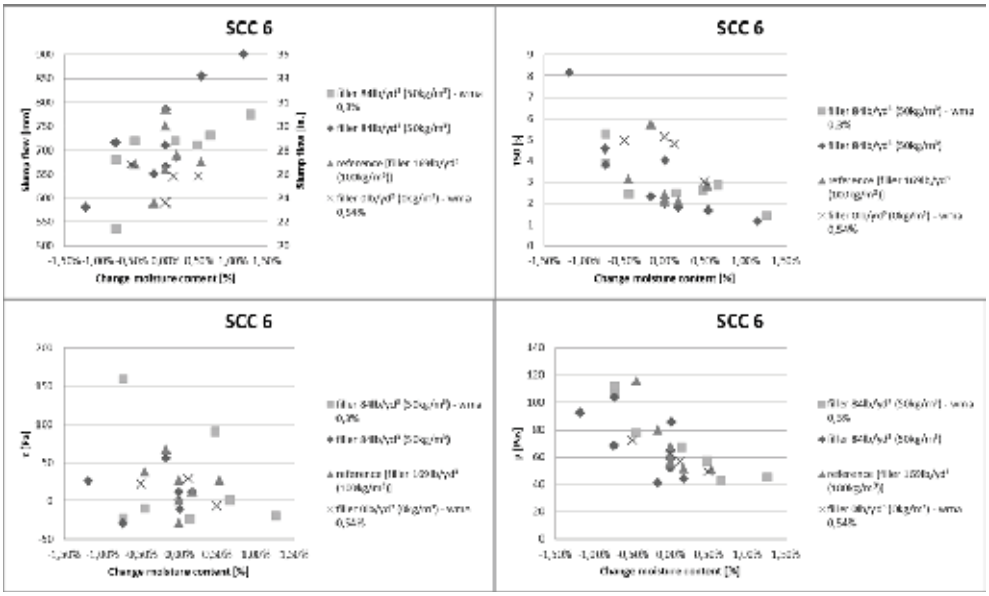

Fig. 10. Influences in Test Series 3 on workability (slump flow, T50 flow time) and rheology (yield stress, τ in ConTec 3 viscometer tests) of sand moisture variations and reduction of filler content. Concrete SCC 6, w/c=0.40, reference limestone filler content: 100 kg/m³ (see Table 3).

Concrete SCC 7, which also had a target slump flow of 650 mm +/- 40 mm and T50 of 3.5 s, was rather sensitive to moisture variations, this was observed both in the workability and rheology tests (see Figure 11). The viscosity of this concrete was far too high during all the tests but this viscosity was, surprisingly, not affected by the addition of VMA. In further tests it is planned to reduce the filler content and optimize the VMA content.

Finally, some limit tests with rather small moisture variations were performed on concrete SCC 8, which aims for a slump flow of 720 mm +/- 40 mm and a T50 of 3.0 s +/- 0.5 s, see Figure 12. The concrete seems to be rather stable when varying water content as well as the contents of both filler and VMA. With VMA and no filler, the concrete still 'felt' and appeared very good, and from the authors' points of view, the SCC would have been accepted on a construction site.

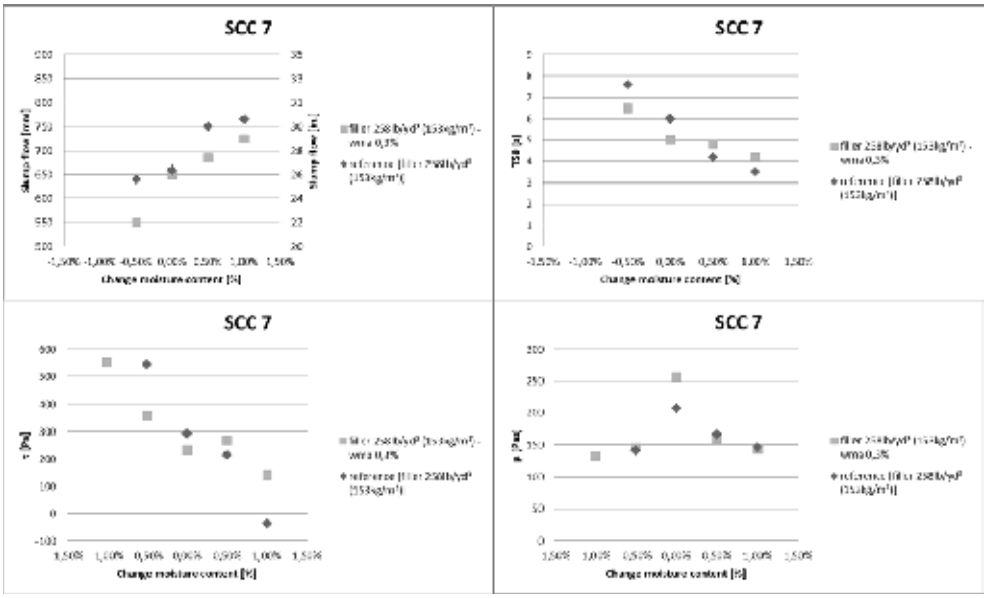

Fig. 11. Influences in Test Series 4 on workability (slump flow, T50, V-funnel flow time) and rheology (yield stress, τ in ConTec 3 viscometer tests) of sand moisture variations. Concrete SCC 7, w/c=0.40, reference limestone filler content: 153 kg/m^3 (see Table 3).

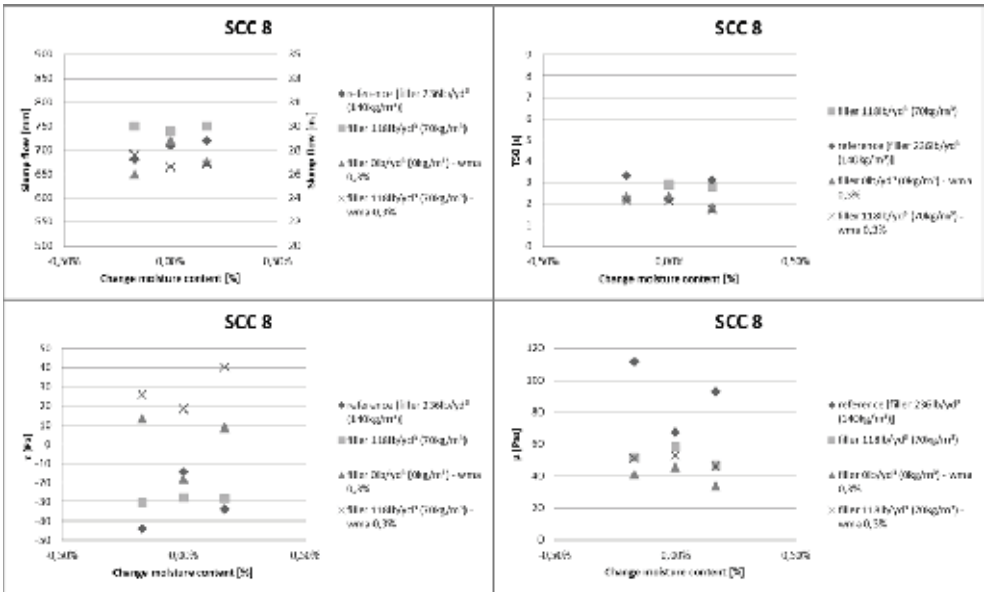

Fig. 12. Influences in Test Series 3 on workability (slump flow, T50, V-funnel flow time) and rheology (yield stress, τ in ConTec 3 viscometer tests) of sand moisture variations and reduction of filler content. Concrete SCC 7, w/c=0.40, reference limestone filler content: 100 kg/m^3 (see Table 3).

4. DISCUSSION AND GENERAL CONCLUSIONS

Based on the results from the laboratory studies, the following observations can be made:

- Reference concrete mixes with proportions determined by the local aggregate, use of additives, manufacturing tradition and various criteria from both contractors and clients in Sweden all seem to be rather insensitive to the variation in aggregate (sand moisture and grading in some cases). This can be explained by a rather high volume of fines (cement paste and filler < 0.125 mm), traditionally used in Sweden for self compacting concrete applied for civil engineering structures.
- Reduction of filler content sometimes results in a degradation in the quality of fresh concrete, especially when contents of say are reduced by more than 50 % of their original level. It is the viscosity (expressed by the parameters T50 or plastic viscosity) that is most influenced.
- Various mix design philosophies such as the use of different aggregates used to obtain the same concrete quality (grade, water content etc.), have an obvious influence on the robustness when the water content (simulated as sand moisture) is varied. The local conditions at the RMC plant have an important effect.
- It seems to be possible to establish mixes for civil engineering purposes without any limestone filler, or similar additive, by the use of a viscosity modifying agent (VMA).
- However, it is thus important that the influence of varying aggregate moisture (and other parameters) is clearly documented for conditions at each RMC plant.

Other studies show a similar influence of VMAs on the general behavior of fresh concrete and especially on its robustness. For instance, in an ongoing Swedish research project, the effect of VMA is being documented for a concrete that is designed for housing, a different mix composition and cement type from those studied in this thesis [25]. It is stated that the incorporation of VMA can increase the robustness of the tested when using sand with varying moisture content; however, this does depend on the type of VMA being used.

Based on their experience, the authors believe that the utilization of SCC in on-site production can be increased considerably. This could happen through better marketing of the concrete, and by educating and making contractors aware of its benefits such as productivity increases, lower costs and faster construction of projects. It is important to consider SCC as a method rather than "just" a building material.

However, there is no room for mistakes when using SCC in a full scale project. An unsuccessful project will create far more skepticism among the users than a successful project would create confidence. Hence, it is important to be focused on all the issues when producing and casting SCC, and it is very important that the product is robust enough.

As a final comment this research demonstrates that a robust SCC, that is not too expensive, can be achieved by reducing the filler content and using VMA instead, without impairing the quality of the product. The concrete mixes studied were robust enough such that their original mixture only needed slight modification. For example, it would be possible to substitute some of the filler (at least 50 % of the original amount) for VMA without compromising the quality of the concrete and hence the quality of any structures built using it. Some of the modified mixes, however, need more testing in the laboratory before they can be used in full scale construction.

REFERENCES

[1] Simonsson, P. (2011). Buildability of concrete structures, Processes, Methods and Material. Doctoral thesis, 2011. Luleå University of Technology, Luleå, Sweden.ISBN: 978-91-7439-243-2. http://pure.ltu.se/portal/sv/publications/buildability-of-concrete-structures(19ad8a36-e956-4023-afa1-5d9e88db643c).html.

[2] Adams, S. (1989). *Practical buildability*. Butterworths, London, UK. ISBN 0-408-03525-0.

[3] Ray, S.S., Barr, J. and Clark, L. (1996). *Bridges - design for improved buildability*. CIRIA Report 155, Westminster, London, UK.

[4] ERMCO., (2005). "The European Guidelines for Self Compacting Concrete, specification, production and use," BIBM, CEMBUREA, EFCA, ERNARC, 68 pp.

[5] Cussigh, F. (2007). SCC in practice: opportunities and bottlenecks. *5th international RILEM symposium on SCC*, 3-5 Sept., Ghent, Belgium, pp 21-27.

[6] Hammer, T. A. (2008). "Specification and Compliance Criteria for SCC – The Norwegian Procedure", Proceeding of the 3rd ASTM conference on Self-Consolidating Concrete, Chicago, 2008, pp 143 – 1501.

[7] Nagataki, S., Kawai, T. and Fujiwara, H. (2010), State of the Art Report on SCC in Japan", Proceedings from the 6th international RILEM symposium on Design, Production and Placement of SCC, Sept 26-29 2010, Montreal. 23 pp.

[8] Emborg, M. and Simonsson, P. (2010). "Increasing the market share of SCC, Concrete Plant International, No 6, 2010, pp 218– 222.

[9] Shah, S.P., Ferron, R.P., Ferrara, L., Tregger, N. and Kwon, S. (2007). "Research on SCC: some emerging themes,"5th international RILEM symposium on SCC 3-5 Sept 2007, Ghent. pp 3-14.

[10]Okamura, H. and Ozawa, K. (1995). "Mix design for self-compacting concrete," Concrete Library of JSCE, No 25, pp 107-120, June 1995.

[11]Ouchi, M., Edamatsu, Y., Ozawa, K. and Okamura, H. (1999). "A simple evaluation method for interaction between coarse aggregate and mortar´s particles in self-compacting concrete," Transaction of the Japan Concrete Institute, Vol 21, 1999, pp 1-6.

[12]De Schutter, G., Barthos, P.J.M., Domone, P. and Gibbs, J. (2008). *Self-Compacting Concrete*. CRC Press, Taylor & Francis Group, Boca Roton, USA. ISBN 978-1-4200-6833-7.

[13]Testing SCC., (2004). "Technical report of the Growth project: Testing SCC Measurement of properties of fresh self-compacting concrete, 2001 – 2004," Coordinator ACM Centre, Univ. of Paisley, UK CONTRACT N° G6RD-CT-2001-00580, 66 pp.

[14]Walraven, J. (2003). "Structural aspects of self compacting concrete," 3rd international RILEM Symposium on SCC 2003, Reykjavik, pp 15-22.

[15]Thrane, L.N., Nielsen, C.V., Pade, C., Glavind, M. and Schou, J. (2008). "Successful in-situ casting with SCC – from an economical and rheological point of view," Proceeding of the 3rd ASTM conference on Self-Consolidating Concrete, Chicago.

[16]Emborg, M. (2008). "How to increase the market of SCC – experiences from Nordic Countries", Proceeding of the 3rd ASTM conference on Self-Consolidating Concrete, Chicago.

[17]Sedran, T. and de Larrard, F. (1999). "Optimization of self-compacting concrete thanks to packing model," In: Proceedings of first international RILEM Symposium on Self-

Compacting Concrete, Stockholm, Sweden, September 1999, RILEM Publication Cachan France, pp 321-332.

[18]Petersson, Ö., Billberg, P. and Van, B.K. (1996). "A model for self-compacting concrete," In; Bartos P J M, Marrs D L and Cleland D J (Eds) Proceedings of RILEM International Conf on Production Methods and Workability of Fresh Concrete, Paisley, June 1996, E&F Spon, London, UK, pp 484- 492.

[19]Petersson, Ö. and Billberg, P. (1999). "Investigation on blocking of self-compacting concrete with different maximum aggregate size and use of viscosity agent instead of filler," In: Proceedings of First International RILEM Symposium on Self-compacting Concrete, Stockholm, Sweden, September 1999, RILEM Cachan, France, pp 333-344.

[20]Wallevik, O.H. and Nielsson, I. (1998). "Self-compacting concrete – a rheological approach," In: Proceedings of International Workshop on Self-compacting Concrete, August 1998, Kochi, Japan, pp 136-159.

[21]Utsi, S. (2008). "Performance based concrete mix-design : aggregate and micro mortar optimization applied on self-compacting concrete containing fly ash," Division of Structural Engineering, Luleå University of Technology, Doctoral thesis 2008:49, 214 pp.

[22]Nanthagopalan, P. and Santhanam, M. (2010). "A new empirical test method for the optimisation of viscosity modifying agent dosage in self-compacting concrete". Materials and Structures, No 43 pp 203-212.

[23]Khayat, K. (1998). "Viscosity-Enhancing Admixtures for Cement-Based Materials – An Overview", Cement and Concrete Composites, Elsevier Science Ltd, No 20, pp 171- 188.

[24]Khayat, K., Hwang S-D. and Belaid, K. (2010). "Performance of Cast-in-Place Self-Consolidating Concrete Made with Various Types of Viscosity-Enhancing Admixtures", Technical Paper, ACI Materials Journal, July-August, pp 403 - 412.

[25]Billberg, P. and Westerholm, M. (2008). "Robustness of fresh VMA-modified SCC to varying aggregate moisture," Nordic Concrete Research No 38, 2/2008, The Nordic Concrete Federation, pp 113- 131.

[26]Wallevik, O. (2003). "Rheology - a scientific approach to develop self-compacting concrete. International RILEM Symposium on Self-Compacting Concrete," (O. Wallevik and I. Nielsson editors), Reykjavik, Aug 2003, pp 23 – 31.

[27]Taguchi, G. (2000). "Robust engineering, Subir Chowdhury", Shin Taguchi ISBN 0-07-134782-8.

[28]Emborg, M., Jonasson, J-E., Nilsson, M., Utsi, S. and Simonsson, P. (2005). "Designing robust SCC for industrial construction with cast in place concrete," 4th International Rilem Symposium, Chicago, pp 1251-1259.

Effects of Surface Reinforcement on Bearing Capacity of Concrete with Anchor Bolts

Martin Nilsson
Ph.D.
Division of Structural and Construction Engineering
Luleå University of Technology
SE-971 87 LULEÅ
Sweden
E-mail: Martin.C.Nilsson@ltu.se

Ulf Ohlsson
Ph.D.
Division of Structural and Construction Engineering
Luleå University of Technology
SE-971 87 LULEÅ
Sweden
E-mail: Ulf.Ohlsson@ltu.se

Lennart Elfgren
Ph.D. Professor emeritus
Division of Structural and Construction Engineering
Luleå University of Technology
SE-971 87 LULEÅ
Sweden
E-mail: Lennart.Elfgren@ltu.se

ABSTRACT
66 tests of the influence of surface reinforcement on the tensile load capacity of cast-in fasteners have been carried through. In the tests threaded rods ∅30 mm with a ∅45 mm nut at the end were cast-in centrically in concrete slabs (1.2 m × 1.2 m × 0.3 m up to 2.2 m × 2.2 m × 0.6 m). The amount of surface reinforcement was varied from 0% up to about 1.2%. There is a considerable increase in the load capacity with surface reinforcement present. The increase depends on the geometry and the amount and placement of the reinforcement.

Key words: fasteners, load capacity, test, reinforcement

1. INTRODUCTION

1.1 General

Fasteners of different kinds are often used to anchor loads in concrete structures. Cast-in-place reinforcement bars have been used ever since reinforced concrete was introduced around 1900. Post-installed mechanical anchors started to be used in the 1960ies with the advance of drilling machines; and bonded anchors were developed during the 1970ies. An overview of the technology is given in [1] and [2]. Typical fasteners used in nuclear applications are cast-in-place reinforcement bars and headed studs. Post-installed mechanical anchors have also been installed during maintenance of the plants. Today mostly fasteners with under-cut anchors are used for new installations in existing structures.

Pipes in nuclear power plants are often fastened to plates that are anchored in concrete walls and slabs by anchor bolts. Design rules are often conservative and based on testing on bonded and/or expansion anchors fastened in un-reinforced concrete. A need for more appropriate rules has been called for in connection with a planned increase of the effect in Swedish nuclear power plants. This is studied within a project named PULS (Power Update under Licensed Safety, OKG 3, Oskarshamn). By testing some actual types of fastenings in reinforced concrete slabs it should be possible to develop more adequate and, hopefully, less conservative design models.

The aim and scope of this paper is to present results from the tests and analyses in order to form a background for revised design recommendations for anchor bolts compared to the methods proposed in Germany, [3] and [4].

2 CODES AND STANDARDS

The American Society of Mechanical Engineers, ASME, published the first rules for pressure vessels in 1911 and the American Nuclear Society, ANS, has published codes for nuclear plants since 1957, see e.g. [5]. Present codes for loads and design of pipes and fastenings in nuclear power plants are given in [6].

The American Concrete Institute, ACI, published the first code for anchor bolts for nuclear applications in 1985 and it has since been developed successively, see [7]. The anchor bolt code is now also included as Appendix D in the general concrete code, [8].

Fastenings to structural concrete and masonry has since 1987 been the subject of a Special Activities Group of the International Federation for Structural Concrete (fib - fédération internationale du béton) and its predecessor the European Committee for Concrete (CEB - Comité Européen du Béton). The group has published a state of the art report and a Design Guide, [9]. A revised version of the design guide is presently under preparation, [10]. An over-view of codes for fasteners is given by [11] and [3].

Round Robin tests and analysis of anchor bolts have been carried out in Sweden and internationally as well as cyclic and fatigue tests of anchor bolts and long-time loading of bonded anchors, see [12], [13], [14], [15] and [16].

2.1 Failures

The capacity of a fastener is governed by its geometry and materials and the properties of the concrete it is fastened in. Several failure modes are possible: failures associated with tensile loading (pullout, pull-through, combined pullout and concrete cone, concrete cone, splitting, steel) and failures associated with shear loading (steel, edge breakout, pry out, pullout). See [10] for a broader description of the different types of failures.

The tests presented in this paper are anchor-bolts subjected to tensile loading.

The resistance in the case of a concrete cone failure, P_c [N], see Figure 1, can, based on tests, see e.g. [2], and Fracture Mechanics size effect relations, be written as

$$P_c = k f_{c,cyl}^{0.5} h_{ef}^{1.5} \tag{1}$$

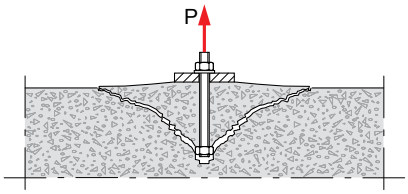

Figure 1 – Concrete cone failure.

where
k = an empirical constant (around 15 $N^{0.5}/mm^{0.5}$ for undercut and headed anchors)
$f_{c,cyl}$ = concrete cylinder strength [MPa]
h_{ef} = effective depth of the anchor [mm]

If several bolts are placed close to one another the capacity is reduced according to the so called CC method (Concrete Capacity) by multiplication with ψ-coefficients. The method was presented by [17] and is also given in [2] and [8].

The capacity for a cast-in-place rebar or a bonded anchor is often governed by a combination of a pull-out and a cone failure, P_p [N], which can be determined from

$$P_p = \tau_R \pi d h_{ef} \tag{2}$$

where
τ_R = bond resistance for cracked or un-cracked concrete [MPa]
d = diameter of bar or drilled hole [mm]

Splitting failure due to anchor loading is usually not verified if adequate surface reinforcement is provided and anchors suitable for application in cracked concrete are used.

Dynamic properties of fasteners have recently been tested by [18], [19] and [11]. The tests indicate that dynamic loads can give a higher resistance than a static load.

It has recently been shown that the assumptions that concrete failures are much more brittle than steel failures are wrong for normal anchor depths, where the yielding of the steel only can provide a very limited deformation, [11].

Fatigue tests indicate that failure occurs when the deformation due to cyclic loading grows larger than the corresponding deformation at a static test. Empirical formula for this is given by [11].

2.3 Comparison between different codes

There are different Load Levels: A, B, C and D and Plant Conditions: PC-1 to PC-5 according to Swedish code [20] and the US codes [6] and [5] with different partial safety factors. According to [5] the spectrum of normal operations and events shall be identified in accordance with their best-estimate frequency of occurrence and divided into five categories according to Table 1.

Table 1 – Plant Condition, PC, frequency/year (F), corresponding Swedish class (Händelse, H) and Load Level. [5], [6] and [20].

Plant Cond.	Best Estimate Frequency of Occurrence (F) per Reactor Year	SSMFS 2008:17 (2008)	Load Level
PC 1	Normal operations	H 1	A
PC 2	$10^{-1} \leq F$	H 2	B
PC 3	$10^{-2} \leq F < 10^{-1}$	H 2	B
PC 4	$10^{-4} \leq F < 10^{-2}$	H 3	C
PC 5	$10^{-6} \leq F < 10^{-4}$	H 4 H 5	D

2.4 Potential for Anchor Bolts

In [3] the German Code [21] is used to calculate the characteristic capacity for a cone failure in cracked concrete, $N_{Rk,c}$. The factor k in (1) is given the value $k = 8.9$ for Load Level A in Table 1 above.

$$P_{Rk,c} = 8.9 f_{c,cyl}^{0.5} h_{ef}^{1.5} \tag{3}$$

For extreme loads corresponding to Load Level D, a further reduction is made with the factor $\alpha_{ductile} = 0.75$ for ductile failures alternatively by a factor $\alpha_{brittle} = 0.54$ for brittle failures. The brittle failure thus gives a capacity which is 0.54/0.75 = 0.72 smaller than the ductile failure.

3 TESTS

In total 66 tests have been carried through for testing the influence of surface reinforcement on the load bearing capacity of cast-in headed bars. In all tests threaded rods with diameter ∅30 mm and a ∅45 mm nut at the end were cast-in centrically in a concrete slab. The width, length and thickness of the concrete slabs were varied from 1.2 m × 1.2 m × 0.3 m up to 2.2 m × 2.2 m

× 0.6 m. In the slabs the amount of top reinforcement was varied from 0% up to about 1.2% (∅16 #100). About half of the tests were cracked centrically through the cast-in rod; the width of the cracks was about 0.5 mm, see Tables 2 and 3.

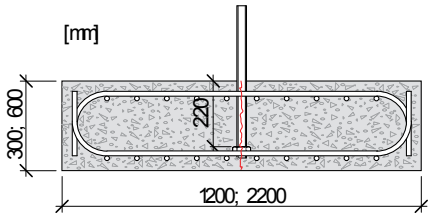

Figure 3 – Typical test slab with cast-in threaded rod and nut, top and bottom reinforcement and initial crack going through the location of the rod.

Table 2 – Summary of test setup: test type, size, concrete cover, amount of top reinforcement, and initial crack width.

Test type.	*L* [m]	H [m]	*c* [mm]	Top reinf.	Crack [mm]
1	1.2	0.3	30	∅16 #100	0.5
2	1.2	0.3	30		0.5
3	1.2	0.3	30	∅16 #100	0
4	1.2	0.3	30		0
10	1.2	0.3	30	∅12 #300	0
11	1.2	0.3	30	∅12 #300	0.5
12	1.2	0.3	30	∅16 #150	0

Test type.	*L* [m]	H [m]	*c* [mm]	Top reinf.	Crack [mm]
13	1.2	0.3	30	∅16 #100	0.5
14	1.2	0.6	30	∅12 #300	0
15	1.2	0.3	50	∅16 #100	0.5
16	2.2	0.3	30	∅12 #150	0
17a	2.2	0.3	30	∅12 #400	0
17b	2.2	0.3	30	∅12 #500	0.5
18	2.2	0.6	30	∅12 #150	0

3.1 Material data

The test specimens were manufactured by Bröderna Hedmans Cementgjuteri in Älvsbyn, Sweden. The threaded rods were of quality 8.8 (f_{ud} = 800 MPa, f_{yk} = 640 MPa). The reinforcement was of quality B500B (f_{yk} = 500 MPa) and the concrete, of quality C25/30, was mixed using the following recipe: gravel 8-16 mm 760 kg/m³, sand 0-8 mm 1050 kg/m³, cement 350 kg/m³, w/c = 0.57.

3.2 Test setup

The test setup is illustrated in Figure 4. The support was for all but the first 12 slabs a stiff ring with an inner diameter of 1.1 m or 2.1 m placed on a thin gypsum layer. The first four slabs were supported at the four corners while the next eight slabs where supported on a ring without or with a thin rubber layer.

Figure 4 – Test set-up: support ring with radius 0.55 m (left) and with radius 1.1 m (right).

Table 3 – Test data: size, amount of top reinforcement, crack width, failure load and deformation.

No.	W [m]	L [m]	H [m]	Top reinf.	Crack [mm]	P^* [kN]	Def. [mm]
1	1.2	1.2	0.3	–	0	186.5	0.36
2	1.2	1.2	0.3	∅16 #100	0	285.3	1.85
3	1.2	1.2	0.3	–	0.5	146.7	4.61
4	1.2	1.2	0.3	∅16 #100	0.5	246.9	2.79
5	1.2	1.2	0.3	–	0	215.5	30.42
6	1.2	1.2	0.3	∅16 #100	0	308.2	1.35
7	1.2	1.2	0.3	–	0.5	165.9	1.94
8	1.2	1.2	0.3	∅16 #100	0.5	240.3	1.58
9	1.2	1.2	0.3	–	0	176.8	0.49
10	1.2	1.2	0.3	∅16 #100	0	267.5	1.74
11	1.2	1.2	0.3	–	0.5	121.7	22.01
12	1.2	1.2	0.3	∅16 #100	0.5	276.3	2.23
13	1.2	1.2	0.3	∅16 #100	0.5	231.7	2.21
14	1.2	1.2	0.3	∅16 #100	0.5	266.8	1.88
15	1.2	1.2	0.3	∅16 #100	0.5	257.2	1.90
16	1.2	1.2	0.3	∅16 #100	0	281.7	5.70
17	1.2	1.2	0.3	∅16 #100	0	329.1	1.78
18	1.2	1.2	0.3	∅16 #100	0	341.4	1.96
19	1.2	1.2	0.3	∅16 #150	0	321.5	9.79
20	1.2	1.2	0.3	∅16 #150	0	321.9	8.73
21	1.2	1.2	0.3	∅16 #150	0	296.5	3.92
22	1.2	1.2	0.3	∅16 #150	0	325.5	6.99
23	1.2	1.2	0.3	∅16 #150	0	332.2	7.92
24	1.2	1.2	0.3	∅16 #150	0	313.5	8.31
25	1.2	1.2	0.3	∅16 #150	0.5	294.3	4.76
26	1.2	1.2	0.3	∅16 #150	0.5	283.8	4.97
27	1.2	1.2	0.3	∅16 #150	0.5	305.4	4.54
28	1.2	1.2	0.3	∅16 #150	0.5	318.8	8.38
29	1.2	1.2	0.3	∅16 #150	0.5	311.7	9.32
30	1.2	1.2	0.3	∅16 #150	0.5	305.1	7.95
31	1.2	1.2	0.3	∅16 #100	0.5	316.3	8.99
32	1.2	1.2	0.3	∅16 #100	0.5	302.9	9.17
33	1.2	1.2	0.3	∅16 #100	0.5	321.7	3.74
34	1.2	1.2	0.3	∅16 #100	0.5	296.4	2.99
35	1.2	1.2	0.3	∅16 #100	0.5	279.1	2.89
36	1.2	1.2	0.3	∅16 #100	0.5	292.9	11.21
37	1.2	1.2	0.3	∅12 #300	0.5	278.7	7.17
38	1.2	1.2	0.3	∅12 #300	0.5	288.9	8.25
39	1.2	1.2	0.3	∅12 #300	0.5	277.9	8.38
40	1.2	1.2	0.3	∅12 #300	0.5	293.8	10.30
41	1.2	1.2	0.3	∅12 #300	0.5	314.0	11.65
42	1.2	1.2	0.3	∅12 #300	0.5	297.5	9.37
43	1.2	1.2	0.3	∅12 #300	0	292.4	9.83
44	1.2	1.2	0.3	∅12 #300	0	287.3	7.85
45	1.2	1.2	0.3	∅12 #300	0	255.4	8.56
46	1.2	1.2	0.3	∅12 #300	0	291.7	9.62
47	1.2	1.2	0.3	∅12 #300	0	249.2	8.72
48	1.2	1.2	0.3	∅12 #300	0	306.4	10.76
49	2.2	2.2	0.3	∅12 #150	0	256.8	8.07
50	2.2	2.2	0.3	∅12 #150	0	262.2	7.62
51	2.2	2.2	0.3	∅12 #150	0	267.2	8.36
52	1.2	1.2	0.6	∅12 #300	0	330.8	8.85
53	1.2	1.2	0.6	∅12 #300	0	365.1	10.24
54	1.2	1.2	0.6	∅12 #300	0	361.9	8.89
55	1.2	1.2	0.6	∅12 #300	0	370.1	10.23
56	1.2	1.2	0.6	∅12 #300	0	344.2	9.83
57	1.2	1.2	0.6	∅12 #300	0	371.0	9.61
58	2.2	2.2	0.3	∅12 #400	0	247.5	9.53
59	2.2	2.2	0.3	∅12 #400	0	241.3	9.78
60	2.2	2.2	0.3	∅12 #400	0	233.9	7.00
61	2.2	2.2	0.3	∅12 #500	0.5	204.2	4.68
62	2.2	2.2	0.3	∅12 #500	0.5	235.7	7.47
63	2.2	2.2	0.3	∅12 #500	0.5	212.5	8.11
64	2.2	2.2	0.6	∅12 #150	0	319.5	7.12
65	2.2	2.2	0.6	∅12 #150	0	333.8	10.24
66	2.2	2.2	0.6	∅12 #150	0.9	261.4	10.74

The compressive and tensile (splitting) strength of the concrete were tested for every slab in order to correct for their age compared to the 28 days strengths.

4 RESULTS

The results of the tests are shown in Figure 5-Figure 7. In Figure 5 the results from the 1.2 m × 1.2 m × 0.3 m specimen without a crack are presented for four different amounts of reinforcement: Ø16 #100 in the bottom, Ø16 #100 in the top and the bottom, Ø16 #150 in the top and bottom, and Ø12 #300 in the top and the bottom.

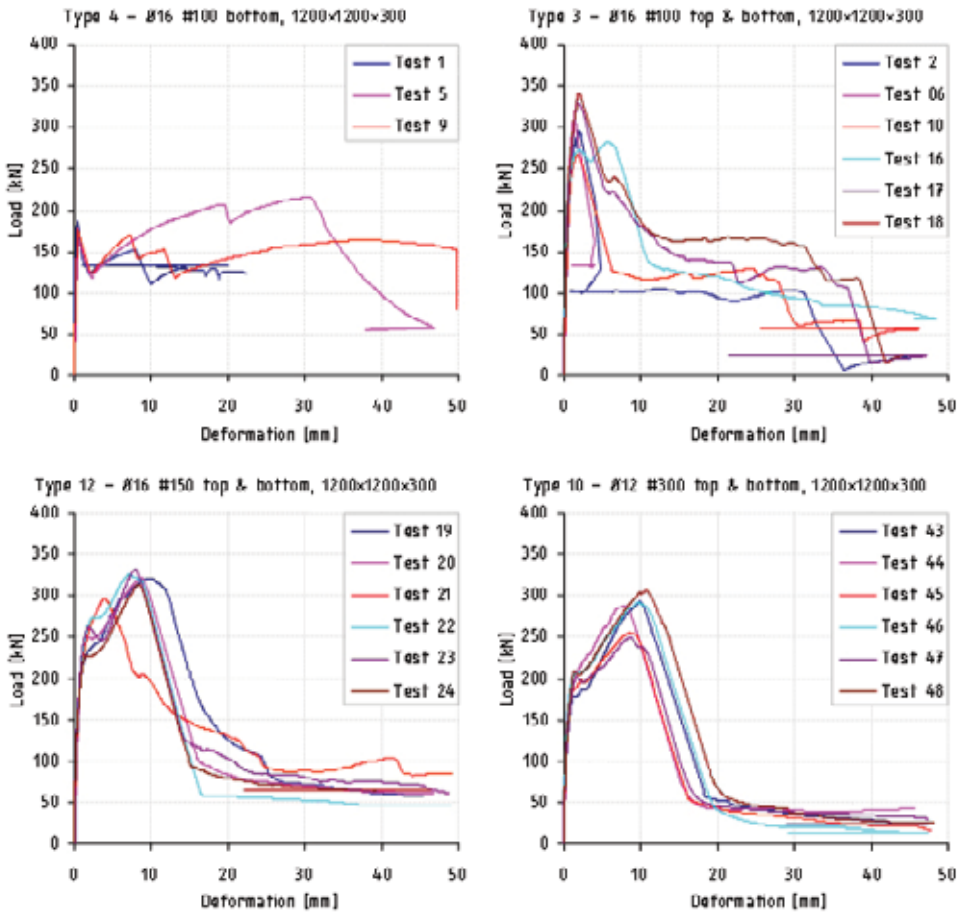

Figure 5 – Test results for slabs without cracks.

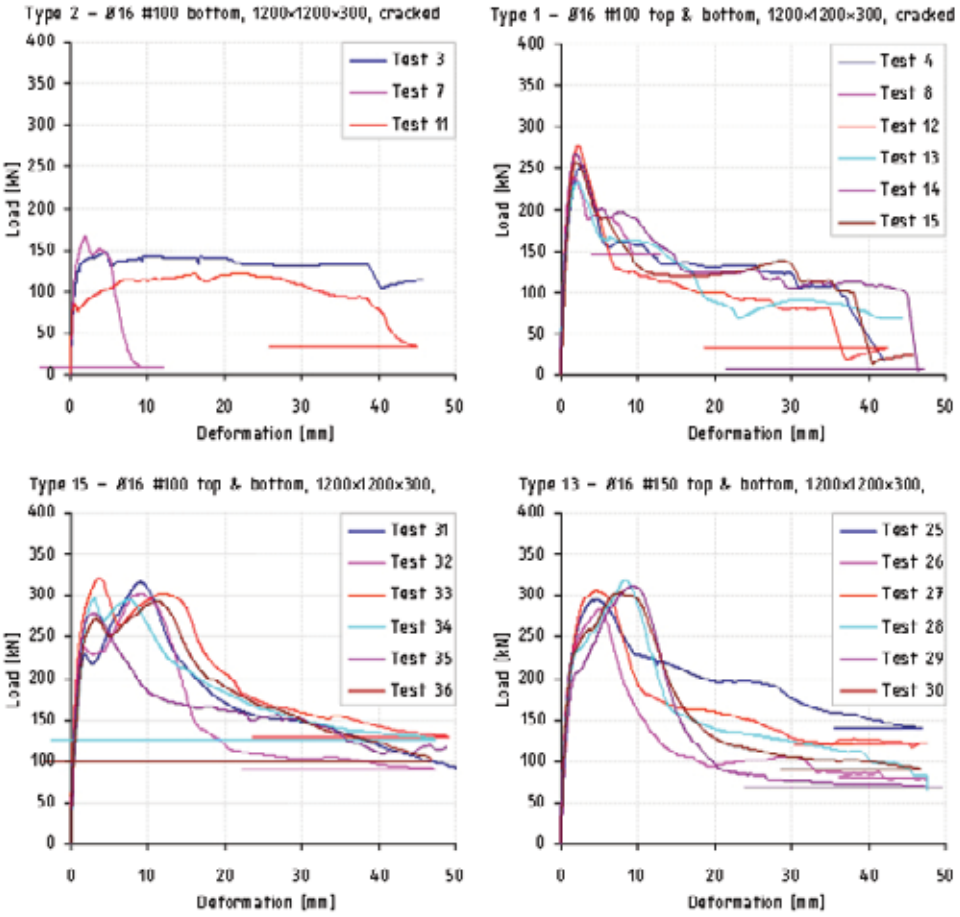

Figure 6 – Test results for slabs with cracks.

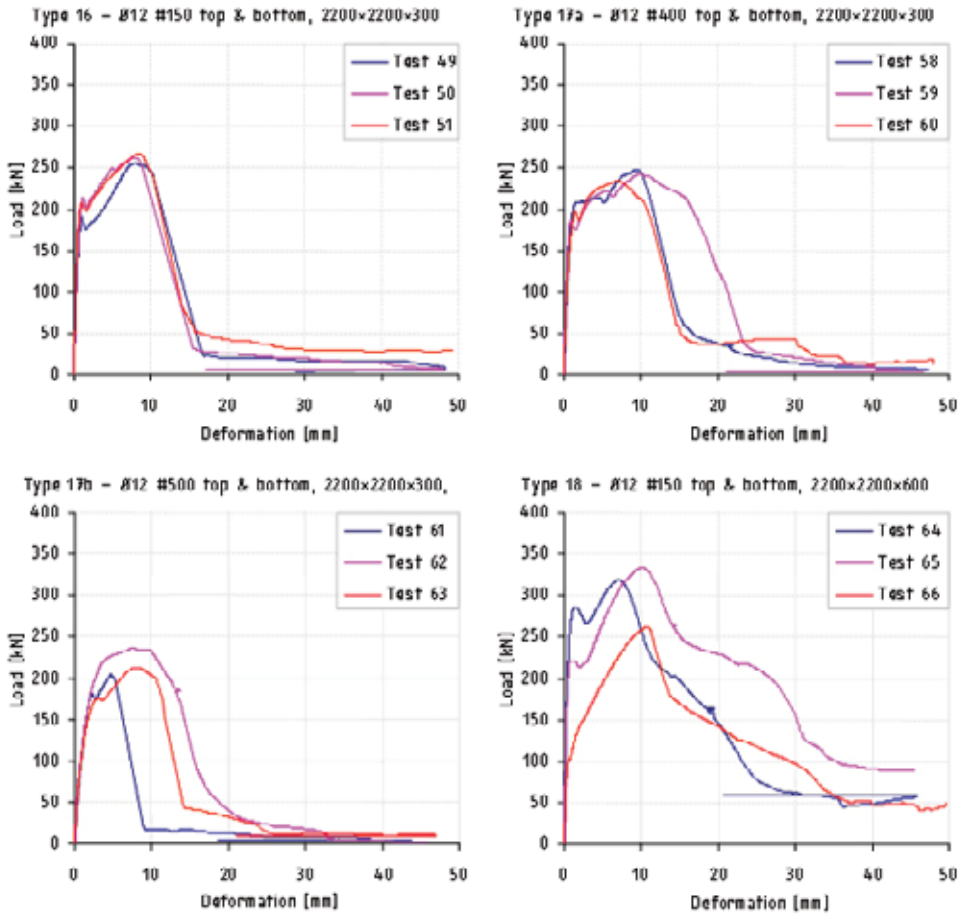

Figure 7 – Test results for larger slabs (2.2 m × 2.2 m), varying amount of top reinforcement and slab thickness.

5 ANALYSIS OF TEST RESULTS

5.1 General

The capacity for concrete cone failure of cast-in headed studs in concrete structures has been tested in order to check the influence of surface reinforcement and other boundary conditions. Ordinarily the failure load is given according to Eq. (1)

$$P_c = k f_{c,cyl}^{0.5} h_{ef}^{1.5}$$

where k is an empirical factor given in several codes. For un-cracked and cracked concrete, characteristic values for k are 12.7 $(N/mm)^{0.5}$ and 8.9 $(N/mm)^{0.5}$ respectively.

5.2 Influence of surface reinforcement

For the specimen without surface reinforcement it can be calculated that the ratio of tested to code capacity P_{test}/P_{code} is less than 1. This is due to the fact that a splitting failure occurred before a cone failure could form. If the slab is thicker (or reinforced) this failure type will be avoided.

For the slabs with surface reinforcement and without cracks the ratio of P_{test}/P_{code} is mostly higher than 1. The ratio is 0.90 for large, thin slabs 2.2 m × 2.2 m × 0.3 m where the stiffness is low causing bending deformations and cracking which reduce the capacity. The slab does not achieve a regular concrete cone failure but is also influenced by a splitting failure and the numbers have therefore been put in parentheses. If the reinforcement is cleared away in an area around the bolt of 0.4 m × 0.4 m, the ratio is further reduced to 0.84. On the other hand, when the thickness of the slab is increased from 0.3 m to 0.6 m, the P_{test}/P_{code} ratio increases from 0.91 to 1.14.

For the slabs with surface reinforcement and with cracks the ratio of P_{test}/P_{code} is between 1.23 and 1.54. The lowest value is occurring for the highest reinforcement ratio which might look confusing. The reason is probably that a high reinforcement ratio makes the slab stiff so that few additional cracks appear before maximum load. For a lower reinforcement ratio the slab will deform more and the reinforcement will have a larger dowel action. The ratio of P_{test}/P_{code} is reduced to 1.05 if the reinforcement is cleared away in an area of 0.5 m × 0.5 m around the bolt. It can also be seen that a thicker reinforcement concrete cover c = 50 mm (instead of c = 30 mm) has a positive influence and increases the ratio from 1.23 to 1.54 for otherwise similar bolts. Some of the slabs, originally without cracks, obtained considerable bending cracks during the testing. It is therefore interesting also to use the design formula for cracked slabs when these slabs are evaluated. It is found that the ratio P_{test}/P_{code} gets a value of 1.29 for large slender slabs with a minimum reinforcement of 0.15% to be compared to the value 1.40 for the smaller slabs. It can also be seen that the ratio is reduced to 1.19 if the reinforcement is cleared away in an area of 0.4 × 0.4 m around the bolt. If also the two thick large originally uncracked slabs are evaluated in this way the ratio get a value of 1.62.

The load bearing capacity for cracked slabs are somewhat smaller for high reinforcement content P_{test}/P_{code} = 1.23 (∅16 #100) than for slabs with lesser reinforcement content P_{test}/P_{code} = 1.47 (∅16 #150) and P_{test}/P_{code} = 1.39 (∅12 #300). This might be due to the fact that a much higher load is needed to obtain a crack in a more heavily reinforced slab than in a less reinforced slab. This causes higher stresses.

The test with L = 2.2 m and an area free from reinforcement around the anchor bolt showed a smaller capacity than other tests. For the un-cracked slabs we obtained P_{test}/P_{code} = 0.90 for ∅12 #300 but only P_{test}/P_{code} = 0.84 when we arranged a reinforcement free space of 400 mm × 400 mm in a slab with ∅12 #150. For a cracked slab we got P_{test}/P_{code} = 1.05 when we arranged a reinforcement free space of 500 mm × 500 mm in a slab with ∅12 #150. This indicates that it is important that the failure cone is crossed by surface reinforcement.

Earlier tests on the influence of surface reinforcement have been made by [22]. They tested expansion anchors of size M10 – M20 and found that a surface reinforcement had little influence on the load-carrying capacity for cone break-out failures. It did have the effect that the

failure got more ductile. They also found that it had a positive influence on the splitting failure. Some tests have also been presented by [23] in a study of fastenings in the concrete tensile zone.

5.3 Influence of initial splitting cracks

We can obtain a failure that is initiated by a bending crack before the concrete cone failure develops. For a bending crack we need a bending moment m_{cr} [Nm] for a slab strip (with the width b = 1.0 m), the height h = 0.3 m and the crack strength f_{ct} = 3 MPa

$$m_{cr} = f_{ct}W = f_{ct}\frac{h^2}{6} = 3\cdot 10^6 \cdot \frac{0.3^2}{6} = 45000 \text{ Nm/m}$$

A line load p [N/m] that is applied transversally in the middle of a simply supported beam with the length L [m] and the width b [m] obtains a bending moment m [Nm/m]

$$m = \frac{pL}{4}$$

The cracking load p_{cr} for a simply supported slab strip with the width b = 1.2 m will then be

$$P_{cr} = pb = \frac{4m}{L}b = \frac{4\cdot 45000}{1.2}\cdot 1.2 = 180000 \text{ N}$$

If the slab thickness is doubled, the crack load will be four times as high P_{cr} = 720 kN. If the length L and the width b are doubled at the same time, this will not influence the crack load. However, the slab is not a simply supported beam but rather a circular slab with the diameter b. According to the theory of elasticity the bending moment will go towards infinity when a concentrated point load acts at its center. According to the yield line theory for concrete slabs the crack (yield) moment can approximately be written as, [24]:

$$P_{cr} = 2\pi m = 2\pi\cdot 45000 = 282743 \text{ N for } h = 0.3 \text{ m and}$$
$$P_{cr} = 2\pi m = 2\pi\cdot 180000 = 1130973 \text{ N for } h = 0.6 \text{ m}$$

From this it is clear that the thin slabs without surface reinforcement are influenced by a concrete splitting failure and thus get failure loads which are lower than the cone failure. This failure is prevented when surface reinforcement is present.

For the large un-cracked thin slab with surface reinforcement ∅12 #300 the capacity is about 90% of the code value. This is due to the fact that the restraints on these slabs are smaller than for the smaller slabs.

The reason why the load carrying capacity for cracked slabs with ∅12 #300 are somewhat higher than for corresponding un-cracked slabs (286 kN and 274 kN respectively) is probably due to natural variations in the concrete properties.

5.4 Influence of thickness

A thicker slab is stiffer and does not deform as much as thin slab and this increases the capacity of a fastener.

6 CONCLUSIONS AND OUTLOOK

The following conclusions can be drawn:

- There is a considerable increase in the load-bearing capacity if surface reinforcement is present
- The increase depends on the geometry and the amount and placement of the reinforcement

Further work is needed regarding

- Numerical modelling of the failure process for different boundary conditions with help of non-linear finite element methods
- Amount and spacing of reinforcement

Further work is also needed regarding the influence of surface reinforcement on

- Cast-in bars
- Bonded anchors

REFERENCES

1. CEB (1991): Fastenings to Concrete and Masonry Structures. State of the Art Report. First issued as Bulletins d'Information No 206 and 207 by Comité Euro-International du Béton (CEB) 1991. Thomas Telford, London 1994. 250 pp. ISBN 0-7277-1937-8.
2. Eligehausen, R., Mallée, R. and Silva, J. F. (2006): Anchorage in Concrete Construction. Berlin: Ernst & Sohn, 378 pp, ISBN 978-3-433-01143-0.
3. Eligehausen, R., Pregartner, T. and Appl, J. (2007): Design of anchor plates with headed studs and cast.in-place rebars valid for the Nuclear Power Plant Oskarshamn 3. Project report to Westinghouse Electric Sweden AB by Institut für Werkstoffe im Bauswesen, Universität Stuttgart, Pfaffenwaldring 4, D-70550 Stuttgart and Engineering Office Eligehausen & Amus, Hauptstrasse 4, D-70563 Stuttgart., 10 May 200, 114 pp.
4. Eligehausen, R., Pregartner, T. (2008): Design of anchor plates with cast.in-place rebars valid for the Nuclear Power Plant Forsmark, sweden. Project report to Forsmark Kraftgrupp AB by Institut für Werkstoffe im Bauswesen, Universität Stuttgart, Pfaffenwaldring 4, D-70550 Stuttgart and Engineering Office Eligehausen & Amus, Hauptstrasse 4, D-70563 Stuttgart., 4 november 2008, 103 pp.
5. ANSI (1983): Nuclear Safety Criteria for the Design of Stationary Pressurized Water Reactor Plants. ANSI/ANS-51.1-1983. An American National Standard published by the American Nuclear Society, 92 pp. Normen drogs in 1998 och har ersatts av bl a ANSI/ANS-2.27-2008: Criteria for Inves-tigations of Nuclear Facility Sites for Seismic Hazard Assessments och ANSI/ANS-58.9-2002: Single Failure Criteria for LWR Safety-Related Fluid Systems.
6. ASME III-1NF (2007): ASME Boiler & Pressure Vessel Code. III – Rules for Construction of Nuclear Facility Components. Division 1 – Subsection NF – Supports.

The American Society of Mechanical Engineers, New York 2007, ISBN 978-0-7918-3058-1, 141 pp. Updated yearly.
7. ACI 349-06 (2006): Code Requirements for Nuclear Safety Related Concrete Structures. ACI 349-06. American Concrete Institute, Farmington Hill, Mich.. Several earlier versions e g ACI 349-90,.1990, 96 pp.
8. ACI 318-08 (2008): Building Code Requirements for Structural Concrete (ACI 318-08) & PCA Notes on ACI 318-08 (EB0708). American Concrete Institute, Farmington Hill, Mich.. Several earlier versions e.g ACI 318-02, 2002, 443 pp.
9. CEB (1995): Design of Fastenings in Concrete. First issued as Bulletins d'Information No 226 by Comité Euro-International du Béton (CEB) 1995. A revised version published by Thomas Telford, London, January 1997. 96 pp. ISBN 9780727735669
10. fib (2009): Design Guide for Fasteners in Concrete. Final Draft, March 2009. International Federation for Concrete (fib - fédération internationale du béton), Special Activities Group on Fasteners to Structural Concrete and Masonry. Introduction 2 pp; Part I – General Provisions, 129 pp; Part II – Characteristic Resistance of Anchorages with Post-installed Expansion Anchors; Undercut Anchors, Screw Anchors and Bonded Expansion An-chors, 36 pp; Part III - Characteristic Resistance of Anchorages with Bonded Anchors and Connections with Post-installed Reinforcing Bars, 22 pp; Part IV - Characteristic Resistance of Anchorages with Cast-in Headed Anchors, 33 pp; Part V - Characteristic Resistance of Anchorages with Cast-in Anchor Channels, 31 pp; References, 9 pp.
11. Hoehler, M. S. (2006): Behavior and Testing of Fasteners to Concrete for use in Seismic Applications. Ph D Thesis, Institut für Werkstoffe im Bauwesen der Universität Stuttgart, 261 pp.
12. Elfgren, L., Broms, C. E., Johansson, H. E., and Rehnström, A. (1980): Anchor Bolts in Reinforced Concrete Foundations. Short Time Tests. Research Report TULEA 1980:36. Division of Structural engineering, University of Luleå, 1980, 117 sid, ISSN0347-0881.
13. Elfgren, L., Cederwall, K., Gylltoft, K. and Broms, C. E. (1982): Fatigue of Anchor Bolts in Reinforced Concrete Foundations. IABSE Colloquium Lausanne 1982. Fatigue of Steel and Concrete Structures, pp 439-470.
14. Elfgren, L., Anneling, R., Eriksson, A., Granlund, S-O. (1987): Adhesive Anchors. Tests with cyclic and long time loads. .SP - Swedish Technical Research Institute, SP-RAPP 1987-39, 87 + 24 pp.
15. Elfgren, L., Eligehausen, R. and Rots, J. G. (2001): Anchor bolts in concrete structures: summary of Round Robin tests and analysis ar-ranged by RILEM TC 90-FMA Fracture Mechanics of Concrete - Applications. Materials and Structures, Vol 34, No 242, October 2001, pp. 451-457. The full report can be downloaded from http://epubl.ltu.se/1402-1528/1998/14/index.html
16. Elfgren, L. and Nohhabai, K. (2002): Tension of reinforced concrete prisms. Bond properties of reinforcement bars embedded in concrete tie elements. Summary of a RILEM round-robin investigation arranged by TC 147-FMB "Fracture Mechanics to Anchorage and Bond. Materials and Structures, Vol 35, No 250, July 2002, p. 318-325. The full report can be downloaded from http://epubl.ltu.se/1402-1528/2001/13/index.html
17. Fuchs, W., Eligehausen, R. and Breen, J. E. (1995): Concrete Capacity Design (CCD) Aprroach for Fastening to Concrete. Code Back-ground Paper. ACI Structural Journal, Vol 92, No. 1, Jan-Feb 1995, pp 73-94.
18. Rodriguez, M., Lotze, D., Gross, J. H., Zhang, Y.-G., Klingner, R. E. and Graves III, H. L. (2001): Dynamic Behavior of Tensile Anchors to Con-crete. ACI Structural Journal, Vol 98, No 4, July-August 2001, pp 511-524.
19. Solomos, G. and Berra, M. (2006): Testing of anchorages in concrete under dynamic tensile loading. Materials and Structures, vol 39:695-706

20. SSMFS 2008:17 (2008): Swedish code for design and construction of nuclear reactors - Strålsäkerhetsmyndighetens föreskrifter och allmänna råd om konstruktion och utförande av kärnkraftsreaktorer. (In Swedish).
21. DIB (2003): Stahlplatte mit einbetonierten Ankerboltzen, ETA No 06.01/15, Common Understanding of Assessment Procedure (CUAP), Deutsches Institut für Bautrechnik, Berlin, March 2003. Cited from Eligehausen et al (2007).
22. Rehm, G. and Pusill-Wachtsmuth, P. (1979): Abschlussbericht des Forschungsvorhabens Einfluss einer Bewehrung auf das Tragverhalten von Dübelverbindungen. (Influence of reinforcement ob the carrying capacity of fasteners. In German) Az.: IV 1 -5- 11/75. Institut für Werkstoffe im Bauwesen, Universität Stuttgart, 22 Nov 1979, 57 pp + 126 appendices.
23. Eligehausen, R., Fuchs, W., Lotze, D. and Reuter, M. (1989): Befestigungen in der Betonzugzone. Beton- und Stahlbetonbau, Vol 84 (1989), Heft 2, pp 27-32, Heft 3, pp 71 – 74.
24. Bengtsson, B. Å, Elfgren, L., Hillerborg, A., and Losberg, A. (1969): Fribärande plattor (Load-bearing slabs. In Swedish). Chapter 336 in "Handboken Bygg, Part 3. Konstruktionsteknik", Byggmästarens förlag, Stockholm 19p 319 – 404.

Durability properties and Deterioration of Concrete Facades Made of Insufficient Frost Resistant Concrete

Jukka Lahdensivu
M.Sc., Lic. Tech.
Tampere University of Technology
Tekniikankatu 12, P.O. Box 600
FI 33101 Tampere
E-mail: jukka.lahdensivu@tut.fi

Hanna Tietäväinen
M.Sc.
Finnish Meteorological Institute
Erik Palménin aukio 1, P. O. Box 503
FI - 00101 Helsinki
E-mail: hanna.tietavainen@fmi.fi

Pentti Pirinen
M.Sc.
Finnish Meteorological Institute
Erik Palménin aukio 1, P. O. Box 503
FI - 00101 Helsinki
E-mail: pentti.pirinen@fmi.fi

ABSTRACT

42.7 % of Finnish concrete facades have visual frost damage. 35.4 % of the damage is localized, and 7.3 % is wide spread. The same phenomena related to frost damage in concrete can be found also in thin-section analyses where incipient frost damage can be found, too. The durability properties related to frost resistance of concrete very rarely fulfil the requirements of Finnish national building codes. According to 2267 protective pore ratio tests, in approximately 70 % of existing concrete facades the protective pore ratio is less than 0.15. Frost damage of concrete has been found to be more common in coastal area than inland.

Key words: Concrete facade, condition assessment, deterioration, frost damage, service life.

1. INTRODUCTION

1.1 On Finnish building stock

The Finnish building stock is rather young compared to the rest of Europe. Since the 1960's a total of approximately 44 million m^2 of concrete panel facades have been built in Finland [1]. In fact, more than 60 % of the Finnish building stock has been built in the 1960's or later. Totally there are 1.2 million apartments in the Finnish block of flat stock [2].

The structures of Finnish concrete buildings have deteriorated due to several different deterioration mechanisms whose progress depends on many structural, exposure and material factors. Thus the service lives of structures vary widely. In some cases the structures have required remarkable and often unexpected, technically significant and costly repairs less than 10 years after their completion. For this reason many new methods have been developed in Finland for maintaining and repairing these concrete structures during the last 20 years. The methods include a condition investigation practice and its extensive utilization, rational repair methods and their selection, as well as first-rate repair products and appropriate instructions for managing repair projects.

Concrete structures have been repaired extensively in Finland since the early 1990's. During the almost 20-year period, approximately 10 percent of the stock built in 1960 until 1980 has been repaired once. It is estimated that the total annual value of building repair work in Finland is approximately 5500 million Euros, of which approximately 30 % involves external structures (walls, balconies, roofs, windows, etc.) [1, 3].

Because of the great amount of these existing concrete structures, it is very important to solve their incident repair need in an economically and technically durable way. This means that the most suitable repair methods have to be used for each case and it is also important to be able to determine the optimal time of the repairs.

1.2 Structures of concrete facade panel

All prefabricated concrete structures in Finland are based on Concrete Element System (BES 1969). This open system defines, among others, preference dimensions of floor-to-floor height and each type of prefabricated elements. The system allows in principle the use of prefabricated element made by any manufacturer in a single multi-storey building.

The concrete panels used in exterior walls of multi-storey residential buildings were, and still are, chiefly prefabricated sandwich type panels where thermal insulation lies between two concrete slabs. Facade panels are made of two relatively thin reinforced concrete slabs connected to each other with truss-type metal ties. The thermal insulation between the slabs is most often mineral wool and its nominal thickness is 60 to 145 mm depending on the building codes in force at the time of design and construction.

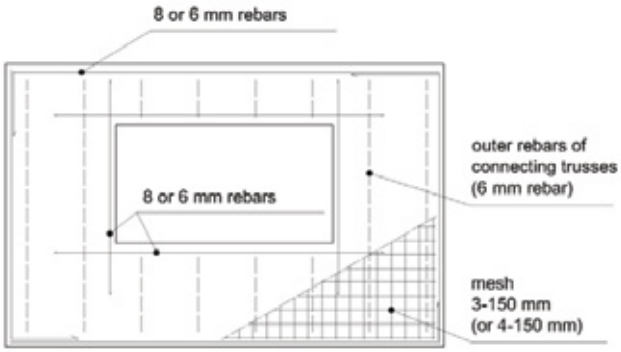

Figure 1 – Typical reinforcement in the outer layer of concrete facade panel [4].

The usual nominal thickness of the outer panels range from 40 to 70 mm while 50 and 60 mm are the most usual values [4]. The panels are most typically reinforced with steel mesh with a bar diameter of 3 mm and spacing of 150 mm. Rebars of 6 to 8 mm in diameter are typically used as so-called edge bars and often also diagonally in the corners of windows and other major openings in the panels, see Figure 1. Used splices are lap splices, which increases the overall thickness of the reinforcement.

The outer layer is generally suspended from the inner layer. The sandwich facade panels are connected to the building frame by the inner slab, usually by cast concrete joints and reinforcement ties. In the Finnish prefabricated concrete building system, the inner layer is load-bearing on the gable facades and non-bearing on the long facades. All vertical and horizontal joints between outer slabs are elastic, most usually made with polymer sealants allowing thermal as well as other movement of the slabs. It is also notable that usually there is no ventilation gap behind the outer slabs of exterior walls made of concrete panels. Thus, if the thermal insulation gets wet for some reason, e.g. due to leakage in the joints, drying of the structure is slow. The drying of the outer slabs is also slow because of the relatively efficient thermal insulation limiting the drying heat flux through the wall. This means that concrete may be moist for a long period.

In the early years of manufacturing prefabricated concrete panels durability and service life issues were not so important compared to the effective production of the concrete panels. As a spirit of the time, in the early 1960's until mid 70's all durability requirements concerned only load-bearing concrete structures leaving the outer layer of facade panels outside of these requirements.

The concrete grade used in the facade panels has been C25 since 1965 until the late 1980's [5]. After that the compressive strength of concrete was raised up to C30 [6] and again 1992 to C45 [7]. The basic idea was to improve the durability of the outdoor concrete structures. However, it was still possible to use lower grade concrete in outdoor structures, but the cover depth of reinforcement had to be increased respectively.

1.2 Objective

The objective of this paper was to study the factors that have actually had an impact to the existence and progress of frost damage in existing Finnish concrete facades.

2. FROST WEATHERING OF CONCRETE

Concrete is a brittle material, it can withstand only limited tensile strain without cracking. Internal tensile stresses due to expansion processes may result in internal cracking and, therefore, disintegration of concrete. Concrete may disintegrate as a result of internal expansion, caused by frost weathering, formation of late ettringite, alkali-aggregate reaction, etc.

2.1 The nature of the frost attack of concrete

Frost attack due to a high moisture load is a common reason for deterioration of concrete structures in Nordic outdoor climate. Concrete is a porous material whose pore system may, depending on the conditions, hold varying amounts of water. As the water in the pore system freezes, it expands about 9 % by volume which creates hydraulic pressure in the system. If the level of water saturation of the system is high, the overpressure cannot escape into air-filled pores and thus damage the internal structure of the concrete resulting in its degradation.

More than 15 different theories or explanation on the frost attack of porous materials have been presented [8]. It can be noticed that frost weathering is a complex process, and frost damage can occur in many different ways [9].

Probably the most widely known frost damage theory is the hydraulic pressure theory by Powers published in 1949. Accordingly, damage occurs as freezing water expands creating hydraulic pressure within the pore structure of a porous material. The pressure is created when part of the water in a capillary pore freezes and expands forcing thereby the unfrozen water out of the pore. The migration of water causes localised internal tensions in the material whereby its strength may fail resulting in cracking [10].

The theory of volume chances in microscopic ice crystals was developed to complete the hydraulic pressure theory. During the freezing process, small ice crystals tend to grow in capillary pores. If there is not enough empty space for growing ice crystals, the growing ice crystals will cause pressure to pore structure and might lead to cracking of pore structure. The growing of microscopic ice crystals will go on despite of the lowering of temperature will stop during freezing phase [11].

The theory of osmotic pressure completes the two previous theories by taking into account also the migration of dissolved chemicals, mainly the alkalis Na_2O and K_2O, in the pore water. Those dissolved chemicals lower the freezing temperature of pore water and increase the concentration of salts in the water surrounding the ice. The concentration of dissolved chemicals tries to get equilibrium between different pore water solutions causing osmotic pressure to pore structure [12].

Litvan noticed in the beginning of 1970's that the water in pore structure of a porous material does not freeze immediately when temperature decreases below 0 °C. Freezing happens first in bigger capillary and gravitation pores. In smaller gel pores water begins to freeze when temperature is approximately -15 to -20 °C. The unfrozen pore water is thus supercooled, which tends to cause drying of paste because the saturation pressure over supercooled water is higher than that over ice. According to Litvan, mechanical damage happens when moisture transfer cannot occur in an orderly manner, i.e. when the rate of freezing is too high, or the distance that water must travel to reach an external surface and freeze is too long [13].

The theory of critical degree of water saturation was developed in the early 1970's [9]. The basic idea of this theory is that there is a critical degree of water saturation above which the porous and brittle material is damaged while freezing. If the actual water saturation is below critical, no damage takes place during freezing.

Increasing of temperature on the facade also increases the temperature of ice in the pore structure. First when temperature decreases, ice in pore structure shrinks, and supercooled pore water can flow capillarily to "new" empty spaces in pores and freezes rapidly. When temperature increases, ice will need more space than before. This causes remarkable hydraulic pressure to pore structure [14]. The thermal expansion coefficient of ice is 50 x 10^{-6} per K. It is 3.5 to 10 times more than the temperature expansion coefficient of concrete [15, 16]. The temperature expansion coefficient of concrete varies a lot and it is influenced by two main constituents of concrete; hydrated cement paste and aggregate [17].

2.2 Effects of the frost weathering

As discussed earlier, the early phase of frost weathering is manifested as inner cracking of concrete or scaling of concrete surface, when hydraulic pressure caused by freezing pore water exceeds the tensile strength of concrete. Cracking will decrease the strength of concrete and increase the capillary water absorption. Continuing freeze-thaw cycles in high moisture content of concrete will lead in the end to frost weathering [18]. The early phase frost weathering is not visible and it cannot be found by hammering the surface of concrete. Finding this inner cracking of concrete necessitates more sophisticated research methods, like thin-section analyses [4].

Far advanced frost weathering is manifested as reduction in strength of the concrete, loss of adhesion, or crazing or chipping off of the surface due to internal expansion, see Figure 2. Disintegration of concrete accelerates also the carbonation of concrete due to cracking and this way also steel corrosion.

Figure 2 – Far advanced frost attack curves the edges of the facade panel.

The degree of frost weathering may vary in different parts of the facade - depending on, for instance, the load and variation in material properties - as well as through the thickness of the

concrete structure. Weathering due to high local moisture load may affect only a very limited area. On the other hand, an improper surface treatment on non frost resistant concrete facade may result in deterioration across most of the wall surface.

3. RESEARCH MATERIAL

The research material consists of a database of deterioration and material properties of existing Finnish concrete facade panels built up between 1961 and 1996, and weather observations since 1961 made by the Finnish Meteorological Institute (FMI).

3.1 Database

The condition assessment systematic for concrete facades and balconies has been developed in Finland since the mid-1980's. A large body of data on implemented repair projects has been accumulated in the form of documents prepared in connection with condition assessments. Approximately 1500 precast concrete apartment blocks have been subjected to a condition assessment, and painstakingly documented material on each one exists, including the buildings structures and accurate reports on observed damage and the need for repairs based on accurate field surveys and laboratory analyses.

The condition assessment data from 947 buildings has been gathered to a database. Those condition assessment reports have been collected from companies which have conducted such investigations as well as from property companies owned by cities. The condition assessment data related to frost resistance and frost damage of concrete consist of different laboratory tests of a total of 3868 samples and visually seen frost damage of the facades.

3.2 Weather Data

The weather data consists of the annual liquid precipitation i.e. rain and wet snow. Both of them can be capillarily adsorbed to the pore structure of concrete. Annual freeze-thaw cycles in the air have been gathered during the period beginning of September to the end of April each year since 1961. Freeze-thaw cycles have been counted in following maximum temperature categories: < 0 °C, < -2 °C, < -5 °C and < -10 °C. Corresponding freeze-thaw cycles have been counted also in cases, where raining or wet snowing has been followed by freezing during three days.

Wind directions and wind speed during rain and at all times (including also snowfall and dry weather) during September to April was gathered, too. All weather data was gathered from Jyväskylä (inland), Vantaa (south costal area) and Turku (coast line) since 1961.

4. RESULTS AND DISCUSSION

Most of the block of flats stock in Finland are situated in the southern part of Finland. In the database the building stock has been divided into three different groups based on their geographical position: coastal area, inland and North Finland. Approximately a third of those buildings are situated in the coastal area and two-thirds in inland. Only a few of the buildings in the database are situated in North Finland.

All prefabricated concrete panels have basically been constructed in the same way, but there are

many differences in their surface finishing and manufacturing. Those have a strong influence, for instance, on the situation of rebars and the quality of concrete. In the database the most common surface finishing is brushed painted concrete, exposed aggregate concrete and painted plain concrete, see Figure 3. The distribution of the surface finishing on the database is shown in Figure 4.

a) Brushed painted concrete

b) Exposed aggregate concrete

c) Painted plain concrete

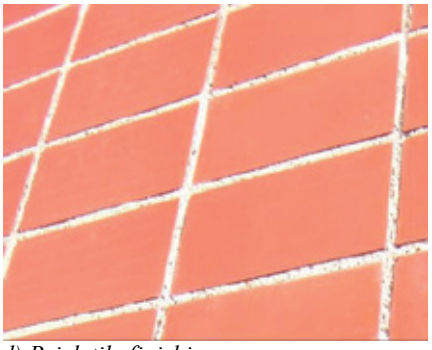

d) Brick tile finishing

Figure 3 – The most typical surface types in Finnish concrete facade panels.

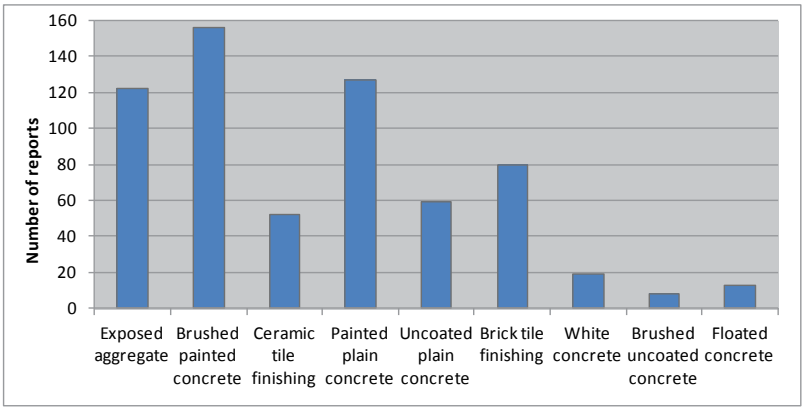

Figure 4 – Distribution of surface finishing in the database (n= 947 single buildings).

4.1 The frost resistance of concrete

According to Finnish guidelines for durability of concrete structures [6], in frost resistant concrete the volume of air-filled voids which cannot be filled with capillary water must be at least 20 % of total pore structure volume. These air-filled voids are called protective pores and the protective pore ratio should be 0.2 or higher, respectively. The protective pore ratio has been tested from concrete samples according to Finnish standard SFS 4475 [19].

According to 2267 protective pore ratio tests, approximately 70 % of existing concrete facades the protective pore ratio is less than 0.15. The frost resistance is very different depending on the surface type of concrete panel, see Figure 5. If the protective pore ratio is less than 0.10, concrete is not frost resistant in Nordic outdoor climate. The worst situation related to frost resistance is in concrete panels with surface type of exposed aggregate concrete, ceramic tile covered concrete and uncoated patterned concrete. The concrete facades made before 1980 have generally poorer material properties related to frost resistance than the newer concrete facades.

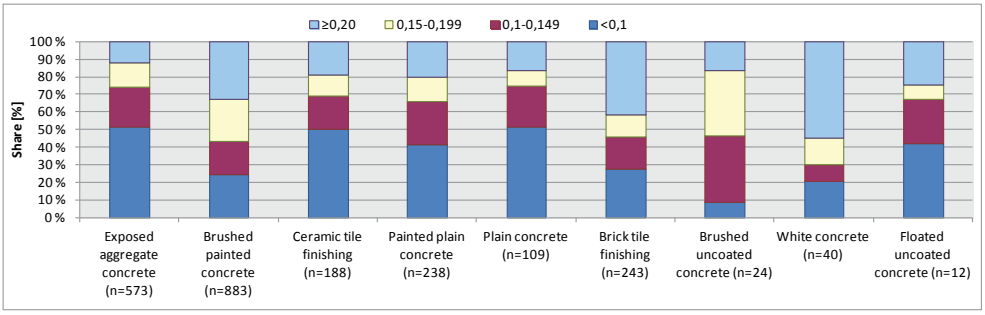

Figure 5 – The distribution of protective pore ratio in different surface finishing of concrete facades [19].

The share of non frost resistant concrete is even higher in all facades according to thin-section analyses (n=1442) than protective pore test shows, see Figure 6. In thin-section analyses the classification of frost resistance bases on the spacing factor of protective pores which is a more accurate method for evaluating frost resistance than the protective pore test.

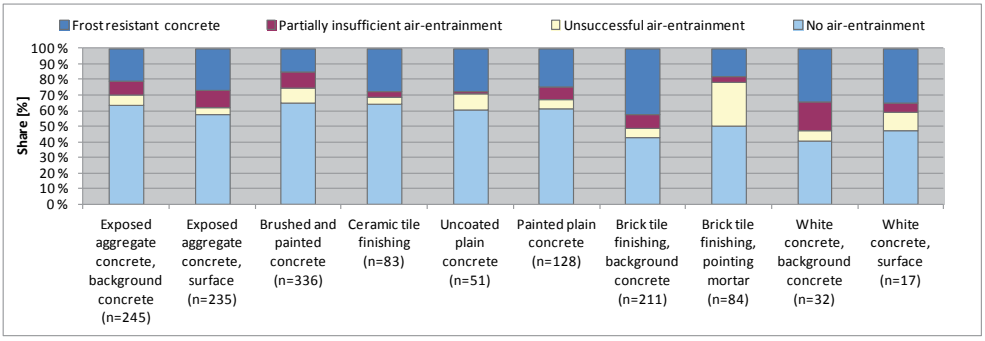

Figure 6 – The distribution of air entrainment according to thin-section analyses in different surface finishing of concrete facades [20].

Air entrainment has been used systematically in concrete since 1976, but the frost resistance of concrete is getting better in facade panels as late as mid 1980's. Material properties concerning frost resistance of concrete are similar in certain facade type made in certain year all around the country.

4.2 Frost damage in concrete facades

According to the database 42.7 % of Finnish concrete facades have visual frost damage. 35.4 % of the damage was localized, and 7.3 % was wide spread. The situation related to frost damage in concrete was similar also in thin-section analyses where incipient frost damage can be found, too. Frost damage of concrete has been found to be more common in coastal area than inland.

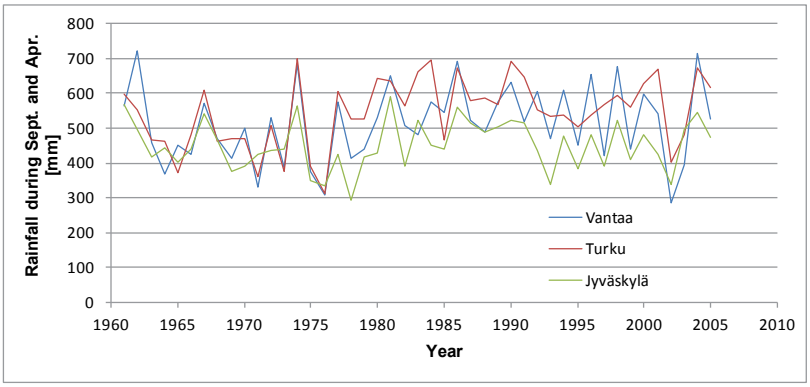

Figure 7 – Liquid precipitation during winter time from September to April at Jyväskylä (inland), Vantaa (south costal area) and Turku (coast line) between 1961 and 2005.

The amount of liquid precipitation i.e. rain and wet snow, during winter time in the coastal area (Turku) and southern Finland (Vantaa) is compared to inland (Jyväskylä) in Figure 7. In the coastal area and southern Finland the amount of rainfall is every year higher than inland. Thus the higher rainfall amounts would be a reasonable explanation for more frost damage in the coastal area than inland, because the material properties of concrete are the same all around the country.

4.3 The influence of prevailing wind direction

The amount of annual rainfall is not uniformly distributed to facades. The distribution of rainfall depends on the height of the building and also prevailing wind directions during rain. According to Jerling and Schechninger [21], the upper parts and corners of facades get more rainfall than lower and central parts. The effect of wind to the distribution of the rainfall on the facade can be seen in practise in Figure 8. An upper part of the concrete building is already wet while the lower part is still dry and no rain is falling on the window facade.

Figure 8 – Head of the concrete building in the beginning of a rain event. The upper parts get more rain than the lower ones.

Prevailing wind directions and wind speeds have a strong influence on the distribution of rainfall on a building. Most of the liquid precipitation in wintertime comes with southerly to westerly winds. Rain events with wind from other directions have been rare, see Figure 9.

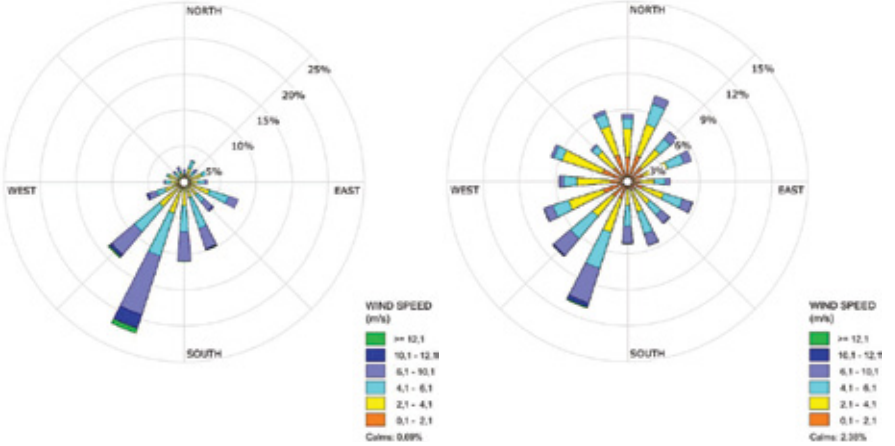

Figure 9 – Prevailing wind directions in wintertime during liquid precipitation on the left and at all times including snowfall and dry weather on the right. Weather data is measured at Helsinki-Vantaa airport during Sept. 1975 to Apr. 1980.

Hardly any frost damage can be seen on the north or east facades despite of the fact that the frost resistance of concrete in those facades is as poor as on the south and west facades. The high outdoor relative humidity in Finland during winter time is not sufficient to upraise the humidity of concrete high enough for frost damage. Thus, the frost damage taking place needs also rainfall. In Finland, prevailing wind directions during rainfall in winter are southerly to westerly. Snowfall cannot be adsorbed in the pore structure of concrete. This is a reasonable explanation for more frost damage on southern and western facades than northern and eastern.

4.4 Annual freeze-thaw cycles

The amount of annual freeze-thaw cycles has a large variation. In general more freeze-thaw cycles occur in inland than coastal area. Average annual freeze-thaw cycles are presented in Table 1. According to Fagerlund [18] frost damage will occur only if concrete is wet enough.

Freeze-thaw cycles are not harmful for dry concrete. For this reason freeze-thaw cycles have been counted also in cases, where raining or wet snowing has been followed by freezing during three days and outdoor temperature decreases to < -2 °C, < -5 °C and < -10 °C.

Table 1 – Average number of annual freeze-thaw cycles during 1961 and 2006 in three meteorological stations.

Measurement station	Outdoor exposure	Temperature [°C]	Number of freeze-thaw cycles average	min.	max.
Helsinki	all	< 0	76.4	26	122
Kaisaniemi	rainfall ≤ 3 days	< -2	22.3	11	34
	before freezing	< -5	14.0	6	23
		< -10	5.9	1	13
Helsinki-Vantaa	all	< 0	89.9	34	150
airport	rainfall ≤ 3 days	< -2	22.0	8	33
	before freezing	< -5	13.6	4	26
		< -10	6.1	2	12
Jyväskylä	all	< 0	91.5	45	132
airport	rainfall ≤ 3 days	< -2	23.5	15	33
	before freezing	< -5	16.4	8	25
		< -10	8.2	2	15

According to thin-section analyses in done condition assessments, the smallest number of freeze-thaw cycles causing the incipient frost damage in concrete was 210 cycles and general frost damage after 207 cycles (t≤ -5 °C) in coastal area. The numbers inland was 270 and 277, respectively. It can be noticed, that the number of required freeze-thaw cycles for same damage level in coastal area is remarkable lower than inland. Because the occurrence of frost damage is more common in coastal area than inland, the amount of rainfall to facades is more crucial than just the number of freeze-thaw cycles.

4.5 Other weathering mechanisms

Alkali aggregate reaction (AAR) and formation of late ettringite might also cause weathering of concrete together with frost damage.

Despite the fact that incipient filling of pore structure of concrete appears in more than 25 % of all facade types, formation of late ettringite has not caused any weathering in Finnish concrete facades. Late ettringite decreases the volume of pore structure and by that way makes frost damage possible even with smaller amount of water than is required for normal frost damage.

AAR is very rare in Finland. Only ten cases from bridges have been found during the last ten years [22]. In this study 1442 thin-section analyses have been made on Finnish concrete facades without any signs of AAR.

5. REPAIR POSSIBILITIES

In Finland concrete facade renovation methods are divided into three categories (repair principles):

- protective repair methods
- cladding
- demolition of outer layer of facade panel and rebuilding.

Protective repair methods are suitable mainly for structures where deterioration has just begun and the damage is not widespread. The most usable protective repair is protective coatings in most of the cases on Finnish concrete facades.

Protective coatings may be utilised if the structure is still in good shape but there is risk of future damage, like in insufficient frost resistant concrete. Concrete that is not air-entrained or is made with alkalisusceptible aggregate or where the carbonation front has advanced near the reinforcement are examples where a protective coating may be a good solution for retarding deterioration. It should be pointed out that protective coatings may not function as expected if the concrete is already damaged. A typical service-life for a protective coating on a concrete facade is around 20 - 25 years.

In many cases facades already have some local damage which can be repaired by patch repairs. Patch repair is a traditional way of repairing local damage in all kinds of concrete structures. It can be a light method in connection with coating renewal, but also involve heavy repair. In the heavy alternative, also areas where the damage is still unseen are repaired.

The basic idea of a patch repair in case of frost damage is to remove deteriorated concrete, and then replace the removed concrete with new material. Cast concrete, shotcrete or, most usually, special repair mortar is used in the work. The surface of the repaired area is finished by different methods depending on the surface type. In the case of painted plain concrete surfaces the whole facade may be treated with finishing mortar and then recoated.

Patch repair is a feasible method when the amount of damage is very limited, like small local incipient disintegration and the repair work is easy and simple. In principle, patch repairs are suitable when the aim is to conserve the present appearance of the building. A typical service-life for a thorough patch repair on a concrete facade is around 20 - 30 years.

If the existing concrete structures are more severely damaged, protective repair methods are no longer effective. In that case, the facade panels are usually added thermal insulation and covered with different metal cassettes etc. In the case, where the outer layers of the facade panels are so extensively and far damaged, that safety of the connections of the panels are endangered, the outer layer of the facade panels is usually demolished and replaced with a new structure, for example rendering over thermal insulation.

6. CONCLUSIONS

According to the condition assessments made to existing concrete facades, the material properties related to frost resistance of concrete very rarely fulfil the requirements of Finnish national building codes. Despite of the insufficient frost resistance of concrete, visually seen far advanced and wide spread frost damage is relative rare. Frost damage appears mostly on facades, which get more rain. In Finland those are upper parts of southern and western facades.

Moisture behaviour and environmental exposure have a strong impact on the actual frost damage of concrete. For instance, the stress on concrete facade depends on the amount of rain, prevailing wind direction during rain and number of freeze-thaw cycles. In most of the cases the insufficient frost resistance has not lead to far advanced or wide spread frost damage. Despite of the similar material properties of concrete in different facades, in several cases it has been

noticed, that the frost damage occurs only on the facades facing south-east to west. This is explained by prevailing wind directions during liquid precipitation.

In approximately 70 % of existing concrete facades the protective pore ratio is less than 0.15. Despite of this 50 to 70 % of buildings, depending on facade type, do not have any visible frost damage. It is possible to have good results with thorough patch repairs and protective coatings in most of the cases, because these protective measures decrease effectively the moisture content in concrete and this stops frost damage completely and also slows the corrosion rate by 30 to 80 %. Again, it has been estimated that it is possible to get 30 years of more service life for concrete facades with protective measures mentioned before compared to not doing measures.

REFERENCES

1. Vainio, T., Lehtinen, E., Nuuttila, H. 2005. Building and renovation of facades. Tampere. VTT. 26 p. + app. 13 p. (in Finnish)
2. Statistics Finland 2011. www.tilastokeskus.fi. Reference date Nov. 17th 2011. (in Finnish)
3. Vainio, T. et al. 2002: Repair, maintenance and improvement work in Finland 2000-2010. Espoo. VTT Research Notes 2154. 60 p. + app. 25 p. (in Finnish)
4. Pentti, M., Mattila, J., Wahlman, J. 1998. Repair of concrete facades and balconies. Part 1: Structures, degradation and condition investigation. Tampere. Tampere University of Technology, Structural Engineering. Publication 87. 156 p. (in Finnish)
5. Vikström, K. 1991. Facades panels from 1950's until today. Proceedings of Damage and repair of concrete structures. Helsinki. October 9-10. Concrete Association of Finland. 30 p. (in Finnish)
6. Guidelines for durability and service life of concrete structures. 1989. BY 32. Helsinki. Concrete Association of Finland. 60 p. (in Finnish)
7. Guidelines for durability and service life of concrete structures. 1992. BY 32. Helsinki. Concrete Association of Finland. 66 p. (in Finnish)
8. Kuosa, H., Vesikari, E. 2000. Ensuring of concrete frost resistance Part 1: Basic data and service life design. VTT Technical Research Centre of Finland . Research notes 2056. 141 p. (in Finnish)
9. Fagerlund, G. 1977. The critical degree of saturation method of assessing the freze/thaw resistance of concrete. Tentative RILEM recommendation. Prepared on behalf of RILEM Committee 4 CDC. Materiaux et Constructions 1977 no 58. Pp. 217-229
10. Powers, T. C. 1949. The air requirement of frost-resistant concrete. Chicago: Portland Cement Association, Research and Development laboratories, Development Department. Bulletin 33.
11. Powers, T. C., Helmuth, R. A. 1953. Theory of volume changes in hardened Portland cement pastes during freezing. In Proceedings of the Highway Research Board 32. Pp. 285-295
12. Pigeon, M., Pleau, R.1995. Durability of concrete in cold climates. Suffolk. E & FN Spon. 244 p.
13. Litvan, G. 1972. Phase transitions of adsorbates IV – Mechanism of frost action in hardened cement paste. Journal of the American Ceramic Society 55 (1). Pp. 38-42
14. Penttala, V. 1998. Freezing-induced strains and pressures in wet porous materials and especially in concrete mortars. Advanced Cement Based Materials 7/1998. Pp. 8 – 19
15. Hedlund, H., Jonasson, J. E. 2000. Effect on stress development of restrained thermal and moisture deformation, In Baroghel-Bouny, V., Aïticin, P.-C. (editors) Shrinkage of concrete, Shrinkage 2000. Cachan Cedex. RILEM Proceedings PRO17. Pp. 355-377
16. Mäkinen, K. 2010. Strength and physical properties of materials, In Builders calendar 2011. Hämeenlinna. Rakennustieto Oy Pp. 375-378 (in Finnish)
17. Neville, A. 1995. Properties of concrete. Essex. Longman Group. 844 p.

18. Fagerlund, G. 2002. Mechanical damage and fatigue effects associated with freeze-thaw of materials. In Setzer, M. J., Auberg, R., Keck, H.-J. (editors) Frost resistance of concrete. Cachan Cedex. RILEM Proceedings PRO24. Pp. 117-132
19. SFS 4475. 1988. Concrete. Frost resistance. Protective pore ratio. Finnish Standards Association SFS. 2 p. (In Finnish)
20. Lahdensivu, J, Varjonen, S, Köliö, A. 2010. Repair strategies of concrete facades and balconies. Tampere, Tampere University of Technology, Department of Structural Engineering, Research report 148. 79 p. (In Finnish)
21. Jerling A., Schechninger B. 1983. Fogars beständighet. Byggforskningrådet. Rapport R89:1083. Stockholm. 172 p. (in Swedish)
22. Pyy, H., Holt, E. 2010. Does Finland have an alkali-aggregate reaction problem? Betoni 4/2010. Helsinki. Suomen Betonitieto Oy. Pp. 46-48. (in Finnish)

Flexural-Shear Failure of a Full Scale Tested RC bridge Strengthened with NSM CFRP. Shear capacity analysis

Gabriel Sas
Ph.D., Researcher
NORUT, N-8504 Narvik, Norway.
Ph.D., Assistant Lecturer
Luleå University of Technology, 971 87, Luleå, Sweden.
Corresponding author: gabriel.sas@ltu.se

Thomas Blanksvärd
Ph.D., Assistant Lecturer
Luleå University of Technology, 971 87, Luleå, Sweden.
thomas.blanksvard@ltu.se

Ola Enochsson
Tech. Lic., PhD Student
Luleå University of Technology, 971 87, Luleå, Sweden
ola.enochsson@ltu.se

Björn Täljsten
Ph.D., Professor
Luleå University of Technology, 971 87, Luleå, Sweden.
bjorn.taljsten@ltu.se

Arto Puurula
Tech. Lic, PhD Student
Luleå University of Technology, 971 87, Luleå, Sweden
Arto.Puurula@savonia.fi

Lennart Elfgren
Ph.D., Emeritus Professor
Luleå University of Technology, 971 87 Luleå, Sweden
lennart.elfgren@ltu.se

ABSTRACT

A test to failure has been carried out on a 50-year-old RC railway trough bridge strengthened in flexure with near-surface mounted (NSM) Carbon Fibre Reinforced Polymers (CFRP) bars. The failure occurred at 11.7 MN load, by a flexural shear failure mechanism. At failure intermediate crack (IC) debonding of the CFRP bars was noticed, and at the same moment the major shear crack opened. The NSM CFRP increased both the flexural and shear capacity of the bridge. The present codes provided conservative estimates of shear force capacity; more accurate models are required for detailed capacity assessments of existing concrete through bridges.

Key words: Bridge tests, Load bearing capacity, Standards and Codes, Fibre reinforced polymer, Reinforced concrete, Shear failure, Debonding

1. INTRODUCTION

Periodical maintenance is required to prevent structural damage of reinforced concrete (RC) bridges, partly because they lose serviceability due to material degradation caused by external factors such as aggressive chemical agents, limited concrete cover, accidental impacts or loads, and extreme environmental conditions. In addition, there are inevitable changes in service loads, notably increases in traffic loads, and/or developments in design codes. *Inter alia*, during the last 50 years there have been important changes in the shear design of concrete structures, regarding: (1) the allowable concrete shear stress, which has declined considerably since 1950 [1]; (2) the interaction between shear and bending, which is not explicitly treated in all codes, see [2,3]; (3) the concrete contribution to shear resistance due to aggregate interlocking [4,5]; and (4) consideration of the influence of element size, which results in the greater brittle failure of larger structures than scaled laboratory specimens [6-8]. These are major concerns since 67 % of European railway bridges are older than 50 years [9], hence most of these bridges require specific monitoring, strength assessment and structural rehabilitation or strengthening as a result of increases in traffic loads, frequencies and speeds. Some of the aspects mentioned above have been addressed, to varying degrees, in recent updates of three of the major design codes: ACI [10], Eurocode [11] and CSA [12]. However, validating the models applied in the codes has been difficult since few results of full-scale failure load tests have been published [13-17], possibly because of time, safety and cost constraints. Such data are extremely valuable for elucidating the complex structural behaviour of bridges and their components, e.g. failure test results of properly scaled structures are highly valuable for describing the effect of the size of RC members on their shear failure [18, 19].

Clearly, there is a need for refining current design methods, and/or developing new techniques, for monitoring and assessing bridges in service, and for testing possible solutions for repairing and strengthening them. These were major aims of the Integrated Research Project ‘‘Sustainable Bridges’’, part of the European Framework Program 6, which incorporated field tests of existing bridges. This paper describes results of the tests on one of the selected bridges; the two-span, concrete railway trough Örnsköldsvik Bridge in Sweden (Figure 1). For all of the above reasons, it was considered to be more scientifically challenging to investigate the shear failure mechanism rather than the flexural failure. Hence, this bridge was strengthened in flexure with NSM CFRP bars in order to ensure a shear failure following loading in the test. The NSM reinforcement strengthening increased the flexural capacity of the bridge, thus resulting in the desired shear failure. However, the complexity of the failure mechanism also increased; the shear failure occurred simultaneously with flexural failure, and intermediary crack (IC) debonding of the NSM reinforcement from the concrete surface was noticed. The paper first describes the test applied to the bridge, and then considers the performance of three of the most widely used shear theories, which are applied in the three major standards mentioned above.

Figure 1 – The tested railway bridge in Örnsköldsvik, Sweden.

2. THE INVESTIGATED BRIDGE

The studied bridge is a RC railway trough bridge located in Örnsköldsvik, Sweden, see Figure 1, which was taken out of service in 2005 when a new high-speed railway line, the Botnia Line, was built. The bridge was a frame bridge with two spans (~ 12+12 m), a slight longitudinal curvature (R = 300 m) and supports skewed with an angle of nearly 17 degrees (16º43'), see Figure 2. The available original calculations showed that a static scheme was considered in the design procedure, with a distributed load over the entire length of the bridge and another with concentrated loads, as documented in [20]. Based on those design procedures the bridge was reinforced for both flexure and shear according to the arrangement presented in Figure 3 and Figure 4.

2.1 Material properties

The bridge was designed using a K 400 (40 MPa) concrete class and Ks 40 (400 MPa) quality steel reinforcement. According to the current European Standard Eurocode [11], the specified concrete had an equivalent strength class of approx. C28/35. The steel reinforcement consisted of hot rolled steel bars with diameters (Ø) of 10, 16 and 25 mm (see also Figure 3 and Figure 4). Prior to the test concrete cylinder core samples were collected and tested. The mean value of the concrete cylinder compressive strength was determined to be 68.5 MPa, with a standard deviation of 8 MPa. According to the Eurocode [21] standard this value corresponded to a characteristic compressive strength of 57 MPa. The steel reinforcement properties were tested according to [22] after the bridge has been demolished. The tests indicated that the Ø 16 and 25 mm bars had tensile strengths of 441 and 411 MPa at yielding (see Figure 5). No Ø 10 mm bars were tested.

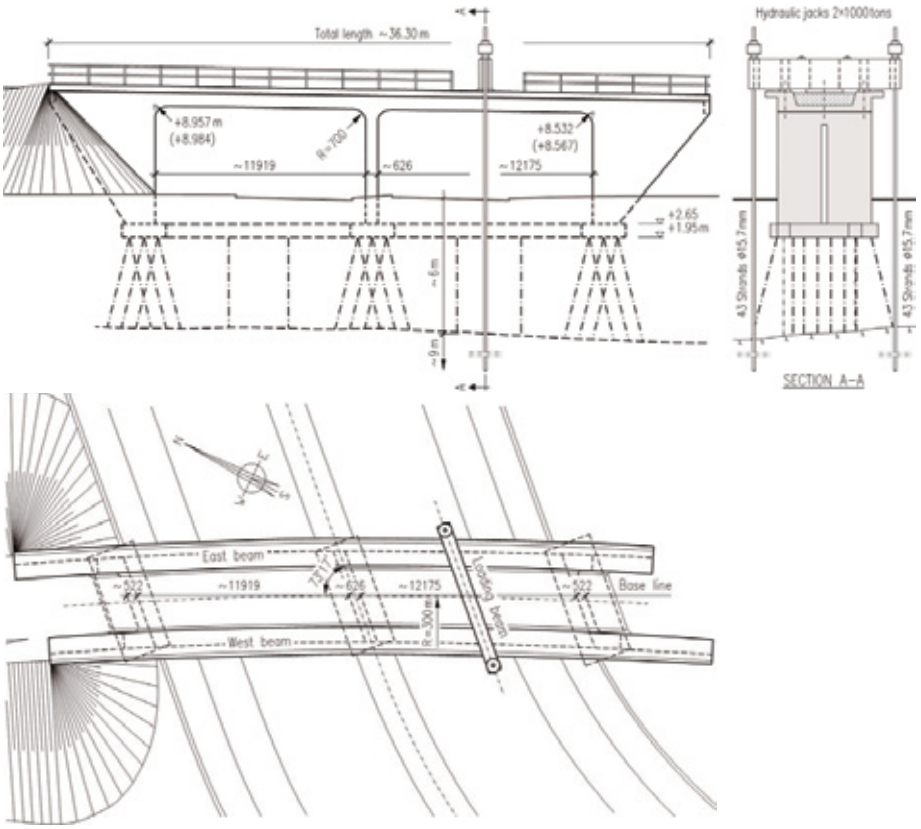

Figure 2 – Elevation, plan and section of the bridge together with the loading arrangement [mm]. The South landfill was removed before the test.

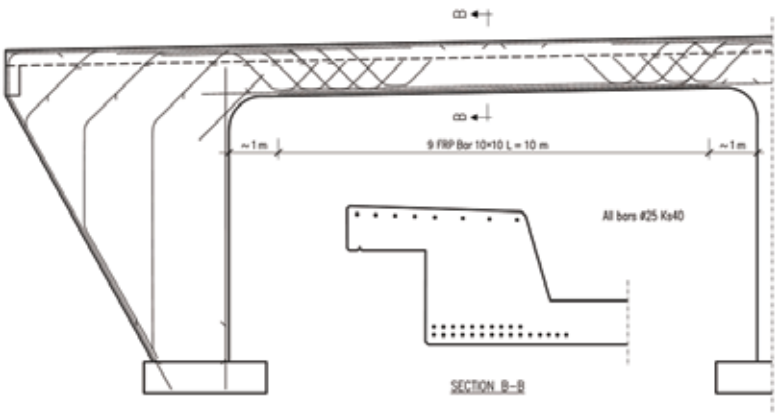

Figure 3 – Longitudinal section from East of the tested span with bending steel reinforcement according to construction drawings from 1954 and the strengthening with NSM CFRP applied before the final test to failure.

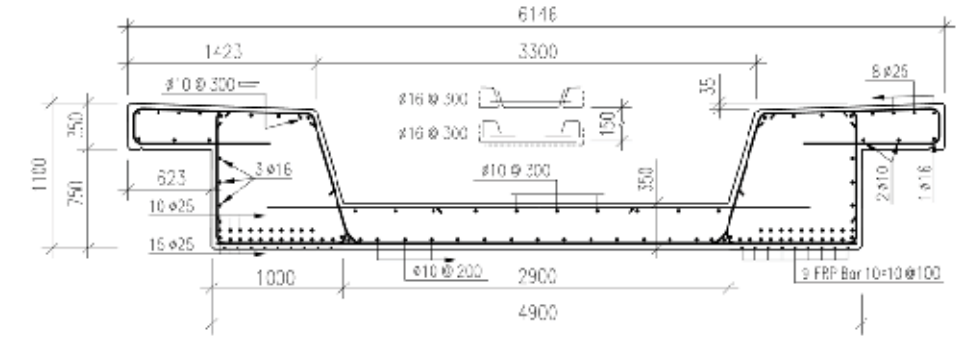

Figure 4 – Cross-section, showing dimensions and reinforcement according to construction drawings from 1954 and the strengthening with NSM CFRP applied before the final test to failure.

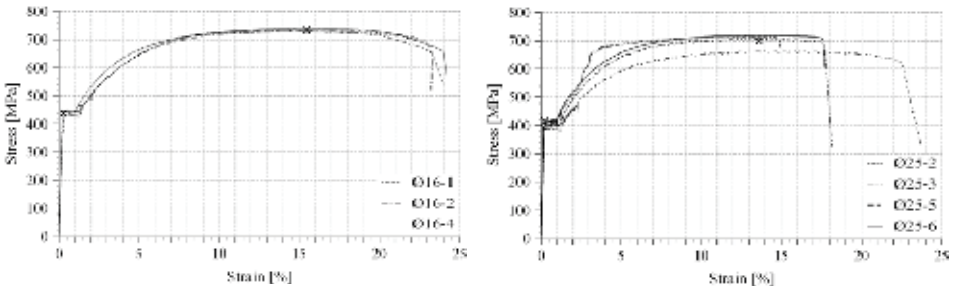

Figure 5 – Steel reinforcement behaviour from material tests. Estimated mean values of yield stress (f_y) and ultimate stress (f_{yu}) are indicated by crosses.

2.2 Test setup

The bridge was tested under a load control regime with a loading protocol designed to facilitate monitoring of the bridge's condition and the development of cracks. The load was generated by two hydraulic jacks, each with a capacity of 1000 tonnes, placed on top of a loading beam, and which exerted a downward force on the loading beam by pulling on steel tendons anchored in the bedrock to a depth of 9 m, see Figure 2. The loading beam was placed over the middle of the second span and positioned so that its longitudinal axis was oriented transverse to the longitudinal direction of the bridge.

3. CAPACITY ASSESSMENT

Calculating the shear capacity of the bridge was not straightforward. At the time of the test two standards were used for this purpose; the Swedish national standard [23] and the draft version of the European standard [11]. The shear capacity provisions in these two standards are different; while the Swedish standard [23] applies a fixed truss model, the European norm uses the variable angle truss model. Given awareness of their conservative nature, to obtain a realistic assessment the shear force capacity was determined using a combination of these two methods.

The concrete's contribution was calculated using the Swedish code and the stirrups' contribution using the European standard, considering a crack inclination angle of 30°. These calculations are detailed in [20], therefore this paper only presents the results that justified the FRP strengthening procedure. The shear force and bending capacity of the bridge before strengthening were determined to be 4.92 MN and 10 MNm**,** respectively. From these values, the permanent load of the bridge produces a shear force of 0.72 MN and a bending moment of 0.76 MNm. The load *P* required for shear failure was estimated to be 8.29 MN and the load required for bending failure 5.76 MN. Since a shear failure was desired the bending capacity needed to be increased, to ca. 14.4 MNm, to accommodate a minimum concentrated load of about 8.3 MN. Thus a bending capacity deficit of ca. 4.4 MNm needed to be carried by the FRP strengthening. Therefore, the bridge was strengthened before the final failure test with 18 (nine per beam) 10 m long NSM CFRP bars, each with a 10×10 mm cross section. The modulus of elasticity and the tensile strain at failure were 250 GPa and 0.8 %, respectively. The detailed design procedure of the NSM strengthening is presented elsewhere [24, 25].

4. TEST RESULTS AND FAILURE

Failure was relatively ductile, as can be seen in Figure 6, and the bridge was intact after the test finished. The recorded failure load *P* was 11.7 MN. The steel tensile reinforcement yielded in both beams. As shown in Figure 7, the strain gauge installed on the tensile reinforcement in the East beam recorded strain values beyond the yield limit (0.2%), in the steel tensile reinforcement and 0.73% in the NSM reinforcement when failure of the bridge occurred.

No strain gauges were installed on the stirrups. Instead, a recently developed photographic monitoring system was used to record the strain that developed at the concrete surface. The area monitored is highlighted as the "speckled" area in Figure 8. A complete description of the use of this photographic monitoring system is presented in [20]. For safety reasons the photographic strain measurements stopped at a loading of 10.8 MN, which is below the failure load of 11.7 MN. As shown in [26], this method can provide very good correlations between the strains measured on the surface of concrete and those measured with discrete gauges. [26] also pointed out that photographic strain measurements are more reliable than discrete gauge measurements. The latter can be highly influenced by the positioning of the gauges with respect to emerging cracks, while the former captures the strains on the surface of the concrete

This can also clearly be seen in Figure 7 in the difference between the load-strain curves for the steel in the East and West beams (in which the yielding did and did not appear, respectively). The vertical strains measured at the surface of the concrete (Figure 9a) show that the stirrups were already yielding at 10.8 MN load, hence it can be assumed that a shear failure was imminent and the shear crack did not develop fully until the stirrups yielded and the FRP bars lost their bond. Moreover, Figure 9a shows that the principal tensile strains at the level of the tensile reinforcement (bottom of Figure 9b) were considerably higher than the strain measured at the same load (10.8 MN) with the strain gauges (Figure 7). The mechanism of failure was a simultaneous flexural-shear failure, resulting in the formation of flexural-shear cracks in both beams at an angle of about 32°. Although both stirrups and the tensile reinforcement yielded at the same time it is not clear if the shear failure triggered the flexural failure or vice versa. However, it is believed that the NSM reinforcement played a major role in the failure process. The video recorded during the test shows that IC debonding occurred simultaneously with the shear failure (see Figure 10).

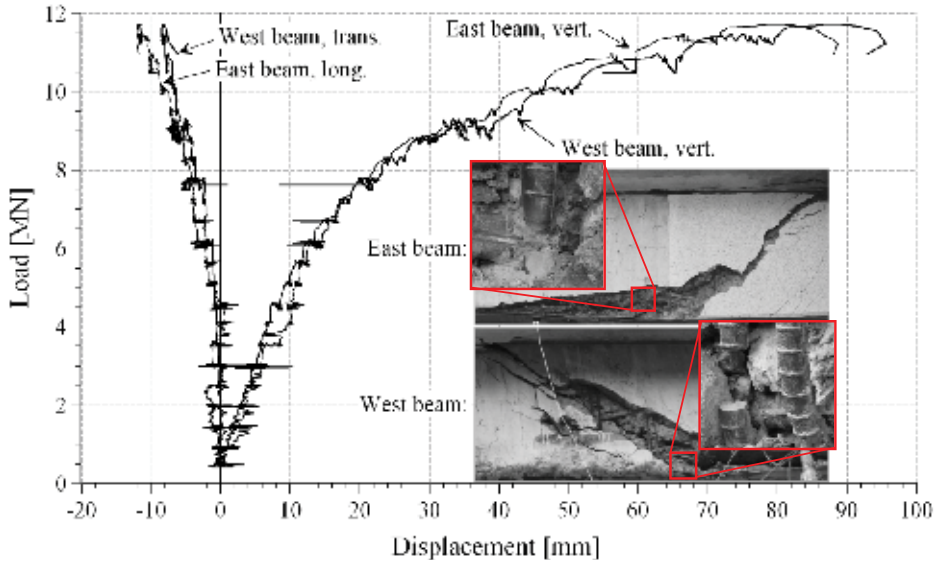

Figure 6 – Load-displacement curves recorded at the mid-section of the bridge and the crack pattern after failure of both beams, see also Figure 7.

Due to the IC bond failure of the CFRP, the force in the CFRP bars suddenly decreased and was transferred partly to the steel tensile reinforcement (see Figure 11a) and partly to the stirrups. The reduction of the force carried by the NSM bars increased the inclination of the concrete struts from θ_0 to θ_1 and reduced the number of stirrups that carried the shear force V, see Figure 11b. Consequently, fewer stirrups had to carry the same load, accelerating deformation of these stirrups and causing the final rupture.

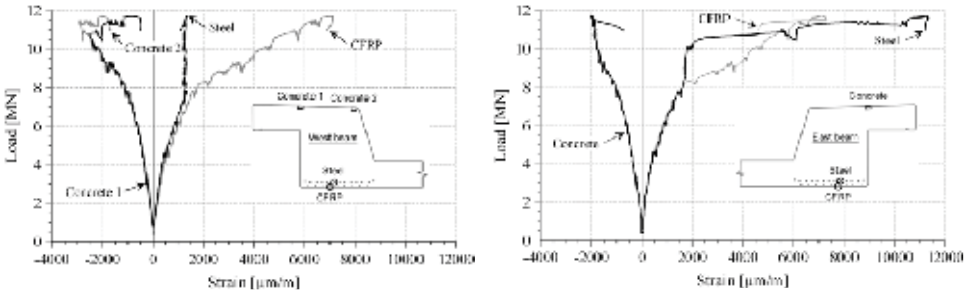

Figure 7 – Load-strain relationships in the most utilized (mid) section, see also Figure 8

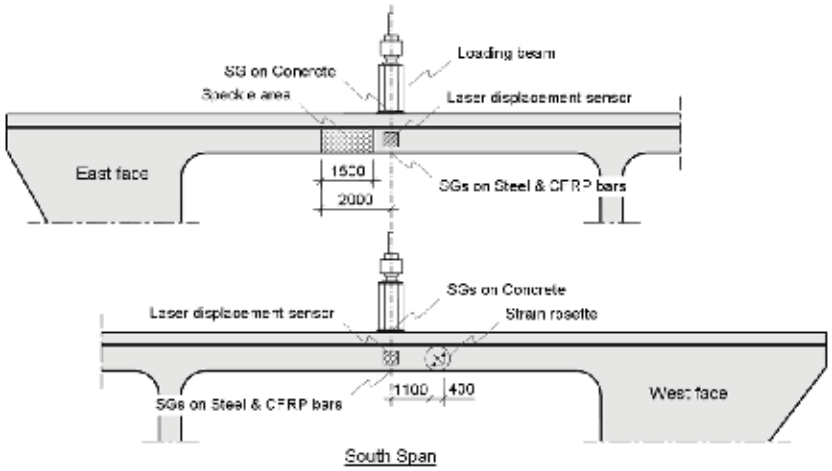

Figure 8 – Instrumentation installed on the bridge

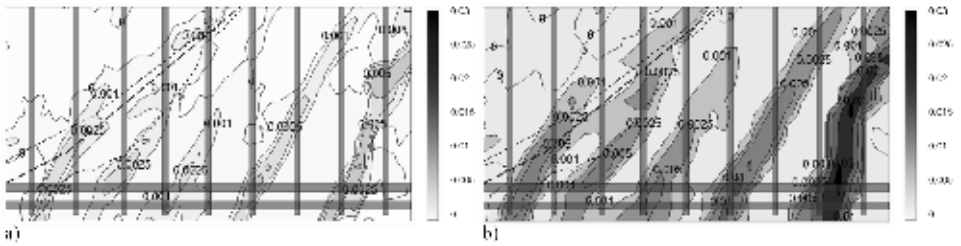

Figure 9 – Tensile strains (a, vertical and b, principal) at the concrete surface on the East beam face measured with photographic tools at P = 10.8 MN load. The approximate positions of the tensile and shear reinforcements are shown, together with the position of the final failure crack. The dashed and dotted lines represent the inclination and contour of the shear crack, respectively.

5. CAPACITY PREDICTIONS BY CURRENT STANDARDS

In this section predictions of the shear force capacity obtained using three major standards [10-12] are compared and analyzed. These codes were selected because they are based on the three major theories currently used for assessing the shear force capacity of structural elements in design processes: the variable angle truss model (VAT), the fixed angle truss model (45°TM) and the modified compression field theory, respectively. Previously presented values for the flexural capacity of the bridge before and after strengthening [20, 27] are used here for calculating the shear force bending moment interaction for one beam, and the shear capacity is considered to be similar for the other beam. The geometrical properties of the calculated beam are presented in Figure 12.

a) b)

c) d)

Figure 10 – Frames from the video recorded during the failure of the bridge. The captions are taken within an interval of 1.5 seconds. a)initiation of the failure b) IC debonding of the NSM CFRP c)opening of the diagonal cracks d) formation of the major diagonal crack and debonding of the NSM CFRP with concrete cover

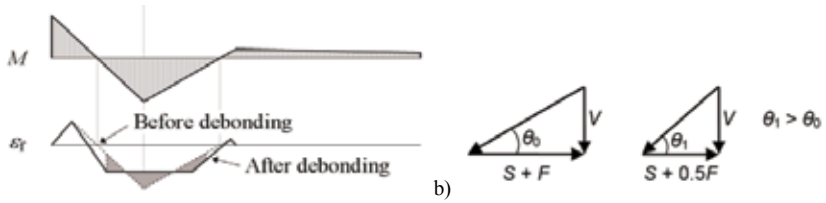

a) b)

Figure 11 – Effect of the NSM bond failure on: a) the strain distribution in the tensile reinforcement and b) the truss mechanism

To evaluate the performance of these models for assessing the examined structural elements the following scenario is considered. It is assumed that the codes are used prior to the test. This means that the real values of the material properties, obtained from standardized tests, are available for concrete but not for the steel reinforcement. The mean concrete compressive strength was determined from concrete cylinder tests, see [20] for further details.

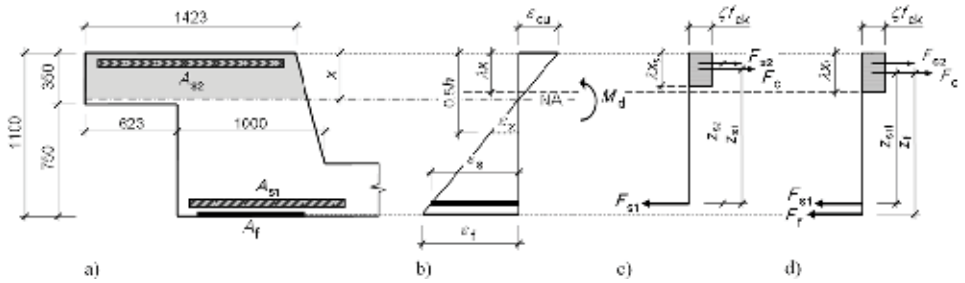

Figure 12 – The cross-section used in the calculations.

Since the strength of the steel reinforcement was determined after the bridge was demolished, the value of the steel strength used to obtain the predictions by each of the standards is the nominal value indicated in the original documentation of the bridge, 400 MPa. The design efforts are determined using linear finite element analysis calculations. The interaction between the shear force and bending moment, as a function of the unit load *P*, is presented in Figure 13. These calculations are more refined and less conservative than those used in the initial assessment, in which a simplified static scheme was used due to time constraints, see [20]. It should be noted that since the dead load was already acting on the bridge, its effect on the efforts (the hatched parts of the diagrams in Figure 13b and c) determined with the finite element analysis have not been considered in the analysis. The predictions of the models are determined for both the non-strengthened (Table 1) and strengthened bridge (Table 2). However, no similar un-strengthened bridge was tested; therefore these results are qualitative and serve only for comparing the effect of adding the CFRP.

5.1 Eurocode

In the European standard Eurocode [11] the shear strength of the beams is treated independently for members with and without shear reinforcement. The theoretical background of the standard relies on concrete plasticity theory [28] for calculating the concrete capacity and the VAT model for determining the shear reinforcement capacity (Figure 14). The truss model assumes that half of the shear force is carried by the top chord (compressed concrete) and the other half by the tensile chord (tensile reinforcement). As long as stirrups are present in the concrete element the shear force capacity is considered solely using the VAT model and is calculated according to equation (1). The VAT procedure assumes an equilibrium condition in the truss formed by the tensile forces in the bottom chord F_t, the compression forces in the diagonal compressed strut D and the shear force resisted by the stirrups V_s, see Figure 14. For design purposes in Eurocode the inclination of the compressive strut with the longitudinal axis, θ, can be chosen between 21.8° to 45°. For our experiment the maximum shear force capacity of one beam would be obtained using an angle of 21.8°, while the minimum would correspond to 45°, see Table 2. Since there is a large difference between the two values, in the assessment the interaction between the bending moment and the shear force needs to be considered in order to estimate the θ angle. The applied shear force will induce an additional force F_{lv} in the tensile reinforcement (eq. 2). The Eurocode provisions state that the additional tensile force will have maximal effect on the bending capacity at a distance x_1, equivalent to the distance from the point where the crack initiates, see Figure 13d. Thus, the bending moment M_1 at a distance x_1 (Figure 13d) will produce a force F_{lm} in the tensile reinforcement, as given in equation 3. In order to form a valid

truss mechanism the two forces described above, F_{lv} and F_{lm}, must be balanced by the tensile reinforcement force F_l resulting from the applied bending moment M (eq.4). The solution of this equality is found by iterating the crack inclination angle θ. Using this procedure, the angle θ, and the corresponding shear force capacity and applied load were calculated to be 33°8', 1.52 MN and 5.44 MN, respectively (Table 2).

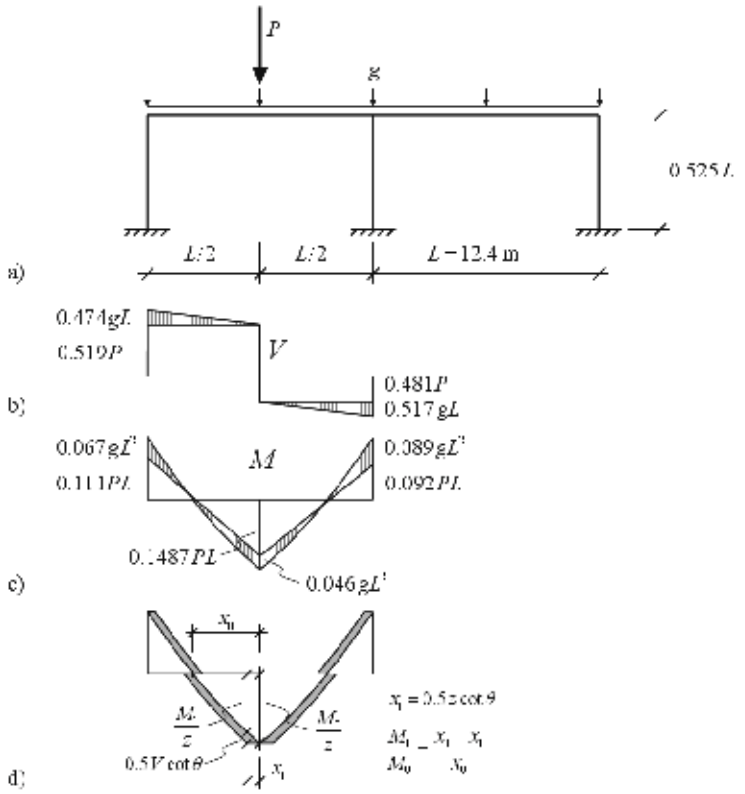

Figure 13 – Shear force and bending moment acting on the bridge under a unit load P = 1 MN and g = 58.7 kN/m. a) geometry, b) shear force V, c) bending moment M, and d) forces in the longitudinal reinforcement due to bending and shear.

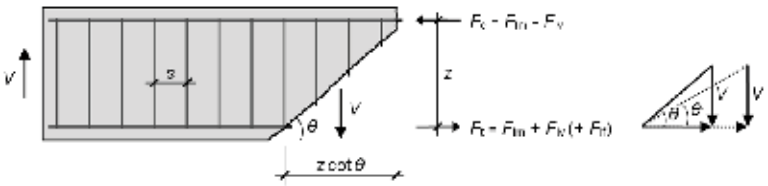

Figure 14 – The VAT model.

$$V_s = \frac{A_{sw} f_y}{s} z \cot\theta \qquad (1)$$

$$F_{lv} = 0.5V\cot\theta \tag{2}$$

$$F_{lm} = M_1/z \tag{3}$$

$$M = A_s f_y z \tag{4}$$

5.2 CSA

In the Canadian standard [12] the general method for calculating the shear capacity of a member is based on the simplified MCFT [5, 29]. In this code, the shear capacity is assumed to be carried by both the concrete and the shear reinforcement. Essentially, the MCFT uses the same equilibrium conditions of the cross-section to derive the equations. In addition to the equations used in VAT, several strain compatibility equations between the concrete, shear and tensile reinforcements are applied. The shear reinforcement contribution is calculated, as in Eurocode using equation 1, while the concrete contribution is expressed as in equation 5. The concrete contribution can be regarded as the tension-stiffening effect on the reinforcement bridging the forming cracks or as shear friction effect (aggregate interlocking) across the inclined cracks, as shown in Figure 15. Describing the concrete contribution is not straightforward, but in the MCFT this is done by refining the cross-sectional equilibrium to accommodate the average tensile stresses in the concrete, f_t, and the upper limit of the ability to transmit shear stresses across the cracks τ_{ci}. In the MCFT these stresses are described by constitutive relationships based on data from numerous shear tests. However, the complexity of these equations has been reduced by calibration and presented as the simplified MCFT, which is currently applied in CSA (equations 5 and 7). Details of the derivation of these equations can be found in [29, 30].

$$V_c = \lambda\beta\sqrt{f_c}\,b_w z \tag{5}$$

$$\theta = 29 + 7000\varepsilon_x \tag{6}$$

$$\beta = \frac{0.4}{(1+1500\varepsilon_x)} \tag{7}$$

$$\varepsilon_x = \frac{M/z + V - V_p + 0.5N - A_p f_{p0}}{2\left(E_s A_s + E_p A_p\right)} \tag{8}$$

The cracking angle θ (eq. 6) and the factor β (eq. 7) accounting for the concrete contribution are given as a function of the longitudinal strain ε_x (eq. 8), calculated at the middle of the cross-section, see Figure 12. It should be noted that use of the longitudinal strain ε_x in equations 6, 7 and 8 implicitly accounts for the shear bending interaction. Thus, here the truss verification used in the previous section cannot be applied. Instead, the procedure for verifying the shear force capacity of the bridge before and after strengthening is iterative, as follows: 1) the longitudinal strain is estimated, 2) the θ angle and the β factors are determined, 3) the shear force is then inserted into equation 8, 4) the resulting value for ε_x is compared with the initial estimate of ε_x, and 5) the process is iterated until convergence. Using this procedure the shear capacity and the load that produces shear failure were determined to be 2.28 MN and 7.67 MN, respectively (Table 2).

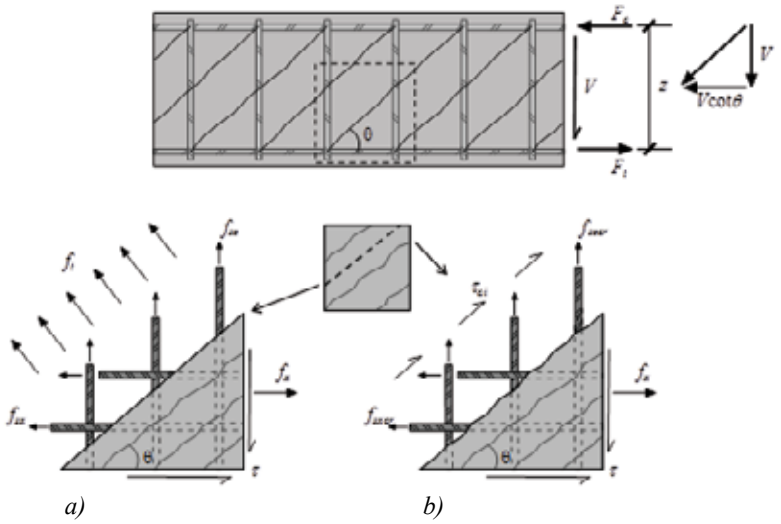

Figure 15 – General description of forces and stresses acting on an element subjected to shear: a) transmission of forces between cracks b) transmission of forces across the cracks

5.3 ACI

In the American standard [10] the sectional approach for modelling shear in one-way flexural members is based on the 45°TM analogy. As in the Canadian Standard approach [12], here the shear capacity is assumed to be carried simultaneously by the concrete and the shear reinforcement. The use of the 45°TM analogy implies that $\cot\theta=1$, therefore the capacity of the stirrups no longer depends on the crack inclination (eq. 9).

$$V_s = \frac{A_{sw} f_y}{s} d \tag{9}$$

The concrete contribution (eq. 10) is purely empirical and has been developed during time, based on regression analysis of many experimental tests [4].

$$V_c = 0.17 \lambda \sqrt{f_c'} b_w d \tag{10}$$

It should be noted that, using equations 9 and 10, this standard does not consider any interaction between bending moment and shear force, hence the CFRP strengthening does not affect the modeled shear response of the bridge. The estimated values of the shear force capacity and the force required for shear failure are 2.29 MN and 7.74 MN, respectively (Table 2).

Table 1 The capacities and the failure loads predicted by the compared standards for the non-strengthened bridge

		EC2		CSA	ACI
θ	21°8’	45°	41°1’	38°6’	45°
V_s (MN)	2.65	1.06	1.21	1.32	1.06
V_c (MN)	-	-	-	0.92	1.24
V_{Rd} (MN)	2.65	1.06	1.21	2.24	2.29
M (MNm)	4.77	4.77	4.77	4.77	4.76
P_V (MN)	9.51	3.81	4.36	7.57	7.74
P_M (MN)	5.17	5.17	5.17	5.17	5.17

Table 2 The capacities and the failure loads predicted by the compared standards for the strengthened bridge

		EC2		CSA	ACI	Test
θ	21°8’	45°	33°8’	37°9’	45°	≈ 32°
V_s (MN)	2.54	1.06	1.52	1.31	1.06	-
V_c (MN)	-	-	-	0.97	1.24	-
V_{Rd} (MN)	2.54	1.02	1.52	2.28	2.29	-
M (MNm)	6.12	6.12	6.12	6.12	6.12	-
P_V (MN)	9.12	3.64	5.44	7.67	7.74	11.7
P_M (MN)	6.64	6.64	6.64	6.64	6.64	11.7

6. DISCUSSION

Clearly all the standards analyzed predict the shear force capacity and the ultimate load of the bridge in a conservative manner. The underlying basis for these shear models is the same, representing the shear mechanism in a beam as a truss mechanism. However, there are major differences in the way this truss mechanism is applied; the ACI [10] and CSA [12] permit use of the concrete’s contribution to the shear capacity, while in Eurocode [11] this is neglected.

Another factor that is responsible for some of the differences in predictions of the shear force is that the codes differ in their treatment of the crack angle inclination. In the ACI code it is assumed to be fixed at 45°, which is a conservative and unrealistic assumption. In the MCFT approach it is determined iteratively from the cross-sectional equilibrium, and is dependent on factors such as the crack spacing, concrete material properties and the average tensile and compressive strains over the cracked sections. Finally, in CSA, the simplified MCFT expression (eq. 6) was adopted, which depends solely on the longitudinal strain ε_x (eq. 8) calculated at the middle of the cross-section (see Figure 12b). However, this equation has been calibrated using data obtained from beams with steel tensile reinforcement, while the bridge was strengthened with FRP reinforcement, a material that displays linear elasticity until failure. This might be one reason why the crack angle estimated by the CSA code does not correspond to the angle observed in the test.

The European standard compensates for the omission of the concrete contribution to the shear capacity by adopting a crack angle that most closely matches the angle observed in the test. In

addition, the VAT model used in Eurocode is a transparent geometrical method and the change in the tensile longitudinal strains due to the addition of the FRP can be easily incorporated in the analysis to obtain cross-sectional equilibrium. As the longitudinal force in the tensile chord of the truss increases, the crack angle is reduced, therefore the assumed crack has to bridge more stirrups in order to obtain equilibrium. In this way Eurocode predicts an increase of the shear force capacity after strengthening. However, disregarding the concrete contribution leads to seriously conservative estimates of the shear capacity.

The other two design codes [10, 12] that incorporate the concrete contribution will give less conservative estimations, but the increase of the longitudinal strains due to the FRP is not captured as straightforwardly as by the VAT used in Eurocode. According to the CSA design code, the addition of the FRP reinforcement (the term E_pA_p in the denominator of eq. 8), will decrease the longitudinal strain at the middle of the cross-section and this reduces the crack angle. Although a lower crack angle implies that more stirrups will carry the shear force, the resulting shear reinforcement contribution V_s is slightly smaller than that estimated without strengthening. However, this loss is compensated by the increase of the concrete contribution V_c. In the ACI design code, the FRP has no influence on the modeled shear force capacity of the strengthened bridge.

7. CONCLUSIONS

This paper describes the full-scale failure test of a bridge strengthened in flexure with NSM CFRP reinforcement, which increased the flexural capacity of the bridge by about 30%. The failure mode observed during the test was a flexural-shear failure, clearly showing that an interaction occurred between the shear and the bending mechanism. However, it is not clear from the measurements obtained during the test if the IC debonding of the FRP triggered the shear failure or vice versa.

The three codes used to predict the shear force capacity of the bridge after the strengthening capture this interaction differently, but all predict the shear force capacity in a conservative manner. One advantage of using Eurocode is that the VAT model predicts the crack inclination angle quite accurately, but it gives the most conservative estimates of the shear capacity because it does not consider the concrete contribution to the total shear capacity (which can lead to unexpected failure modes).

The ACI model is a fixed model that does not consider the flexural shear interaction. The advantages of using this model for such assessment are that it is simple, direct and provides the most realistic estimates.

The CSA model captures the flexural shear interaction in a conservative manner compared to Eurocode. The shear crack angle predicted by this standard and used in the estimation of the shear force capacity leads to more conservative results for the stirrups' contribution than Eurocode, but higher estimates than the ACI model. The authors believe that this is connected to the fact that the longitudinal strain at the middle of the cross-section has been calibrated with test results obtained from steel reinforced concrete beams rather than FRP strengthened beams.
In general, when utilizing FRP to increase flexural capacity, the longitudinal strains increase at the ultimate limit state because the capacity increases. The Eurocode estimates that this will have a positive effect on the shear capacity, lowering the crack angle and thus activating more shear reinforcement due to cross-sectional equilibrium. This effect is not so pronounced when

using the CSA and ACI approaches, because the influencing factors have been calibrated using data obtained from tests on elements with steel reinforcement, not FRP. Therefore, the CSA will give marginally higher estimates of shear capacity for flexural strengthened specimens, and since the ACI code does not consider any bending moment shear force interaction, its estimates of the shear capacity will not be affected by including such strengthening.

In assessments of concrete bridges it is important to use more refined models regarding shear strength than the simple code models presented above, as recently discussed in a shear symposium [31]. Examples of more refined shear models are the MCFT and non linear finite element methods.

NOTATIONS

A_s = area of the tensile reinforcement
A_{sw} = area of the steel stirrups
A_p = area of the prestressing tendons
E_s = steel Young modulus
F_t = tensile force in the bottom chord of the truss
F_{lm} = force in the tensile reinforcement produced by the M_1 bending moment
F_{lv} = force in the tensile reinforcement produced by the shear force
M = maximum bending moment
M_1 = bending moment at the distance x_1 from the maximum bending moment M
N = axial shear force
P_V = the applied force that produces shear failure
P_M = the applied force that produces bending failure
V = shear force
V_c = shear force carried by concrete
V_p = prestressing shear force
V_{Rd} = shear force resistance
V_s = shear force carried by stirrups
b_w = web width of the cross-section
d = effective depth of the cross-section
f'_c = mean value of the concrete compressive strength
f_{p0} = prestressing stress
f_y = yield strength of the steel reinforcement
s = spacing of the stirrups
z = internal lever arm of the non-strengthened cross-section
β = factor accounting for the concrete contribution
ε_x = longitudinal strain at the middle of the cross-section
λ = factor accounting for the use of lightweight concrete
θ = crack angle inclination

REFERENCES

1. Enochsson, O., Puurula, A., and Elfgren, L. (2004). Assessmentof the Load Carrying Capacity of Concrete Bridges. Interaction between torsion, shear and bending in the Källösund Bridge. In Swedish.(eds):Elfgren, L., Luleå University of Technology, Luleå.
2. Thürlimann, B. (1978). "Plastic analysis of reinforced concrete beams. Introductory report from Colloquium Copenhagen 1979: Plasticity in Reinforced Concrete. Reports of the working commissions". City: International Association for Bridges and Structural Engineering (IABSE). Zürich, Switzerland: Zürich pp. 71-90.
3. Elfgren, L. (1979). "Torsion-Bending-Shear in Concrete Beams: A Kinematic Model. Final report from Colloquium Copenhagen 1979: Plasticity in Reinforced Concrete". City: International Association for Bridge and Structural Engineering (IABSE). Zürich, Switzerland, pp. 111-118.
4. ASCE-ACI 445. (1998). "Shear and Torsion: recent approaches to shear design of structural concrete." *Journal of Structural Engineering*, 124(12), pp. 1375-1417.
5. Collins, M., Mitchell, D., and Bentz, E. (2008). "Shear design of concrete structures." *The Structural Engineer*, 86(10), pp. 32-39.
6. Elfgren, L. (1989). "Fracture Mechanics of Concrete Structures. From theory to Applications. A RILEM State of the Art Report". City: Chapman & Hall, London, UK., pp. 407.
7. Elfgren, L., and Noghabai, K. (2002). "Tension of reinforced concrete prisms. Bond properties of reinforcement bars embedded in concrete tie elements. Summary of a RILEM round-robin investigation arranged by TC 147-FMB 'Fracture Mechanics to Anchorage and Bond'." *Materials and Structures*, 35(250), pp. 318-325.
8. Bazant, Z. P., Yu, Q., Gerstle, W., Hanson, J., and Ju, W. (2008). "Justification of ACI 446 proposal for updating ACI code provisions for shear design of reinforced concrete beams." *ACI Structural Journal*, 105(4), pp. 512-515.
9. Bell, B. (2004). "European railway bridge demography", European FP 6 Integrated project "Sustainable Bridges": Assessment for Future Traffic Demands and Longer Lives, http://www.sustainablebridges.net, WP1, accessed date Dec 2011.
10. ACI-318 (2008). "Building code requirements for structural concrete and commentary", Farmington Hills, Michigan: American Concrete Institute, pp. 473, ISBN 978-0-87031-283-0.
11. CEN (2005a). "Eurocode 2: Design of concrete structures - Part 1-1: General rules and rules for buildings", Brussels. European Committee for Standardization, pp. 225, ICS: 91.010.30; 91.080.40.
12. CSA-A23.3 (2009). "Design of concrete structures", Mississauga, Ontario, Canada: Canadian Standards Association, pp. 352, ISBN 1-55397-559-6.
13. Scordelis, A., Larsen, P., and Elfgren, L. (1977). "Ultimate strength of curved RC box girder bridge." *Journal of the Structural Division. Proceedings of the AmericanSociety of Civil Engineers (ASCE)*, 103(8), pp. 1525-1542.
14. Scordelis, A., Elfgren, L., and Larsen, P. (1979). "Time-dependent behaviour of concrete box girder bridges." *ACI Structural Journal*, 76(9), pp. 159-177.
15. Plos, M. (1990). "Full scale shear test of a reinforced concrete slab frame bridge. In Swedish", Gothenburg, Sweden: Division of Concrete Structures, Chalmers University of Technology, Gothenburg, Sweden., pp. 45-72, ISBN 0349-8573.
16. Täljsten, B. (1994). "Plate bonding. Strengthening of existing concrete structures with epoxy bonded plates of steel or fibre reinforced plastics", PhD Thesis, Luleå University of Technology, Luleå, Sweden, pp. 283, ISSN 0348-8373.

17. Plos, M. (1995). "Application of fracture mechanics to concrete bridges. Finite element analysis and experiments", Gothenburg, Sweden: Chalmers University of Technology, pp. 57-70, ISBN 91-7197-218-8.
18. Bazant, Z. P., and Yu, Q. (2005a). "Designing against size effect on shear strength of reinforced concrete beams without stirrups: I. Formulation." *Journal of Structural Engineering*, 131(12), pp. 1877-1885.
19. Bazant, Z. P., and Yu, Q. (2005b). "Designing against size effect on shear strength of reinforced concrete beams without stirrups: II. Verification and calibration." *Journal of Structural Engineering*, 131(12), pp. 1886-1897.
20. Elfgren, L., Enochsson, O., and Thun, H. (2008). "Field test of a concrete bridge in Örnsköldsvik, Sweden", European FP 6 Integrated project "Sustainable Bridges": Assessment for Future Traffic Demands and Longer Lives, http://www.sustainablebridges.net/main.php/SB7.3.pdf?fileitem=22708646, accessed date Dec 2011.
21. CEN (2006). "Assesment of in-situ compessive strength in structures and precast concrete components.", Brussels. European Committee for Standardization, pp., prEN 13971:2006.
22. CEN (2005b). "Steel for reinforcement of concrete – Weldable reinforcing steel – General", Brussels. European Committee for Standardization., pp. 71, EN 10080:2005.
23. BBK04 (2007). "Design rules for concrete structures. In Swedish", Karlskrona, Sweden: Boverket, pp. 272, ISBN 9171478167.
24. Täljsten, B. (2006). "FRP strengthening of existing concrete structures", 4th Edition, Luleå: Luleå University of Technology, pp. 208, 91-89580-03-6.
25. Täljsten, B., Carolin, A., and Pedersen, H. (2008). "Repair and strengthening of railway bridges - Guideline", European FP 6 Integrated project "Sustainable Bridges": Assessment for Future Traffic Demands and Longer Lives, http://www.sustainablebridges.net/main.php/SB6.1_Guideline_STR.pdf?fileitem=14043927, accessed date Dec 2011.
26. Blanksvärd, T. (2007). "Strengthening of concrete structures by the use of mineral based composites", Licentiate Thesis, Luleå University of Technology, Luleå, Sweden.
27. Bergstrom, M., Taljsten, B., and Carolin, A. (2009). "Failure load test of a CFRP strengthened railway bridge in Örnsköldsvik, Sweden." *Journal of Bridge Engineering*, 14(5), pp. 300-308.
28. Nielsen, M. P. (1999). "Limit analysis and concrete plasticity", 2nd ed, Florida, USA: CRC Press LLC, pp. 908, ISBN 0-8493-9126-1.
29. Bentz, E. C., Vecchio, F. J., and Collins, M. R. (2006). "Simplified modified compression field theory for calculating shear strength of reinforced concrete elements." *ACI Structural Journal*, 103(4), pp. 614-624.
30. Collins, M. P., and Mitchell, D. (1991). "Prestressed concrete structures", New Jersey: Prentice-Hall, Inc, pp., 0 13 691635-X.
31. fib-Bulletin 57 (2010). "Shear and punching in RC and FRC elements. Workshop 15-16 October 2010, Salò (Italy)", Lausanne, Switzerland: International Federation for Structural Concrete, pp. 350, 978-2-88394-097-0.

Research Committee and Editorial Board for Nordic Concrete Research

Prof. Dr. Olafur H. Wallevik, Chairman for the Research Committee
Dr. Dirch H. Bager, Editor of Nordic Concrete Research

Danish Concrete Association	Dr. Dirch H. Bager DHB-Consult Lavendelparken 5 DK - 9310 Vodskov Tel: +45 98292412 Mobile: +45 2049 7324 E-mail: dirch.bager@webspeed.dk	Mr. Claus Pade Concrete Centre, Danish Technological Institute Gregersensvej DK - 2630 Taastrup Tel: + 45 7220 2183 E-mail: cpa@teknologisk.dk
Finnish Concrete Association	Prof., Dr. Jussi Mattila Concrete Association of Finland Unioninkatu 14 PL 381 FI - 00131 Helsinki Tel: +358 9 12911 Mobile: +358 400 637 224 E-mail: Jussi.mattila@betoniyhdistys.fi	Lic.Sc.Tech. Klaus Juvas Consolis Technology Box 72 FI – 21291 Rusko Mobile: +358 40 5160 316 E-mail: klaus.juvas@consolis.com
Icelandic Concrete Association	Prof., Dr. Børge Johannes Wigum Mannvit Grensásvegur 1 IS - 108 Reykjavik Tel: +354 422 3030 Mobile: +354 896-0756 E-mail: wigum@mannvit.is	Prof. Dr. Olafur H. Wallevik Innovation Center Iceland IS - 112 Keldnaholti Tel: +354 522 9000 Mobile: +354 E-mail: wallevik@ru.is
Norwegian Concrete Association	Dr. Terje F. Rønning Norcem, FoU Department P.O.Box 38 N - 3991 Brevik Tel.: +47 3557 2347 Mobile: +47 9157 6046 E-mail: terje.ronning@norcem.no	Dr. Ing. Helge Brå Norwegian Public Road Authority Abelsgate 5 N – 7030 Trondheim Mobile: +47 9709 5277 E-mail: helge.braa@vegvesen.no
Swedish Concrete Association	Tekn.Dr, Prof. Mikael Hallgren Tyréns AB Peter Myndes Backe 16 SE - 118 86 Stockholm Tel: +46 104 522 351 Mobile: +46 70 661 05 33 E-mail: Mikael.Hallgren@tyrens.se	Tekn. Dr. Peter Utgenannt CBI Swedish Cement and Concrete Research Institute P.O. Box 857 SE - 501 15 Borås Tel: +46 105 166 870 Mobile:+46 706 452 008 E-mail: peter.utgenannt@cbi.se

30 November 2011

Active reviewers for Nordic Concrete Research as per November 2011

DENMARK	
Dr.	Dirch H. Bager
Prof., Dr.	Lars Damkilde
Dr.	Mette Glavind
Prof., Dr.	Per Goltermann
Mr.	Oscar Klinghoffer
Prof., Dr.	John Forbes Olesen
Mr	Claus Pade
Prof., Dr.	Eigil V. Sørensen
Prof., Dr.	Jens Peder Ulfkjær
FINLAND	
Dr.	Klaus Juvas
Dr.	Matti V. Leskala
Prof., Dr.	Jussi Mattila
Mr.	Erik Nordenswan
Dr.	Jouni Punkki
ICELAND	
Mr.	Einar Einarsson
Mr.	Haukur J. Eiriksson
Dr.	Gisli Gudmundsson
Mr.	Karsten Iversen
Mr.	Sveinbjörn Sveinbjörnsson
Dr.	Jon E. Wallevik
Prof., Dr.	Olafur H. Wallevik
Prof., Dr.	Børge J. Wigum
NORWAY	
Dr.	Helge Brå
Ms.	Danielle Bosnjak
Mr.	Anton Gjørven
Mr.	Steinar Helland
Dr.	Bernt Jacobsen
Prof., Dr.	Terje Kanstad
Dr.	Terje F. Rønning
Mr.	Tor Kristian Sandaker
Mr.	Sverre Smeplass
Mr.	Hans Stemland
SWEDEN	
Prof., Dr.	Anders Ansell
Dr.	Thomas Blanksvärd
Prof.	Lennart Elfgren
Prof., Dr.	Mats Emborg
Prof., Dr.	Kent Gylltoft
Prof., Dr.	Mikael Hallgren
Prof., Dr.	Jan-Erik Jonasson
Prof., Dr.	Björn Lagerblad
Prof., Dr.	Karin Lundgren
Prof., Dr.	Tang Luping
Prof., Dr.	Per-Erik Petersson
Dr.	Peter Simonsson
Dr.	Peter Utgenannt